Delft University of Technology

# Modeling Electrode Materials
## Bridging Nanoscale to Mesoscale

Vasileiadis, Alexandros

**DOI**
10.4233/uuid:3a0da462-b912-4a60-9ff3-6f66b2cd0884

**Publication date**
2018

**Document Version**
Publisher's PDF, also known as Version of record

**Citation (APA)**
Vasileiadis, A. (2018). Modeling Electrode Materials: Bridging Nanoscale to Mesoscale DOI:
10.4233/uuid:3a0da462-b912-4a60-9ff3-6f66b2cd0884

**Important note**
To cite this publication, please use the final published version (if applicable).
Please check the document version above.

**Copyright**
Other than for strictly personal use, it is not permitted to download, forward or distribute the text or part of it, without the consent of the author(s) and/or copyright holder(s), unless the work is under an open content license such as Creative Commons.

**Takedown policy**
Please contact us and provide details if you believe this document breaches copyrights.
We will remove access to the work immediately and investigate your claim.

*This work is downloaded from Delft University of Technology.*
*For technical reasons the number of authors shown on this cover page is limited to a maximum of 10.*

# Modeling Electrode Materials

## Bridging Nanoscale to Mesoscale

**Dissertation**

For the purposes of obtaining the degree of doctor
at Delft University of Technology
by the authority of the Rector Magnificus prof. dr. ir. T.H.J.J. van der Hagen
to be defended publicly on
Thursday 27 September 2018 at 15:00 o'clock

by

**Alexandros VASILEIADIS**

Master of Science in Sustainable Energy Technology, Delft University of Technology, the Netherlands
born in Larisa, Greece

This dissertation has been approved by the promotors.

Composition of the doctoral committee:

| | |
|---|---|
| Rector Magnificus | chairperson |
| Prof. dr. E.H. Brück | Delft University of Technology, promotor |
| Dr. ir. M. Wagemaker | Delft University of Technology, promotor |

Independent members:

| | |
|---|---|
| Prof. dr. B. Dam | Delft University of Technology |
| Prof. dr. M. Huijben | University of Twente |
| Dr. F.C. Grozema | Delft University of Technology |
| Dr. ir. M.H.F. Sluiter | Delft University of Technology |
| Dr. ir. E.M. Kelder | Delft University of Technology |

The research carried out in this thesis has been financially supported by the European Research Council under the European Union's Seventh Framework Program (FP/2007-2013)/ERC Grant Agreement No. [307161].

Printed by Proefschriftmaken
Cover Design by Fenna Schaap
Copyright © 2018 by Alexandros Vasileiadis
ISBN: 978-94-93019-51-5

An electronic version of this dissertation is available at
http://repository.tudelft.nl/.

To my family

# Prologue

«πᾶσά τε ἐπιστήμη χωριζομένη δικαιοσύνης καὶ τῆς ἄλλης ἀρετῆς πανουργία, οὐ σοφία φαίνεται»

“Every form of knowledge when sundered from justice and the rest of virtue is seen to be plain roguery rather than wisdom”

Plato

Plato, *Menexenus*, 246e8 – 247a2, *Plato in Twelve Volumes*, vol. 9, translated by W. R. M. Lamb, Cambridge, MA, Harvard University Press, 1925.

## 1. Nature and Technology

In ancient Greece, two great philosophers, Plato and Aristotle, integrated in their Schools a programme to promote through research and showcase the significance of moral and political values, paired with grounding the development of the sciences[1]. Within this programme: Ethical philosophy will propose a series of values, which will be faithfully served by men in their activities, including their scientific ones. Political philosophy will define the field in which man as a political and moral being shall use the scientific domain. Therefore, at that time, not only the foundations of the sciences were set, but at the same time the foundations of a moral and political control were put into practice as a tool for promoting the well-being of the citizen and society.[2]

However, since the Enlightenment, the perception of the autonomous presence of science and its deification as an intrinsic value has prevailed, disconnected from a moral and political problem in relation to the goals and values it is intended to serve[3]. Thus, science and its applicability to technology, actually and ultimately serve non-evident values and objectives that remain hidden behind the "neutral" scientific and technological discourse and use it as a means. The results of this uncritical acceptance of science and technology also include, thanks to their decisive mediation, man's dominance over nature[4]: It is its savage exploitation and destruction with the problems that ecological thinking has already highlighted.

Nonetheless, in the past decades the dominant perception of man's prevalence over nature has been radically challenged. This challenge directs us to a real ecological resolution, where technology will be used in a way that will lead us to live in harmony rather than in conflict with nature[5]. And this will be achieved if technology treats nature as a subject rather than a raw material, if it becomes a tool that truly serves humans and respects the environment. And if, ultimately, the reflection of this ecological issue were directly related to practice.

Of course, in modern times, science and technology are so closely interdependent that they are considered the two sides of the same coin. Furthermore, we are well aware of the notion that technology does not embody values and principles on its own but it is a tool used to serve values and to achieve goals set by the people. Thus, in order to properly evaluate the relationship between technology and nature and guide it to a correct, desired direction, we need to integrate it into a wider social and humanistic context, striving to predict all its possible outcomes.

## 2. Environment and Sustainable Development

As environmental problems in the past were only local and not generalised and since we had not, perhaps, realised that man too is a part of nature, we could not foresee that the intense and systematic disturbance of ecological balance, beyond certain limits, could affect even human's life. We started realising the globality of environmental problems only in the 1960s and were forced to admit that we are in direct need of a survival policy on the planet. In other words, we need to develop a policy with the intention of bequeathing a viable planet to future generations.

It is a fact that the savage exploitation of the natural environment has led to a difficult to manage ecological crisis. It seems that the originally positive link between development and sustainability tends to turn into negative and contradictory, since uncontrolled development degrades the environment, which in turn undermines the prospects for further growth and prosperity. The undesirable side effects of this development, the environmental problems it has created and their resolution have been the concern of the Global Community many times in recent years.[6]

The idea for sustainable development[7], consolidated in 1987 by the competent World Commission[8], is precisely aimed at restoring the positive relationship between development and environment, allowing us to meet the needs of the present without, however, damaging the conditions for the future. Attention now focuses on both material levels of resource abuse and human needs with extensions to lifestyle and quality of life[9]. Sustainable development is now based on the rational management of natural resources through the convergence of economic and environmental objectives[10] and the recognition of the boundaries of science and technology. It is based on the acceptance of a sustainable society that can be flexible and wise enough not to undermine its physical as well as its social support systems. It is also based on acceptance of social and political responsibility, but also on building universal values. It focuses on promoting less energy-intensive and fairer social development[11].

## References

**1** & **2**. See in the works of Plato: Laws, Republic, Timaeus, Phaedrus, Crito, Menexenus, Meno, Politicus, Theaetetus and in the works of Aristotle: Physics, Politics, Metaphysics, Nicomachean Ethics, Rhetoric, The Organon, Mechanical Problems.

**3**. Absolute scientism became evident already in the beginning of the 17th century in the works of Francis Bacon. See: Francis Bacon, A selection of his Works, ed. Sidney Warhaft, Macmillan, Toronto, 1965, Anthony Kenny, A new history of Western Philosophy, Oxford University Press, New York, 2010.

**4**. Descartes first puts forward as the greatest value - goal man's prevalence, dominance over nature with science as an instrument. See: R. Descartes, Discourse on Method, The Philosophical Works of Descartes, trans. E. Haldane and G. Ross, New York, Dover Books, 1955.

**5**. "In harmony with Nature": An expression stemming from the first principle of the Rio Declaration: "Human beings are entitled to a healthy and productive life in harmony with nature". See also in the World Charter for Nature: The map stated that humanity is a part of nature and life depends on the uninterrupted operation of natural systems. The WCS (Wildlife Conservation Society) initiative culminated with its approval.

**6**. Stockholm Conference (1972), United Nations Conference on Environment and Development, (Rio de Janeiro, 1992), Kyoto Protocol (Kyoto, Japan 1997), United Nations Climate Change Conference, COP 6, (The Hague, Netherlands, 2000), World Summit on Sustainable Development, (Johannesburg, 2002), United Nations Climate Change Conference, COP 23, (Bonn, Germany, 2017).

**7**. The pillars of Sustainable Development are the economy, the environment and society and its goal is their equal and balanced presence. The concept and the individual notions of the term have been developed in the framework of international committees and conferences at the state level under the auspices of the United Nations.

**8**. In 1987, the World Commission on Environment and Development (WCED), published a report entitled "Our Common Future". The document came to be known as the "Brundtland Report". It developed guiding principles for sustainable development. See WCED – World Commission on Environment and Development, Our Common Future, New York, Oxford University Press, 1987.

**9**. One of the definitions of Sustainable Development is to improve the quality of life within the carrying capacity of supportive ecosystems. See in this regard: International Union for Conservation of Nature (IUCN) - United Nations Environmental Programme (UNEP) - World Wildlife Fund (WWF).

**10**. The World Bank, World Development Report 1992: Development and the Environment, New York, Oxford University Press, 1992.

**11**. The European Summit in Gothenburg (2001) adopted the first EU Sustainable Strategy to promote a democratic and just society.

# Contents

1. Introduction ........................................................................................1

1.1 Renewable Energy for a Sustainable Energy Future ............................3

1.2 A Wind of Change ..............................................................................4

1.3 The Importance of Energy Storage ......................................................5

1.4 Batteries ...............................................................................................6

1.4.1 Working Principles ..........................................................................7

1.4.2 Battery Performance .........................................................................9

1.4.3 Li-Ion vs. Na-Ion Batteries ...............................................................9

1.5 Computational Modeling ......................................................................11

1.6 Thesis Outline and Goals ......................................................................14

References ................................................................................................16

2. Methods ..................................................................................................19

2.1 Density Functional Theory ...................................................................21

2.1.1 Basic Principles ................................................................................21

2.1.2 Electron Wavefunction Approaches and Software ...............................25

2.1.3 Battery Related Property Predictions ..................................................26

2.2 Phase Field Modeling ...........................................................................30

2.2.1 Towards Battery Research .................................................................32

2.2.2 Application in Batteries .....................................................................33

2.2.3 Model Overview ...............................................................................34

References ................................................................................................39

3. The Fine Line between a Two-Phase and Solid Solution Phase Transformation and Highly Mobile Phase Interfaces in Spinel $Li_{4+x}Ti_5O_{12}$ ....................................43

Abstract ....................................................................................................46

3.1 Introduction ..........................................................................................47

3.2 Thermodynamics of Li Ions in $Li_4Ti_5O_{12}$ ............................................49

3.3 Kinetics of Li Ions in $Li_4Ti_5O_{12}$ ............................................57

3.4 Conclusions ............................................71

3.5 Methods ............................................72

References ............................................73

4. Towards Optimal Performance and In-Depth Understanding of Spinel $Li_4Ti_5O_{12}$ Electrodes Through Phase Field Modeling ............................................79

Abstract............................................82

4.1 Introduction ............................................83

4.2 Methods ............................................85

4.2.1 Parametrizing the Phase Field Model for LTO ............................................85

4.2.2 Analysis of the Overpotential ............................................88

4.2.3 Experimental Section ............................................89

4.3 Results ............................................89

4.3.1 Single LTO Particles............................................90

4.3.2 Validation of the Model, Impact of Electrode Thickness and Porosity ............................................93

4.3.3 Electrode Optimization ............................................108

4.3.4 Active Particle Fraction in LTO Electrodes............................................115

4.4 Conclusions ............................................119

References ............................................120

5. Thermodynamics and Kinetics of Na-Ion Insertion into Hollandite-$TiO_2$ and O3-Layered $NaTiO_2$: an Unexpected Link between Two Promising Anodes Materials for Na-Ion Batteries............................................129

Abstract............................................132

5.1 Introduction ............................................133

5.2 Computational Methods............................................136

5.3 Dilute-Limit Na-Ion and Li-Ion Insertion in $TiO_2$ (H) ............................................137

5.4 The Monoclinic $Na_{0.25}TiO_2$ (H) Phase ....... 143
5.5 Formation Enthalpies and the Voltage Profile ....... 145
5.6 Towards the O3 Layered $NaTiO_2$ Structure ....... 149
5.7 Na-Ion Diffusion ....... 151
5.8 Conclusive Remarks ....... 157
References ....... 159

6. Ab-initio Study of Sodium Insertion in the λ-$Mn_2O_4$ and Dis/Ordered λ-$Mn_{1.5}Ni_{0.5}O_4$ Spinels ....... 167
Abstract ....... 170
6.1 Introduction ....... 171
6.2 Computational Methods ....... 173
6.3 λ-$Mn_2O_4$ and λ-$Mn_{1.5}Ni_{0.5}O_4$ Host Structures ....... 175
6.4 Na-Ion Insertion in λ-$Mn_2O_4$ ....... 179
6.5 Na-Ion Insertion in λ-$Mn_{1.5}Ni_{0.5}O_4$ and Mn/Ni Ordering – Reaction Mechanisms Dependence ....... 185
6.6 Na-Ion Kinetics, Ni Migration and Inverse Spinel Insights via MD Simulations ....... 191
6.7 Conclusions ....... 197
References ....... 199
Summary ....... 207
Samenvatting ....... 209
Appendix ....... 213
List of Publications ....... 219
Conferences ....... 221
Acknowledgments ....... 223
Curriculum Vitae ....... 225

# 1

# Introduction

> “When the wind of change blows, some people build walls, others build windmills”
>
> Chinese proverb

## 1.1 Renewable Energy for a Sustainable Energy Future

The use of energy is currently at the heart of most human activities, and many of the environmental problems of modern societies have technologies producing and using energy as their point of reference. The key issue now emerging concerns environmental sustainability: In order for our global ecosystem to survive the ever-increasing levels of human technological and economic activity it has become apparent that it is necessary to develop a political and economic environment in which sustainable energy technologies respond to global energy challenges. A broad application of alternative technologies to achieve sustainable development and a sustainable energy future is thus required[1].

The perceived exhaustion of non-renewable mineral resources, the gradual decline in our planet's conventional energy supplies, combined with the ever-increasing demand for energy and the gradual worsening of environmental problems has led modern societies to switch to energy-saving and rational energy use and to the use of renewable energy. Such energy sources, known since the ancient times, are renewable energy reserves that can be replenished on a human timescale, while their use can be friendly to the environment (Figure 1.1). The Summits, Rio in 1992 and in Johannesburg in 2002 focused on the future of our planet and on sustainable development. These goals, which essentially concern the continuation of life on our planet, cannot be achieved without radical changes in the structure of the global energy system. At the same time, “Agenda 21”[2], endorsed by the United Nations, calls for new policies and new programs aimed at increasing the contribution of environmentally safe, reliable and low-cost energy systems. Particular mention is made of energy systems using renewable energy sources to reduce environmental impact and make more efficient use of energy, its transmission, distribution and end-use. Turning to renewable energy is the most successful sustainable development strategy.

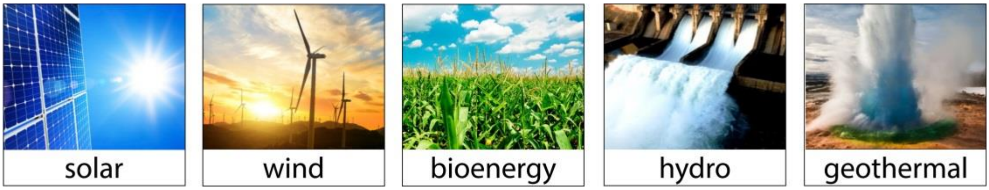

**Figure 1.1:** Main renewable energy sources

## 1.2 A Wind of Change

In the 20th century's energy model, Renewable Energy Sources (RES) were seen as complementary to fossil fuels. Today, however, the share of RES in the overall energy mix has increased significantly thanks to technological leaps, to the growing penetration of RES in industrial production and to the ever-diminishing cost of its application. A recent report by the International Renewable Energy Agency (IRENA) predicts that RES costs will fall significantly by 2020, reaching the same, if not lower, levels than fossil fuels[3]. These cost reductions are unprecedented and representative of the extent to which renewable energy is disrupting the global energy system. Turning to RES is not merely an environmentally conscious decision, but a sheer economic decision. It is clear that these new dynamics signify a compelling shift in the energy model.

**Figure 1.2:** Claude Monet, Windmills near Zaandam, 1871, Van Gogh Museum, Amsterdam, Netherlands.

These new data create the conditions for a significant shift from a fossil energy-based to an RES-based perspective, clearly evidenced by the decisions taken in recent years by the European community. In October 2014, the European

Council agreed on a new set of energy and climate targets for the period up to 2030 (European Council, 2014), including a minimum target of 27% for the share of renewable energy consumed in the EU. This agreement was followed by the Energy Union framework strategy of February 2015, which aims to make the EU "the world leader in renewable energy" (European Commission, 2015)[4]. Furthermore, the USA's recent decision to withdraw from the Paris Climate Change Agreement in December 2017, was a major catalyst for China to take the reins of renewable energy. Tim Buckley, director of IEEFA (The Institute for Energy Economics and Financial Analysis), stated: "Although China isn't necessarily intending to fill the climate leadership void left by the US withdrawal from Paris, it will certainly be very comfortable providing technology leadership and financial capacity so as to dominate fast-growing sectors such as solar energy, electric vehicles and batteries"[5].

We now see a dynamic shift towards RES that marks a new era for the energy potential of many countries around the world.

## 1.3 The Importance of Energy Storage

For the implementation of renewable energy technology, sufficient energy storage is required. This is because solar and wind energy, the two most important renewable energy sources, introduce a severe complication. Their power output is fluctuating with respect to the time and place of the power production as well as with local environmental conditions such as cloudiness and wind speed. One could think that integrating power production over large areas will effectively average out these fluctuations but even continent size grids, combining solar and wind energy, result in a strongly varying electricity generation.[6] As a result, a significant mismatch between production and demand is created.

Two significant, time related dimensions of the problem are the daily and seasonal effect. Wind and solar power availability during the day and summer is remarkably higher than the one during the night and winter respectively. In order to cancel the daily and seasonal effect we need to integrate larger areas, expanding cables from the Western to Eastern and the Northern to Southern hemisphere respectively. This approach, however, implies huge loses and is unfeasible.

A real solution can be achieved by developing efficient storage applications, both on a daily time scale as well as on a seasonal time scale[6], in order to bridge the production-demand mismatch. Energy will be sufficiently stored at times of high production and/or low demand and will be readily available for distribution at times of low production and/or high demand.

There is a wide variety of options regarding energy storage with hydrogen and electrochemical storage being the common examples of energy storage in materials. The prior, is extremely promising and suitable for long-term, strategic reserve storage and is still in early development. The latter, is ideal for daily, short term storage, and plays a key role in every aspect of today's life as it covers a wide range of applications. For the particular case of renewable energy sources, the implementation of static rechargeable batteries with high efficiency and long cycle life, similar to the one realized in Li-ion batteries[7, 8], is a viable option.

## 1.4 Batteries

Batteries are electrochemical systems that play a pivotal role in today's society enabling a vast variety of applications. Due to their high efficiency, power and energy density, batteries are widely implemented in technologically advanced applications ranging from pacemakers and cell phones (~ W) to electrical vehicles and households (~ kW). In addition, batteries for large scale storage and grid stabilization applications (~ MW) are developed in the context of renewable energy sources and sustainable development (Figure 1.3).

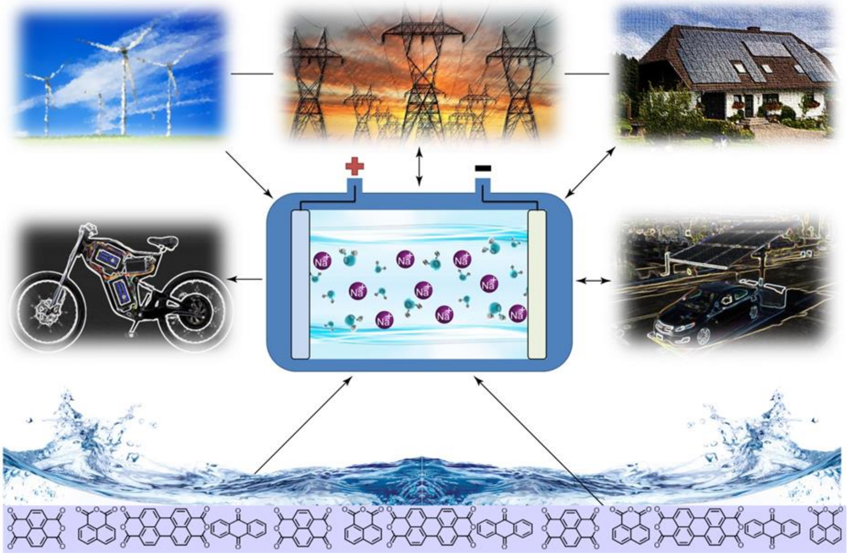

**Figure 1.3:** Illustration of various battery applications ranging from mobile applications to grid stabilization applications. The chosen illustration depicts a Na aqueous battery (battery that uses water as electrolyte and Na as a charge carrier) based on cheap organic electrode materials which is a cost-effective and environmentally friendly option.

### 1.4.1 Working Principles

Batteries convert chemical energy into electrical energy and *vice versa*. The main battery components are the anode and cathode electrode materials, electrolyte and current collectors. Every battery involves the exchange of a charge carrier between the anode and the cathode side. The most common charge carrier is the Li-ion and we will use it as an example case to explain the working principle[9]. A schematic representation of a battery along with the relevant lengthscales is presented in Figure 1.4.

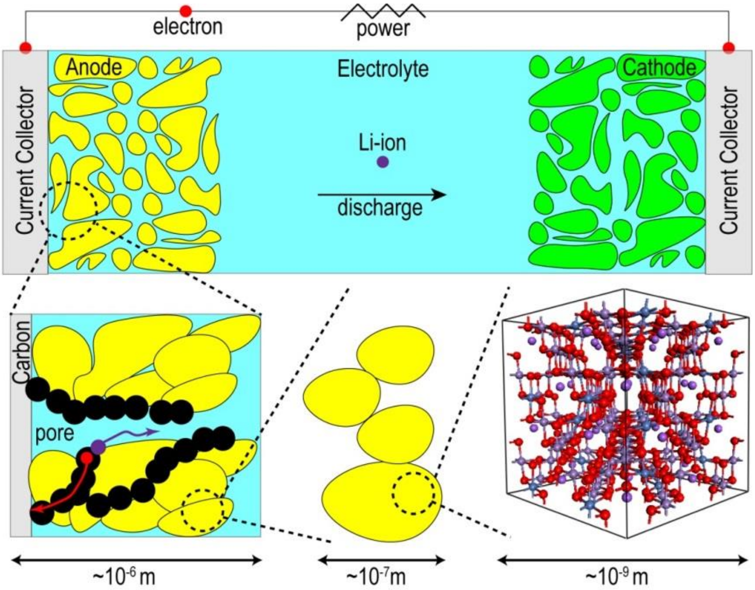

**Figure 1.4:** Li-ion battery with porous electrodes. The relevant lengthscales of the battery components are presented.

The driving force enabling discharge is the chemical potential ($\mu$) difference between the electrodes (anode and cathode). Li is initially located in the anode side at a relatively unstable energy state (high energy). Since in nature all systems relax towards the lowest energy configuration, Li experiences a driving force to leave the anode material and react with the cathode side. This is because Li is energetically more stable in the environment of the cathode, lowering the systems energy. By placing an electrolyte between the anode and the cathode we allow only Li-ions to travel through while blocking the electrons. This leads to a potential build up in the battery (open circuit voltage). By connecting the current collectors of the two sides via an application, electrons are now allowed to follow the Li-ion motion and travel to the cathode side via the outside circuit, delivering power. This process is spontaneous (discharge). During charge, energy is required to force Li-ions back to the unstable side, completing a battery cycle.

Generally, there are three ways Li-ions can react with the electrode material, namely reconstitute, decompose or insert/intercalate into it. Reconstitution and decomposition reactions are based on alloying or changing the electrode material upon ion uptake. Although, these reactions offer high Li-ion concentrations per unit formula, they cause huge structural changes that lead to mechanical failure after a few cycles. On the other hand, materials that have empty interstitial sites can act as hosts for reversible Li-ion (de)insertion without large volume changes. Those materials are encountered in almost all modern applications and as they are delivering the demanded cycle life.

The chemical potential of the electrochemical system can be found by differentiating the Gibbs free energy, $G(x)$, with respect to the Li concentration x. Under constant temperature and pressure, the open circuit voltage ($V_{cell}$), indicator of electrical work, equals the chemical potential difference between the two electrodes, indicator of chemical work.

$$V_{cell} = -\frac{\mu(x)_{cathode} - \mu(x)_{anode}}{e} \tag{1.1}$$

The theoretical maximum specific capacity (C) quantifies the number of Li-ions that an electrode material can uptake (in mAh/g) and is expressed as:

$$C = \frac{x_{max}\, F}{3.6\, M_{host}} \tag{1.2}$$

where $x_{max}$ is the maximum number of Li-ions per unit host, F is the Faraday constant, $M_{host}$ the molecular weight (grams/mol) of active material and 3.6 a conversion factor to convert C/mol to mAh/mol.

During battery operation, non-equilibrium conditions apply. Different kinetic mechanisms may limit battery performance, namely the electronic conductivity, ionic transport through the electrolyte, the charge transfer reaction over the electrolyte/electrode interface, and the solid-state transport process (Li diffusion in the solid electrode). [10] Which of these mechanisms is limiting, depends on the applied current as well as on morphological properties of the electrodes such as electrode porosity, tortuosity and thickness.

### 1.4.2 Battery Performance

Battery performance is quantified by the power and energy density and cycle life. Other important considerations include safety, environmental friendliness and cost. Which of these properties is of primary importance depends on the application. For example mobile applications prioritise very light and energy dense batteries (energy density). Energy density quantifies the amount of energy stored per weight (gravimetric) or volume (volumetric) unit. Power density, on the other hand, quantifies how fast this energy can be available and is measured in energy per time (power), per weight unit. Transport and grid stabilization applications for example, require adequate power to respond fast to the vehicle (de)charging time requirements and grid fluctuations respectively.

Static/large-scale applications prioritize cost, and cycle life while aiming in more environmentally friendly options in alignment with renewable energy sources. Cycle life quantifies the stability of the battery and refers to the number of cycles the battery can last without degrading its performance below 80% of the nominal one. Cost depends on the abundancy and availability of the materials implemented along with the complexity of the synthesis and assembling processes involved in making the battery. Finally, safety has mainly to do with the flammability of the liquid organic electrolytes and the reactivity of the electrode materials. Non-flammable and non-toxic compounds are generally preferred, especially for transport and large scale applications.

### 1.4.3 Li-Ion vs. Na-Ion Batteries

Having established the criteria of selecting the right battery chemistry for a specific application we will introduce the state-of-the-art Li-ion batteries in comparison with the Na-ion battery technology which is an alternative uprising chemistry.

Since first introduced in the early 90s, Li-ion batteries have dominated the market of mobile and transport applications. Li-ion batteries enabled next generation mobile phones and laptop computers along with high performing electrical vehicles, offering high energy density and long cycle life. Their cell cost has decreased by a factor of 5 in the last 30 years (from 1000 € kWh$^{-1}$ to 200 € kWh$^{-1}$)[11] due to continuous research and scaling up production. Currently, Li-ion batteries are considered a suitable option regarding medium and large-scale storage as well. This is demonstrated by the commercially available kWh of Li-ion batteries in households, for example storing solar energy[12, 13] and by grid stabilization applications, covering the mismatches between energy demand and renewable energy generation (~100 MWh batteries)[14, 15].

The success of the Li-ion battery has to do with the electropositive property of the Li element which, in addition, is very light and has a relatively small ionic radius. Thus, upon insertion in both layered and 3D oxide and phosphate electrode materials, the host structure remains relatively intact, causing volume changes in the order of a few percent (~ 5%) typically resulting in a long cycle life. Another advantage is the high operating voltage, around 3.6 V, leading to a high energy density. In addition, Li-ion batteries have a high storage efficiency, a low self-discharge rate and a wide temperature range of operation.

Despite the so-far unchallenged status of Li-ion batteries, looking into the future raises several concerns. Li-ion batteries utilize organic electrolytes based on relatively expensive Li-salts. The Li-ion battery production processes are costly, requiring an oxygen and water free environment.[16, 17] Further, the expected mass production of electric vehicles will create a tremendous rise in material demands. It appears often controversial if Li is abundant enough to cover the future needs. What is of no dispute is the accessibility of Li world-wide, where the majority is localized in just a few countries in Latin America and China. This creates a high risk in the supply chain.[18] Finally, the use of organic electrolytes compromises safety issues based on their flammability, causing accidents by overcharging or by piercing the battery[19].

In this context, Na-ion and Na-aqueous batteries are highly appealing due to the larger abundancy and better accessibility of sodium. This is reflected in the much cheaper Na-salts compared to the Li counterparts.[20] If Na is combined with cheap and environmentally friendly electrodes it makes a great case for large scale applications. Further, Na, being in the same chemical group with Li, is expected to have a similar electrochemical behaviour speeding up the identification process of possible host materials. Furthermore, replacing the organic electrolyte with water (Na-aqueous) will eliminate the flammability risks, albeit at the cost of energy density.

The key challenge for Na-ion batteries is structural stability. Na has a larger ionic radius than Li leading to large volume changes and stresses upon insertion reducing the cycle life of the battery. Thus, stable host materials are needed. The Na-ion redox potential is thermodynamically lower by 0.3 V compared to Li but due to the energy penalties related to structural distortions caused by Na-ion insertion this voltage difference is often larger (~0.6 V). The lower voltages for aqueous chemistries result in lower energy densities, which is not, however, a priority for large scale storage. Finally, when considering the Na-aqueous chemistry we need also to consider the stability window of water.[21]

## 1.5 Computational Modeling

Computational modeling is the use of computers to study the behaviour of complex systems based on mathematical, physical and computer science principles.[22] The modeling field is experiencing a tremendous growth over the last decades. As computational power increases, modeling is becoming a more common approach in many research groups while it is also becoming more widely implemented in companies. This indicates that besides the pure scientific drive, computational modeling can "make money" or to put it accurately "save money". The applicability of computational modeling has a tremendous range. Material science, biology, atmospheric science, aerospace engineering and seismology are a few examples.

The success of modeling can be understood by examining its main attributes and capabilities. The number one reason is control. We can view modeling as an experiment in a controlled environment. Via modeling we can isolate the property/process/phenomenon of interest and figure out how it affects the system achieving in-depth understanding. Further, modeling can be used to predict properties before doing the experiments. A model, that has been proven to work for a system, can be used to predict the response of the system to changing conditions/parameters. Furthermore, modeling can sometimes study systems for which experiments are simply too difficult to be conducted. Take for example the study of phase transformations in the earth's inner core[23], a system where pressure and temperature are extremely difficult to replicate in the lab. Modeling can also accelerate and catalyse research and save resources by allowing scientists to conduct thousands of computations in order to identify the right experiments that will maximize the impact in finding the solution to the problem being studied. It is important to remember that the goal of modeling is to guide experiments and not to replace them. In fact, modeling and experiments can become different sides of the same coin where the one is a critical verification of the other and *vice versa*.

We have established that modeling can save time, money, and materials, by studying a problem in the computer rather than in the laboratory. One very important prerequisite, however, is the development of reliable models that can adequately simulate the real problem. Considering the complexity and enormous amount of processes and parameters in a real battery, this is not an easy task.

Models need to include many assumptions and approximations to simplify the problem and simulate reality adequately. Testing these approximations is of primary importance to check the liability of the model. The difficulty of approaching reality was nicely expressed by Professor Gerbrand Ceder, who posed a clear distinction between modeling and simulation, stating that the two concepts are not to be confused with each other.[23] Full reality is too complex to "simulate" so that we can only effectively isolate specific parts of it and perform computations based on a model. This underlines once more that computational modeling requires a careful examination as for what parameters are important to include in the model. As a result, for an effective computation one must truly understand the science of the field of application.

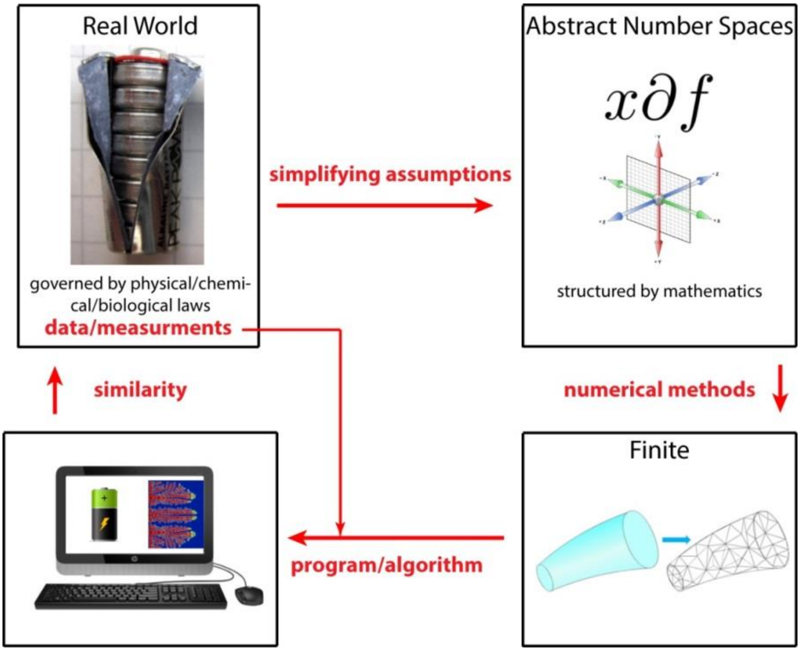
Real World
governed by physical/chemical/biological laws
data/measurments
simplifying assumptions
Abstract Number Spaces
$x\partial f$
structured by mathematics
similarity
numerical methods
Finite
program/algorithm

**Figure 1.5:** Schematic illustration of the steps required to develop a computational model.

A typical computational model[24] can be summarized in the scheme presented in Figure 1.5. We first consider a part of the real world of which the model is to be set up. The physical concepts of this reality are then formulated into a mathematical model, which is an equation or set of equations whose solution describe the physical behaviour of the physical system. For instance, Maxwell's equations describe electrodynamic phenomena and Schrodinger’s equation describes quantum phenomena. This leads to a mapping of the real world that is represented in an continuous, abstract number space where real numbers are represented as symbols.

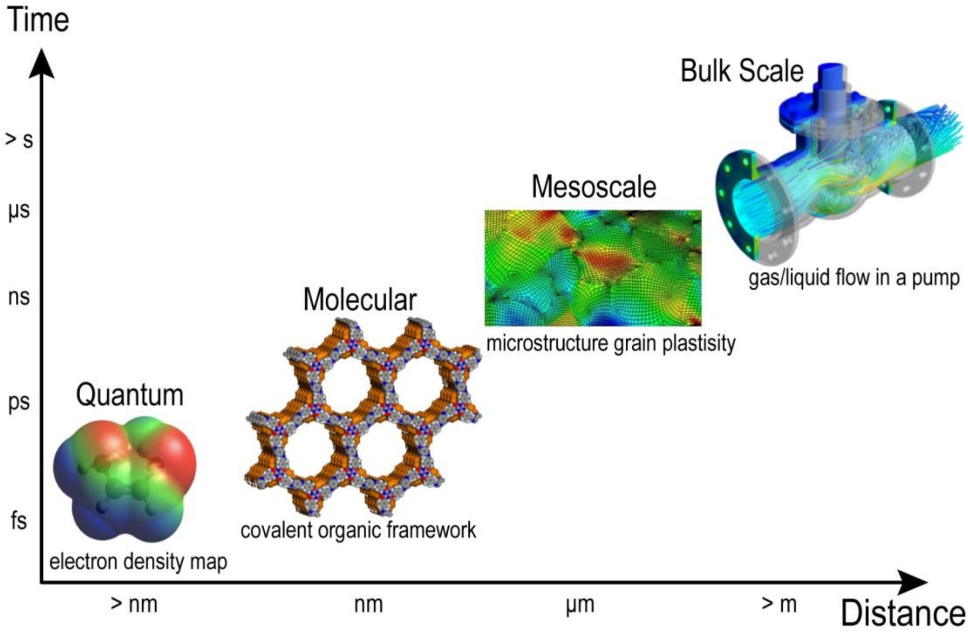
Time
> s
μs
ns
ps
fs
Bulk Scale
gas/liquid flow in a pump
Mesoscale
microstructure grain plastisity
Molecular
covalent organic framework
Quantum
electron density map
> nm
nm
μm
> m
Distance

**Figure 1.6:** Classification of computational models with respect the lengthscales and timescales.

To move towards a computational model we need to approximate the mathematical model. Since computers have a finite amount of memory, a discrete space or grid containing a finite number of points needs to be constructed. In order to provide solutions to the discretized system, the numerical approach is required. Solving numerical relations is not always trivial as they might not converge to the exact solution or become unstable. This requires numerical analysis of the implemented approximations. The computer is the final stage of this scheme. Smart algorithms written in a high-level programming languages are employed to provide solutions. Input parameters in the computational model usually come from data/ measurements performed on the real system. Finally, the results obtained from the computational model need to be rationalized and compared with the behaviour of the real systems.

Modeling is usually categorized with respect to the length and time scale it covers. For example one way to categorize simulations is quantum, molecular (atomistic), mesoscale, and bulk according to the length scale the model is suitable for (Figure 1.6). This means the same model can study systems of various fields (e.g. chemistry, biology) as long as the length scale is applicable.

## 1.6 Thesis Outline and Goals

Batteries are complex systems affected by many, often interconnected, microscopic and macroscopic parameters. Studying these thermodynamic and kinetic properties is critical to achieve deeper understanding of the fundamental processes and improve battery performance. For this purpose, scientists employ both experimental and computational techniques.

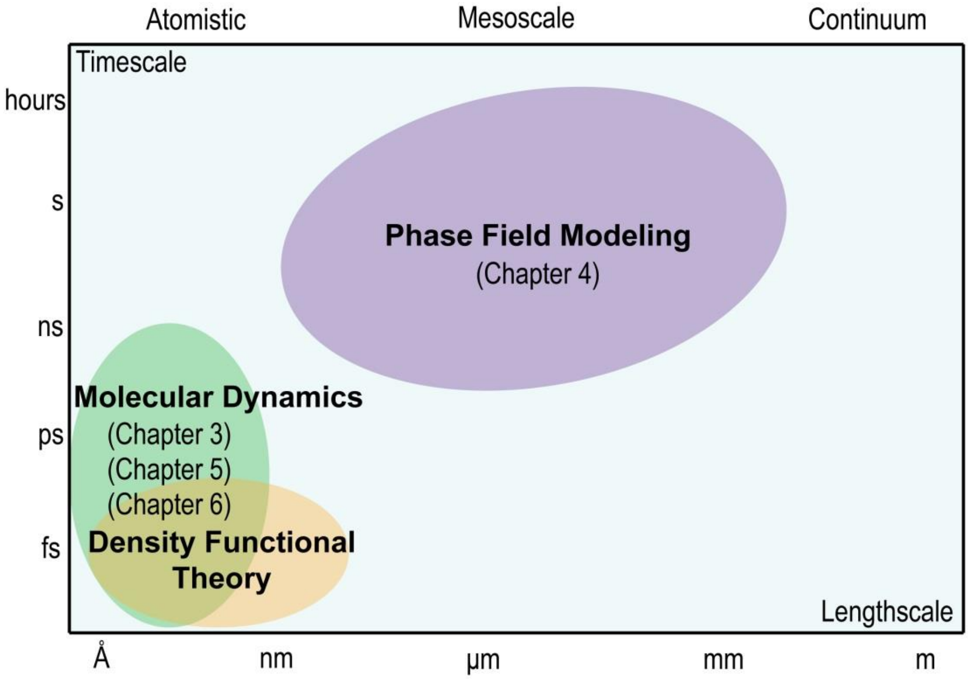
Atomistic
Mesoscale
Continuum
Timescale
hours
s
ns
ps
fs
Phase Field Modeling
(Chapter 4)
Molecular Dynamics
(Chapter 3)
(Chapter 5)
(Chapter 6)
Density Functional Theory
Lengthscale
Å
nm
μm
mm
m

**Figure 1.7:** mapping of the chapters of the thesis with respect the lengthscale and timescale as well as the method used.

The main focus of this thesis is the comprehensive, thermodynamic and kinetic understanding of battery electrode materials via nanoscopic and mesoscopic modeling. With nanoscopic molecular modeling we describe the chemical systems at atomic level of detail and with mesoscale modeling we employ finite volume methods and non-equilibrium thermodynamics to study microstructures of electrode materials in complete battery systems.

In Chapter 2, the implemented computational methods are presented. Basic Density Functional Theory (DFT) principles are introduced along with its capabilities for battery research. Further, mesoscale modeling principles are discussed and the Phase Field Modeling method is presented.

In the first half of the thesis (Chapters 3 & 4) , the properties of $Li_4Ti_5O_{12}$ (LTO), an extremely stable anode material for Li-ion batteries, are explored. This is done by Density Functional Theory at the nanoscale (Chapter 3) and Phase Field Modeling at the mesoscale (Chapter 4). Key properties explored by atomistic modeling (DFT) are integrated into mesoscale modeling (Phase Fields), creating a consistent description that eliminates the fitted, unknown parameters. In this way, a step forward towards a complete, consistent and thorough description of the material is taken.

The second half of the thesis explores the Na-ion battery chemistry, an alternative to Li-ion, that is more suitable for large scale applications. Using DFT modeling we study key thermodynamic and kinetic properties of both anode (Chapter 5) and high voltage cathode (Chapter 6) materials. The detailed atomistic picture gives us insight regarding the phase stability, structural characteristics and reaction mechanisms. DFT based Molecular Dynamics computations unravel the kinetic mechanics and allow calculations of energy barriers for Na-ion diffusion. Thus a clear picture on the limitations of the electrode materials is drawn.

In retrospect, the current thesis bridges the gap between two length-scales (nanoscale, mesoscale) by allowing implementation of fundamental properties determined with atomistic DFT calculations, such as the Gibbs free energy, in the mesoscale phase field model. The work presented herein can set the foundation for applying the same approach in different electrode materials as well as solid electrolyte materials. In addition, it explores the limitations of Na-ion battery technology for large scale applications toward a renewable energy future. In Figure 1.7 the thesis content is presented with respect to the timescale and lengthscale as well as the methodology used.

## References

**1**. The five priority areas adopted in the 1997 Nairobi Declaration (UNEP) also include the transfer of technology, in which efforts are being made to develop a political and economic environment where sustainable energy can respond to global energy challenges. (UNEP, *Annual Review*, Nairobi, Kenya: United Nations Environment Programme, 1997). Changing the behaviour and attitude of financial institutions to support investment in sustainable energy technologies is a constituent element of UNEP's Sustainable Energy Initiative (SEFI).

**2**. Agenda 21: Programme of Action for Sustainable Development: Rio Declaration on Environment and Development, United Nations Publications, 1993.

**3**. Renewable Power Generation Costs in 2017, IRENA Publications, January 2018.

**4**. Renewable Energy Prospects for the European Union: https://www.irena.org/-/media/Files/IRENA/Agency/Publication/2018/Jan/IRENA_REmap_EU_preview_2018.

**5**. Helen Davidson, China on track to lead in renewables as us retreats, report says, *The Guardian* https://www.theguardian.com/environment/2018/jan/10/china-on-track-to-lead-in-renewables-as-us-retreats-report-says.

**6**. Mulder, F. M. Implications of diurnal and seasonal variations in renewable energy generation for large scale energy storage. *J. Renewable Sustainable Energy* 2014, 6, 033105.

**7**. Kim, S. K.; Seo, D. H.; Ma, X. Electrode Materials for Rechargeable Sodium-Ion Batteries: Potential Alternatives to Current Lithium-Ion Batteries. *Adv. Energy Mater.* 2012, 2, 710-721.

**8**. Lee, D. H., Xu, J. and Meng, Y.S. An advanced cathode for Na-ion batteries with high rate and excellent structural stability. *Phys. Chem. Chem. Phys.* 2013, 15, 3304.

**9**. TU Delft course: Energy Storage in Batteries (CH3222SET), instructor: Dr.ir. M. Wagemaker, 2018.

**10**. de Klerk, N. J. J.; Vasileiadis, A.; Smith, R. B.; Bazant, M. Z.; Wagemaker, M. Explaining key properties of lithiation in TiO2-anatase Li-ion battery electrodes using phase-field modeling. *Phys. Rev. Mater.* 2017, 1, 025404.

**11**. Nayak, P. K.; Yang, L. T.; Brehm, W.; Adelhelm, P. From Lithium-Ion to Sodium-Ion Batteries: Advantages, Challenges, and Surprises. *Angew Chem. Int. Edit.* 2018, 57, 102-120.

**12**. SolarEdge, *StorEdge Solution Applications: Connection and Configuration Guide*, 2016.

**13**. NRECA *Technology Advisory – Tesla Energy PowerWall*; National Rural Electric Cooperative Association, 2015.

**14**. EnergyStorage, AES Advancion® Fleet Accelerates Energy Storage Market in Europe, 2016.

**15**. NL, E. S. Het Amerikaanse AES wil opslag in Zeeland bouwen als vermogen voor primaire reserve Tennet 2015.

**16**. Pan, H. L.; Hu, Y. S.; Chen, L. Q. Room-temperature stationary sodium-ion batteries for large-scale electric energy storage. *Energy Environ. Sci.* 2013, 6, 2338-2360.

**17**. Wood, D. L.; Li, J.; Daniel, C. Prospects for reducing the processing cost of lithium ion batteries. *J. Power Sources* 2015, 275, 234-242.

**18**. Kundu, D.; Talaie, E.; Duffort, V.; Nazar, L. F. The Emerging Chemistry of Sodium Ion Batteries for Electrochemical Energy Storage. *Angew. Chem.* 2015, 54, 3431-3448.

**19**. Kim, H.; Hong, J.; Park, K. Y.; Kim, H.; Kim, S. W.; Kang, K. Aqueous Rechargeable Li and Na Ion Batteries. *Chem. Rev.* 2014, 114, 11788-11827.

**20**. Palomares, V.; Casas-Cabanas, M.; Castillo-Martinez, E.; Han, M. H.; Rojo, T. Update on Na-based battery materials. A growing research path. *Energy Environ. Sci.* 2013, 6, 2312-2337.

**21**. Whitacre, J. F.; Wiley, T.; Shanbhag, S. An aqueous electrolyte, sodium ion functional, large format energy storage device for stationary applications. *J. Power Sources* 2012, 213, 255-264.

**22**. Computational Modeling, National Institute of Biomedical Imaging and Bioengineering, 2016, https://www.nibib.nih.gov/science-education/science-topics/computational-modeling

**23**. MIT course 3.320, Atomistic Computer Modeling of Materials, G. Ceder, 2009, online: https://www.youtube.com/watch?v=tynCH4dosA8&t=1620s

**24**. TU Delft course: Computational Modelling of Flow and Transport (CIE4340), instructor: Dr.ir. M. Zijlema , 2017.

# 2

# Methods

«ἐπεὶ δὲ φανερὸν ὅτι τῶν ἐξ ἀρχῆς αἰτίων δεῖ λαβεῖν ἐπιστήμην ... δῆλον δή ὃτι ἡμῖν τὰ πρῶτα ἐπαγωγῇ γνωρίζειν ἀναγκαῖον»

“It is clear that we must obtain knowledge of the primary causes ... thus it is plain that we must get to know the primitives by induction”

Aristotle

Aristotle, *Metaphysics*, A, 983a 24-25, translated by Hugh Tredennick, Harvard University Press, Cambridge, MA, 1989 and Aristotle, *Posterior Analytics*, B, 100b 3–5, translated by J. Barnes, Claredon Press, Oxford, 1993.

## 2.1 Density Functional Theory

Density functional theory (DFT) is a quantum mechanical modeling method used to study the electronic structure of matter. It is applied in various scientific fields such as physics, chemistry and material science and has been recognized as the most successful way of studying many-body systems such as molecules, crystals and classical fluids.[1]

Obtaining the quantum mechanical wavefunction of a given system would, in principle, provide all the necessary information to describe it. An exact solution of the Schrödinger equation, however, is possible only for single electron systems like the hydrogen atom. DFT, using the electron density as its main property, offers an approximate solution for the time-independent, non-relativistic, Schrödinger equation in order to obtain the wavefunction and thus determine the ground state of the many-body system. The ground state is the most stable configuration of the system, having the lowest energy amongst all other configurations. Knowing the ground state (total energy and electronic charge density) allows the computation of all fundamental material properties.

DFT simulations are best-suited for the atomistic length-scales, studying systems ranging from Angstroms to nanometers and may include in extreme cases up to a few hundred atoms. As computational power increases the capabilities of DFT increases as well.

### 2.1.1 Basic Principles[1, 2]

As mentioned above, the main objective in computational chemistry is to determine the ground state of a collection of particles, for example a crystal. This requires to solve the the many-body Schrödinger equation (equation 2.1) where

$$\hat{\mathrm{H}}\psi(\{\mathbf{r}_\mathrm{i}\},\{\mathbf{R}_\mathrm{i}\}) = \mathrm{E}\psi(\{\mathbf{r}_\mathrm{i}\},\{\mathbf{R}_\mathrm{i}\}) \qquad 2.1$$

$\hat{\mathrm{H}}$ is the Hamiltonian energy operator that includes kinetic and Coulombic potential contributions, $\psi$ is the wave function and E the energy. It is evident form equation 2.1 that studying an atom (i) of the system requires the knowledge of the nucleus position ($\mathbf{R}_\mathrm{i}$) as well as the electron position ($\mathbf{r}_\mathrm{i}$). The first step toward simplifying the problem is the Born-Oppenheimer approximation.[3] Considering that the electron mass is thousands times smaller than the mass of the nucleus, similar forces will result to a quite uneven distribution of kinetic energies. Thus, within typical nuclear motion timescales, the rapidly moving electron cloud is assumed to respond faster to the changes of its surroundings, relaxing instantaneously to the ground-state configuration. The above assumption is formulated in the Born-Oppenheimer approximation which separates electronic and nuclear motion, allowing the Schrödinger equation to be initially solved for the electrons while considering the atomic nuclei fixed. The decoupling of the wavefunction is shown in equation 2.2.

$$\psi(\{\mathbf{r}_i\},\{\mathbf{R}_i\}) \rightarrow \psi_{elec}(\{\mathbf{r}_i\} + \psi_{Nuc}\{\mathbf{R}_i\}) \qquad 2.2$$

So far we have seen that the many particle problem can be reduced into solving the Schrödinger equation for electrons (equation 2.3).

$$\hat{H}\psi(\mathbf{r}_1,\mathbf{r}_2,\mathbf{r}_3,..,\mathbf{r}_N) = E\psi(\mathbf{r}_1,\mathbf{r}_2,\mathbf{r}_3,..,\mathbf{r}_N) \qquad 2.3$$

The Hamiltonian in the above expression has now an electron focus and consists from the following contributions (equation 2.4):

$$\hat{H} = -\frac{\hbar}{2m_e}\sum_{i}^{N_e}\nabla_i^2 + \sum_{i}^{N_e} V_{ext}(\mathbf{r}_i) + \sum_{i=1}^{N_e}\sum_{j>1} U(\mathbf{r}_i,\mathbf{r}_j) \qquad 2.4$$

The first term represents the kinetic energy, the second term captures the nuclei-electron interactions that are experienced by the electron as an external potential. The third term captures the electron–electron repulsions.

Let’s now consider a realistic example. We are interested in the properties of a large organic molecule like naphthalene diimide. The molecule consists of 16 C, 10 H, 4 O and 2 N atoms which adds up to a total of 152 electrons. Considering that each electron is described by three spatial coordinates the Schrödinger equation becomes a 456 dimensional problem. Scaling is quite apparent, one can imagine that the examination of crystal structures or nanoclusters that contain hundreds of atoms would create thousands of dimensions making it extremely difficult to approach the many-body Schrödinger equation for all practical materials. This is where the importance of density functional theory kicks in. In DFT the most fundamental property is the electron density, a function of just 3 spatial dimensions. The electron density can be defined through the wavefunction (equation 2.5).

$$n(\mathbf{r}) = \psi^*(\mathbf{r}_1,\mathbf{r}_2,\mathbf{r}_3,..,\mathbf{r}_N)\psi(\mathbf{r}_1,\mathbf{r}_2,\mathbf{r}_3,..,\mathbf{r}_N) \qquad 2.5$$

Before we dive in the core of DFT we will introduce the orbital approximation. The orbital approximation, allows any electron to be treated as a point charge in the field created by all other electrons, thus simplifying the many electron problem into many one electron problems (equation 2.6):

$$\psi(r_1, r_2, r_3, .., r_N) = \psi(r1) * \psi(r2) * \psi(r3) * \ldots * \psi(r_N) \qquad 2.6$$

so that the electron density can be redefined in terms of all the single electron wavefunctions (equation 2.7).

$$n(\mathbf{r}) = 2\sum_i \psi_i^*(\mathbf{r})\psi_i(\mathbf{r}) \qquad 2.7$$

We are approaching now the heart of DFT that is expressed through two fundamental theorems by Hohenberg and Kohn.[4] The first theorem states that the ground state energy E is a unique functional of the electron density (equation 2.8).

$$E = E[n(\mathbf{r})] \qquad 2.8$$

In other words, the electron density uniquely determines the ground state energy. This, one to one, correlation is of great importance reducing an otherwise unsolvable problem with thousands of dimensions into a three dimension problem. The second theorem gives us a direction on how to find the electron density stating that the electron density that minimizes the energy of the overall functional is the true ground state electron density (equation 2.9).

$$E[n(\mathbf{r})] > E_0[n_0(\mathbf{r})] \qquad 2.9$$

This means that if the true energy functional form is known then the electron density can be varied until the energy of the functional becomes minimum. Thus, the question has now become: how to find the energy functional?

The energy functional can be split into two terms:

$$E[\{\psi_i\}] = E_{known}[\{\psi_i\}] + E_{XC}[\{\psi_i\}] \qquad 2.10$$

$E_{known}$ is the known energy functional term including all the known contributions, namely the electron kinetic energy and all the Coulomb potential contributions (electron - nuclei, electron – electron, nuclei-nuclei interactions).

$E_{XC}$ is the exchange correlation functional and basically includes all the quantum mechanical interactions between electrons. This functional is not known and thus in all DFT calculations it needs to be approximated. The most common approximations are the Local Density Approximation (LDA) and the Generalized Gradient Approximation (GGA).[5] The exchange correlation functional is a function of the electron density in the case of LDA. LDA fails however to capture systems where the electron density changes very rapidly. GGA, being an upgrade of LDA, is a function of both the electron density and the gradient of the electron density. In the past a lot of effort is put to improve the exchange correlation functional description producing a considerable amount of approximations.[6] The functional choice is one of the most important choices when performing a DFT calculation and depends on the property of interest.

One year after the Hohenberg and Kohn theorems, Kohn and Sham proposed a way of obtaining the ground state electron density.[7] The Kohn-Sham scheme is based on solving a set of single-electron wave functions that only depend on three spatial dimensions ($\psi_i(\mathbf{r})$). These sets of functions are not interacting with each other since the effect of one electron to another is implicitly accounted for in the potentials introduced in each equation (equation 2.11).

$$\left[-\frac{\hbar}{2m_e}\nabla^2 + V_{ext}(\mathbf{r}) + V_H(\mathbf{r}) + V_{XC}(r)\right]\psi_i(\mathbf{r}) = \varepsilon_i(\mathbf{r})\psi_i \qquad 2.11$$

In equation 2.11 we recognize once again the kinetic contribution, external potential contribution (Coulombic electron – nuclei interaction) and the unknown exchange correlation potential capturing quantum mechanical interactions. The new term here is the Hartee potential $V_H(\mathbf{r})$ which is basically a term defined by the electron density $n(\mathbf{r})$ and captures the electron interactions with the electron density.

Ultimately, we have reached a point where: to solve the Kohn-Sham set of equations (2.11), we need to define the Hartree potential, and to define the Hartree potential $V_H(\mathbf{r})$ we need to know the electron density $n(\mathbf{r})$. But to find the electron density, we must know the single-electron wave functions, and to know these wave functions we must solve the Kohn-Sham equations.

To break this loop we can follow the following, self–consistent, scheme. An initial, trial electron density, $n(\mathbf{r})$, should be defined. Then by solving the Kohn–Sham equations using the trial electron density we can obtain the single-particle wave functions $\psi_i(\mathbf{r})$. Now it is possible to calculate the electron density based on the single electron wave function definition (equation 2.7). Finally, we compare the calculated electron density and the one initially assumed. If the two densities are the same, then this is the ground-state electron density, and it can be used to compute the total energy. If the two densities are different, then the trial electron density must be updated in some way and we must start again until we reach self-consistency (Figure 2.1).

Once the electron ground state is obtained it is relatively easy to compute the forces on the ions. Ions then are moved according to those forces following the steepest decent toward the ionic ground state.

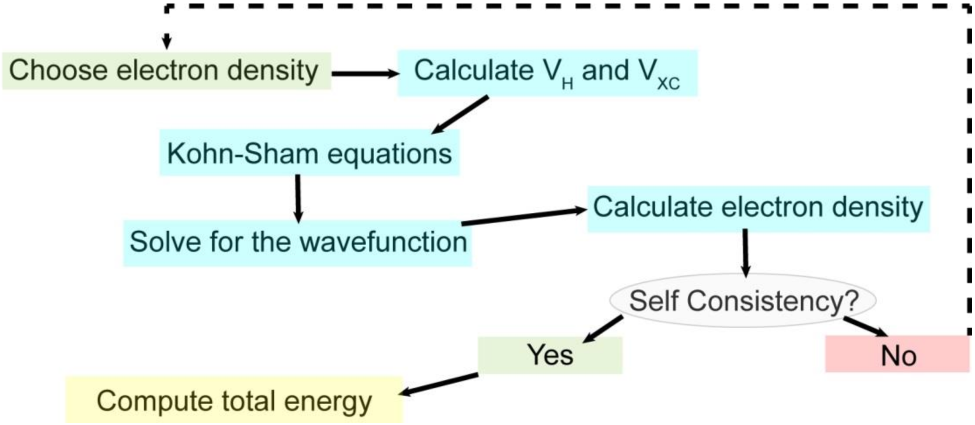

**Figure 2.1:** Schematic overview of the Kohn and Sham scheme.

### 2.1.2 Electron Wavefunction Approaches and Software

Solving the Kohn and Sham scheme is carried out by implementing the problem in the computer. To do so we need to approach the electron wavefunction in an suitable numerical way. This is done by defining a basis set. A basis set is a set of functions that algebraically represents the electronic wave function for efficient implementation on a computer. The more functions we include in a basis set the more accurate and closer to the real description we get. At the same time, however, we increase the needed computational time.

There is no mathematical restriction on how to approach the wave function. The two most common ways are the all-electron numerical orbital description and the plane wave description. In this thesis we focus on the latter.

Most battery materials are crystalline. A crystal is a periodic arrangement of atoms and can be described by a periodic potential. In addition, a free electron can be represented by a plane wave. When an electron exists in a periodic environment its wave is perturbed. Thus, the electron plane wave is modulated by the periodic potential of the crystal (Bloch wave description).

According to Bloch's theorem, electronic wavefunctions can be infinitely expanded in terms of a discrete plane-wave basis set. Numerically, it is impossible to deal with infinite sums, thus there should be a cutoff. Each plane wave has a kinetic energy proportional to the square of the wave vector. We set the program to include only plane waves that have kinetic energies that are smaller than a cutoff energy. The choice of the cutoff energy must be tested with respect to energy convergence in calculations.

Anohter important concept is the k-point, describing how the calculation is divided over the first Brillouin zone (reciprocal space). We could go in more details on the concepts of the reciprocal lattice and Bloch wave formulations but this deviates from the scope of a general introduction.

There is a wide variety of commercial source codes available that can run DFT calculations. The main classification of the codes is done by the way they approach the electron wavefunction (electron orbital or plane waves). Herein, the VASP commercial package is implemented.

### 2.1.3 Battery Related Property Predictions[8, 9]

From the wide range of DFT applications we will now focus on batteries. This section lists various possibilities for studying electrode and electrolyte materials. The most basic calculation is the energy minimization of the atomic configuration of interest, referred to as “structure relaxation”. DFT relaxations occur at the temperature of 0 K. Using the obtained energy (property of the ground state) as a starting point, many fundamental thermodynamic and kinetic properties can be predicted. An overview of the various options is presented in Figure 2.2.

#### Host Structure – Predicting New Materials

In order to perform a DFT calculation on a material we need to know its crystal structure (or molecular configuration) and composition. Structure and composition are two independent inputs in DFT giving the user the power of easily composing new materials that can potentially outperform or improve the state-of-the-art ones. Computational exploration of materials is considered faster than experimental preparation and testing thus saving time and resources. An efficient approach that is often encountered in literature is picking a crystal lattice family (space group) as a starting point and systematically vary the composition. For example, consider the transition metal spinel structure $M_2O_4$ where M can be varied between Mn, Ti, Ni, Co transition metals. Relaxation of the constructed configurations will provide useful information of structural and electronic characteristics while comparison between energies, knowing that the lowest one points to the preferred configuration, will give insight regarding phase stability. DFT is usually very sensitive to parameter choices such as cutoff energy and k-points and thus a reliable comparison must involve the same parameters.

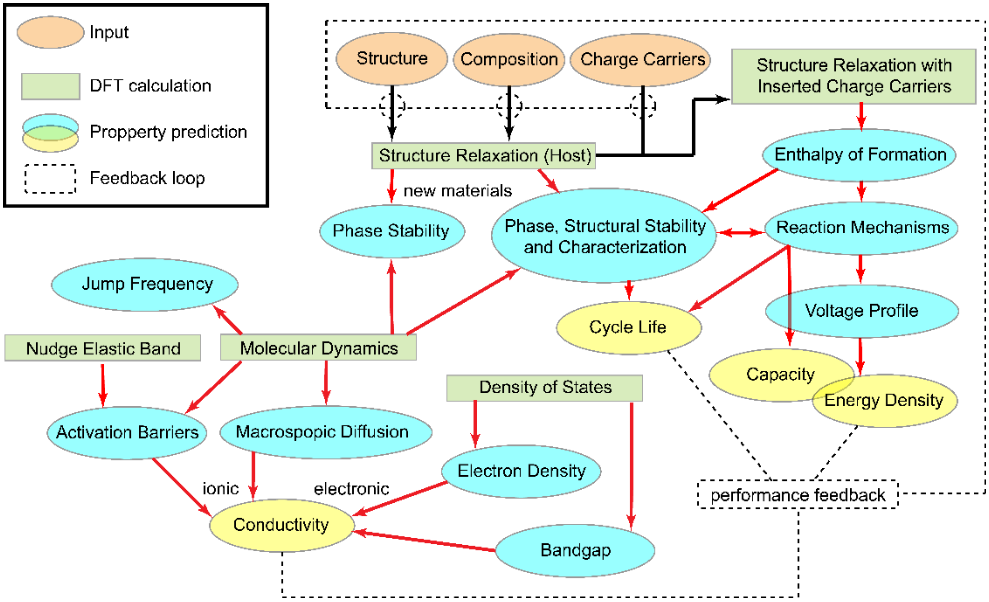
Input
DFT calculation
Propperty prediction
Feedback loop
Structure
Composition
Charge Carriers
Structure Relaxation with Inserted Charge Carriers
Structure Relaxation (Host)
Enthalpy of Formation
new materials
Phase Stability
Phase, Structural Stability and Characterization
Reaction Mechanisms
Jump Frequency
Cycle Life
Voltage Profile
Nudge Elastic Band
Molecular Dynamics
Capacity
Density of States
Energy Density
Activation Barriers
Macrospopic Diffusion
Electron Density
ionic
electronic
performance feedback
Conductivity
Bandgap

**Figure 2.2:** Schematic overview of battery related DFT calculations.

For an existing material, comparison between the experimental interatomic distances, angles, volume and lattice parameters is the first quality test of whether the computation was successful or not. In the case of a new material, this is the first evaluation regarding stability as well, at least at 0 K. This is done by checking if the material remained in the intended symmetry and by checking if all the bond lengths are realistic.

### Charge Carrier Insertion

Simulating a battery requires ion insertion in the lattice of the host structure. This is done by recognising possible interstitial positions (free space within the crystal) where charge carriers can be accommodated. These positions are usually identified and classified (Wyckoff notations). The most important charge carrier in the current era is Li and thus we will use Li for the rest of this section as an example case. Other charge carriers such as Na or the multivalent Mn and Zn are computationally investigated rapidly in the last decade as well.

Li is placed within the host structure throughout the lithiation range of the studied material starting from an empty to a fully lithiated host. For example, if the studied unit cell contains 16 formula units of $MnO_2$, so in total 48 atoms ($Mn_{16}O_{32}$), we can place 1 Li per Mn so that in total we can study 16 discrete phases (Li concentration steps) to reach the fully lithiated structure (x = 1 in $Li_xMnO_2$). For each concentration step, in order to determine the lowest energy configuration we must relax all the inequivalent positions of Li placement. The lowest energy between them will be the most probable structure at this particular concentration.

## Enthalpies of Formation – Stable Phases – Reaction Mechanisms

The lowest energy, however, can only give an indication of which phase (Li concentration step) will be stable during battery operation. The most relevant quantity is the enthalpy of formation ($\Delta_f E$). Using the total crystal energy as a starting point we can determine the relative stability of the intermediate phases through equation 2.12:[10, 11]

$$\Delta_f E = E_{Li_x Host} - x E_{Li_{x_{max}} Host} - (1 - x) E_{Host} \qquad 2.12$$

$\Delta_f E$ represents the relative stability of a particular configuration, $E_{Li_x Host}$ is the total crystal energy of the particular configuration with x fractional lithium concentration. $E_{Li_{x_{max}} Host}$ is the energy of the fully lithiated structure and $E_{Host}$ is the energy of the empty host. The enthalpy of formation can be viewed as the Gibbs free energy without entropy.

Configurations with a negative formation enthalpy are thermodynamically favourable compared to the endmember configurations (reference phases) and thus are likely to appear during the lithiation process. This does not mean, however that they will occur necessarily. In order to find the stable phases we need to construct a set of lines called convex hull. The convex hull can be viewed as the free energy at 0 K. The lines connect the lowest energy phases throughout the lithiation range following the lowest enthalpy path. This means that certain phases (lowest energy configuration at a certain concentration) might be skipped since the material will choose to lower its energy path by phase separating into Li-poor and Li-rich phases upon lithiation.

Thus, knowing the convex hull gives us direct information of the reaction mechanisms during lithiation (homogenous vs. phase separation). Phase separation is the result of a first-order phase transition where the first derivative of the free energy (chemical potential) with respect to some thermodynamic variable (in this case Li concentration) exhibits discontinuity. The voltage curve, kinetic performance and cycling stability depend on whether the lithiation process involves homogeneous Li-ion filling of the electrode or phase separation between Li-poor and Li-rich regions.

## Voltage Profile

Based on the formation energies, the voltage profile can be calculated. The potential difference between the positive and negative electrodes is determined by the difference in $Li/Li^+$ potential according to the Nernst equation[12, 13]:

$$V(x) = -\frac{\mu_{Li}(x) - \mu_{Li}^{ref}(x)}{e} \qquad 2.13$$

The chemical potential is per definition the derivative of the free energy with respect to the Li-ion concentration which, disregarding the entropy and assuming Li-metal as reference, leads to the following expression[8, 13]:

$$\bar{V} = \frac{-[E_{Li_xHost} - (x-y)E_{Li_s} - E_{Li_yHost}]}{(x-y)e} \qquad 2.14$$

$E_{Li_xHost}$ and $E_{Li_yHost}$ are the total energies of the $Li_xHost$ and $Li_yHost$ configurations, respectively. $E_{Li_s}$ is the lithium energy and e is the electron charge.

## Structural Changes upon Insertion and Material Characterization

By looking at the changes in the crystal structure material of the stable phases we can evaluate the structural stability of the structure. For example, Li insertion that causes volume changes >10% might indicate short cycle life due to mechanical instability upon cycling. In that way DFT can help in the determination of the optimum cycling window for maximum performance. In addition, having a relaxed optimized structure (either in lithiated or delithiated form) enables full material characterization. Simulated powder X-ray patterns, nuclear magnetic resonance chemical shifts and Raman spectra are a few examples that can either fully determine an otherwise unsolved structure or help experimentalists to understand their observations.

### Electron Density

One of the most important outputs of DFT is the density of states. Knowing where the electrons reside enables bandgap calculations in order to address the electronic properties of the material. In batteries this technique is mostly used to compare the electronic density of the lithiated structure with the empty host material. In that way one can evaluate the change in electronic properties caused by lithiation. In addition, plotting the electron density difference (lithiated-empty) will reveal which atoms are most active in attracting electrons (redox of transition metals or oxygen).

### Ion Hopping and Diffusion

The kinetic performance of the ions inside the electrode material can be investigated as well. There are mainly two ways to do so, namely the Nudge Elastic Band method (NEB) and Molecular Dynamic (MD) simulations. Li-ions diffuse in the lattice by performing hops from one interstitial position to another. Depending on the local environment there is a wide variety of activation barriers that need to be overcome in order to have a successful hop. In NEB, a number of "images" (configurations with the ion in intermediate positions between the two hopping positions) is created. Energy minimization of the images will determine the lowest energy pathway the ion can follow between the two positions. Molecular dynamics calculations, on the other hand, are based on statistics. A temperature is introduced producing random motion. Thermal and collective atomic vibration contributions will produce jumps inside the crystal. The number of jumps with respect to the time of the simulation will reveal how easily the ion can diffuse in the specific environment. MD simulations are considered expensive since in order to acquire good statistics several simulated ps are required. With the current computational power this will involve real computational time in the range of days or weeks depending also on the mobility of the material being studied.

## 2.2 Phase Field Modeling

The phase field method, is a modeling technique designed to capture kinetic and thermodynamic processes at the mesoscale. Phase-field modeling has become a powerful tool for studying the kinetics of microstructure evolution using thermodynamic data. A microstructure can be defined as a thermodynamically unstable system that evolves in time and consists of a number of grains and domains which differ in structure, orientation and composition. The physical and mechanical properties of a material in the macroscopic scale depend on the shape, size and mutual distribution of the grains and domains constituting its microstructure. The description of the characteristics of the grains is done by the phase field variables. Within a grain the phase field variables have nearly constant values related to the grain’s structure, orientation and composition. The surface region where two grains are in contact is called interface and in this narrow region the phase field variables gradually vary between the distinct values of the neighbouring grains. The modeling approach that includes this smooth variation is called diffuse interface description and incorporates curvature driven physics, creation, destruction and merging of interfaces phenomena which are difficult to capture with sharp interface models. The evolution and shape of the grains is directly related with the position of the interfaces between them and they can be predicted as a function of time by the phase field variables.

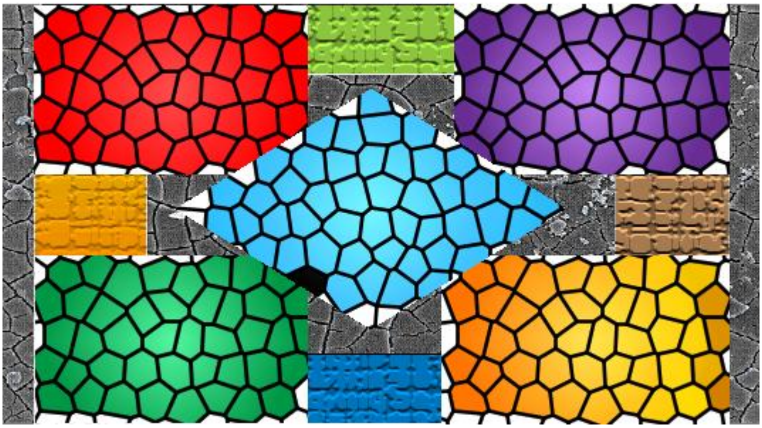

**Figure 2.3:** Abstract illustration of a microstructure.

Typical phase field parameters used in phase-field modeling are the composition variables (concentration and molar fraction), order parameters that distinguish energetically equivalent atom occupations and crystallographic orientations, and phase parameters that distinguish different phases.

The strongest advantage of the phase-field method is that there is no need to track down individual interfaces, something that requires complicated mathematical equations and a priori assumption of a starting position of the grains. The results are obtained by solving a set of partial differential equations numerically. The equations are derived by general thermodynamic and kinetic principles without any consideration of the individual atoms. As a result, material specific properties should be introduced in the form of parameters based on theoretical and experimental information, giving a phenomenological dimension to the process.

The range of physical phenomena suitable for study with the phase field models is quite significant including solidification, solid state phase transformation, grain growth and phase simulation but also dislocation dynamics, crack propagation, solid state sintering and electro-migration. Phase field models are also used to study the nucleation mechanisms upon ion intercalation and de-intercalation. The study of nucleation remains a tough task since it is difficult to observe it experimentally. Furthermore, nucleation is out of the reach of ab-initio molecular simulation (consider that a 10nm particle contains 25000 atoms) or bulk continuum models. It is the thermodynamic treatment of nucleation without the artificial placement of the phase boundaries in mesoscale lengths and times that makes phase field modeling an advantageous tool of understanding microstructure evolution in batteries.

### 2.2.1 Towards Battery Research

Developing a phase field model requires a significant amount of effort. The first step is to recognise all the physical phenomena taking place in the system of interest. For batteries, a sufficient kinetic description should capture the solid diffusion, ion transport in electrolyte, reaction kinetics over the electrolyte electrode interface and electronic resistances. Further, a very important consideration in battery electrode materials is the nature of the phase transitions that are induced upon lithium storage. The electrode voltage curve, how fast it can be charged and how many times it can be recharged depend on whether the lithiation process involves homogeneous Li-ion filling of the electrode or phase separation between Li-poor and Li-rich regions. Most state-of-the-art materials such as $LiFePO_4$, graphite and spinel $Li_4Ti_5O_{12}$ (LTO) display phase separation. Thus, a thermodynamic accurate description, taking into account the phase transformation reaction mechanisms is very important in phase field modeling.

Once all the physical processes are recognised, numerical methods need to be developed and optimized in order to incorporate the physics in the computer. This is not trivial and requires advanced computational and programming knowledge. Finite volume methods, that discretize the battery parts are usually implemented.

### 2.2.2 Applications in Batteries.

Accurate description of the electrochemistry of Li-ion electrodes requires detailed consideration of the Li-ion kinetics and the thermodynamic properties. Electrochemical phase-field modeling[14-17] has been shown to be successful in capturing the phase transformation behavior in Li-ion battery materials. In the prototypical case of $LiFePO_4$ (LFP)[15, 18], the phase field method predicted intercalation waves along the active crystal facet[19, 20], successfully explained the smaller miscibility and spinodal gaps in nanoparticles[21-24] observed experimentally[25, 26], and predicted the suppression of phase separation during lithium insertion above a critical current[27], which was experimentally observed a few years later[28-30]. The addition of coherency strain in the Gibbs free energy description enabled the prediction of striped morphologies and phase boundary orientations in LFP nano-particles[23], which were experimentally validated by microbeam diffraction[31], while enhancing the predicted rate-dependent suppression of phase separation. Further addition of composition-dependent surface energy led to a theory of size-dependent nucleation in nanoparticles[32] and explained the slightly tilted plateau in the open circuit voltage when integrated in a porous electrode model[16]. Furthermore, the same general framework of multiphase porous electrode theory[15-17] (MPET) predicted the transition from particle-by-particle mosaic to concurrent intercalation in LFP observed by *in situ* x-ray and electron imaging[33]. Properly accounting for experimentally observed mosaic instabilities in porous graphite anodes[34] is an essential first step toward the prediction of capacity fade and aging due to side reactions, such as SEI growth and lithium plating, which depend on electrochemical heterogeneities.

Recently, the concentration evolution of individual LFP nanoparticles has been observed *in operando* during cycling under realistic conditions by scanning tunneling x-ray microscopy (STXM), which paves the way for unprecedented validation and application of phase-field models at the nanoscale[35]. The local exchange current density versus concentration was extracted from a massive dataset of STXM movies, and its behavior in the spinodal region, coupled with direct observations of phase separation, confirmed the theory that phase separation is suppressed by auto-inhibition during insertion and enhanced by auto-catalysis during extraction[36]. With advances in 3D simulations of LFP nanoparticles[20, 22], a comprehensive picture of the lithium intercalation is emerging. The same approach is beginning to be applied to anode materials, such as graphite[18, 37, 38] and $TiO_2$ anatase[39], which exhibit multiple phase transitions.

### 2.2.3 Model Overview

In the current thesis, we modified and used the multiphase porous electrode model[15-17] (MPET) developed by Prof. Martin Bazant and colleagues at the Massachusetts Institute of Technology (MIT). Thus, the reader is referred to the their work for a thorough presentation of the developed theory and modeling details.[15-17] Below, an overview of the model is presented where the fundamental physics and computational principles incorporated in the model are discussed.

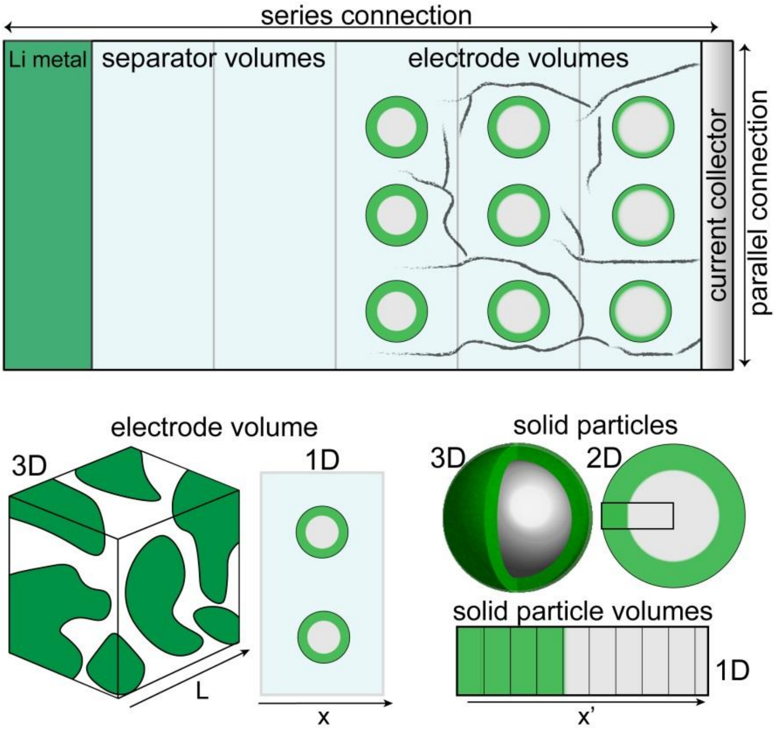
series connection
Li metal
separator volumes
electrode volumes
current collector
parallel connection
electrode volume
3D
1D
L
x
solid particles
3D
2D
solid particle volumes
1D
x'

**Figure 2.4:** Schematic model overview: Here the battery (half-cell) is divided into two separator and three electrode volumes, solid particles are submerged into the electrolyte bath and act as Li-ion sinks/sources.

As in classical porous electrode theory, the battery is conceptually divided into a collection of finite electrolyte volumes, which include the separator and electrode. All of the electrolyte volumes are connected in series, and thus describe the depth information of the simulated battery. The active material is modeled as a collection of solid particles that are in contact with the electrolyte ion reservoir, having a parallel connection within an electrolyte volume. The porosity ($\varepsilon$) represents the volume fraction taken up by electrolyte in a single volume. The thermodynamics inside the particles are described by discretization into solid grid volumes along the intercalation coordinate (x-axis). An overview of the model is shown in Figure 2.4.

The system is fully characterized by the determination of several field variables at each time step throughout the (de)lithiation process, namely the electrolyte potential $\varphi_{\mathrm{lyte}}$, the electrolyte concentration $c_{\mathrm{lyte}}$, the lithium concentration in the solid $c_s$, the potential in the solid $\phi_s$, and the diffusional chemical potential for intercalated lithium $\mu_{\mathrm{Li,LTO}}$. The latter represents the free energy change per interstitial position upon lithium intercalation[38, 51] and is related to the driving force of the insertion reaction. As an example, the insertion reaction of $\mathrm{Li_4Ti_5O_{12}}$ is presented:

$$\mathrm{Li_4Ti_5O_{12}} + \mathrm{e^-} + \mathrm{xLi^+} \leftrightharpoons \mathrm{Li_{4+x}Ti_5O_{12}} \qquad 2.15$$

To capture the thermodynamic behavior of the electrode material, the regular solution model[38] is implemented based on its ability to probe solid solution vs. phase separating systems. The Gibbs free energy per site, $g(\widetilde{c_s})$, is given by the following equation:

$$g(\widetilde{c_s}) = k_B T(\widetilde{c_s}\ln(\widetilde{c_s}) + (1-\widetilde{c_s})\ln(1-\widetilde{c_s})) + \Omega_a \widetilde{c_s}(1-\widetilde{c_s}) + \widetilde{c_s}\mu_i^{\Theta} + \frac{1}{2}\frac{\kappa}{c_{\mathrm{max}}}|\nabla\widetilde{c_s}|^2 \qquad 2.16$$

where $k_B$ is Boltzmann's constant, T the temperature in Kelvin, $\widetilde{c_s}$ the normalized concentration in the solid particles, $\Omega_a$ the enthalpy of mixing, $\mu_i^{\Theta}$ the equilibrium potential versus Li/Li$^+$ (-1.55eV), $\kappa$ the gradient penalty parameter and $c_{\mathrm{max}}$ the maximum concentration of Li. The enthalpy of mixing ($\Omega_a$) quantifies the interactions of intercalated Li-ions within the host material. If $\Omega_a < 2k_BT$ the system favours a solid solution insertion mechanism, while if $\Omega_a > 2k_BT$ the enthalpy term overcomes the competing entropy term leading to phase segregation. A dimensionless simple example of the Gibbs free energy as a function of various $\Omega_a$ along with the responding voltage profile is presented in Figure 2.5. The last term is the gradient penalty term that penalizes steep gradients which occur at phase interfaces. The gradient penalty parameter ($\kappa$) can be linked to the width $\lambda_b$ and interfacial tension $\gamma_b$ of a diffuse phase boundary through formula 2.17.[38]

$$\kappa \propto {\lambda_b}^2 c_{\mathrm{max}}\Omega_a \propto \frac{\gamma_b^2}{c_{\mathrm{max}}\Omega_a} \qquad 2.17$$

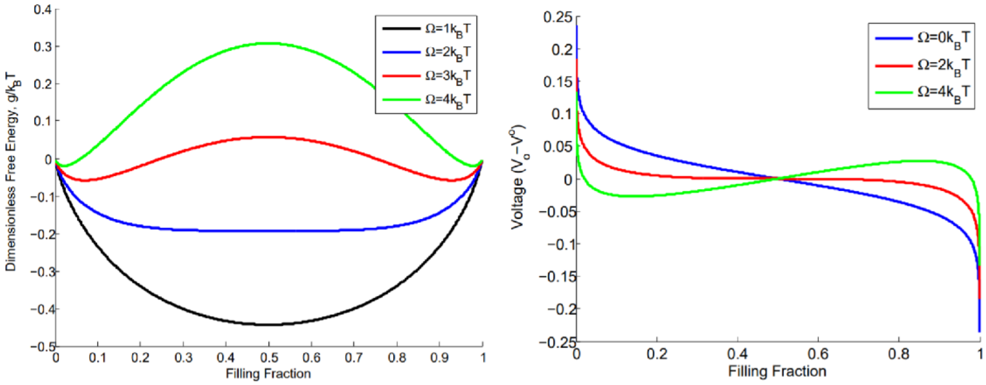

**Figure 2.5:** Obtained from Ferguson and Bazant[15] (left) Regular solution model for the free energy of a homogeneous mixture. This figure shows the effect of the regular solution parameter **Ω** (mean pair interaction energy) and temperature T on the free energy versus composition of a regular solution of atoms and vacancies on a lattice. For **Ω** < 2kBT, there is a single minimum. For **Ω** > 2kBT, there are two minima. This produces phase separation, as the system is unstable with respect to infinitesimal perturbations near the spinodal concentration, which is where the curvature of the free energy changes. (right) Open circuit potential for different regular solution parameter values. The battery voltage is the change in free energy per electron transferred. In this model, the homogeneous voltage curve is non-monotonic when the system has a tendency for phase separation.

The larger the gradient penalty κ, the greater the interfacial tension between phases, and, for a given particle size, the less likely the material is to phase separate. By variationally differentiating the Gibbs free energy with respect to the concentration, the diffusional chemical potential ($\mu_{\mathrm{Li,LTO}}$) of lithium inserted in LTO can be obtained.

$$\mu_{\mathrm{Li,LTO}} = \frac{\partial g}{\partial c_s} - \nabla \cdot \frac{\partial g}{\partial \nabla c_s} = \mu^{\Theta} + k_B T \ln\left(\frac{\widetilde{c_s}}{1-\widetilde{c_s}}\right) + \Omega_a(1-2\widetilde{c_s}) - \frac{\kappa}{c_{\max}} \nabla^2 \widetilde{c_s} \tag*{2.18}$$

Assuming linear irreversible thermodynamics, the Li-ion flux in the solid particles is proportional to the gradient of the diffusional chemical potential $\nabla\mu_{\mathrm{Li,LTO}}$ and can be expressed with a vacancy diffusion mechanism as[38]:

$$F = -\frac{D_{\mathrm{Li}}}{k_B T} c_s(1-\tilde{c}_s)\nabla\mu_{\mathrm{Li,LTO}} \tag*{2.19}$$

where $D_{\mathrm{Li}}$ is the tracer diffusivity of isolated Li-ions in the LTO lattice, which is assumed to be a scalar for isotropic diffusion. Since LTO also has negligible coherency strain (which usually introduces strong crystal anisotropy), we further assume spherically symmetric radial diffusion and core-shell phase separation, which is a convenient and reasonable simplification of the single-particle model for LTO, and allows for more efficient simulations.

The charge transfer reaction current (I) controls the Li-ion flow between the electrolyte and the solid particles. The generalized Butler-Volmer equation[38, 39], is implemented to describe the Li-flux at the electrolyte/solid boundary resulting from Faradaic intercalation reactions:

$$\mathrm{I} = \mathrm{k_0} \frac{\mathrm{a_{Li,lyte}^{1-\alpha} a_{Li,s}^{\alpha}}}{\gamma_{\mathrm{TS}}} [\exp\left(-\frac{\alpha e \eta_{\mathrm{eff}}}{\mathrm{k_B T}}\right) - \exp\left(\frac{(1-\alpha) e \eta_{\mathrm{eff}}}{\mathrm{k_B T}}\right)] \qquad 2.20$$

where $k_0$ is the rate constant per intercalation site, and $\alpha$ is the symmetry factor of the activation barrier along the reaction coordinate. The exchange current depends upon the activity of lithium, both in the electrolyte ($\mathrm{a_{Li,lyte,}}$) and solid $\left(\mathrm{a_{Li,s}}\right)$. The choice of transition state activity coefficient[38], $\gamma_{\mathrm{TS}} = (1 - \tilde{c}_s)^{-1}$, which assumes one excluded site for the transition state during lithium insertion, leads to an asymmetric exchange current versus concentration, peaking at low concentrations, which has recently been validated by local measurements of the intercalation rate in LFP nanoparticles[59]. As a result, the insertion reaction is auto-inhibitory (and the extraction reaction is auto-catalytic) across the spinodal region, which leads to suppression of phase separation during insertion (and enhancement during extraction), as predicted theoretically[51, 60] and later confirmed by in operando imaging of nanoparticle concentration profiles[59]. The effective overpotential $\eta_{\mathrm{eff}}$ includes film resistance ($\mathrm{R_{film}}$) in series with the Faradaic reaction [41],

$$\eta_{\mathrm{eff}} = \eta + \mathrm{IR_{film}} \qquad 2.21$$

which helps to accurately fit experimental data with MPET[58], as well as with classical porous electrode models. This common approximation yields a curved Tafel plot, which could result from an actual series reaction resistance, such as a thin film or Stern layer hindering electron or ion transport to the reaction site. Alternatively, the curved Tafel plot may signify quantum mechanical deviations from Butler-Volmer kinetics[41], as predicted by the Marcus theory of electron transfer and consistent with experiments on LFP[67].

The overpotential $\eta$ is calculated through its local thermodynamic definition:

$$\eta \equiv \Delta\phi - \Delta\phi^{\mathrm{eq}} \qquad 2.22$$

with $\Delta\phi = \phi_{\mathrm{s}} - \phi_{\mathrm{lyte}}$ being the potential difference between the solid electron-conducting phase and the electrolyte at the electron-transfer reaction site. The equilibrium potential $\Delta\phi^{\mathrm{eq}}$ is determined through the Nernst equation:

$$\Delta\phi^{eq} \approx -\frac{\mu_{Li,LTO}}{e} + \frac{k_B T}{e} \ln \frac{c_{lyte}}{c_0} \qquad 2.23$$

where we neglect Frumkin corrections associated with charged double layers[68], by setting $\phi_{lyte}$ and $c_{lyte}$ to their nearly constant local values in the bulk electrolyte, which are assumed to vary only over the macroscopic electrode length scale. We also neglect concentration-dependent variations of the liquid-state Li-ion activity coefficient in the Nernst equation, since our focus is on the larger variations of Li-ion activity in the solid captured by the phase-field model. The Li-ion transport in the electrolyte is described using the Stefan-Maxwell concentrated electrolyte model.[41] A linear Ohmic-like function was implemented to describe electronic wiring in the electrode[41]:

$$j_{electronic} = -\sigma \nabla \phi_s \qquad 2.24$$

where σ is the electronic conductivity.

# References

**1**. Marthinsen, A. Fundamentals and applications of density functional theory. https://www.youtube.com/watch?v=SXvhDLCycxc

**2**. Kohanoff, J. Electronic Structure Calculations for Solids and Molecules. *Cambridge University Press*, 2006.

**3**. Born, M. Oppenheimer, R., Quantum theory of molecules. *Ann. Phys-Berlin* 1927, 84, 0457-0484.

**4**. Hohenberg, P.; Kohn, W., Inhomogeneous Electron Gas. *Phys. Rev. B* 1964, 136, B864.

**5**. Perdew, J. P.; Burke, K.; Ernzerhof, M. Generalized gradient approximation made simple. *Phys. Rev. Lett.* 1996, 77, 3865-3868.

**6**. Hamprecht, F. A.; Cohen, A. J.; Tozer, D. J.; Handy, N. C. Development and assessment of new exchange-correlation functionals. *J. Chem. Phys.* 1998, 109, 6264-6271.

**7**. Kohn, W.; Sham, L. J. Self-Consistent Equations Including Exchange and Correlation Effects. *Phys. Rev.* 1965, 140, 1133.

**8**. Islam, M. S.; Fisher, C. A. J. Lithium and sodium battery cathode materials: computational insights into voltage, diffusion and nanostructural properties. *Chem. Soc. Rev.* 2014, 43,185-204.

**9**. Meng, Y. S.; Arroyo-de Dompablo, M. E. First principles computational materials design for energy storage materials in lithium ion batteries. *Energy Environ. Sci.* 2009, 2, 589-609.

**10**. Van der Ven, A.; Aydinol, M. K.; Ceder, G.; Kresse, G.; Hafner, J. First-principles investigation of phase stability in $Li_xCoO_2$. *Phys. Rev. B* 1998, 58, 2975-2987.

**11**. Wagemaker, M.; Van Der Ven, A.; Morgan, D.; Ceder, G.; Mulder, F. M.; Kearley, G. J. Thermodynamics of spinel $Li_xTiO_2$ from first principles. *Chem. Phys.* 2005, 317, 130-136.

**12**. Dalton, A. S.; Belak, A. A.; Van der Ven, A. Thermodynamics of Lithium in $TiO_2$ (B) from First Principles. *Chem. Mater.* 2012, 24,1568-1574.

**13**. Aydinol, M. K.; Kohan, A. F.; Ceder, G.; Cho, K.; Joannopoulos, J. Ab initio study of lithium intercalation in metal oxides and metal dichalcogenides. *Phys. Rev. B* 1997, 56, 1354-1365.

**14**. Bazant, M. Z., Theory of Chemical Kinetics and Charge Transfer based on Nonequilibrium Thermodynamics. *Accounts Chem. Res.* 2013, 46, 1144-1160.

**15**. Ferguson, T. R.; Bazant, M. Z., Nonequilibrium Thermodynamics of Porous Electrodes. *J. Electrochem. Soc.* 2012, 159, A1967-A1985.

**16**. Open source MPET softwere, https://bitbucket.org/bazantgroup/mpet.

**17**. Smith, R. B.; Bazant, M. Z. Multiphase Porous Electrode Theory J. Electrochem. Soc. 2017, 164, E3291-E3310.

**18**. Ferguson, T. R.; Bazant, M. Z. Phase Transformation Dynamics in Porous Battery Electrodes. *Electrochim. Acta* 2014, 146, 89-97.

**19**. Singh, G. K.; Ceder, G.; Bazant, M. Z. Intercalation dynamics in rechargeable battery materials: General theory and phase-transformation waves in $LiFePO_4$. *Electrochim. Acta* 2008, 53, 7599-7613.

**20**. Tang, M.; Belak, J. F.; Dorr, M. R. Anisotropic Phase Boundary Morphology in Nanoscale Olivine Electrode Particles. *J. Phys. Chem. C* 2011**,** 115, 4922-4926.

**21**. Burch, D.; Bazant, M. Z., Size-Dependent Spinodal and Miscibility Gaps for Intercalation in Nanoparticles. *Nano Lett.* 2009, 9, 3795-3800.

**22**. Welland, M. J.; Karpeyev, D.; O'Connor, D. T.; Heinonen, O. Miscibility Gap Closure, Interface Morphology, and Phase Microstructure of 3D $Li_xFePO_4$ Nanoparticles from Surface Wetting and Coherency Strain. *ACS Nano* 2015, 9, 9757-9771.

**23**. Cogswell, D. A.; Bazant, M. Z. Coherency Strain and the Kinetics of Phase Separation in LiFePO4 Nanoparticles. *ACS Nano* 2012, 6, 2215-2225.

**24**. Tang, M.; Carter, W. C.; Chiang, Y. M., Electrochemically Driven Phase Transitions in Insertion Electrodes or Lithium-Ion Batteries: Examples in Lithium Metal Phosphate Olivines. *Annu. Rev. Mater. Res.* 2010, 40, 501-529.

**25**. Kobayashi, G.; Nishimura, S. I.; Park, M. S.; Kanno, R.; Yashima, M.; Ida, T.; Yamada, A. Isolation of Solid Solution Phases in Size-Controlled $Li_xFePO_4$ at Room Temperature. *Adv. Funct. Mater.* 2009, 19, 395-403.

**26**. Wagemaker, M.; Singh, D. P.; Borghols, W. J. H.; Lafont, U.; Haverkate, L.; Peterson, V. K.; Mulder, F. M. Dynamic Solubility Limits in Nanosized Olivine $LiFePO_4$. *J. Am. Chem. Soc.* 2011, 133, 10222-10228.

**27**. Bai, P.; Cogswell, D. A.; Bazant, M. Z., Suppression of Phase Separation in $LiFePO_4$ Nanoparticles During Battery Discharge. *Nano Lett.* 2011**,** 11, 4890-4896.

**28**. Liu, H.; Strobridge, F. C.; Borkiewicz, O. J.; Wiaderek, K. M.; Chapman, K. W.; Chupas, P. J.; Grey, C. P. Capturing metastable structures during high-rate cycling of $LiFePO_4$ nanoparticle electrodes. *Science* 2014, 344, 6191.

**29**. Zhang, X. Y.; van Hulzen, M.; Singh, D. P.; Brownrigg, A.; Wright, J. P.; van Dijk, N. H.; Wagemaker, M. Rate-Induced Solubility and Suppression of the First-Order Phase Transition in Olivine $LiFePO_4$. *Nano Lett.* 2014, 14, 2279-2285.

**30**. Niu, J. J.; Kushima, A.; Qian, X. F.; Qi, L.; Xiang, K.; Chiang, Y. M.; Li, J. In Situ Observation of Random Solid Solution Zone in $LiFePO_4$ Electrode. *Nano Lett.* 2014, 14, 4005-4010.

**31**. Zhang, X. Y.; van Hulzen, M.; Singh, D. P.; Brownrigg, A.; Wright, J. P.; van Dijk, N. H.; Wagemaker, M. Direct view on the phase evolution in individual $LiFePO_4$ nanoparticles during Li-ion battery cycling. *Nat. Commun.* 2015, 6, 8333.

**32**. Cogswell, D. A.; Bazant, M. Z., Theory of Coherent Nucleation in Phase-Separating Nanoparticles. *Nano Lett.* 2013**,** 13, 3036-3041.

**33**. Li, Y. Y.; El Gabaly, F.; Ferguson, T. R.; Smith, R. B.; Bartelt, N. C.; Sugar, J. D.; Fenton, K. R.; Cogswell, D. A.; Kilcoyne, A. L. D.; Tyliszczak, T.; Bazant, M. Z.; Chueh, W. C. Current-induced transition from particle-by-particle to concurrent intercalation in phase-separating battery electrodes. *Nat. Mater.* 2014**,** 13, 1149-1156.

**34**. Thomas-Alyea, K. E.; Jung, C.; Smith, R. B.; Bazant, M. Z. In Situ Observation and Mathematical Modeling of Lithium Distribution within Graphite. *J. Electrochem. Soc.* 2017, 164, E3063-E3072.

**35**. Lim, J.; Li, Y. Y.; Alsem, D. H.; So, H.; Lee, S. C.; Bai, P.; Cogswell, D. A.; Liu, X. Z.; Jin, N.; Yu, Y. S.; Salmon, N. J.; Shapiro, D. A.; Bazant, M. Z.; Tyliszczak, T.; Chueh, W. C. Origin and hysteresis of lithium compositional spatiodynamics within battery primary particles. *Science* 2016**,** 353, 566-571.

**36**. Bazant, M. Z. Thermodynamic Stability of Driven Open Systems and Control of Phase Separation by Electro-autocatalysis. *Faraday Discuss.* 2017**,** 199, 422-463.

**37**. Smith, R. B.; Bazant, M. Z. Intercalation kinetics in multiphase layered materials. *J. Phys. Chem. C*, 2017, 121, 12505-12523

**38**. Guo, Y. S.; Smith, R. B.; Yu, Z. H.; Efetov, D. K.; Wang, J. P.; Kim, P.; Bazant, M. Z.; Brus, L. E., Li Intercalation into Graphite: Direct Optical Imaging and Cahn-Hilliard Reaction Dynamics. *J. Phys. Chem. Lett.* 2016, 7, 2151-2156.

**39**. de Klerk, N. J. J.; Vasileiadis, A.; Smith, R. B.; Bazant, M. Z.; Wagemaker, M. Explaining key propperties of lithiation in $TiO_2$-anatase Li-ion battery electrodes using phase field modeling *Phys. Rev. Mater.* 2017, 1, 025404.

# 3

# The Fine Line between a Two-Phase and Solid Solution Phase Transformation and Highly Mobile Phase Interfaces in Spinel $Li_{4+x}Ti_5O_{12}$

«ὅταν δέ τις τὸ μὲν ἀπολίπῃ, τὸ δὲ ἐκβάλῃ ὁμοίως σύμφωνον ὂν τῷ φαινομένῳ, δῆλον ὅτι καὶ ἐκ παντὸς ἐκπίπτει φυσιολογήματος ἐπὶ δὲ τὸν μῦθον καταρρεῖ»

“But when we pick and choose among explanations, rejecting one equally consistent with the phenomena, we clearly fall away from the study of nature altogether and tumble into myth”

Epicurus

Diogenes Laertius, *Lives of Eminent Philosophers*, Book X, *EPICURUS*, 87, with an English translation by R. D. Hicks, Harvard University Press, Cambridge, Massachusetts, 1995.

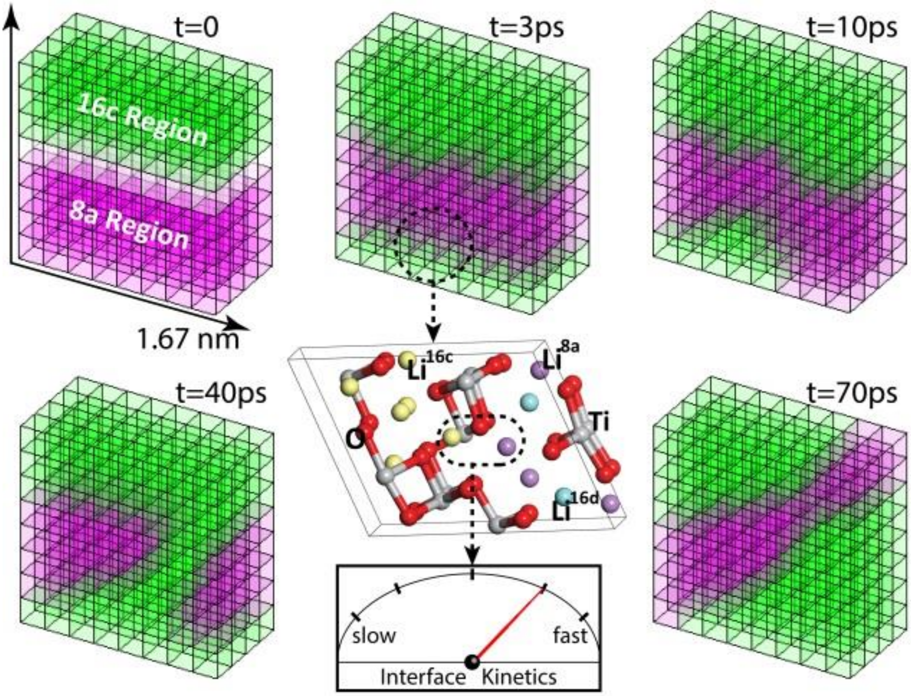
t=0
16c Region
8a Region
1.67 nm
t=3ps
t=10ps
Li16c
Li8a
O
Ti
Li16d
t=40ps
t=70ps
slow
fast
Interface Kinetics

## Abstract

Phase transitions play a crucial role in Li-ion battery electrodes being decisive for both the power density and cycle life. The kinetic properties of phase transitions are relatively unexplored and the nature of the phase transition in defective spinel $Li_{4+x}Ti_5O_{12}$ introduces a controversy as the very constant (dis)charge potential, associated with a first-order phase transition, appears to contradict the exceptionally high rate performance associated with a solid-solution reaction. With the present DFT study, a microscopic mechanism is put forward that provides deeper insight in this intriguing and technologically relevant material. The local substitution of Ti with Li in the spinel $Li_{4+x}Ti_5O_{12}$ lattice stabilizes the phase boundaries that are introduced upon Li-ion insertion. This facilitates a sub-nanometer phase coexistence in equilibrium, which although very similar to a solid solution should be considered a true first-order phase transition. The resulting interfaces are predicted to be very mobile due to the high mobility of the Li-ions located at the interfaces. This highly mobile, almost liquid-like, sub-nanometer phase morphology is able to respond very fast to non-equilibrium conditions during battery operation, explaining the excellent rate performance in combination with a first-order phase transition.

Based on the homonymous paper:
Ganapathy[†], S.; Vasileiadis[†], A.; Heringa, J. R.; Wagemaker, M. The Fine Line between a Two-Phase and Solid-Solution Phase Transformation and Highly Mobile Phase Interfaces in Spinel $Li_{4+x}Ti_5O_{12}$ *Adv. Energy Mater*. 2017, 7, 1601781.
(† co-first author).

## 3.1 Introduction

Electrochemical energy storage in Li-ion batteries is a key technology for the development of portable electronics and electrical vehicles. In addition it is now considered as a storage media for bridging the difference between supply of renewable energy sources and the societal demand. The working principle of Li-ion batteries is based on the reversible insertion and extraction of Li-ions in the crystal structure of the positive and negative electrode materials. The nature of the phase transitions in the electrode materials induced by the insertion of Li-ions is of large practical importance for Li-ion battery performance as it affects both the cycle life and power density. First-order phase transitions result in an attractive flat electrode potential, the phase boundaries formed, however, are thought to be responsible for poor rate performance and typically lead to poor cycle performance by strain-induced mechanical failure. Interestingly, two intensively studied electrode materials, olivine $LiFePO_4$[1] and spinel $Li_4Ti_5O_{12}$[2, 3] appear to be exceptions, showing excellent rate performance in combination with a long cycle life. For olivine $LiFePO_4$, recent studies have provided first insights in the phase-transition kinetics of electrode materials. Metastable intermediate phases were observed, induced by the high (dis)charge rates[4, 5] and the first-order phase transition was predicted and observed to be bypassed.[6-11] In addition, the phase transition morphology in individual grains was shown to depend on the (dis)charge rate.[9] For spinel $Li_4Ti_5O_{12}$, the fundamental nature of the first-order phase transition is unclear. This is demonstrated by the fundamentally different phase transition behaviour that has been reported: (1) a complete solid solution,[12] (2) a nanoscale phase separated system[13-15] or (3) a macroscopically phase separated system[16, 17].

Herein, the experimental difficulty is to distinguish between the structurally very similar $Li_4Ti_5O_{12}$ and $Li_7Ti_5O_{12}$ endmember crystalline lattices.[2, 3, 13, 16] Upon lithiation the spinel $Li_4Ti_5O_{12}$ endmember phase undergoes a phase transition towards the rock-salt $Li_7Ti_5O_{12}$ endmember phase while maintaining its symmetry with a volume change of only 0.2%.[2, 3, 16, 18-21] This so-called ‘zero-strain’ property allows the material to go through thousands of charge-discharge cycles with marginal capacity loss and also suggests that interfaces between the endmember phases, $Li_4Ti_5O_{12}$ and $Li_7Ti_5O_{12}$, can be associated with a very small energy penalty[22] unlike in other Li-ion electrode materials such as anatase $TiO_2$[23] and $LiFePO_4$.[7, 24] Although the very flat voltage profile suggests macroscopic two phase separation[16] which is supported by electron microscopy studies,[17] temperature-dependent X-ray diffraction advocates that intermediate $Li_{4+x}Ti_5O_{12}$ compositions macroscopically phase separate below 80 K whereas at higher temperatures they segregate into nano-domains of the endmember phases[13] which is supported by NMR experiments.[14] Recent NMR experiments even indicate a homogeneous solid solution phase for intermediate compositions.[12] Several NMR studies indicate that the individual endmember phases have high barriers for Li-ion diffusion resulting in poor Li-ion mobility[12, 14, 25, 26] which is supported by static DFT calculations,[27] whereas intermediate compositions display high Li-ion mobility[12, 14, 25, 26] which is also supported by DFT calculations.[28] The assumption of macroscopic phase coexistence of the endmember phases poses a fundamental contradiction: how can a macroscopic sum of two poor Li-ion conductors give rise to the high mobility observed in intermediate compositions both with NMR[12, 14, 25, 26] and macroscopic electrochemical[29-33] techniques?

Using ab-initio DFT calculations this work aims at a fundamental understanding of the nature of the phase transition behavior and Li-ion kinetics in spinel $Li_4Ti_5O_{12}$ and how this transition is correlated with the material's excellent electrode performance in Li-ion batteries. The results reveal a crucial role for the interfaces between the two endmember phases, the abundant existence of which is facilitated by the partial replacement of Ti with Li. The intimate mixing of sub-nanometer domains of the endmember phases structurally appears as a solid solution, however it should be considered as a first-order phase transition, a consequence of the very small energy associated with the coherent interfaces. Molecular dynamics simulations display ultra-fast interface kinetics of the sub-nanometer phase separated system driving the very high Li-ion mobility in the spinel $Li_{4+x}Ti_5O_{12}$ lattice. The nature of the interfaces explains the contradicting observations and the excellent rate performance of this intriguing material, giving insight in the relation between atomic scale properties and excellent Li-ion battery performance.

## 3.2 Thermodynamics of Li Ions in $Li_4Ti_5O_{12}$

The use of pure spinel $Li_xTiO_2$ and defective spinel $Li_{4+x}Ti_5O_{12}$ as electrode materials in Li-ion batteries relies on its ability to store Li-ions at two distinct crystallographic sites, the tetrahedral 8a site, referred to as $Li^{8a}$, and the octahedral 16c site, referred to as $Li^{16c}$. Additionally in spinel $Li_{4+x}Ti_5O_{12}$ Li-ions reside on the Ti (16d) sub-lattice in a ratio of 1:5 Li:Ti, referred to as $Li^{16d}$. These Li-ions are strongly bonded and therefore do not participate in the Li-ion insertion and extraction during battery operation.

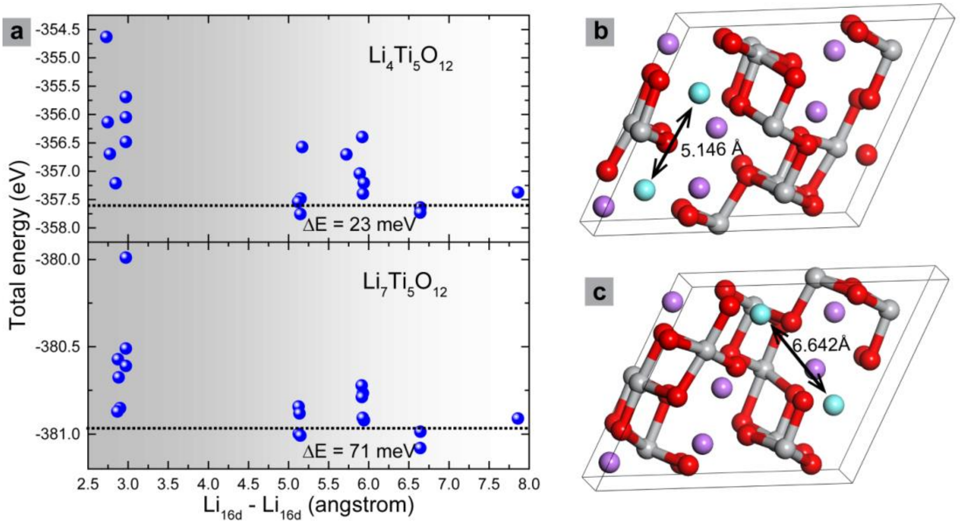

**Figure 3.1: a)** Total energy of all possible arrangements of Li and Ti (ratio 1:5) on the 16d sub-lattice after relaxation in both endmembers stoichiometry's $Li_4Ti_5O_{12}$ (supercell $Li_6^{8a}[Li_2Ti_{10}]^{16d}O_{24}$) and $Li_7Ti_5O_{12}$ (supercell $Li_{12}^{16c}[Li_2Ti_{10}]^{16d}O_{24}$). **b) / c)** The two lowest energy configurations of $Li_4Ti_5O_{12}$ obtained from a). The cyan, purple, grey, and red spheres represent $Li^{16d}$, $Li^{8a}$, Ti and O atoms respectively.

Their presence ascertains almost identical lattice parameters for the $Li_4Ti_5O_{12}$ and $Li_7Ti_5O_{12}$ endmembers, which is in turn responsible for the zero-strain property.[18] We start with predicting the distribution of the electrochemically inactive Li-ions over the Ti (16d) sub-lattice. This is achieved by calculating the lowest energy $Li^{16d}$ – $Ti^{16d}$ configuration, that will serve as a starting point considering the Li-vacancy energetics on the electrochemically active Li 8a and 16c sub-lattices. The Li – Ti disorder on the 16d sub-lattice is calculated in both

$Li_4Ti_5O_{12}$ and $Li_7Ti_5O_{12}$ endmember phases, by using a three-fold primitive cell in the smallest supercell, which is the smallest supercell having the correct stoichiometry. For the 1:5 Li:Ti ratio this results in 19 symmetrically distinct configurations. The resulting total energies of these configurations after ionic relaxation, calculated using the generalized gradient approximation (GGA) in density functional theory (DFT),[34-36] are shown in Figure 3.1a**.** All calculations were performed without considering spin polarization because this does not change the energies significantly[37] indicating that magnetization does not play a significant role in the energetics of spinel $Li_{4+x}Ti_5O_{12}$. The two lowest $Li^{16d}$ – $Ti^{16d}$ energy configurations in $Li_4Ti_5O_{12}$, shown in Figure 3.1b/c**,** are identical to the two lowest $Li^{16d}$ – $Ti^{16d}$ energy configurations in $Li_7Ti_5O_{12}$.

Analysis of the various $Li^{16d}$ – $Ti^{16d}$ configurations reveals that the energy systematically increases with decreasing $Li^{16d}$ – $Li^{16d}$ distance. A small $Li^{16d}$ – $Li^{16d}$ distance introduces a repulsive energy (the minimum 16d – 16d distance is 2.974 Å) explaining why the maximum $Li^{16d}$ – $Li^{16d}$ distances, 5.146 Å and 6.642 Å, results in the lowest total energy. The energy difference between the two lowest energy configurations is small, amounting to 23 meV and 71 meV for the $Li_8Ti_{10}O_{24}$ and the $Li_{14}Ti_{10}O_{24}$ endmember supercells respectively. This indicates, that, in practice, the $Li^{16d}$ – $Ti^{16d}$ disorder may consist of a mixture of these two configurations.

We shall refer to the two different low-energy 16d sub-lattice configurations as LTO-1 ($Li^{16d}$ – $Li^{16d}$ distance 5.146 Å) shown in Figure 3.1b and LTO-2 ($Li^{16d}$ – $Li^{16d}$ distance 6.642 Å) shown in Figure 3.1c. Given the small difference in ground state energy of the LTO-1 and LTO-2 configurations, the lithium-vacancy energetics on the 8a and 16c sub-lattices is calculated for both starting structures, using the initial part of the code for cluster expansion developed by Van de Ven and co-workers to obtain symmetrically unique configurations.[38-40]. Because the $Li^{16d}$ ions are not participating in the insertion/extraction reaction during battery operation, the configuration of these ions as well as the O and Ti atoms is fixed (though the ionic positions are relaxed during the energy minimizations). For comparative purposes also the previously reported[37, 41] lithium-vacancy energetics on the 8a and 16c sub-lattices in pure spinel $Li_xTi_2O_4$ are calculated.

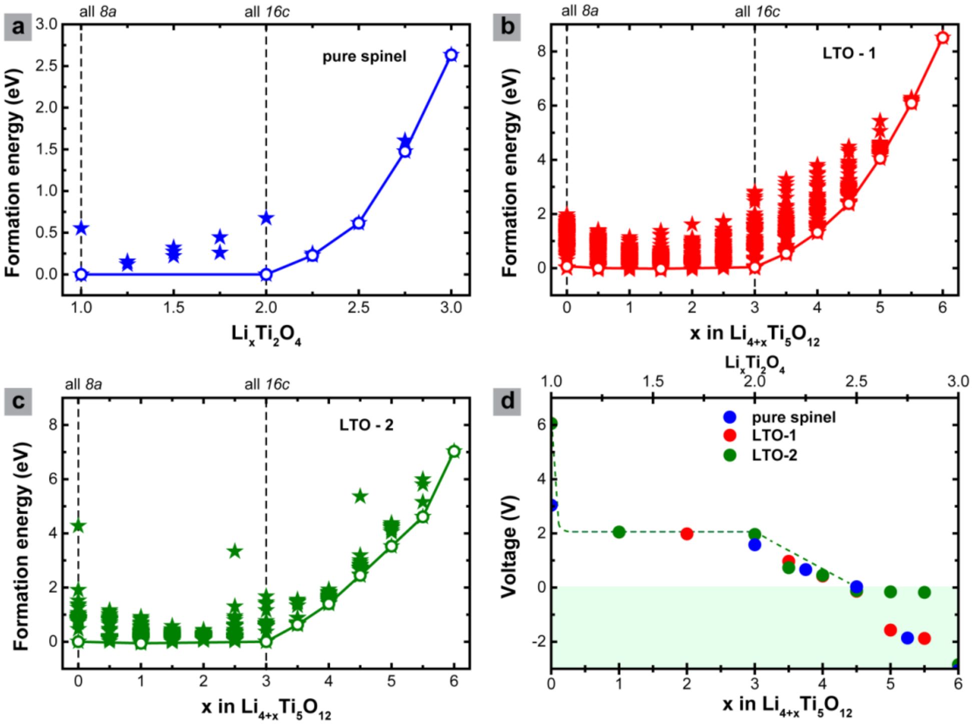

**Figure 3.2:** Formation energies (stars) of **a)** pure spinel $Li_xTi_2O_4$, **b)** LTO-1 and **c)** LTO-2 configurations. Formation energies were determined per formula unit of $Li_xTi_2O_4$ and $Li_{4+x}Ti_5O_{12}$ respectively. The bold line represents the convex hull comprised of the most stable ground states (hollow circles) that were determined in each case. **d)** Insertion voltages determined for the pure $Li_xTi_2O_4$ and defective spinel $Li_{4+x}Ti_5O_{12}$ from the total energies between consecutive points (Li-configurations) on the convex hull at 0 K. The dotted line is a guide to the eye.

Putting vacancies in the pure spinel primitive cell on the 8a and 16c sub lattices results in 24 symmetrically distinct lithium-vacancy configurations. The large size of the $Li_{4+x}Ti_5O_{12}$ (LTO-1/2) supercells (three times the primitive cell) and the reduced local symmetry, introduced by the $Li^{16d}$ atoms, results in a much larger amount of symmetrically distinct lithium-vacancy configurations on the 8a and 16c sub-lattices of which we have considered 2653 in LTO-1 and 1490 in LTO-2. Figures 3.2a-c shows the formation enthalpies per formula unit $Li_xTi_2O_4$ ($1 \leq x \leq 3$) and $Li_{4+x}Ti_5O_{12}$ ($0 \leq x \leq 6$) for all calculated Li-vacancy arrangements, reflecting the relative stability of the different configurations. Herein, the focus is on the reversible $1 \leq x \leq 2$ and $0 \leq x \leq 3$ concentration range for $Li_xTi_2O_4$ and $Li_{4+x}Ti_5O_{12}$ respectively.

The formation enthalpy for the defective spinel can be defined as:

$$E_{\mathrm{form}} = E_{\mathrm{Li_{4+x}Ti_5O_{12}}} - \frac{x}{3}E_{\mathrm{Li_7Ti_5O_{12}}} - (1-\frac{x}{3})E_{\mathrm{Li_4Ti_5O_{12}}}$$

Where E is the energy of a specific Li-vacancy arrangement at a concentration x, $E_{\mathrm{Li_7Ti_5O_{12}}}$ is the energy of the endmember phase where all octahedral 16c sites are occupied and $E_{\mathrm{Li_4Ti_5O_{12}}}$ is the energy of the endmember phase where all tetrahedral 8a sites are occupied. The formation enthalpy of the pure spinel is described in detail elsewhere.[37, 41] Considering the formation enthalpies makes it possible to study the relative stability of the different configurations, and thereby predicting the thermodynamic path upon (de)lithiation. The lines in Figures 3.2a-c, represent part of the convex-hull which is constructed by connecting a line between the most stable (ground state) structures at 0 K as a function of Li composition. Before considering LTO-1 and LTO-2 it is illustrative to start with the formation enthalpies of the pure spinel phase shown in Figure 3.2a. Starting at the $Li_1Ti_2O_4$ ground state, where the 8a sub-lattice is completely occupied by Li-ions, additional Li-ion insertion results in configurations with a mixed $Li^{8a}/Li^{16c}$ occupancy, before reaching the $Li_2Ti_2O_4$ ground state, where all 16c sites are occupied. The formation energies of these mixed $Li^{8a}/Li^{16c}$ configurations are positioned significantly above the convex hull connecting the $Li_1Ti_2O_4$ and $Li_2Ti_2O_4$ ground states indicating a thermodynamic driving force for the first-order phase transition between these ground states in agreement with experimental observations and previous calculations.[31,39] Figures 3.2b and 3.2c show the formation enthalpies of both LTO-1 and LTO-2 for the same compositional range, from lithium occupying all 8a sites in $Li_4Ti_5O_{12}$ to lithium occupying all 16c sites in $Li_7Ti_5O_{12}$. Comparison shows that LTO-1 and LTO-2 have very similar ground state energies upon Li-ion insertion in the 8a and 16c sub-lattices that differs fundamentally from those predicted for pure spinel. In contrast to pure spinel, both LTO-1 and LTO-2 result in several mixed -$Li^{8a}/Li^{16c}$ configurations ($0 \leq x \leq 3$) that have a formation enthalpy very close and even positioned on the convex hull (two additional for LTO-1 and one for LTO-2). This implies that in spinel $Li_{4+x}Ti_5O_{12}$ configurations with mixed Li-ion occupancy of 8a and 16c sites are relatively stable and likely to occur in practice. This in contrast to pure spinel $Li_{1+x}Ti_2O_4$ where the large formation energy of these mixed $Li^{8a}/Li^{16c}$ configurations provides a driving force towards macroscopic phase separation in domains of occupied 8a sites and domains of occupied 16c sites.

The voltage profile in Figure 3.2d is determined from the most stable consecutive ground state configurations, positioned on the convex hull, shown for the complete concentration range in Figure 3.2a-c. As expected, the similar convex hull of LTO-1 and LTO-2 result in very similar voltage profiles. For compositions between $Li_7Ti_5O_{12}$ and $Li_{8.4}Ti_5O_{12}$, in addition to all the 16c sites being occupied, additional Li-ions occupy the 8a sites, causing distortions in the neighbouring $TiO_6$ octahedra, seen both in LTO-1 and LTO-2, in agreement with previous theoretical studies.[42] Compositions in excess of $Li_7Ti_5O_{12}$ have also been observed experimentally for nano LTO, in agreement with our observations wherein in addition to full 16c occupancy; partial 8a occupancy was reported, via neutron diffraction.[43] LTO-1 and LTO-2 only significantly differing at compositions exceeding $Li_{8.4}Ti_5O_{12}$, at which point the voltages obtained for Li insertion are negative. The negative voltage indicates that the free energy is lower than that of metallic lithium and hence Li-plating is preferred over exceeding the $Li_{8.4}Ti_5O_{12}$ composition. This is in good agreement with values predicted by Zhong and co-workers[42] and those obtained via chemical/electrochemical insertion in nano $Li_{4+x}Ti_5O_{12}$.[43, 44] For pure spinel $Li_xTi_2O_4$ the voltage profiles reported in the literature have been obtained by performing Monte Carlo simulations at 300 K based on a cluster expansion using the DFT energies[37, 41] whereas at present we report the voltage curve solely based on the ground state enthalpies, and therefore the configurational entropy is not included. In the composition range $0 \leq x \leq 3$ in $Li_{4+x}Ti_5O_{12}$ the voltages are predicted to be almost constant at $2.00 \pm 0.04$ V, both for LTO-1 and LTO-2. This calculated value is higher than the experimentally observed plateau voltage which is $\approx 1.55$ V vs. metallic Li.[16, 20] These discrepancies between calculated and experimental insertion voltages are often reported using DFT calculations,[45, 46] and do not influence any trends in the voltage drop observed as a function of increased Li-concentration.

Although both pure spinel $Li_xTi_2O_4$ and defective $Li_{4+x}Ti_5O_{12}$ display a constant voltage plateau, the underlying structural changes are very different. In the $Li_xTi_2O_4$ the formation energies in Figure 3.2a indicate that it is due to a macroscopic phase separation, driven by the large energy penalty of mixed - $Li^{8a}/Li^{16c}$ sites, in practice leading to domains where Li-ions occupy the 8a sites and domains where the Li-ions occupy 16c sites thereby avoiding the mixed - $Li^{8a}/Li^{16c}$ site occupancy. However in $Li_{4+x}Ti_5O_{12}$, a number of configurations with mixed $Li^{8a}/Li^{16c}$ site occupancy are close or even on the convex-hull, indicating that the material will transform from $Li_4Ti_5O_{12}$ to $Li_7Ti_5O_{12}$ via these $Li^{8a}/Li^{16c}$ configurations. Because the only difference between $Li_xTi_2O_4$ and $Li_{4+x}Ti_5O_{12}$ is the presence of Li-ions on the Ti 16d sub-lattice, these ions appear to stabilize the mixed $Li^{8a}/Li^{16c}$ site occupancy.

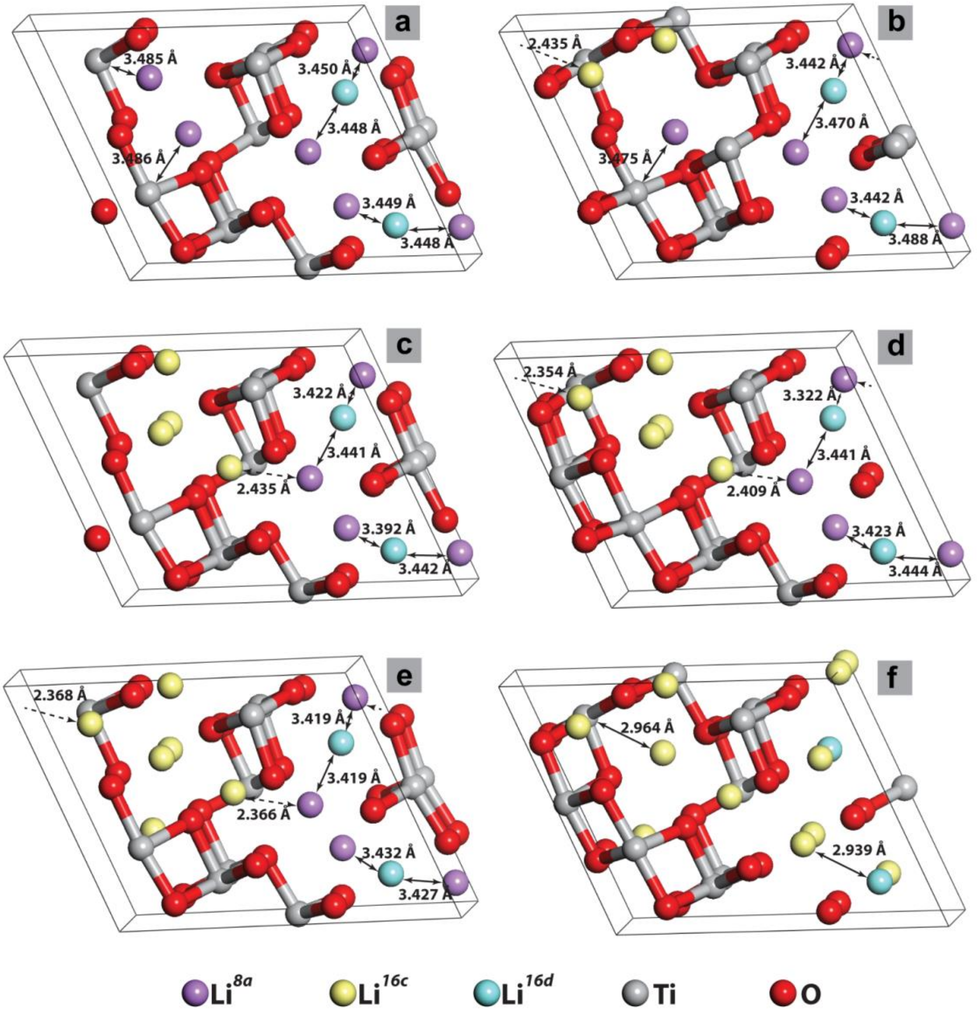
a
3.485 Å
3.450 Å
3.448 Å
3.486 Å
3.449 Å
3.448 Å
b
2.435 Å
3.442 Å
3.470 Å
3.475 Å
3.442 Å
3.488 Å
c
3.422 Å
3.441 Å
2.435 Å
3.392 Å
3.442 Å
d
2.354 Å
3.322 Å
3.441 Å
2.409 Å
3.423 Å
3.444 Å
e
2.368 Å
3.419 Å
3.419 Å
2.366 Å
3.432 Å
3.427 Å
f
2.964 Å
2.939 Å
Li8a
Li16c
Li16d
Ti
O

**Figure 3.3:** Structures corresponding to the lowest energy configurations of LTO-1 where panels **a)** – **f)** correspond to $Li_4Ti_5O_{12}$, $Li_{4.5}Ti_5O_{12}$, $Li_5Ti_5O_{12}$, $Li_{5.5}Ti_5O_{12}$, $Li_6Ti_5O_{12}$, and $Li_{6.5}Ti_5O_{12}$ respectively some of which fall on the convex hull. The red and grey balls correspond to O and Ti, while the cyan, violet, and yellow balls correspond to Li at the 16d, 8a, and 16c sites respectively.

To gain insight in this mechanism the $Li_{4+x}Ti_5O_{12}$ lowest energy configurations, three of which are positioned on the convex hull, as shown in Figure 3.2b-c, are studied in more detail. The structure of the all $Li^{8a}$ occupied, $Li_4Ti_5O_{12}$ of LTO-1, shown in Figure 3.3a, has relatively short $Li^{8a}$ – $Li^{16d}$ distances (3.448 – 3.450  Å) as compared to the $Li^{8a}$ – $Ti^{16d}$ distances (3.485 – 3.486 Å). The mixed $Li^{8a}$/$Li^{16c}$ occupancy is observed in Figures 3.3b-e, corresponding to LTO-1 configurations with compositions of $Li_{4.5}Ti_5O_{12}$ up to $Li_6Ti_5O_{12}$, where it is observed that the nearest $Li^{16c}$ – $Li^{8a}$ pairs occur near the $Li^{16d}$ position. This indicates that the $Li^{16d}$ atom stabilizes the $Li^{8a}$ – $Li^{16c}$ nearest neighbors, albeit up to a certain maximum Li concentration. When the composition exceeds $Li_6Ti_5O_{12}$, the $Li^{8a}$ ions move to neighboring 16c sites as observed in Figure 3.3f. In pure spinel the nearest $Li^{8a}$ – $Li^{16c}$ neighbors would result in a interatomic distance of 1.82 Å[41] and hence a large Coulombic repulsion making these configurations energetically unfavorable.

In LTO the nearby $Li^{16d}$ sites allow the $Li^{8a}$ – $Li^{16c}$ distance to relax to a distance in the range of 2.354 – 2.435 Å (lowering the Coulombic repulsion) as shown in Figures 3.3d-e. Configurations with a smaller $Li^{8a}$ – $Li^{16c}$ distance result in a higher formation enthalpy. For example the composition $Li_{5.5}Ti_5O_{12}$ of LTO-1, where the lowest energy configuration has been depicted in Figure 3.3d, has a $Li^{8a}$ – $Li^{16c}$ distance between 2.354 – 2.435 Å. At the same composition the configuration with a 200 meV/Li higher formation enthalpy, shown in Figure 3.4a, contains several $Li^{8a}$ – $Li^{16c}$ nearest neighbors, however, of which all but one have a $Li^{16d}$ adjoining atom. Because the $Li^{8a}$ atoms are not able to relax towards the $Ti^{16d}$ atoms the $Li^{8a}$ – $Li^{16c}$ distances are relatively small (1.986 – 2.122 Å) which is responsible for the higher formation enthalpy. The same stabilization mechanism is observed in LTO-2 (Figure 3.4b).

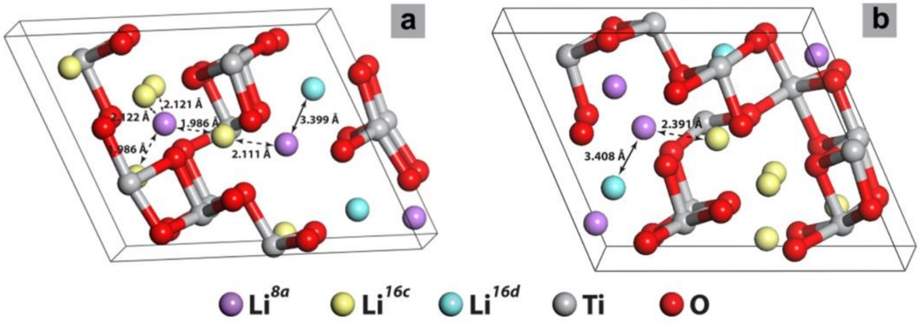

**Figure 3.4: a)** Structure corresponding to the highest energy configuration of LTO-1 at a concentration of $Li_{5.5}Ti_5O_{12}$. The red and grey balls correspond to O and Ti, while the blue, violet, and yellow balls correspond to Li at the 16d, 8a, and 16c sites respectively. Distances between $Li^{8a}$ – $Li^{16d}$ and $Li^{8a}$ – $Li^{16c}$ are given by solid and dashed lines respectively. **b)** Structure corresponding to the lowest energy configuration of LTO-2 with a composition of $Li_{5.5}Ti_5O_{12}$. The red and grey balls correspond to O and Ti, while the blue, violet, and yellow balls correspond to Li at the 16d, 8a, and 16c sites respectively.

A consequence of the nearest $Li^{8a}$ – $Li^{16c}$ stabilization adjacent to $Li^{16d}$ atoms in spinel $Li_{4+x}Ti_5O_{12}$ is that the phase separation between domains of 8a occupancy and 16c occupancy, representing the first-order phase transition, is mixed on a sub-nanometer length scale in contrast to pure spinel.

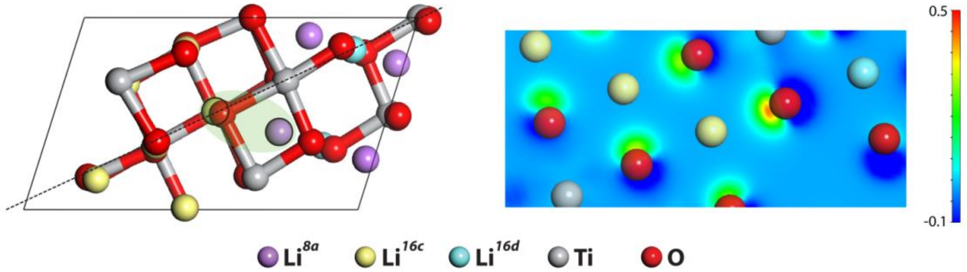

**Figure 3.5:** Lowest energy $Li_6Ti_5O_{12}$ configuration of LTO-1 (Left) and a cross section of the difference in charge density (Right) between the $Li_6Ti_5O_{12}$ configuration and the $Li_1Ti_4O_{12}$ configuration consisting only of $Li^{16d}$ . The cross-sectional plane chosen passes through the $Li^{16d}$ – $Li^{16c}$ – $Ti^{16d}$ atoms indicated by the dotted line. Of these atoms the $Li^{16c}$ forms part of the nearest neighbor $Li^{8a}$ – $Li^{16c}$ pair denoted by the green shaded oval.

The stabilization mechanism of adjoining $Li^{8a}$ and $Li^{16c}$ is further investigated by considering the difference in valence electron density upon lithium addition between the most stable $Li_6Ti_5O_{12}$ (LTO-1) and $Li_1Ti_5O_{12}$ (LTO-1) configurations shown in Figure 3.5. From a cross section of the charge density difference it is observed that upon lithium addition, the electron density is donated to the 2p-O and 3d-Ti orbitals of the neighboring O and Ti atoms. Consequentially, the $Li^{16c}$ atom neighboring the $Li^{8a}$ (nearest to the $Li^{16d}$) seen in the left panel of Figure 3.5 is better shielded by the electrons residing on the O orbitals in its vicinity in comparison with other $Li^{16c}$ atoms, with a larger charge density being transferred to the oxygen atom adjacent to the $Li^{16d}$. In addition to the larger $Li^{8a}$ – $Li^{16c}$ nearest neighbor distances allowed in the vicinity of a $Li^{16d}$, the electron density screening is responsible for the stabilization of the nearest $Li^{8a}$ and $Li^{16c}$ neighbors in spinel $Li_{4+x}Ti_5O_{12}$, resulting in the formation of sub-nanometer 8a-rich and 16c-rich domains.

## 3.3 Kinetics of Li Ions in $Li_4Ti_5O_{12}$

To investigate the kinetics of the Li-ions on the 8a and 16c sub-lattice Molecular Dynamics (MD) simulations were performed using DFT for intermediate compositions 0<x<3 in spinel $Li_{4+x}Ti_5O_{12}$ hosting a mixture of 8a and 16c site occupancies. A 2x1x2 supercell was constructed with an initial (001) orientation of the interface between the domains of $Li^{8a}$ and $Li^{16c}$ occupancy, as shown in Figure 3.6, which was suggested to be a preferential interface orientation by TEM[17] and static (0 K) DFT calculations[22]. Such sharp coherent interfaces, separating domains of $Li^{8a}$ and $Li^{16c}$, were observed using electron microscopy[15] reporting a small interface width of only a few Angstroms. At the (001) interface one layer of 8a positions and 16c positions is purposely left unoccupied, to create a space for the interface to relax during the MD simulations, see Figure 3.6. The periodic boundary conditions introduce a second interface between the $Li^{8a}$ and $Li^{16c}$ domains also with the (001) orientation connecting the bottom of the supercell with the top, in this case introducing nearest $Li^{8a}$ – $Li^{16c}$ neighbors. Several supercell configurations that differ in size and stoichiometry were simulated for a calculation time of up to 200 ps for a wide range of temperatures (300 to 600K).

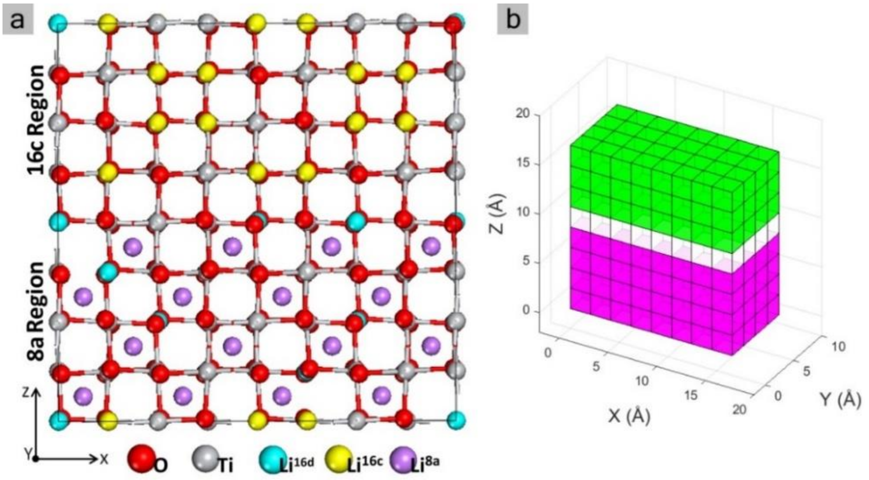

**Figure 3.6: a)** 2x1x2 LTO supercell, starting point of the MD simulations. **b)** 3D representation of the phase separated initial supercell: in green the Li-rich endmember ($Li_7Ti_5O_{12}$) phase where all electrochemically active Li-ions occupy the 16c sites and in purple the Li-poor endmember ($Li_4Ti_5O_{12}$) phase where all electrochemically active ions occupy the 8a sites. The dimensions of the supercell are 1.67·0.83·1.67 $nm^3$ and the DFT calculations are performed under periodic boundary conditions.

The studied supercells, temperatures (T) and total simulation time (t) of the performed MD simulations are presented in Table 3.1. The supercells A and B have the same configuration. The difference is that in supercell B we did not introduce an empty layer between the Li-poor and Li-rich phases resulting in a different stoichiometry. Both qualitative and quantitative results were similar for all the supercells responding to intermediate Li-ion concentrations (A, B, C). MD simulations were also performed for the endmember phases (supercells D, E). Not a single Li-ion hop was observed in similar timescales (200 ps) and high temperatures (600 K) showing the difficulty of Li-ion diffusion at the perfectly ordered endmember phases.

**Table 3.1:** Characteristics of the studied structures.

| Supercell | Composition | Atoms | T (K) | t (ps) |
|---|---|---|---|---|
| A:2x1x2 | $Li_{5.2}Ti_5O_{12}$ | 237 | 300/420/520/600 | 96/85/185/70 |
| B:2x1x2 | $Li_{5.7}Ti_5O_{12}$ | 241 | 600 | 55 |
| C:2x2x2 | $Li_{5.6}Ti_5O_{12}$ | 488 | 600 | 10 |
| D:1x2x1 | $Li_4Ti_5O_{12}$ | 112 | 600 | 200 |
| E:1x2x1 | $Li_7Ti_5O_{12}$ | 128 | 600 | 200 |

During the first 2 ps (the initial stage of the MD simulations) the supercell shown in Figure 3.6 immediately relaxes at the interfaces towards a variety of local $Li^{8a}$ - $Li^{16c}$ - $Li^{16d}$ configurations, between which it fluctuates. These local configurations are very similar to the ground state configurations predicted by the static DFT calculations in the previous section where nearest $Li^{8a}$ – $Li^{16c}$ neighbors were shown to be stabilized by adjacent $Li^{16d}$ atoms, see Figures 3.3c-e. The kinetics of the local configurations will be discussed in detail in a following paragraph. After the initial 2 ps the MD simulations show a highly mobile, liquid like, interface and domain structure moving through the crystal lattice as shown in Figure 3.7. MD-simulations of the same supercell at different temperatures show similar results, however differing in the exact evolution of the morphology indicating the random character of the mobile domain interface (Figure 3.8).

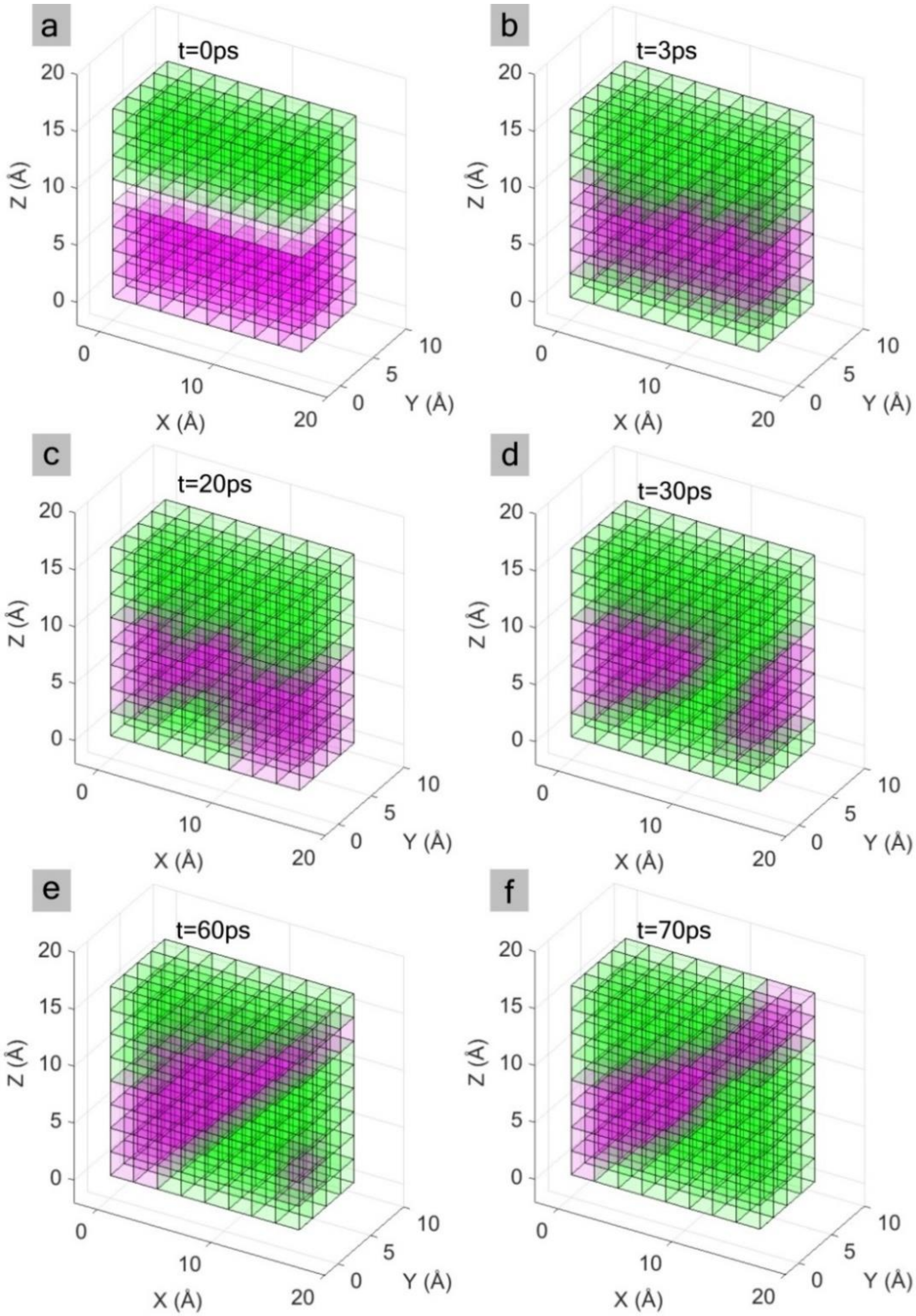
a
t=0ps
Z (Å)
20
15
10
5
0
0
10
20
X (Å)
0
5
10
Y (Å)
b
t=3ps
c
t=20ps
d
t=30ps
e
t=60ps
f
t=70ps

**Figure 3.7:** Snapshots of the phase morphology during the MD simulation showing the evolution of the Li-poor endmember ($Li^{8a}$) and Li-rich endmember ($Li^{16c}$) domains and the interface during 70 ps in the 2x1x2 supercell at 600 K.

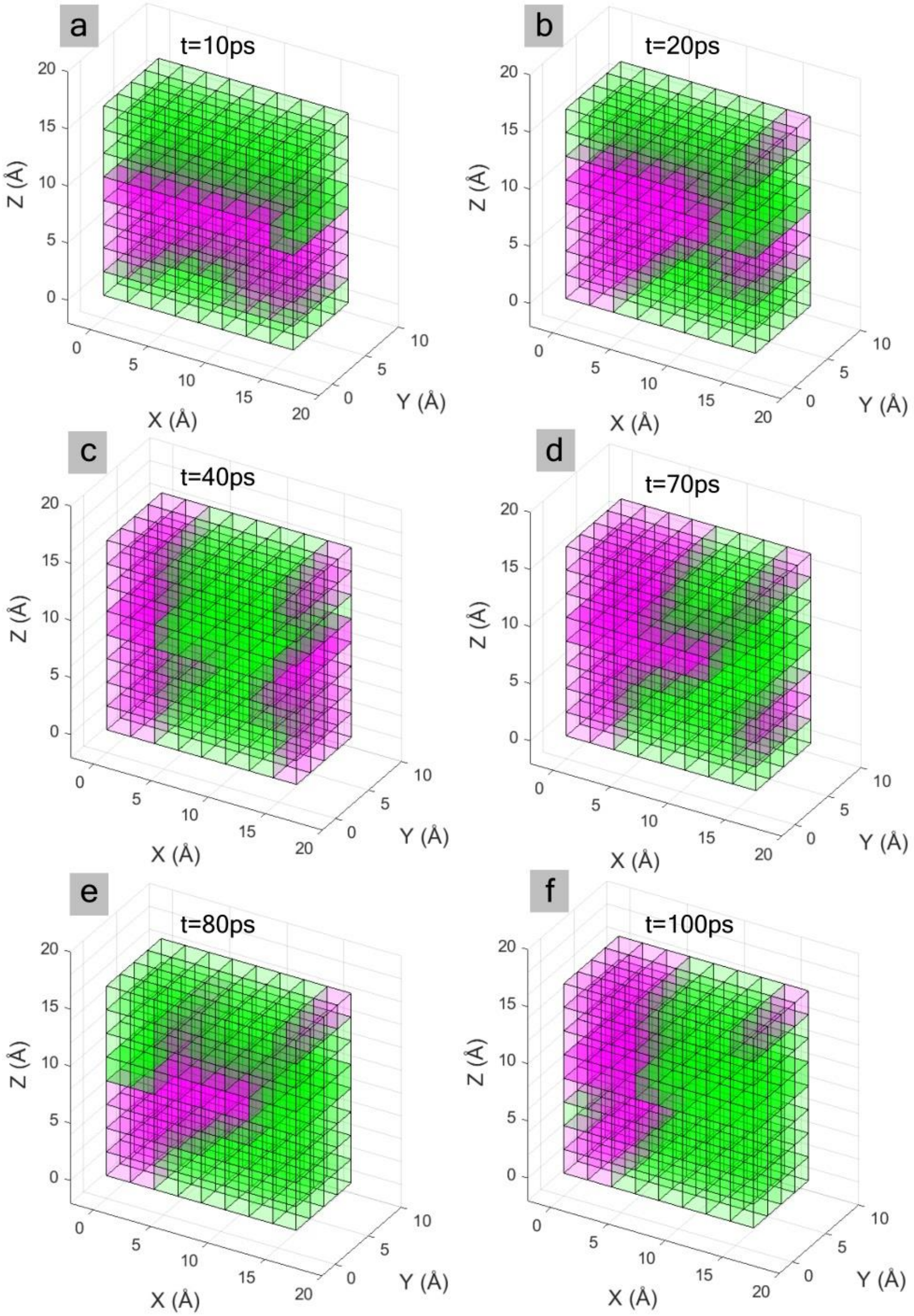
a
t=10ps
b
t=20ps
c
t=40ps
d
t=70ps
e
t=80ps
f
t=100ps
Z (Å)
20
15
10
5
0
X (Å)
0
5
10
15
20
Y (Å)
0
5
10

**Figure 3.8:** Snapshots of the phase morphology during the MD simulation showing the evolution of the Li-poor endmember ($Li^{8a}$) and Li-rich endmember ($Li^{16c}$) domains and the interface during 100 ps in the 2x1x2 supercell at 520 K.

The mobility of the Li$^{8a}$ and Li$^{16c}$ domain-interface morphology is a consequence of the high Li-ion mobility over the 8a and 16c sub-lattices. This is illustrated by Figure 3.9a and 3.9b that display the relative positions of the 8a and 16c sites and the integrated Li-ion density during the first 100 out of the total 185 ps MD simulation at 520 K of a fraction of the supercell shown in Figure 3.6. It reveals the diagonal pathways connecting every 8a site to another 8a site in four directions, via a 16c site, creating a 3D diffusional network. Figure 3.9c displays the mean square displacement (MSD) as a function of the MD simulation time.

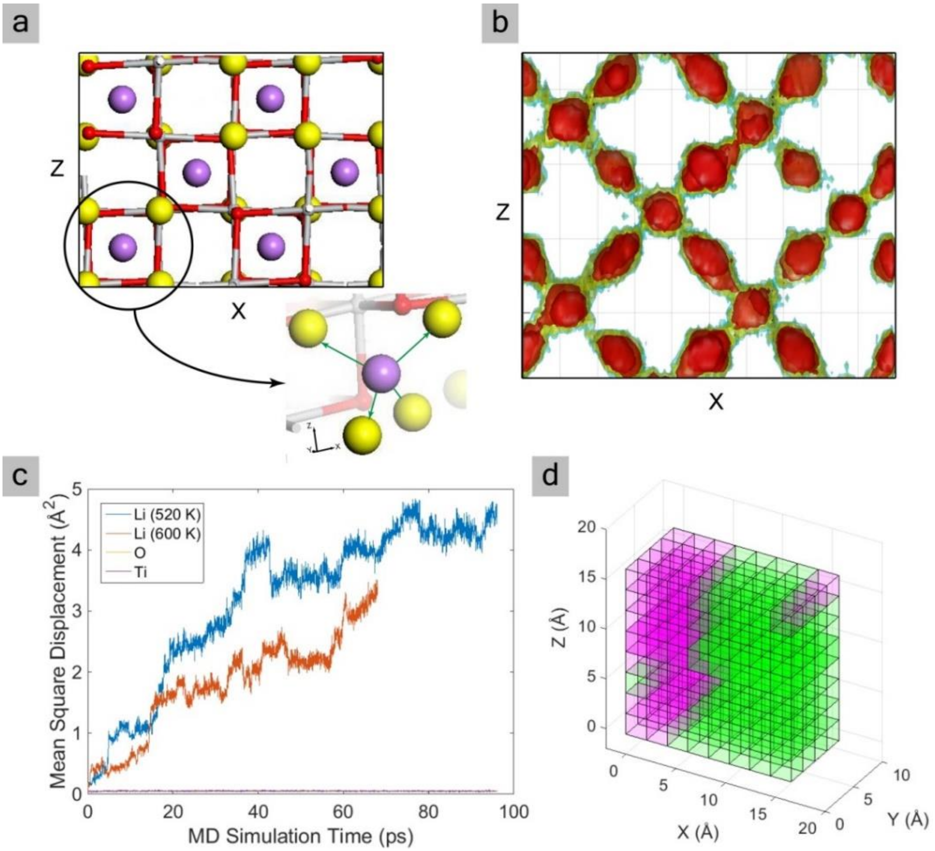

**Figure 3.9: a)** Schematic representation of the all possible 8a and 16c sites in a zoom-in fraction of the supercell and **b)** Li-ion density plot integrated over the first 100 ps of the MD-simulation at 520 K matching in size the schematic fraction presented in Figure 3.9a, red colour represents high density, green represents lower Li-ion density indicating the characteristic diagonal (110) (011) (101) Li-ion diffusion pathways. **c)** Mean square displacement (MSD) of all elements in the supercell for the first 100 ps out of the total 185 ps at 520 K and the total 70 ps at 600 K. **d)** Representative 3D configuration for the configurations occurring after the first 100 ps.

After approximately 100 ps the MSD reaches a plateau which is accompanied by an apparent stabilization of the interface in the (100) direction, see Figure 3.9d. For the cubic symmetry of spinel $Li_{4+x}Ti_5O_{12}$ this is equivalent to the (010) and the (001) orientation from which the MD simulation was started. However, close examination at the atomic scale shows that locally no preferred interface exists. The diffusion of the Li-ions, and thereby the interface and domain mobility, is dictated by the $Li^{16d}$ atoms, as will be discussed below. Given the stabilization of the MSD after approximately 100 ps, this should be considered as an equilibration of the system from the initial conditions shown in Figure 3.6. Therefore it is necessary to distinguish the Li-ion kinetics before and after the initial approximately 100 ps as this equilibration results in a MSD of the Li-ions, as observed in Figure 3.9c, whereas after 100 ps only local mobility is observed leading to fluctuations of the interface region between the $Li^{8a}$ and $Li^{16c}$ domains, presented in Figure 3.10. The stabilization of the MSD indicates that the MD system during the first 100 ps is not in equilibrium, a condition similar to that imposed during the operation of Li-ion battery electrodes where electrochemically driven insertion or extraction of Li-ions induces a non-equilibrium condition. We suggest that the diffusional relaxation mechanism is of interest for the understanding of the functioning of spinel $Li_{4+x}Ti_5O_{12}$ as Li-ion battery electrode.

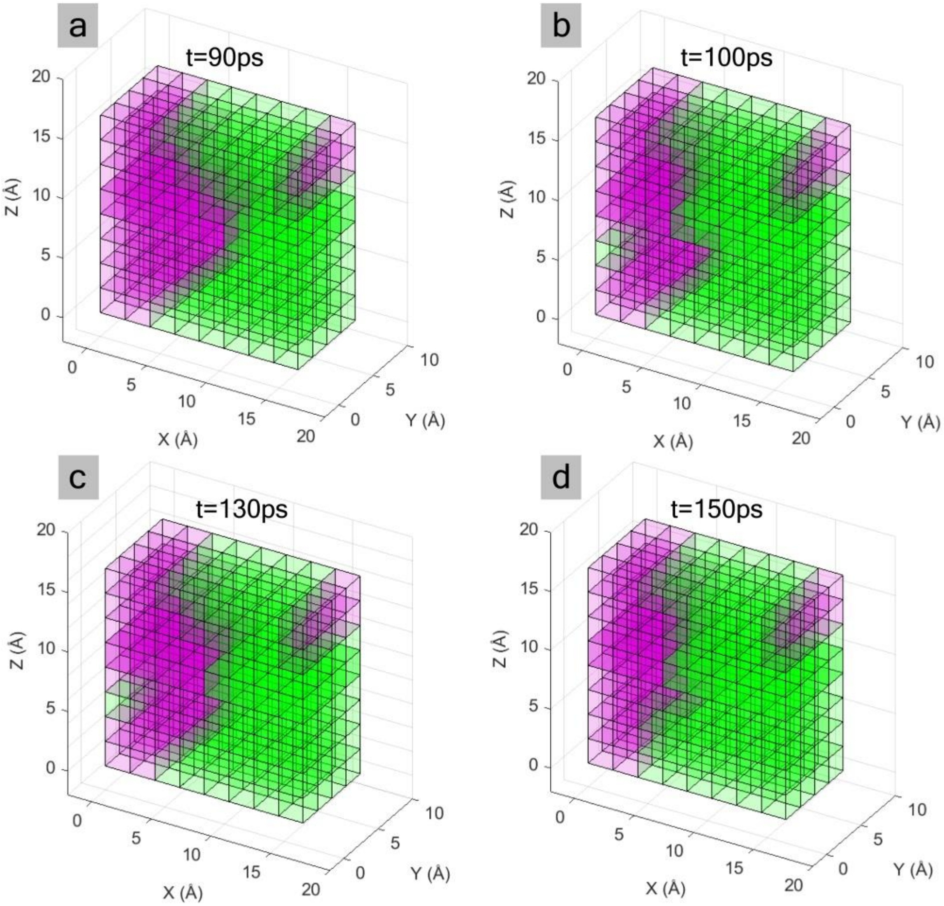

**Figure 3.10:** Time lapse after the interface equilibration in the 2x1x2 supercell at 520K that depicts the slight changes after the equilibration period (90 to 100ps), It should be realized that the DFT calculations are performed under periodic boundary conditions.

From all possible Li-ion diffusional transitions (16c–16c, 8a–8a, 16d–16c, 16c–16d, 16d–8a, 8a–16d, 8a–16c and 16c–8a) only the 16c–8a and 8a–16c transitions occur during the MD simulations, consistent with the high energy barriers for the other transitions measured with local probes and predicted by ab-initio calculations.[12, 14, 25-28]. The most interesting observation is that the large majority of the transitions (>99.5%) takes place at interfaces between the $\mathrm{Li}^{8a}$ - domains and $\mathrm{Li}^{16c}$ - domains and practically no transitions occur within the $\mathrm{Li}^{8a}$ - domains and $\mathrm{Li}^{16c}$ - domains during the time of the MD simulations, the latter in agreement with experimental observations[12, 14, 25, 26] pointing out sluggish diffusion at the endmember phases. This was further confirmed by MD simulations of the endmember phases $Li_4Ti_5O_{12}$ ($Li^{8a}$) and $Li_7Ti_5O_{12}$ ($Li^{16c}$) where no transitions were predicted at 600 K and up to 200 ps simulation time. This indicates that the high mobility of the Li-ions in spinel $Li_4Ti_5O_{12}$ [12, 14, 26, 29, 32] should be attributed to high Li-ion mobility at the interfaces between the $Li^{8a}$ - domains and $Li^{16c}$ - domains. As concluded from the most stable configurations in Figure 3.3, the interfaces are stabilized by the $Li^{16d}$ atoms resulting in sub-nanometer domains and hence a large abundance of these interfaces. As a consequence $Li_{4+x}Ti_5O_{12}$ for the compositions $0<x<3$ is an excellent Li-ion conductor due to the highly mobile and apparently abundant $Li^{16d}$ stabilized interfaces.

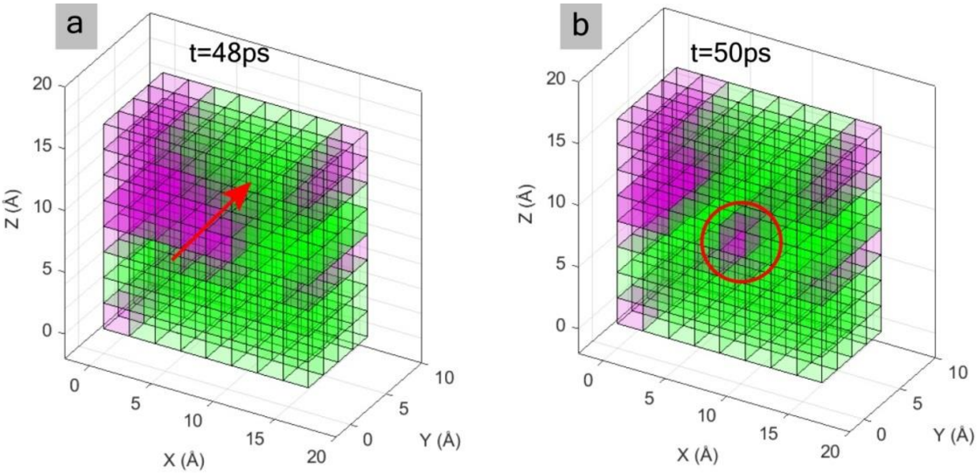

**Figure 3.11:** Fast moving interface cuts out a Li-poor region and vacancies within the Li-rich region, there is a $Li^{16d}$ within the red circle.

The rare conditions that lead to Li-ion transitions within the $Li^{8a}$ - domains and $Li^{16c}$ - domains (0.05% of all transitions) are analyzed below. The fast moving interface can cut out an area of one endmember phase within the other (Figure 3.11). In this example, that occurred twice (520K, 420K) during our MD simulations, a Li-poor region that is stabilized by the Li in a 16d position is cut out within the Li-rich region. For a few pico seconds some back and forth jumps occurred in the area indicated with the red circle transforming it into $Li^{16c}$ (green) and $Li^{8a}$ (purple) domains respectively. This was possible due to the high amount of vacancies that the fast moving interface trapped inside the Li-rich region when isolating the $Li^{8a}$ region (red circle) from the rest Li-poor region. In addition, both examples occurred near Li occupation in the 16d site, further suggesting the decisive role of $Li^{16d}$ for stabilizing $Li^{8a}$ site and catalyzing the diffusion process. Eventually, in both cases the interface passed by the isolated area a second time, reconnecting it with the Li-poor phase.

The energy barrier for the 8a – 16c and 16c – 8a transitions occurring at the domain interfaces are quantified by the mean jump rate $\nu$ according to $\nu = J/(N\,t)$ where J represents the number of the 16c – 8a or 16c – 8a transitions during the MD simulation, N the total number of Li-ions in the supercell and t the total simulation time. The respective activation barriers for the 8a – 16c and 16c-8a interface transitions are calculated using transition state theory by $E_a = -kT \ln(\nu/\nu_0)$ [47] where $\nu_0$ represents the attempt frequency, typically assumed to be $10^{13}$ $sec^{-1}$ [48], k is Boltzmann's constant and T the temperature, the results of which are presented in Table 3.2.

**Table 3.2:** Activation energies of the 8a-16c and 16c-8a transitions resulting from various MD simulations where t is the total simulation time. The equilibration time is defined as the time disregarded for any analysis.

| Composition | T (K) | t (ps) | Equilibration Time (ps) | Threshold Time (ps) | E (eV) 8a → 16c | E (eV) 16c → 8a |
|---|---|---|---|---|---|---|
| A:$Li_{5.2}Ti_5O_{12}$ | 520 | 185 | 3 | 0.1 | 0.28 | 0.28 |
| A:$Li_{5.2}Ti_5O_{12}$ | 520 | 185 | 100 | 0.1 | 0.31 | 0.31 |
| A:$Li_{5.2}Ti_5O_{12}$ | 600 | 70 | 3 | 0.1 | 0.30 | 0.31 |
| B:$Li_{5.7}Ti_5O_{12}$ | 600 | 54 | 3 | 0.1 | 0.29 | 0.29 |

The equilibration time has little influence on the calculated energy barriers as shown in Table 3.2. The energy barriers are slightly increasing when the equilibration time is increased to 100 ps where the MSD starts to flatten (Figure 3.9c). As expected for a system near equilibrium the barriers for 8a – 16c and 16c – 8a transition are symmetric, and they are in good agreement with NMR experiments [12, 14, 25, 26] as well as with static DFT calculations based on the Nudged Elastic Band (NEB) approach[27, 28]. To examine whether the results depend on the starting conditions of the MD simulations or on temperature several simulations were performed, giving very similar results as shown in Appendix A. Figure 3.12 presents an overview of reported activation energies in literature, including the present results. Compared to the static NEB calculations[27, 28], based on non-stoichiometric cells, the MD simulations have the advantage to include the lattice kinetics and to give insight in the timescale of the most probable transitions. Figure

3.12 indicates that high Li-ion mobility is expected for intermediate compositions, $0<x<3$ in $Li_{4+x}Ti_5O_{12}$. The present results show that this is due to the $Li^{16d}$ stabilized $Li^{8a}$-$Li^{16c}$ nearest neighbors which induce interfaces between the $Li^{8a}$ and $Li^{16c}$ domains with partially filled sites allowing facile Li-ion transitions. In contrast, the vacant sites in the endmembers (16c sites in $Li_4Ti_5O_{12}$ and 8a sites in $Li_7Ti_5O_{12}$) are unstable due to occupancy of all nearest neighbors. As a consequence there are effectively no vacancies to facilitate Li-ion diffusion resulting in the high activation energies observed and predicted[12, 14, 25-28].

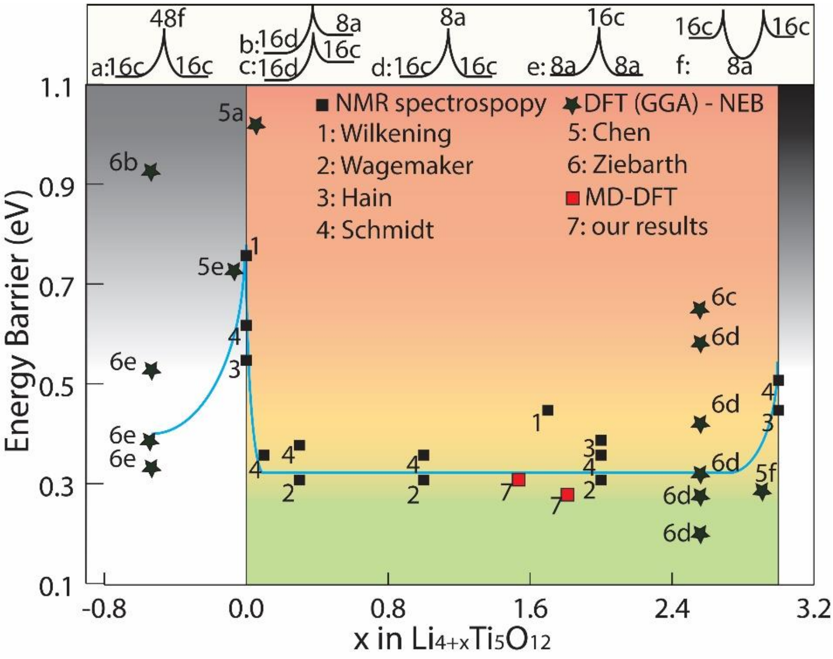

**Figure 3.12:** Overview of the activation energy for Li-ion diffusion in spinel $Li_{4+x}Ti_5O_{12}$ as a function of concentration, where the blue line represents the weighted average.

Considering the MSD during the first 100 ps equilibration time, a self-diffusion coefficient (D) can be determined using $D = MSD/(2N_dt)$[49] where $N_d$ is the dimensionality of the diffusion (in this case $N_d = 3$ for the 3D diffusional work demonstrated by Figure 3.9), and t the time, resulting in $D = 7.3 \cdot 10^{-7}$ $cm^2/s$ at 520 K. One could argue whether during the equilibration, where there is a driving force towards a lower energy state, this can be considered to be a self-diffusion coefficient. However, given the very small energy gain during the simulation,

~0.021 eV per Li-ion, we suggest that this is a realistic prediction of the self-diffusion coefficient. Given the calculated activation energy, see Table 3.2, this results in a room temperature self-diffusion coefficient of $D = 7.5 \cdot 10^{-9}$ cm$^2$/s which is in the upper range of chemical diffusion coefficients reported by electrochemical methods[21, 32]. However, it should be realized that, in particular for non-dilute systems such as LTO, the chemical and self-diffusion coefficients may differ considerably. The MSD obtained from the 70 ps calculation at 600 K results in a self-diffusion coefficient of $D = 8.3 \cdot 10^{-7}$ cm$^2$/s which at room temperature amounts to $D = 3 \cdot 10^{-9}$cm$^2$/s, which is of the same order of magnitude as the MD simulation at 520 K.

To gain insight in this very high Li-ion mobility the local interface configurations and Li-ion transitions during the MD simulations are studied to highlight the origin of the high Li-ion conductivity of spinel $Li_{4+x}Ti_5O_{12}$. This results in three distinct interface configurations between which the system fluctuates as will be illustrated by the snap-shots of an MD simulation showing a typical evolution of the interface region in Figure 3.13a-f. Figure 3.13 is a 2D projection of the 3D 8a and 16c site configuration on the xz plane, covering 8.3 Å of depth in the y-direction, also indicating the $Li^{16d}$ atoms nearest to the shown 8a and 16c sites as well as a schematic indication of the phase boundary. The starting frame, Figure 9a, depicts two of the three possible local interface configurations that occur during the simulations. For local configuration type 1 an occupied $Li^{8a}$ site ($Li_2$) has only one out of four nearest $Li^{16c}$ ($Li_3$) sites occupied. The resulting $Li^{8a} – Li^{16c}$ nearest neighbor pair is stabilized by the neighboring $Li^{16d}$, representing the type of configuration shown in Figure 3.3 that were found to have the lowest formation energy. The thermal fluctuations during the MD simulation result in a $Li^{8a} – Li^{16c}$ nearest neighbor distance between 2.2 and 2.7 Å, mediated by the relaxation near the $Li^{16d}$, consistent with the relaxation results that predict a value close to 2.4 Å (Figure 3.3c,d,e). This configuration allows several possible transitions as indicated by the straight dashed lines in Figure 3.13a Local configuration type 2 is characterized by empty 8a and 16c sites at the interface between the $Li^{8a}$ and $Li^{16c}$ domains forming a (100) or (001) boundary (and (010) in 3D), see for instance near $Li_4$ and $Li_5$ in Figure 3.13a. The straight solid line in Figure 3.13b indicates an actual 8a – 16c transition during the simulation, creating a new $Li^{8a} – Li^{16c}$ nearest neighbor ($Li_2$ and $Li_7$), having interface configuration type 1, stabilized by the nearest $Li^{16d}$. This is followed by an 8a to 16c transition ($Li_7$) in Figure 3.13c resulting in configuration type 2. The transitions from Figure 3.13c to 3.13e proceed via another type 1 interface configuration, characterized by the $Li^{8a}$ - $Li^{16c}$ nearest neighbor pair, indicated with a red arrow in Figure 3.13**.** The sequence from Figure 3.13a to 3.13e effectively causes the interface between the $Li^{8a}$ and $Li^{16c}$ domains to move, responsible for the dynamic domains structure shown in Figure 3.9, to reach the final interface configuration type 3 depicted in Figure 3.13f that occurs several pico-seconds later. In this interface type a diagonal empty layer of 16c sites exist between the two phases (area between $Li_3$, $Li_9$, $Li_4$). To transform this type 3 interface into a type 1 or 2 requires either a number of type 1 and type 2 transitions, or a 16c – 8a – 16c transition which in this case actually occurs during the simulations, as indicated in Figure 3.13f, the result of which is again a type 1 interface configuration. This type of transition occurs approximately only 1 out of 100 transitions, the small probability of which is a consequence of the energetically unfavorable 8a occupancy by the $Li_9$ atom having two nearest $Li^{16c}$ neighbors and no adjacent stabilizing $Li^{16d}$. The poor stability of the intermediate state of this transition is illustrated by its short 0.01 ps life time compared to the typical life time of the configurations shown in Figure 3.13 which is generally more than 0.1 ps. This explains why 16c-8a transitions in $Li^{16c}$ domains and 8a-16c transitions in $Li^{8a}$ domains are energetically very unfavorable and do not occur during the present MD simulations, consistent with NMR experiments[14, 25, 26] and static DFT calculations[27, 28]. The transitions from Figure 3.13b to 3.13e is completed within 0.4 ps indicating that the transitions at the interface may be strongly correlated. In order to investigate if the supercell size in the y-direction influences the result, a 2x2x2 supercell was simulated. Although the size of this supercell limits the total simulation time to 10 ps a number of similar correlated transitions were observed, indicating that these transitions are not induced by the periodic boundary conditions. Analyzing the interface configurations during the MD simulations reveals that adjacent type 1 configurations as well as adjacent type 1 and type 2 configurations are avoided, and that preferably a mixture of type 1 and type 2 or type 3 configurations is formed. This explains the equilibration during the MD simulations shown in Figure 3.7/3.8 where the middle interface exists of adjacent type 2 configurations, and the interface at the bottom of the supercell, which is connected to the top, exists of adjacent type 1 configurations. This unfavorable situation relaxes during the MD simulation to a mixture of interface types as illustrated by the transitions during the initial stages of the MD simulations in Appendix B. During as well as after the equilibration, of approximately 100 ps the same type of fluctuations between the three interface configurations are observed. The only difference is that the non-equilibrium conditions during the initial 100 ps cause a higher calculated transition frequency, responsible for the slightly lower energy barriers during the equilibration time in Table 3.2.

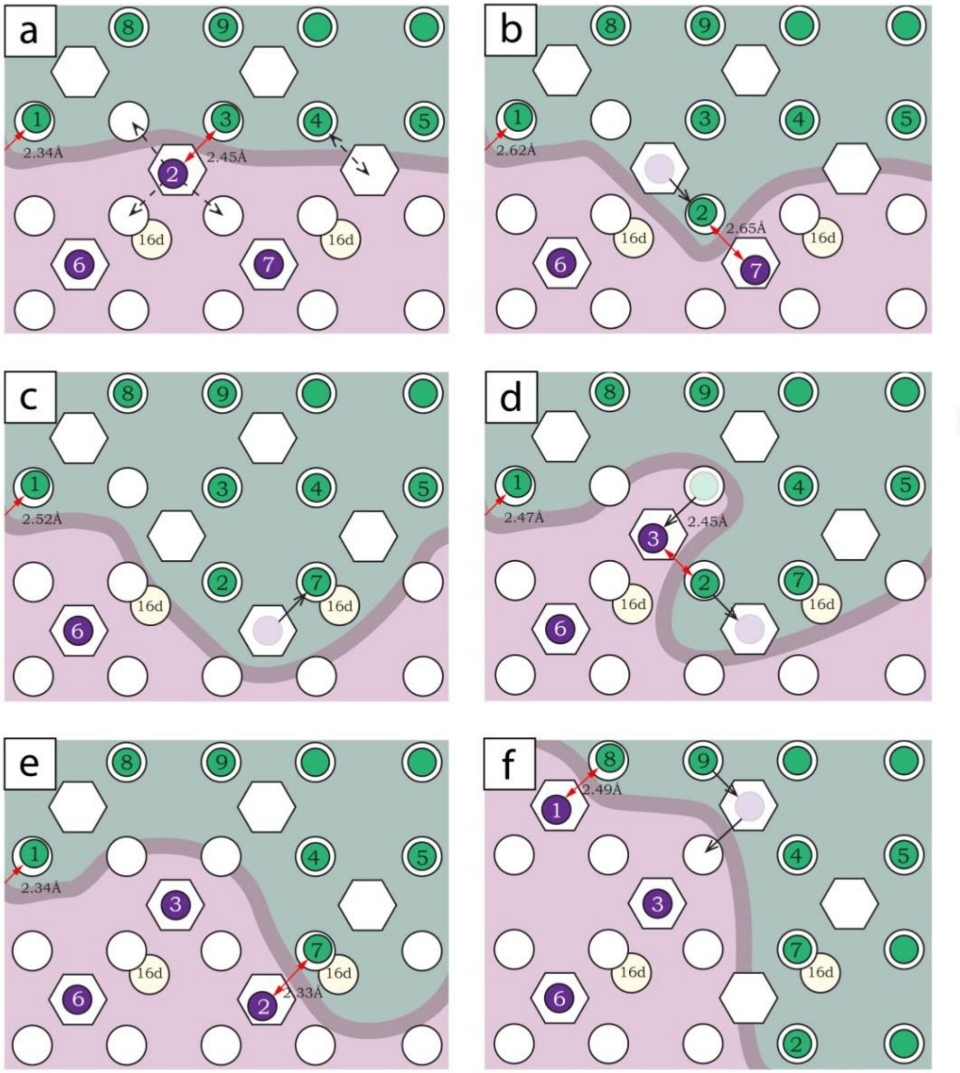
a
8
9
1
3
4
5
2.34Å
2.45Å
2
16d
16d
6
7
b
8
9
1
3
4
5
2.62Å
2
2.65Å
16d
16d
6
7
c
8
9
1
3
4
5
2.52Å
2
7
16d
16d
6
d
8
9
1
4
5
2.47Å
2.45Å
3
2
7
16d
16d
6
e
8
9
1
4
5
2.34Å
3
7
16d
16d
6
2
2.33Å
f
8
9
2.49Å
1
4
5
3
7
16d
16d
6
2

**Figure 3.13:** Schematic 2D representation of the evolution of the 3D 8a and 16c site configuration during a sequence of snap-shots (during 5 ps) resulting from the Molecular Dynamics simulations (2x1x2 $Li_{5.2}Ti_5O_{12}$, 520 K). The hexagons represent the tetrahedral 8a sites and the circles represent the octahedral 16c sites. The color of the enumerated Li-ions (smaller circles) reflect the type of site they occupy, purple for 8a and green for 16c. The Li-ions residing at the 16d sites are indicated with a small offset in the xz plane making them visible behind the 16c sites but their distance to the two nearest 8a sites is equal. A schematic boundary is drawn separating the Li-poor ($Li^{8a}$) and Li-rich ($Li^{16c}$) domains . As indicated in the figure only diagonal transitions can occur connecting 8a sites via a 16c site and vice versa.

The described mechanism demonstrates the crucial role of the $Li^{16d}$ sites which locally stabilize type 1 interface configurations consistent with the most stable configurations in Figure 3.3. Because the $Li^{16d}$ sites prefer to be well distributed through the lattice (Figure 3.1), with an average distance between 5.146 Å and 6.642 Å, this facilitates an abundance of interfaces. The MD simulations indicate that this results in $Li^{8a}$ and $Li^{16c}$ domain sizes as small as 1 nm in diameter, although the restricted supercell may influence this. The intimate mixing of the $Li^{8a}$ and $Li^{16c}$ domains is consistent with the recently observed percolating endmember phase mixture[50]. Moreover, the associated distribution in local configurations explain the local NMR observations[14] and temperature dependent diffraction[13] suggesting nanometer scale domains or even a complete solid solution[12]. Nevertheless the predicted sub-nanometer morphology represents a true first-order phase transition, as the chemical potential, the first derivative of the Gibbs free energy, is discontinuous as observed in Figure 3.3d. Solid solution like phases are experimentally observed in materials that are chemically lithiated. We anticipate that under the high-rate like conditions, associated with chemical lithiation, many particles react concurrently resulting in many particles that are partially lithiated in which the sub-nano morphology will establish. In contrast, relatively slow electrochemical lithiation is likely to activate only a small amount of grains leading to a macroscopic separation of the phases over different grains. This long-range phase separation may prevent reaching the equilibrium conditions described at present rendering the macroscopic phase separation a metastable condition, which explains the experimental observations of macroscopic phase separation[16, 17, 22].

The $Li^{16d}$ stabilized local interface configurations facilitate the high Li-ion mobility observed in the MD simulations, causing transitions between the type 1-3 interface configurations described in Figure 3.13. The high Li-ion mobility at the domain interfaces is responsible for the high mobility of the domain interface-morphology as observed in Figure 3.7, even at equilibrium conditions. Therefore we conclude that the high mobility of the Li-ions at the interface is responsible for the excellent conductivity of spinel $Li_{4+x}Ti_5O_{12}$. In addition, the interfaces are most likely responsible for the increased electronic conductivity observed[50-53] during battery cycling as they introduce an abundancy of mixed $Ti^{+4}/Ti^{+3}$ oxidation states that were recently shown, by electrochemical and spectroscopic tools[51], to be responsible for enhancing electronic transport. (De)lithiation of the endmember phases introduces the highly mobile interfaces that effectively activate the material by introducing high ionic and electronic mobility, consistent with experimental observations[12, 14, 32, 50-53]. Therefore the presence of the interfaces allows the system to respond very fast to non-equilibrium conditions occurring in Li-ion batteries, explaining the excellent rate capabilities of spinel $Li_{4+x}Ti_5O_{12}$.

## 3.4 Conclusions

Evaluation of the lowest energy configurations predicted by DFT calculations provides fundamental insight into the role of the $Li^{16d}$ sites in disordered spinel $Li_{4+x}Ti_5O_{12}$. The $Li^{16d}$ ions energetically prefer to be well distributed through the LTO lattice, and stabilize the adjacent nearest $Li^{8a}$ – $Li^{16c}$ neighbors. This in contrast to pure spinel $Li_{1+x}Ti_2O_4$ where $Li^{8a}$ – $Li^{16c}$ nearest neighbors are energetically highly unfavorable inducing macroscopic phase separation.

In spinel $Li_{4+x}Ti_5O_{12}$ the stabilization of $Li^{8a}$ – $Li^{16c}$ nearest neighbors allows intimate mixing of the $Li^{8a}$ and $Li^{16c}$ domains explaining both the solid solution interpretations and the observation of domain structures. It represents, however, a true thermodynamic first-order phase transition consistent with the observed flat potential profile. The $Li^{16d}$ stabilized $Li^{8a}$ – $Li^{16c}$ nearest neighbors also play a pivotal role in the kinetics of the system as illustrated by the Molecular Dynamics simulations, by allowing facile transitions between a few stable local interface configurations. These transitions induce rapidly moving interfaces between the $Li^{8a}$ and $Li^{16c}$ domains, explaining the very fast response on non-equilibrium conditions such as those occurring in Li-ion batteries. Thereby, unlike in other known first-order electrode materials, the low energy associated with the coexisting phases, makes that the phase separation in LTO appears to occur spontaneously towards sub-nanometer domains. This suggests that the first-order phase transformation appears to be driven by spinodal decomposition rather than nucleation.

The simulations in this work suggest that it is this local environment that is responsible for the excellent rate performance and cycle life of spinel $Li_{4+x}Ti_5O_{12}$ as Li-ion battery electrode. Nevertheless, it is possible that macroscopic phase separation can occur under non-equilibrium conditions during battery operation as the inter particle diffusion over large distances may prevent reaching the equilibrium conditions described at present, rendering macroscopic phase separation a metastable condition. Thereby the detailed local environment as described by the present DFT calculations brings forward a consistent understanding of the thermodynamics and kinetics of the spinel $Li_{4+x}Ti_5O_{12}$ Li-ion battery electrode material.

## 3.5 Methods

Calculations were performed using the Vienna *ab-initio* simulation package (VASP)[54] wherein the ground state energies were determined by the use of the generalized gradient approximation (GGA) to density functional theory (DFT).[34-36] To describe the electron-ion-core interactions the projector augmented method (PAW)[55, 56] was used. The cutoff was set to 400 eV for accurate calculations. The total energy convergence was ensured to be within $10^{-4}$ eV per formula unit between successive iterations with respect to the k-point sampling. For the MD simulations a k-point mesh of 4x4x4 was applied for supercell relaxations and total energy calculations. The k-point mesh was reduced to 1x1x1 for the MD simulation to ensure feasible computational times. The cutoff energy was set to 400 eV and a 2 fs time step appeared appropriate for the simulations. To determine the position of the mobile Li-ions during the MD simulations the distance of the Li-ions from the crystallographic sites in LTO[49] were monitored. A Li-ion within a radius of 0.8 Å from the crystallographic positions was interpreted as occupying the specific position. A variety of threshold and equilibration times were applied to test the consistency in the hopping time scales. Finally, visualization tools (Material Studio and Mat lab) were used to derive the macroscopic and microscopic pictures of the moving interface.

The difference in Gibbs free energy ΔG for the Li insertion reaction can be used to determine the average voltage for Li insertion as[57]

$$\overline{V} = \frac{-\Delta G}{(x_2 - x_1)F}$$

where $x_1$ and $x_2$ are the two end Li-compositions between which insertion occurs ($x_2 > x_1$) and F is Faradays constant. This is further simplified by the assumption that the changes that occur in volume and entropy are very small during this reaction as a result of which the average insertion voltage can be approximated to

$$\overline{V} = \frac{-\Delta E}{(x_2 - x_1)F}$$

where ΔE is the calculated total energy difference of the two Li-composition limits taking metallic Li as a reference.

## References

**1**. Padhi, A. K.; Nanjundaswamy, K. S.; Goodenough, J. B. Phospho-olivines as positive-electrode materials for rechargeable lithium batteries. *J. Electrochem. Soc.* 1997, 144,1188-1194.

**2**. Deschanv, A.; Raveau, B.; Sekkal, Z. Synthesis and Crystallographic Study of New Solid Solution of Spinelle $Li_{1+x}Ti_{2-x}O_4$. *Mater. Res. Bull.* 1971, 6, 699-704.

**3**. Colbow, K. M.; Dahn, J. R.; Haering, R. R. Structure and Electrochemistry of the Spinel Oxides $LiTi_2O_4$ and $Li_{4/3}Ti_{5/3}O_4$. *J. Power Sources* 1989, 26, 397-402.

**4**. Orikasa, Y.; Maeda, T.; Koyama, Y.; Murayama, H.; Fukuda, K.; Tanida, H.; Arai, H.; Matsubara, E.; Uchimoto, Y.; Ogumi, Z. Direct Observation of a Metastable Crystal Phase of $Li_xFePO_4$ under Electrochemical Phase Transition. *J. Am. Chem. Soc.* 2013, 135, 5497-5500.

**5**. Orikasa, Y.; Maeda, T.; Koyama, Y.; Murayama, H.; Fukuda, K.; Tanida, H.; Arai, H.; Matsubara, E.; Uchimoto, Y.; Ogumi, Z. Transient Phase Change in Two Phase Reaction between $LiFePO_4$ and $FePO_4$ under Battery Operation. *Chem. Mat.* 2013, 25, 1032-1039.

**6**. Zhang, X.; van Hulzen, M.; Singh, D. P.; Brownrigg, A.; Wright, J. P.; van Dijk, N. H.; Wagemaker, M. Rate-Induced Solubility and Suppression of the First-Order Phase Transition in Olivine $LiFePO_4$. *Nano Lett.* 2014, 14, 2279-2285.

**7**. Bai, P.; Cogswell, D. A.; Bazant, M. Z., Suppression of Phase Separation in $LiFePO_4$ Nanoparticles During Battery Discharge. *Nano Lett.* 2011, 11, 4890-4896.

**8**. Cogswell, D. A.; Bazant, M. Z., Coherency Strain and the Kinetics of Phase Separation in $LiFePO_4$ Nanoparticles. *ACS Nano* 2012, 6, 2215-2225.

**9**. Zhang, X.; van Hulzen, M.; Singh, D. P.; Brownrigg, A.; Wright, J. P.; van Dijk, N. H.; Wagemaker, M. Direct view on the phase evolution in individual $LiFePO_4$ nanoparticles during Li-ion battery cycling. *Nat. Commun.* 2015, 6, 8333.

**10**. Liu, H.; Strobridge, F. C.; Borkiewicz, O. J.; Wiaderek, K. M.; Chapman, K. W.; Chupas, P. J.; Grey, C. P. Capturing metastable structures during high-rate cycling of $LiFePO_4$ nanoparticle electrodes. *Science* 2014, 344, 6191.

**11**. Hess, M.; Sasaki, T.; Villevieille, C.; Novak, P. Combined operando X-ray diffraction-electrochemical impedance spectroscopy detecting solid solution reactions of $LiFePO_4$ in batteries. *Nat. Commun.* 2015, 6, 8169.

**12**. Schmidt, W.; Bottke, P.; Sternad, M.; Gollob, P.; Hennige, V.; Wilkening, M. Small Change-Great Effect: Steep Increase of Li Ion Dynamics in $Li_4Ti_5O_{12}$ at the Early Stages of Chemical Li Insertion. *Chem. Mat.* 2015, 27,1740-1750.

**13**. Wagemaker, M.; Simon, D. R.; Kelder, E. M.; Schoonman, J.; Ringpfeil, C.; Haake, U.; Lützenkirchen-Hecht, D.; Frahm, R.; Mulder, F. M. A Kinetic Two-Phase and Equilibrium Solid Solution in Spinel $Li_{4+x}Ti_5O_{12}$. *Adv. Mater.* 2006, 18, 3169-3173.

**14**. Wagemaker, M.; van Eck, E. R. H.; Kentgens, A. P. M.; Mulder, F. M., Li-Ion Diffusion in the Equilibrium Nanomorphology of Spinel $Li_{4+x}Ti_5O_{12}$. *J. Phys. Chem. B* 2009, 113, 224-230.

**15**. Lu, X.; Zhao, L.; He, X. Q.; Xiao, R. J.; Gu, L.; Hu, Y. S.; Li, H.; Wang, Z. X.; Duan, X. F.; Chen, L. Q.; Maier, J.; Ikuhara, Y. Lithium Storage in $Li_4Ti_5O_{12}$ Spinel: The Full Static Picture from Electron Microscopy. *Adv. Mater.* 2012, 24, 3233-3238.

**16**. Scharner, S.; Weppner, W.; Schmid-Beurmann, P. Evidence of two-phase formation upon lithium insertion into the $Li_{1.33}Ti_{1.6}7O_4$ spinel. *J. Electrochem. Soc.* 1999, 146, 857-861.

**17**. Kitta, M.; Akita, T.; Tanaka, S.; Kohyama, M. Two-phase separation in a lithiated spinel $Li_4Ti_5O_{12}$ crystal as confirmed by electron energy-loss spectroscopy. *J. Power Sources* 2014, 257, 120-125.

**18**. Ohzuku, T.; Ueda, A.; Yamamoto, N. Zero-Strain Insertion Material of $Li[Li_{1/3}Ti_{5/3}]O_4$ for Rechargeable Lithium Cells. *J. Electrochem. Soc.* 1995, 142, 1431-1435.

**19**. Johnston, D. C. Superconducting and Normal State Properties of $Li_{1+x}Ti_{2-x}O_4$ Spinel Compounds. 1. Preparation, Crystallography, Superconducting Properties, Electrical-Resistivity, Dielectric Behavior, and Magnetic-Susceptibility. *J. Low Temp. Phys.* 1976, 25,145-175.

**20**. Ferg, E.; Gummow, R. J.; Dekock, A.; Thackeray, M. M. Spinal Anodes for Lithium-Ion Batteries. *J. Electrochem. Soc.* 1994, 141, L147-L150.

**21**. Kavan, L.; Gratzel, M., Facile synthesis of nanocrystalline $Li_4Ti_5O_{12}$ (spinel) exhibiting fast Li insertion. *Electrochem. Solid State Lett.* 2002, 5, A39-A42.

**22**. Tanaka, S.; Kitta, M.; Tamura, T.; Maeda, Y.; Akita, T.; Kohyama, M. Atomic and electronic structures of $Li_4Ti_5O_{12}/Li_7Ti_5O_{12}$ (001) interfaces by first-principles calculations. *J. Mater. Sci.* 2014, 49, 4032-4037.

**23**. Wagemaker, M.; Borghols, W. J. H.; Mulder, F. M. Large impact of particle size on insertion reactions, A case of anatase $Li_xTiO_2$ *J. Am. Chem. Soc.* 2007, 129, 4323.

**24**. Wagemaker, M.; Mulder, F. M.; van der Ven, A. The role of surface and interface energy on phase stability of nanosized insertion compounds. *Adv. Mater.* 2009, 21, 1-7.

**25**. Wilkening, M.; Iwaniak, W.; Heine, J.; Epp, V.; Kleinert, A.; Behrens, M.; Nuspl, G.; Bensch, W.; Heitjans, P. Microscopic Li self-diffusion parameters in the lithiated anode material $Li_{4+x}Ti_5O_{12}$ (0 <= x <= 3) measured by Li-7 solid state NMR. *Phys. Chem. Chem. Phys.* 2007, 9, 6199-6202.

**26**. Hain, H.; Scheuermann, M.; Heinzmann, R.; Wunsche, L.; Hahn, H.; Indris, S. Study of local structure and Li dynamics in $Li_{4+x}Ti_5O_{12}$ (0 <= x <= 5) using Li-6 and Li-7 NMR spectroscopy. *Solid State Nucl. Magn. Reson.* 2012, 42, 9-16.

**27**. Chen, Y. C.; Ouyang, C. Y.; Song, L. J.; Sun, Z. L. Lithium ion diffusion in $Li_{4+x}Ti_5O_{12}$: From ab initio studies. *Electrochim. Acta* 2011, 56, 6084-6088.

**28**. Ziebarth, B.; Klinsmann, M.; Eckl, T.; Elsasser, C. Lithium diffusion in the spinel phase $Li_4Ti_5O_{12}$ and in the rocksalt phase $Li_7Ti_5O_{12}$ of lithium titanate from first principles. *Phys. Rev. B* 2014, 89, 174301.

**29**. Rho, Y. H.; Kanamura, K. $Li^+$ ion diffusion in $Li_4Ti_5O_{12}$ thin film electrode prepared by PVP sol-gel method. *J. Solid State Chem.* 2004, 177, 2094-2100.

**30**. Zaghib, K.; Simoneau, M.; Armand, M.; Gauthier, M. Electrochemical study of $Li_4Ti_5O_{12}$ as negative electrode for Li-ion polymer rechargeable batteries. *J. Power Sources* 1999, 81, 300-305.

**31**. Bach, S.; Pereira-Ramos, J. P.; Baffier, N. Electrochemical properties of sol-gel $Li_{4/3}Ti_{5/3}O_4$. *J. Power Sources* 1999, 81, 273-276.

**32**. Kavan, L.; Prochazka, J.; Spitler, T. M.; Kalbac, M.; Zukalova, M. T.; Drezen, T.; Gratzel, M. Li insertion into $Li_4Ti_5O_{12}$ (Spinel) - Charge capability vs. particle size in thin-film electrodes. *J. Electrochem. Soc.* 2003, 150, A1000-A1007.

**33**. Takami, N.; Hoshina, K.; Inagaki, H., Lithium Diffusion in $Li_{4/3}Ti_{5/3}O_4$ Particles during Insertion and Extraction. *J. Electrochem. Soc.* 2011, 158, A725-A730.

**34**. Hohenberg, P.; Kohn, W. Inhomogeneous Electron Gas. *Phys. Rev.* 1964, 136, B864.

**35**. Perdew, J. P.; Burke, K.; Wang, Y. Generalized gradient approximation for the exchange-correlation hole of a many-electron system. *Phys. Rev. B* 1996, 54, 16533-16539.

**36**. Perdew, J. P.; Chevary, J. A.; Vosko, S. H.; Jackson, K. A.; Pederson, M. R.; Singh, D. J.; Fiolhais, C. Atoms, molecules, solids, and surfaces: Applications of the generalized gradient approximation for exchange and correlation. *Phys. Rev. B* 1992, 46, 6671-6687.

**37**. Bhattacharya, J.; Van der Ven, A. Phase stability and nondilute Li diffusion in spinel $Li_{1+x}Ti_2O_4$. *Phys. Rev. B* 2010, 81, 104304.

**38**. Van der Ven, A.; Aydinol, M. K.; Ceder, G.; Kresse, G.; Hafner, J. First-principles investigation of phase stability in $Li_xCoO_2$. *Phys. Rev. B* 1998, 58, 2975-2987.

**39**. Van der Ven, A.; Ceder, G., Electrochemical properties of spinel $Li_xCoO_2$: A first-principles investigation. *Phys. Rev. B* 1999, 59, 742-749.

**40**. Van der Ven, A.; Marianetti, C.; Morgan, D.; Ceder, G. Phase transformations and volume changes in spinel $Li_xMn_2O_4$. *Solid State Ionics* 2000, 135, 21-32.

**41**. Wagemaker, M.; Van Der Ven, A.; Morgan, D.; Ceder, G.; Mulder, F. M.; Kearley, G. J. Thermodynamics of spinel $Li_xTiO_2$ from first principles. *Chem. Phys.* 2005, 317,130-136.

**42**. Zhong, Z. Y.; Ouyang, C. Y.; Shi, S. Q.; Lei, M. S. Ab initio studies on $Li_{4+x}Ti_5O_{12}$ compounds as anode materials for lithium-ion batteries. *Chem. Phys. Phys. Chem.* 2008, 9, 2104-2108.

**43**. Borghols, W. J. H.; Wagemaker, M.; Lafont, U.; Kelder, E. M.; Mulder, F. M. Size Effects in the $Li_{4+x}Ti_5O_{12}$ Spinel. *J. Am. Chem. Soc.* 2009, 131,17786-17792.

**44**. Ge, H.; Li, N.; Li, D. Y.; Dai, C. S.; Wang, D. L. Electrochemical characteristics of spinel $Li_4Ti_5O_{12}$ discharged to 0.01 V. *Electrochem. Commun.* 2008, 10, 719-722.

**45**. Armstrong, A. R.; Lyness, C.; Panchmatia, P. M.; Islam, M. S.; Bruce, P. G. The lithium intercalation process in the low-voltage lithium battery anode $Li_{1+x}V_{1-x}O_2$. *Nat. Mater.* 2011, 10, 223-229.

**46**. Meng, Y. S.; Arroyo-de Dompablo, M. E. First principles computational materials design for energy storage materials in lithium ion batteries. *Energy Environ. Sci.* 2009, 2, 589-609.

**47**. Vineyard, G. H. Frequency Factors and Isotope Effects in Solid State Rate Processes. *J. Phys. Chem. Solids* 1957, 3, 121-127.

**48**. Van der Ven, A.; Ceder, G.; Asta, M.; Tepesch, P. D. First-principles theory of ionic diffusion with nondilute carriers. *Phys. Rev. B* 2001, 64, 184307 .

**49**. de Klerk, N. J. J.; Wagemaker, M. Diffusion Mechanism of the Sodium-Ion Solid Electrolyte $Na_3PS_4$ and Potential Improvements of Halogen Doping. *Chem. Mater.* 2016, 28, 3122–3130

**50**. Verde, M. G.; Baggetto, L.; Balke, N.; Veith, G. M.; Seo, J. K.; Wang, Z. Y.; Meng, Y. S. Elucidating the Phase Transformation of $Li_4Ti_5O_{12}$ Lithiation at the Nanoscale. *ACS Nano* 2016, 10, 4312-4321.

**51**. Kim, C.; Norberg, N. S.; Alexander, C. T.; Kostecki, R.; Cabana, J. Mechanism of Phase Propagation During Lithiation in Carbon-Free $Li_4Ti_5O_{12}$ Battery Electrodes. *Adv. Funct. Mater.* 2013, 23, 1214-1222.

**52**. Young, D.; Ransil, A.; Amin, R.; Li, Z.; Chiang, Y. M. Electronic Conductivity in the $Li_{4/3}Ti_{5/3}O_4$-$Li_{7/3}Ti_{5/3}O_4$ System and Variation with State-of-Charge as a Li Battery Anode. *Adv. Energy Mater.* 2013, 3, 1125-1129.

**53**. Song, M. S.; Benayad, A.; Choi, Y. M.; Park, K. S. Does $Li_4Ti_5O_{12}$ need carbon in lithium ion batteries? Carbon-free electrode with exceptionally high electrode capacity. *Chem. Commun.* 2012, 48, 516-518.

**54**. Kresse, G.; Furthmüller, J. Efficient iterative schemes for ab initio total-energy calculations using a plane-wave basis set. *Phys. Rev. B* 1996, 54, 11169-11186.

**55**. Blochl, P. E., Projector Augmented-Wave Method. *Phys. Rev. B* 1994, 50, 17953-17979.

**56**. Kresse, G.; Joubert, D. From ultrasoft pseudopotentials to the projector augmented-wave method. *Phys. Rev. B* 1999, 59, 1758.

**57**. Aydinol, M. K.; Kohan, A. F.; Ceder, G.; Cho, K.; Joannopoulos, J. Ab initio study of lithium intercalation in metal oxides and metal dichalcogenides. *Phys. Rev. B* 1997, 56, 1354-1365.

# 4

# Towards Optimal Performance and In-Depth Understanding of Spinel $Li_4Ti_5O_{12}$ Electrodes through Phase Field Modeling

«εἰ γὰρ ἐν μικρῷ κόσμῳ γίνεται, καὶ ἐν μεγάλῳ· καὶ εἰ ἐν τῷ κόσμῳ καὶ ἐν τῷ ἀπείρῳ»

“If it happens in the microcosm, then also in the macrocosm. And if in the cosmos, then also in the infinite”

Aristotle

Aristotle, *Physics*, Book VIII, 252b, translated by D. W. Graham, Clarendon Press, Oxford, 1999.

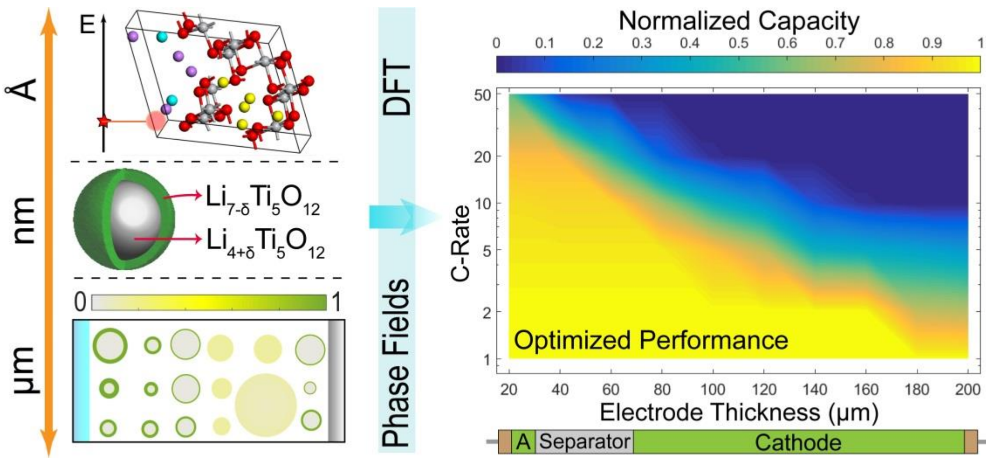
Å
nm
μm
E
$Li_{7-\delta}Ti_5O_{12}$
$Li_{4+\delta}Ti_5O_{12}$
0
1
DFT
Phase Fields
Normalized Capacity
0
0.1
0.2
0.3
0.4
0.5
0.6
0.7
0.8
0.9
1
C-Rate
50
20
10
5
2
1
Optimized Performance
20
40
60
80
100
120
140
160
180
200
Electrode Thickness (μm)
A
Separator
Cathode

## Abstract

Computational modeling is vital for the fundamental understanding of processes in Li-ion batteries. However, capturing nanoscopic to mesoscopic phase thermodynamics and kinetics in the solid electrode particles embedded in realistic electrode morphologies is challenging. In particular for electrode materials displaying a first order phase transition, such as $LiFePO_4$, graphite and spinel $Li_4Ti_5O_{12}$, predicting the macroscopic electrochemical behavior requires an accurate physical model. Herein, we present a thermodynamic phase field model for Li-ion insertion in spinel $Li_4Ti_5O_{12}$ which captures the performance limitations presented in literature as a function of all relevant electrode parameters. The phase stability in the model is based on ab-initio DFT calculations and the Li-ion diffusion parameters on nanoscopic NMR measurements of Li-ion mobility, resulting in a parameter free model. The direct comparison with prepared electrodes shows good agreement over three orders of magnitude in the discharge current. Overpotentials associated with the various charge transport processes, as well as the active particle fraction relevant for local hotspots in batteries, are analyzed. It is demonstrated which process limits the electrode performance under a variety of realistic conditions, providing comprehensive understanding of the nanoscopic to microscopic properties. These results provide concrete directions towards the design of optimally performing $Li_4Ti_5O_{12}$ electrodes.

Based on the homonymous paper:
Vasileiadis, A.; de Klerk, N. J. J.; Smith, R. B.; Ganapathy, S.; Harks, P. P. R. M. L.; Bazant, M. Z.; Wagemaker, M. Toward Optimal Performance and In-Depth Understanding of Spinel $Li_4Ti_5O_{12}$ Electrodes through Phase Field Modeling. *Adv. Funct. Mat.* 2018, 28, 1705992.

## 4.1 Introduction

Li-ion batteries are widely implemented in mobile and static applications that require high standards of energy and power density, as well as a prolonged and stable cycle life.[1, 2] The most commonly used anode is graphite, a material which usually fails to meet the high rate, safety and cycle-stability requirements for next generation applications.[3-6] As a result, negative electrode candidates with superior electrochemical characteristics are required. One of the most prominent and well-studied negative electrode materials is the spinel $Li_4Ti_5O_{12}$ (LTO). LTO can be cycled reversibly up to its theoretical capacity of 175 mAh/g[7, 8] and has a stable voltage plateau at 1.55 V vs. $Li/Li^+$ [9, 10]. Despite the relatively large potential for a negative electrode and small capacity,  compromising the energy density, it allows safe operation inside the stability window of most organic electrolytes. Consequently, dendrite and solid electrolyte interface (SEI) formation is minimized, enabling LTO to meet superior safety standards and performance.[4, 5, 11] Besides the reduction of undesirable side reactions, the exceptional cycle life of LTO is also the consequence of its “zero strain” property.[12, 13] During lithiation the lattice parameters remain almost unchanged, resulting in a negligible volume change of 0.2% [14, 15] minimizing mechanical instabilities induced by lattice strain and volume changes during cycling. In combination with the low costs for preparation[16], the excellent safety and performance characteristics of the LTO material make it an ideal candidate for sustainable energy storage and transport applications.[5, 6]

Although LTO is already applied in Li-ion batteries for modern commercial applications[4, 17-23], a number of crucial challenges remain. These include avoiding gas evolution[24, 25] (CO, $H_2$ and $CO_2$) upon cycling, improving the battery energy density and improving the power performance.[26] In an effort to achieve enhanced electrode performance a huge variety of experimental optimization methods has been investigated[4, 6, 27, 28], including doping, surface coating, nanostructuring, and controlling the  morphology of the material.

The crystal lattice of the spinel $Li_4Ti_5O_{12}$ is described by the cubic Fd-3m space group (no. 227).[10] In $Li_4Ti_5O_{12}$ the Li ions reside in the tetrahedral 8a sites, and partially (1/6) in the electrochemically inactive octahedral 16d sites. Upon lithiation the 8a site becomes unstable, and the inserted Li-ions and Li-ions at the 8a sites will occupy the 16c octahedral sites.[29-31] This topotactic transition causes the structure to undergo a phase transition from a spinel to a rock-salt lattice, reaching a final composition of $Li_7Ti_5O_{12}$. This process is accompanied by a redox reaction reducing $Ti^{+4}$ to $Ti^{+3}$. The material is believed to transform via a core-shell, two-phase separation mechanism between the two spinel endmember phases $Li_4Ti_5O_{12}$ and $Li_7Ti_5O_{12}$.[6, 7, 14, 32, 33] This description is consistent with the exceptionally flat voltage profile which suggests sharp solubility limits ($\delta = 0.09$, $Li_{4+\delta}Ti_5O_{12}$, $Li_{7-\delta}Ti_5O_{12}$).[34] A detailed recent density functional theory (DFT) investigation revealed that the phase interface is stabilized by adjacent Li-ion occupation in 8a and 16c sites, the mixing of which creates the conditions for fast Li-ion diffusion and excellent electronic conductivity.[35] The phase transition in the material nevertheless remains a first order transition, since the 16c and 8a regions remain separated, albeit on a sub-nanometer length scale[35], consistent with electron microscopy observations which reveal phase separation with a sharp phase interface.[36]

Relatively few models have been developed for LTO, most having a specific system focus and limited range of parameter coverage.[37-39] Kashkooli et. al.[37] matched a model with experiments utilizing LTO monodisperse nanoparticles. He focused on the effect of nanosizing for optimal electrode performance covering rates up to 5C. Stewart et. al.[39] focused on optimizing a LFP-LTO battery system and an asymmetric hybrid super-capacitor consisting of LTO and activated carbon. The aim was to investigate if the systems meets the requirements for hybrid electric vehicles applications. Christensen et. al[38] also focused on full-cells consisting of $LiMn_2O_4$ and LTO, investigating the effect of porosity and thickness as well as the particle size. All previous LTO models are based on the pioneering work of Newman and collaborators, which focuses on the description of Li-ion diffusion, but does not include a thermodynamic description of phase-separating electrode materials.

In the present work we develop a phase-field model for LTO based on nonequilibrium electrochemical thermodynamics, where all necessary physical and chemical parameters are based on available experimental and ab-initio results. The developed model is able to reproduce presented and published experimental results and is able to capture and explain the fine balance between the various possible limiting factors in the battery, including Li-ion diffusion, Li-ion transport and electronic transport. Thereby our work validates the physical principles of the phase field method, and the importance of including a complete thermodynamic description in battery models. This allows us to provide concrete guidelines towards optimized electrode performance, guiding the design of optimal electrodes for Li-ion batteries. In addition, in-depth understanding of the lithiation mechanism is achieved by following the active particle fraction during discharge.

## 4.2 Methods

The computational principles of phase field modeling along with the key implemented equations are presented and discussed in the methods section (chapter 2.2). Below we will calibrate the model specifically for the LTO electrode.

### 4.2.1 Parametrizing the Phase Field Model for LTO

To capture the nature of the phase transition in electrode materials requires the enthalpy of mixing ($\Omega_a$), which in most thermodynamic models is obtained by fitting the equilibrium voltage profile. Based on the equilibrium voltage profile of LTO[10, 40] this results in: $\Omega_a = 1.52 \cdot 10^{-20}$ J/Li, a value corresponding to a phase separation between x=0.09 and x=2.91 in $Li_{4+x}Ti_5O_{12}$.[34] Aiming at reducing the amount of fitted parameters, a more direct way to obtain the thermodynamic properties is to determine the enthalpy of mixing based on extensive DFT calculations recently published[35] The convex hull determined for lithium insertion in LTO is presented in Figure 4.1a.

In Figure 4.1a it is shown that the formation enthalpy of several configurations at intermediate concentrations are positioned on the convex hull, suggesting solid solution behavior for $Li_{4<x<7}Ti_5O_{12}$. However, upon examining the lowest energy configurations, lithium clustering into 8a and 16c regions is observed within single unit cells, representing a sub-nanometer phase separation[35]. An example of this is shown in Figure 4.1b**,** in which the lowest energy configuration of the $Li_{5.5}Ti_5O_{12}$ phase consists of phase separated regions of the end-member phases. The enthalpy difference between the lowest enthalpy configuration (displaying phase separation) and the configurations in which the 16c and 8a Li-ion occupation is mixed (displaying solid solution) provides a quantification of the enthalpy of mixing. This is demonstrated in Figure 4.1c for $Li_{5.5}Ti_5O_{12}$, where the Li-positions are shown for several configurations with different formation enthalpies.

The difference in formation energy between the most stable configuration (un-mixed) and the completely mixed configuration for $Li_{5.5}Ti_5O_{12}$ results in $\Omega_a = 1.43 \cdot 10^{-20}$ J/Li. This result compares very well with the fitting result of the enthalpy of mixing towards the equilibrium voltage profile, motivating the use of this value for the phase field model. The interface width (λ) in LTO has been determined by experimental[36, 41] and computational[35, 42] studies, both indicating a narrow interface width of a few Angstroms wide (2.5 to 7 Å).

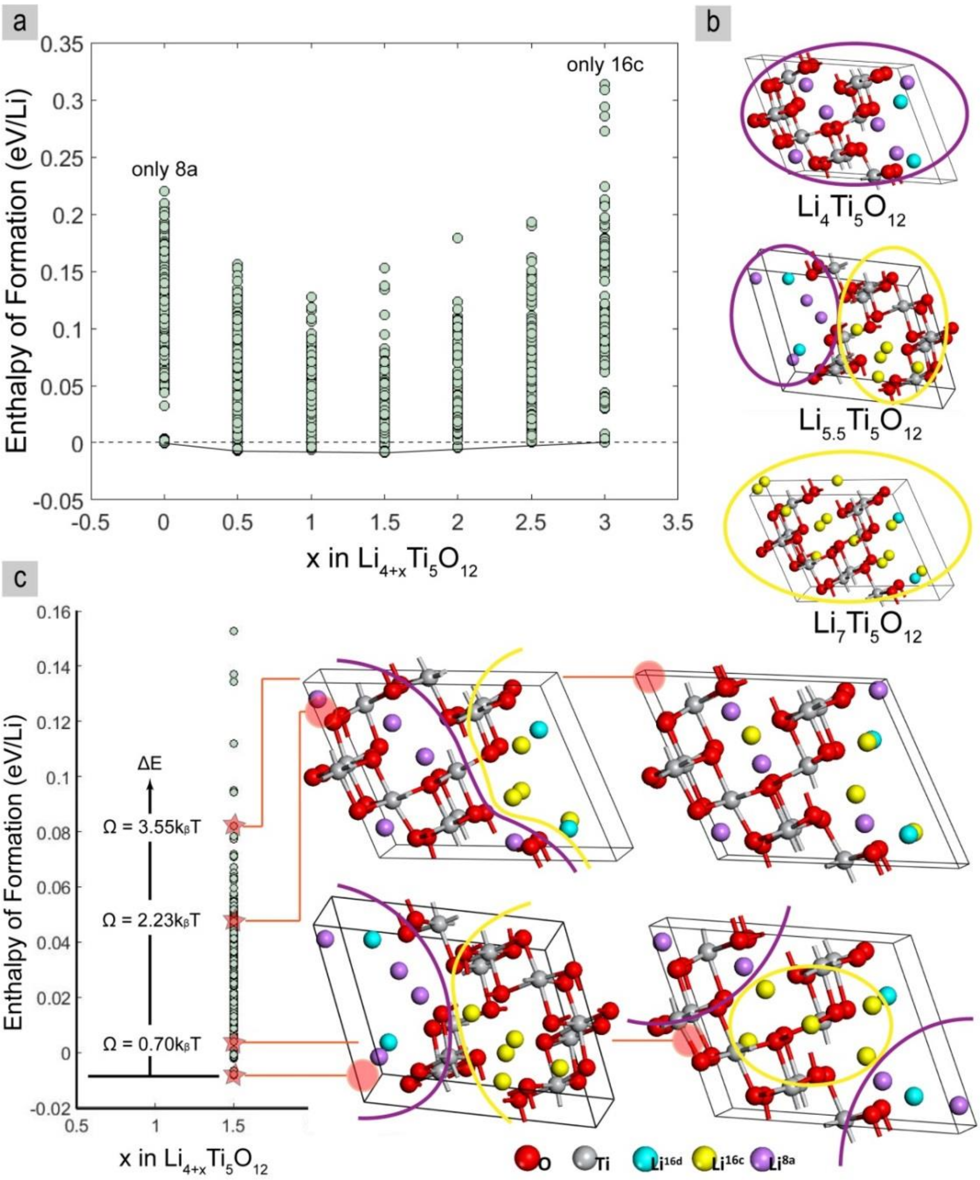

**Figure 4.1: a)** Enthalpies of formation for Li-ion insertion in LTO and the resulting convex hull, the line connecting the lowest energy configurations referenced to the $Li_4Ti_5O_{12}$ (all electrochemically active Li-ion on the 8a positions) and $Li_7Ti_5O_{12}$ (all electrochemically active Li-ion on the 16a positions) end-member compositions. **b)** Lowest energy configuration in the end-member and intermediate concentrations. **c)** Enthalpies of formation for the $Li_{5.5}Ti_5O_{12}$ phase. The enthalpy of mixing is defined as the enthalpy difference (ΔE) between the lowest energy configuration and the lowest one without a clear phase-interface.

Using equation 2.17 this results in a gradient energy penalty of $\kappa = 1 \cdot 10^{-10}\,\mathrm{J/m}$ , reflecting that the energy penalty for creating an interface between the two endmember phases is relatively small, for comparison, approximately 5 times smaller compared to the two coexisting phases in $LiFePO_4$.

Li-ion diffusion in the spinel LTO lattice has been extensively studied with nuclear magnetic resonance (NMR) spectroscopy[34, 43-45], DFT [35, 46, 47] and electrochemical methods[8 48-52] reporting a range of chemical diffusivities from $10^{-8}$ to $10^{-12}$ $cm^2/s$. NMR[34, 43-45] and DFT[35, 46, 47] studies consistently reveal excellent diffusivities for intermediate Li-ion concentrations, $Li_{4<x<7}Ti_5O_{12}$, and poor diffusivities for the end-member phases $Li_4Ti_5O_{12}$ and $Li_7Ti_5O_{12}$. It is suggested[34, 43] that the intimate mixing of the 8a and 16c domains is responsible for the dramatic Li-ion diffusion enhancement at intermediate concentrations. This was also predicted by recent DFT molecular dynamic simulations, demonstrating that Li-ions are very mobile at the phase interfaces, the abundance of which is enhanced by the interface stabilization through Li-ions on the 16d metal positions.[36] For the current phase field model the (tracer) self-diffusion coefficient was used as determined by NMR spectroscopy amounting to $D_{\mathrm{Li}} = 4 \cdot 10^{-12}\,\mathrm{cm^2/s}$ [34], consistent with values determined by other NMR investigations[53, 54] and electrochemical measurements[9, 51, 52].

Particle aggregation and agglomeration is commonly observed for LTO materials when synthesized via conventional techniques[6, 52, 55]. Because the diffusion length of Li-ions is determined by the particle size this has a large effect on the time scale of Li-ion insertion and extraction, and therefore it is essential to accurately represent experimental particle size distributions. A lognormal description was found to adequately capture experimentally observed grain size distributions[56, 57]. Due to the long “tail” of the lognormal function  the presence of a few big aggregates is ensured, which, as will be shown, have an important effect on electrode performance. To manage computational time the number of particles in the phase field model was restricted to be between 35 and 200, depending on the particle size, having a size distribution consistent with the log-normal distribution determined from SEM images.

The electronically insulating nature of spinel $Li_4Ti_5O_{12}$[40, 58] resulted in a considerable experimental effort to improve the electronic conductivity of LTO electrodes[4, 28, 59]. However, Song et al. indicated that $Li_4Ti_5O_{12}/Li_7Ti_5O_{12}$ phase interfaces are highly electronically conducting[60] and in line with this, carbon free LTO batteries were tested, showing excellent rate capability[60, 61]. Conductivity measurements during electrochemical cycling of LTO report a tremendous increase in electronic conductivity of several orders of magnitude at the very first stages (4%) of the lithiation process[61, 62]. Thus it was suggested that either Li-ion diffusion in the solid phase[62] or Li-ion transport through the electrolyte in the pores of the electrode[61, 63] may limit the rate performance. Previous modeling attempts integrated both extremely small and large values of the electronic conductivity. Christensen et. al,[38] assuming that matrix conductivity is not rate limiting due to the addition of carbon, used an arbitrary value of 100 S/m while Kashkooli et al.[37] implemented a value of just 0.02 S/m. In the current phase field model an effective electronic conductivity of 10 S/m is implemented, which is a typical value for a 10% conductive additive. Additionally, in order to investigate the influence of the effective electronic conductivity, further calculations with larger and smaller values were performed.

Tortuosity quantifies the effect of the electrode microstructure on the kinetic properties of the electrolyte in the electrode pores. The generalized Bruggeman relation[64, 65], relating the porosity ($\varepsilon$) with the tortuosity ($\tau$) via the Bruggeman exponent (p), was implemented.

$$\tau = \varepsilon^{p} \qquad 4.1$$

The Bruggeman exponent was set to -0.5, which corresponds to the ideal case for spherical particles. Additionally, the effect of the tortuosity on the capacity of LTO electrodes was studied.

### 4.2.2 Analysis of the Overpotential

The various contributions to the total overpotential were estimated in order to gain insight into the rate limiting mechanism of LTO electrodes. The contributions were measured by simulating the respective electrode at a certain rate, while switching off one kinetic mechanism (transport, diffusion, electronic, transfer) at a time and measuring the potential gain compared with the voltage obtained from an actual simulation. The kinetic mechanisms were switched off by increasing the related property by several orders of magnitude (for example electronic conductivity was increased from 10 to 1000 S/m). Due to the interconnected character of the kinetic mechanisms, adding up the overpotential contributions coming from switching off one mechanism at a time, adds up to ~104% of the original voltage line. This is sufficient to ensure that no significant information has been lost and that the rate limiting mechanism has been correctly determined.

### 4.2.3 Experimental Section

Non-carbon-coated, commercially available LTO (Süd-Chemie AG), with a primary particle size of approximately 140 nm, was used. The LTO particle size distribution was measured using a scanning electron microscope (SEM, Philips/FEI XL 40 FEG), at an acceleration voltage of 15 kV. The porosity was calculated based on the geometry and weight of the electrodes and the density of the constituents. The electrodes were cut into discs with a fixed diameter and their thickness and weight were carefully determined using a digital indicator and an analytical balance, respectively.

The electrodes consisted of 70 wt% LTO powder (Süd-chemie), 15 wt% carbon Super P (Timcal) and 15 wt% polyvinylidene fluoride binder. The electrodes were tested in half-cells with lithium metal as reference/counter electrode and a fiber-glass separator. The separators were soaked with electrolyte (1 M $LiPF_6$ in 1:1 vol% ethylene carbonate/dimethyl carbonate). The cells were assembled inside an Ar filled glovebox with oxygen and water content below 1 ppm. Galvanostatic cycling experiments were performed with a programmable Maccor 4000 series galvanostat. The electrodes were cycled between 1 and 2.5 V vs. $Li/Li^+$ at various C-rates (1C = 175 mA $g^{-1}$).

## 4.3 Results

The default parameters used for the phase field simulations are summarized in Table 4.1 unless otherwise indicated. Electrode thickness and porosity will be specified for the respective electrodes in the following sections. Note that all the thermodynamic parameters are obtained from literature. In combination with a known electrode geometry it allows us to run the simulations without fitting any parameters. All simulations were performed at 25 degrees Celsius.

**Table 4.1:** Default parameters for the LTO phase field model

| Thermodynamic Parameters | Value | Based on |
|---|---|---|
| Enthalpy of Mixing ($\Omega_a$) | $1.43 \cdot 10^{-20}$ J/Li | DFT *[35] |
| Gradient Penalty ($\kappa$) | $1 \cdot 10^{-10}$ J/m | TEM[36], DFT [35, 42] |
| Equilibrium potential ($\mu^{\Theta}$) | 1.55 V | Electrochemical experiments[9, 10, 34] |
| LTO density ($\varrho_{LTO}$) | $3.5\ g/cm^3$ | |
| Kinetic Parameters | | |
| Li-ion Tracer Diffusivity ($D_{Li}$) | $4 \cdot 10^{-16}\ m^2/s$ | NMR[34] |
| Effective Electronic Conductivity ($\sigma$) | 10 S/m | Electrochemical experiments[62] |
| Electrolyte Anion Diffusion | $2.94 \cdot 10^{-10}\ m^2/s$ | Commercial LiPF6 EC/DMC |
| Electrolyte Cation Diffusion | $2.2 \cdot 10^{-10}\ m^2/s$ | Commercial LiPF6 EC/DMC |
| Reaction Rate Constant ($k_0$) | $3.6\ A/m^2$ | Electrochemical experiments[66] |
| Geometry Parameters | | |
| Particle Morphology | Spherical | SEM images ** |
| Particle Radius (R) | 45 – 280 nm | SEM images ** |
| Separator Length ($L_s$) | 200 μm | Commercial Whatman GF *** |
| Separator Porosity ($\varepsilon_s$) | 87 % | Commercial Whatman GF *** |
| LTO Volume Loading ($PL_c$) | 57 % | Synthesis process * |
| Bruggeman Exponent (p) | -0.5 | Spherical morphology** |
| *this work, **Figure 4.3 ***effective property when confined in a battery setup[67] | | |

### 4.3.1 Single LTO Particles

Single particle simulations, using the parameters shown in Table 4.1, result in phase separation during lithiation, forming a lithium-rich phase close to the surface and a sharp phase-interface that propagates towards the centre of the particle as shown in Figure 4.2a. The calculated voltage profile shown in Figure 4.2a displays the characteristic voltage plateau for LTO at 1.55 V vs. Li metal for a slow rate discharge (0.1C). The voltage dip observed at the early stages of lithiation is a known attribute of single particle electrochemical behaviour (in the absence of heterogeneous nucleation at surfaces[68]), because the lack of thermodynamic noise fails to push the Gibbs free energy out of the metastable state (by homogeneous nucleation) until the spinodal point is reached.[69] For phase-separating porous electrodes, the near-equilibrium voltage profile will be flatter, with some overshooting of the voltage plateau and oscillations due to many-particle mosaic instabilities[69, 70].

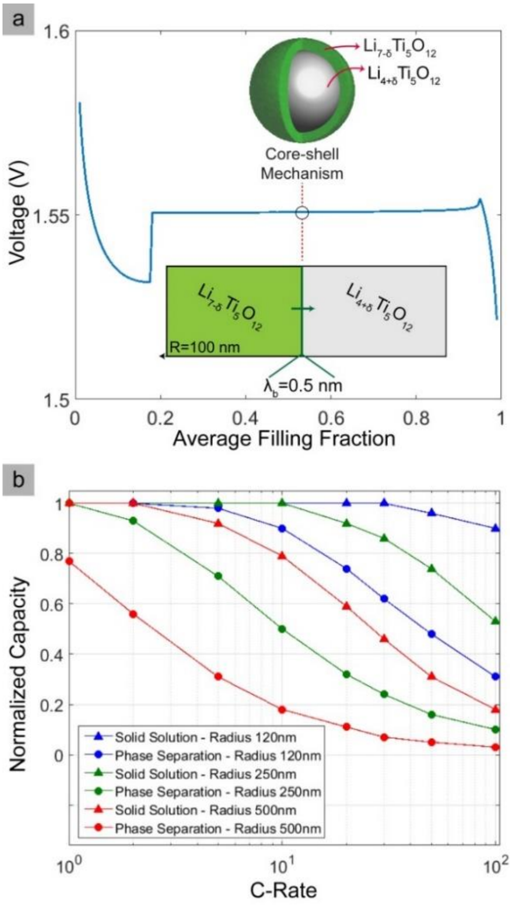

**Figure 4.2: a)** Galvanostatic discharge voltage profile of a single LTO particle at 0.1C and lithium concentration profile in the solid particle showing a core-shell-like, two-phase separation mechanism with a very thin phase-interface width. **b)** Difference in maximum capacity of single particles between a solid solution description ($\Omega_a = 0.6 \cdot 10^{-20}$J/Li) and a stable phase separation ($\Omega_a = 1.43 \cdot 10^{-20}$ J/Li) Note that the x-axis is logarithmic.

A core-shell, two-phase separation description is the generally accepted lithiation mechanism for LTO[6, 7, 14, 32, 33, 71] and is successfully captured by implementing the enthalpy of mixing value from DFT calculations. In order to understand the importance of the phase separation and how it affects the electrochemical performance, phase separation is compared with the solid solution mechanism. In Figure 4.2b the maximum obtainable capacity of LTO single particles is presented for the case of a solid solution description ($\Omega_a = 0.6 \cdot 10^{-20}\,\mathrm{J/Li} < 2\mathrm{kT}$) vs. a phase separation description ($\Omega_a = 1.43 \cdot 10^{-20}\,\mathrm{J/Li} > 2\mathrm{kT}$) for three particle sizes at different C-rates. The difference is substantial. A solid solution description leads to high lithiation levels, even for bulk particles as big as 1 μm, which can be filled to 80% at 10C. On the other hand, implementing a stable phase separation, as indicated by DFT calculations, slows down lithiation significantly, and the 1 μm particle is able to reach only 20% capacity at 10C.

The effect of the enthalpy of mixing $\Omega_\mathrm{a}$ can be understood as follows. Stable phase separation will lead to the formation of a high concentration phase ($Li_{7-\delta}Ti_5O_{12}$) near the surface of the particle. A high concentration at the surface would increase the reaction resistance by lowering the exchange current (equation 2.20), and this would lead to larger overpotentials and lower cell voltage, before any diffusion limitation sets in. Eventually, the measured voltage is expected to be lower at higher rates.. Furthermore, the existence of a high concentration end-member phase will reduce the Li-ion diffusion (equation 2.19) due to the lower Li-vacancy concentration. As a result, the more stable the phase separation ($\delta \rightarrow 0$ for $Li_{7-\delta}Ti_5O_{12}$and $Li_{4+\delta}Ti_5O_{12}$) the easier it is to reach diffusion limitations in the particles. This description is thus able to capture the sluggish Li-ion diffusion within the end-member phases, as is consistently reported by NMR[34, 43-45, 72] and DFT[35, 46, 47] studies. Recently, the fitting of a LTO model without a phase field thermodynamic description to experimental results[37] required assuming a relatively small diffusion coefficient of $\mathrm{D_{Li}} = 2.3 \cdot 10^{-13}\,\mathrm{cm^2/s}$, which is about an order of magnitude below NMR experimental results[34, 44, 72]. Interestingly, it has been argued that the enormous range of diffusivities and exchange currents reported for LFP is also due to improper accounting for phase separation[70]. Similarly, to match the capacity of the phase separating description, the diffusion coefficient in the solid solution phase field model needs to be decreased to an unrealistically small $\mathrm{D_{Li}} = 3.8 \cdot 10^{-13}\,\mathrm{cm^2/s}$. The results in Figure 4.2b show that the experimental result reported[37], 74% lithiation for monodisperse particles with a radius of 250 nm at 5C, can be reproduced by the present phase-separating phase field model, resulting in 72% lithiation, using measured diffusion coefficients.

### 4.3.2 Validation of the Model, Impact of Electrode Thickness and Porosity

In order to further validate our model, multiphase porous electrode calculations are compared to several prepared electrodes, summarized in Table 4.2. In battery 1 the LTO electrode is relatively thin (20 µm) and highly porous (70%). As a consequence the Li-ion diffusion and the phase transition behavior inside the LTO can be expected to dominate the performance, which allows further validation of the present LTO phase field description. To validate the charge transport description in the model through the porous electrodes, two additional electrodes were prepared where thickness (battery 2) and porosity (battery 3) were varied (Table 4.2). All LTO electrodes were tested in half-cells vs Li metal, as described in the methods section, and have a relatively large carbon content (15%) to be entirely sure that the electronic conductivity does not contribute significantly to the internal resistance. The particle size distribution in the porous phase field model was determined based on SEM images of the LTO material, shown in Figure 4.3.

The cubic structure of LTO ensures an isotropic 3D diffusion network. For particles that are perfectly wetted with electrolyte, Li-ions will follow the shortest distance in the solid phase. Different particle distributions were tested in order to match the SEM pictures obtained for battery 1.

All the relevant parameters for the phase field model of battery 1 are shown in Table 4.1 while the additional morphology aspects (porosity and thickness) are provided in Table 4.2. The phase field model predictions for batteries 2 and 3 were performed before actual electrodes were prepared and for the simulations of the three batteries no parameters were fitted.

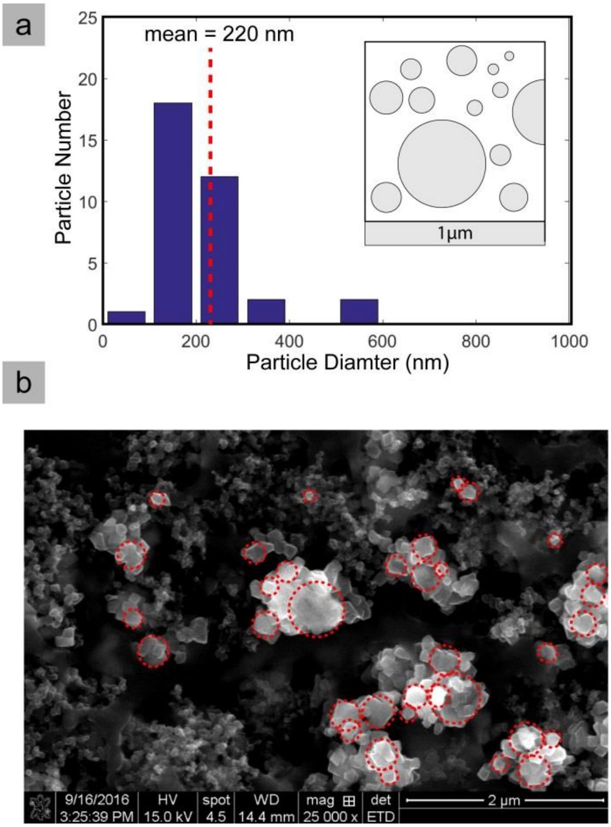

**Figure 4.3: a)** Particle distribution with a mean size of 220 nm (created with a standard deviation of 50 nm from particles with a radius of 100 nm). **b)** The particle distribution on top of the electrode SEM image of battery 1.

**Table 4.2:** Electrode characteristics of battery 1, 2 and 3. The aim of battery 1 is to switch off electronic and ionic transport, battery 2 aims to test Li-ion transport behaviour due to electrode thickness and battery 3 aims to test Li-ion transport behaviour due to electrode porosity.

| Aspect | Battery 1 | Battery 2 | Battery 3 |
|---|---|---|---|
| Experimental Thickness ($L_c$) | 20 μm | 245.5 μm | 225.5 μm |
| Experimental Porosity ($\varepsilon$) | 70 % | 67% | 52% |
| Simulated Thickness ($L_c$) | 20 μm | 250 μm | 250 μm |
| Simulated Porosity ($\varepsilon$) | 70 % | 70% | 50% |

Comparison between the experimental and the simulated rate capability for battery 1 in Figure 4.4a shows the characteristic declining capacity "staircase" upon increasing C-rate. The experimentally obtained and simulated capacities are in excellent agreement with each other over almost 3 decades in discharge rate, showing just 2% difference in the capacities.

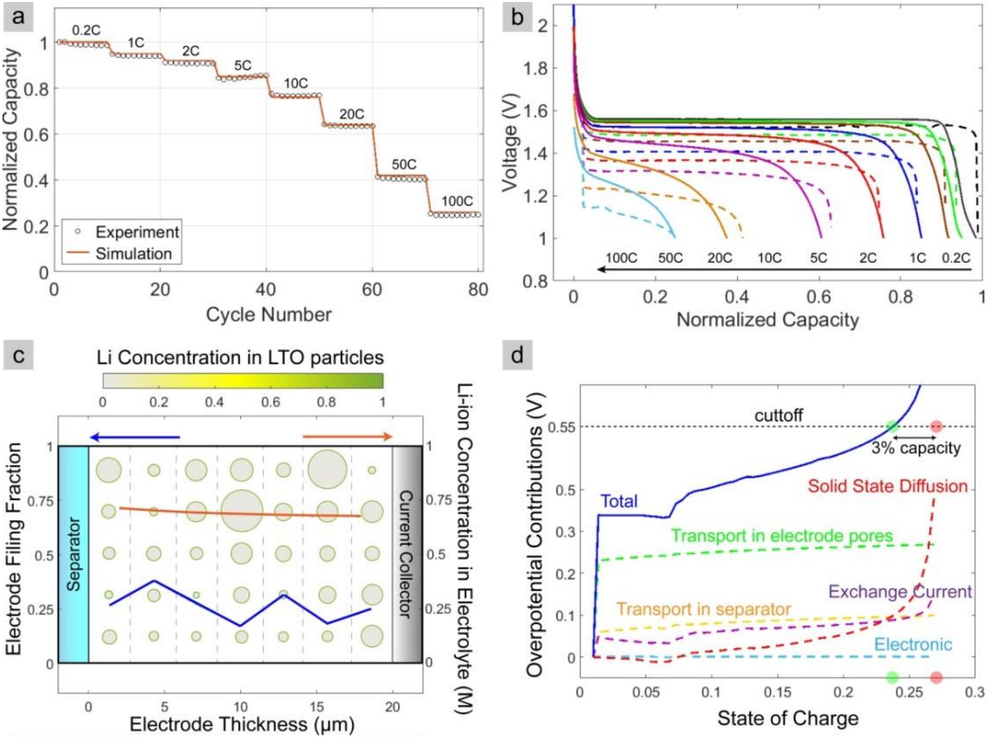

**Figure 4.4: a)** Comparison between the experimental (scatter) and the simulated (line) capacities for battery 1. **b)** Experimental (solid lines) and simulated (dashed lines) voltage curves at different C-rates. **c)** Li-ion end concentration in the particles, the average filling fractions in the solid phase (blue line - left axis) and Li-ion concentration in the electrolyte (orange line - right axis) plotted as a function of electrode depth at the end of a 100C simulation for the battery 1 half-cell. **d)** Overpotential contributions to the total overpotential as a function of the state of charge for 100C discharge of battery 1.

In order to show the consistency of the model, in Figure 4.5 we present the capacity results for all other randomly created particle distributions with slightly differing mean particle sizes. The reader can observe that all the simulated characteristic C-rate "staircases" match extremely well with the experimental one for all the distributions. As long as the mean particle size remains around ~200 nm along with the presence of a few large particles, which is the realistic particle description according to the SEM images, the results are accurate and reproducible.

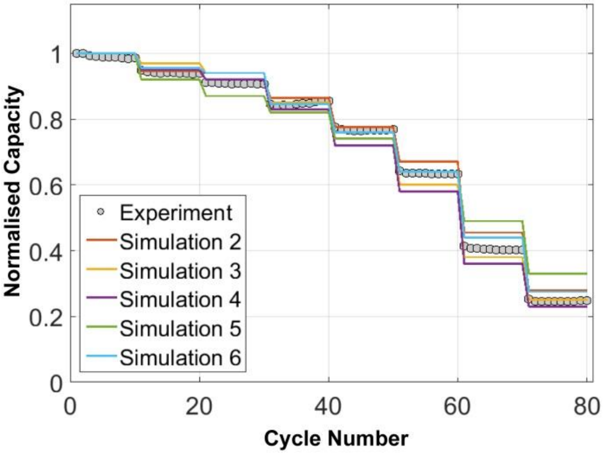

**Figure 4.5:** Experimental results for battery 1 vs. simulations for 5 additional randomly created particle distributions.

However, the porous phase field model has a mismatch with the overall shape of experimental voltage curves shown in Figure 4.4b. Clearly, our model overestimated the reaction resistance at low concentration since the initial voltage drop, prior to any phase separation or diffusion limitation, is much larger than the experimental results. After the initial drop, the experiments show steeper voltage decline than the phase-field simulations. Below we will address several reasons that might be responsible for such behaviour and to what extent this discrepancy may signify incomplete physical understanding.

One reason may be the breakdown of the standard assumption of spherical symmetry, which promotes shrinking-core phase separation within each active particle. In the case of LFP, the canonical two-phase material, it is well established that the initial shrinking core model[73] cannot capture various surface phenomena predicted by phase-field models that relaxed this assumption[53, 54, 70, 74-78], such as the electro-autocatalytic control of phase separation by surface reaction kinetics[79, 80], which was later verified experimentally[81-83] with definitive proof by *in operando* imaging of nanoparticles.[84] It is also important to note that a 1D phase field model of LFP nanoparticles[85] similar to our LTO model, which allowed for surface nucleation and departures from shrinking core morphologies, such as radial spinodal decomposition and annual stripes, also produced flat voltage profiles resembling ours for LTO and failed to capture the observed rate-dependent phase behaviour in LFP.

Let us briefly discuss how departures from spherical symmetry that allow for electro-autocatalytic control of phase separation[74] may help explain varying voltage profiles in LTO. As discussed earlier, DFT results indicate that the phase interfaces are stabilized by mixed 8a/16c Li site occupation that resemble solid solution conditions on top of the nanoscale two phase separation, explaining the fast Li-ion mobility and phase-interface stabilization in LTO.[35] This picture was recently confirmed by a thorough experimental (*in situ* XANES) and computational (*ab initio)* study pointing towards a reaction process that involves mixed quasi-solid solution/macroscopic two-phase transformations.[86] As a result, deviations from a shrinking core phase separation are expected in reality. The material may not display one uniform phase front (core-shell) but several, thus exposing Li-poor phases close to the particle surface. It is nontrivial and beyond the scope of this initial work to capture driven phase separation in 2D or 3D, although that is a key direction for future work. Since the penalty to form phase interfaces is extremely small, nanoscale alternating Li-rich and Li-poor phases would be in principle possible. For example, a chessboard-like, nano-domain lithiation mechanism has been predicted for graphite[87]. Further, if phase separation can occur in the tangential direction over all the surface (contrary to shrinking core), then it is strongly influenced by surface reactions. Whenever the reaction is auto-inhibitory during insertion as predicted by our theory, then phase separation is suppressed during insertion, and the overpotential grows over time, leading to voltage curves that drop off more like the experimental data. We have growing unpublished evidence that this effect is important in multiple battery materials, not only suppressing, but in some cases enhancing concentration instabilities (i.e. making a solid solution system appear to phase separate at high rates into non-equilibrium states of stationary reaction rate), as predicted by the general theory[74]. Furthermore, a simpler reason for breaking the spherical symmetry might be the non-perfect character of the real crystals, meaning that the grain boundaries might affect the phase boundaries, leading to local growing/shrinking core shell structures. In this case larger particles may not display one uniform phase front (core shell) but several, having more Li-poor regions near the surface, and thus lower overpotentials.

Another reason for the different shape of the voltage curves could be the breakdown of standard assumption of Butler-Volmer reaction kinetics, as was recently implicated in the similar case of LFP.[88] A different, physics-based alternative to the empirical Butler-Volmer equation is provided by quantum mechanical theories of electron transfer[89], such as the Marcus-Hush-Chidsey model (MHC)[90] which predicts an electron-transfer reaction-limited current that cannot be exceeded even at high over-potential[91] (opposite to BV theory, which predicts faster kinetics at higher overpotential). A generalized theory of mixed ion-electron transfer in solids[92], combining MHC kinetics with nonequilibrium thermodynamics[74], predicts an approximately linear decrease in exchange current vs concentration, $I_0$ ~ 1-c, for mixed ion-electron transfer into a solid intercalation material, consistent with experimental measurement of $I_0(c)$ in LFP[80], which can explain the linearly decreasing capacity at low rates. A preliminary result from implementing the generalized MHC theory in our LTO phase-field model is presented in Appendix C, which indeed shows a steeper decline in the voltage curve, closer to the experimental data.

Another possible important extension of our model would be to take into account many particle effects within the continuum volumes. In this way the spatial nonuniformity of electrochemical resistances can be captured, causing a distribution of voltages. Particles within one volume (same electrode depth) have a unique (higher or lower) connection to the average electrode potential, based on their unique aspects (tortuosity, crystalline orientation, size, particle-particle contact)[93]. For example, the inclusion of a contact resistance in phase field modeling resulted in good voltage fitting in the case of graphite.[93] In addition, the more sloping nature of the experimental voltage curves can be attributed to a voltage distribution due to the size distribution of the LTO powder not taken into account by the current phase field model. For small particle sizes, the relatively large surface area makes that the surface energy increasingly changes the potential. As a consequence, a size distribution leads to a distribution of insertion potentials[94-96]. Finally, another approach would be to use more complex empirical functions for the concentration-dependent solid diffusivity. Such functions have been shown to fit the LFP voltage profiles quite well[73], and might lead to a more accurate fitting of the LTO voltage profile as well. This is however outside the scope of this work, which aims at the development of the first LTO phase field model without fitting parameters, and very practically and accurately captures the lithiation properties of LTO based on its fundamental thermodynamic properties.

To investigate what limits the capacity at large C-rates, the Li-ion distribution through the electrodes and in the LTO particles, as well as the origin of the overpotential is analyzed in detail. In Figure 4.4c the Li concentration profile in the solid phase and in the electrolyte with respect to electrode depth is presented for 100C at the fully discharged state for battery 1. The simulations indicate that at 100C, all particles are lithiated concurrently throughout the electrode. The concentration profile in the solid phase is dominated by the distribution of particle sizes along the depth of the electrode, with smaller particles  at a larger state of discharge. The average Li-ion concentration in the particles is nearly constant throughout the electrode depth. This qualitatively indicates that for this thin (20 μm), porous (70%) electrode Li-ion transport in the solid LTO particles limits the Li-ion transport and the resulting capacity. The various contributions to the overpotential for battery 1 are quantified as a function of state of discharge in Figure 4.4d. Although Figure 4.4c shows that the electrolyte is only partially depleted, the Li-ion transport through the electrolyte in the pores of the electrode already contributes significantly to the overpotential. At these large rates, the Li-ion concentration decreases, gradually increasing the overpotential. This gradually decreases the voltage until the cutoff potential is reached, thus the capacity is mainly limited by the Li-ion transport through the electrolyte. In contrast, at lower rates a sharper decrease in discharge voltage is observed. The origin of this is illustrated in Figure 4.4d, in which the overpotential contributions are displayed for 100C rate beyond the 1 V cutoff. Just beyond the voltage cutoff the overpotential due to Li-ion diffusion through the LTO particles sharply increases. At lower rates this regime is entered before the 1 V cutoff is reached because the overpotential due to Li-ion transport though the electrolyte is smaller. Therefore the shape of the voltage profile towards the voltage cutoff can be directly used to identify which transport phenomena limits the total capacity, which may serve as guide to improve the performance. Specifically for battery 1, Figure 4.4d indicates that improving the charge transport through the electrolyte, for instance by a larger Li-ion concentration or larger porosity, will only lead to a gain of about 3% in capacity. At that stage the Li-ion diffusion through the LTO particles sets in, indicating that particle size limits the capacity.

According to the analysis presented in Figure 4.4d, electronic limitations do not play a significant role for the electrode in battery 1 for which a conductivity of 10 S/m was set. To evaluate the impact of the electronic conductivity simulations were performed with lower electronic conductivities, shown in Figure 4.6. Reducing the electronic conductivity to 0.3 S/m shows a minimal effect on the capacity (~2%), despite the high current (100C).

The next step is the validation of the Li-ion transport behaviour of the porous phase field model by varying the electrode thickness and porosity in two subsequent steps. As summarized in Table 4.2, compared to battery 1 the porosity of battery 2 is kept constant, but the electrode thickness is increased from 20 μm to

250 µm. For battery 3 the electrode thickness is kept the same as for battery 2 and the porosity is decreased.

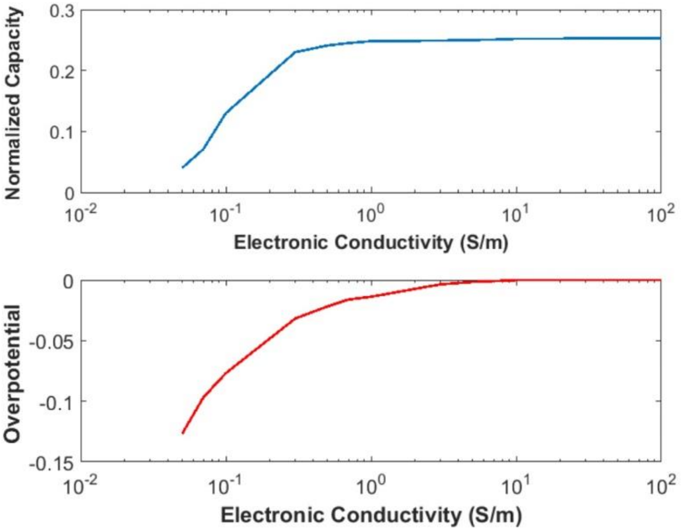

**Figure 4.6:** Effective electronic conductivities vs. normalized capacity and induced overpotential at 100C for battery 1. The overpotential on the y axis of the bottom figure refers to the isolated contribution of electronic conductivity to the total overpotential and is measured as the voltage drop from the voltage obtained for the highest electronic conductivity. The x-axis is logarithmic.

For battery 2 the simulated and the experimentally obtained voltage profiles are shown in Figure 4.7a. The model predicts that above 5C the voltage drops quickly towards the cutoff voltage, leading to a sharp decrease in capacity at 10C, in good agreement with the experimental result. The predicted capacities for different discharge rates are in excellent agreement with the experiments (within 4%). In Figure 4.7b the simulations at 10C display an interesting distribution of Li-ions over the LTO particles as a function of depth, and a clear gradient in the Li-ion concentration in the electrolyte. In contrast to the thin electrode of battery 1 in Figure 4.4c, this indicates that in these much thicker electrodes, Li-ion transport through the electrolyte contributes more to the overpotential than Li-ion diffusion trough the LTO particles, a direct consequence of the larger diffusion distance through the electrolyte. As a consequence, the discharge capacity is dominated by the Li-ion transport down to much lower rates. This is qualitatively observed by the gradual decrease in voltage during discharge (indicating that the Li-ion electrolyte transport dominates the overpotential) as compared to the sharp decrease in voltage (indicating Li-ion diffusion in the LTO particles dominates the overpotential). By quantifying the overpotential contributions coming from the various kinetic mechanisms to the total overpotential in Figure 4.5a we can directly observe the dominant character of Li-ion transport in the electrode behaviour at 10C discharge rate. The contribution of electronic transport seems to play a more significant role compared to battery 1. This makes sense if we consider that the Ohmic resistance runs over the larger length of battery 2. Evidence that for this thick electrode (battery 2) the electronic wiring is an issue is also visible in Figure 4.7b, where a reversed Li concentration gradient can be seen in the solid phase near the current collector side. To investigate the impact of the electronic conductivity of battery 2, the electronic conductivity was varied at 10C discharge, the results of which are shown in Figure 4.8. Starting at 10 S/m, and reducing the electronic conductivity steeply reduces the capacity and increases the electronically induced overpotential, while larger electronic conductivity values (100 S/m) lead to better capacities and less overpotential.

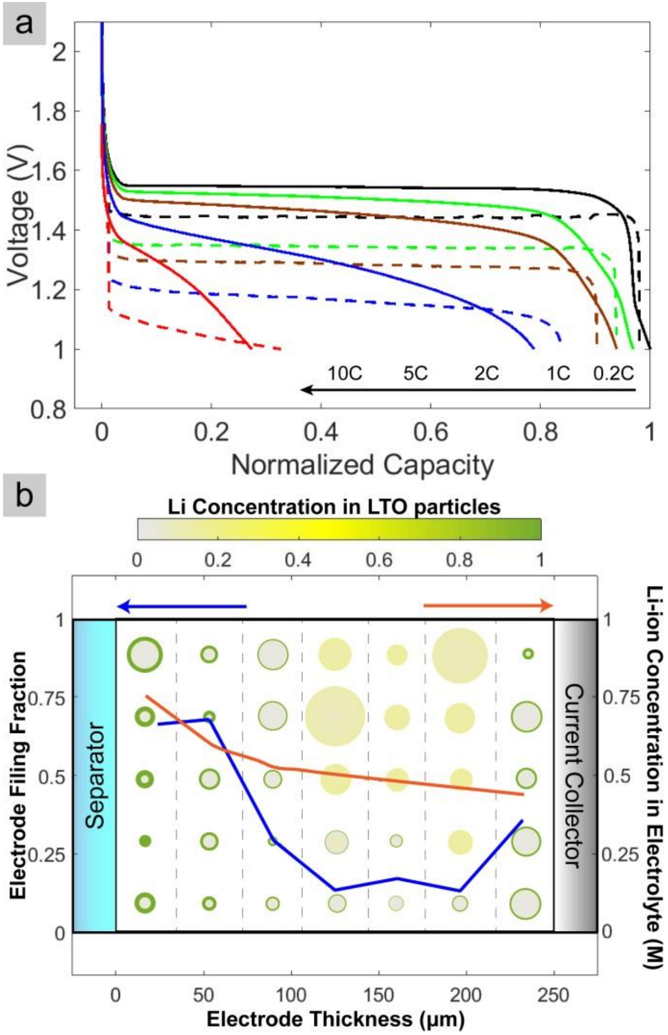

**Figure 4.7: a)** Simulated (dashed line) and experimental (solid line) voltage profiles of battery 2. **b)** Li-ion end concentration in the particles, the average filling fractions in the solid phase (blue line - left axis) and Li-ion concentration in the electrolyte (orange line - right axis) plotted as a function of electrode depth at the end of a 10C simulation for the battery 2 half-cell.

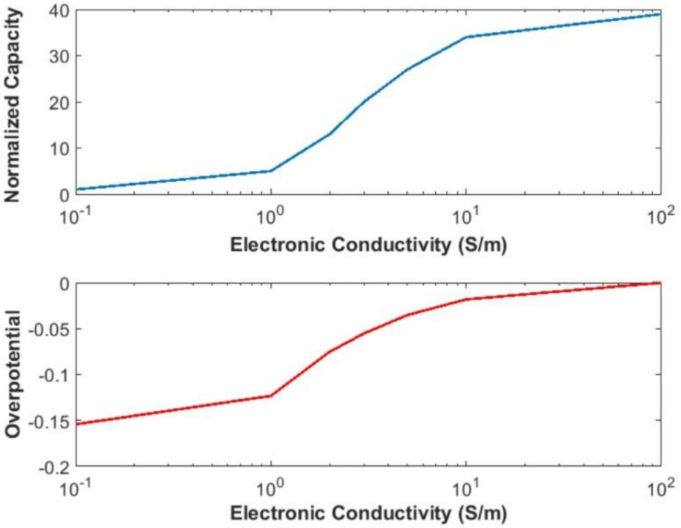

**Figure 4.8:** Effective electronic conductivities vs. normalized capacity and overpotential at 10C for battery 2. The overpotential on the y axis of the bottom figure refers to the isolated contribution of electronic conductivity to the total overpotential and is measured as the voltage drop from the voltage obtained for the highest electronic conductivity. The x-axis is logarithmic.

Battery 3 has a similar thickness compared to battery 2, but a lower porosity, which is beneficial for the energy density of a full battery but compromises Li-ion transport through the electrolyte in the pores of the electrode. We initially performed simulations in order to investigate the effect of porosity on a 250 µm thick electrode. The impact of the porosity on the capacity, at a cutoff voltage of 1 V, is summarized in Figure 4.9b. Also for battery 3 the agreement with the experimentally obtained capacities is excellent. As expected, decreasing the porosity dramatically reduces the capacity at high discharge rates. Lowering the porosity induces a larger overpotential due to the Li-ion transport through the electrolyte, enhancing the effect seen and discussed in Figure 4.9a. In transport limited systems such as battery 2 and 3, the total capacity is more likely to be determined by the balance between the overpotential build up and the cutoff voltage (as shown for example in Figure 4.9a. In this case, the voltage mismatch, observed in Figures 4.4b and 4.7a, might be a cause of concern, but our simulations show that this is not the case. Despite the initial overestimation of the overpotential, an accurate description of the rate limiting mechanisms and total capacities is achieved even at extreme electrode morphologies (250 µm thickness).

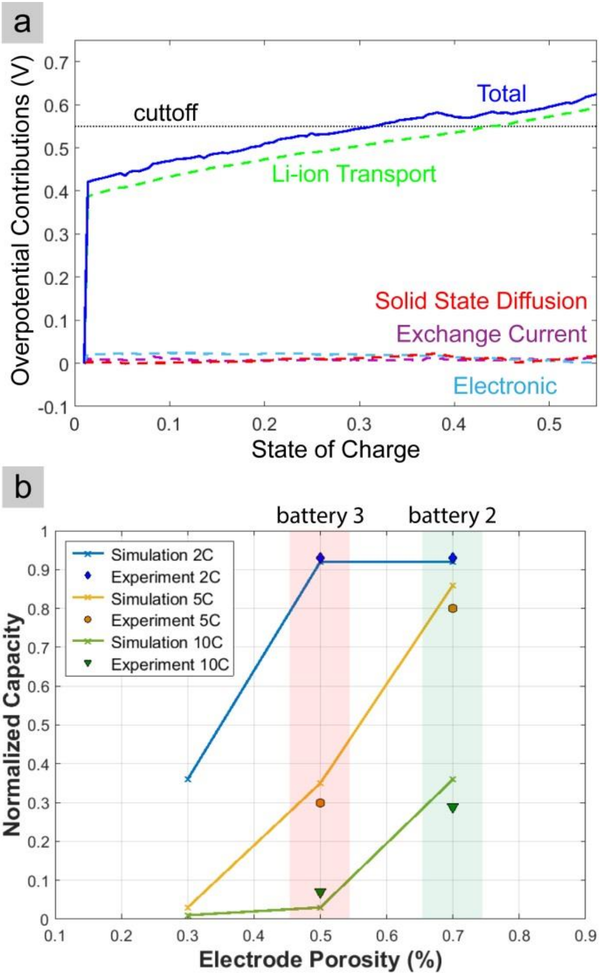

**Figure 4.9: a)** Overpotential contributions to the total overpotential as a function of the state of charge during a 10C discharge of battery 2. **b)** Simulated vs. experimental capacity obtained as a function of porosity for a 250 µm thick electrode at various rates.

The LTO model is also compared with a literature study in which the carbon content and electrode thickness are systematically varied. In addition, the particle size utilized is different from the one used for batteries 1, 2, and 3. In this way, the adaptability of the model towards different electrode morphologies is demonstrated. The model is able to explain the equivalent electrochemical behaviour[61, 97] observed when cycling, up to 10C, for LTO electrodes with and without carbon.

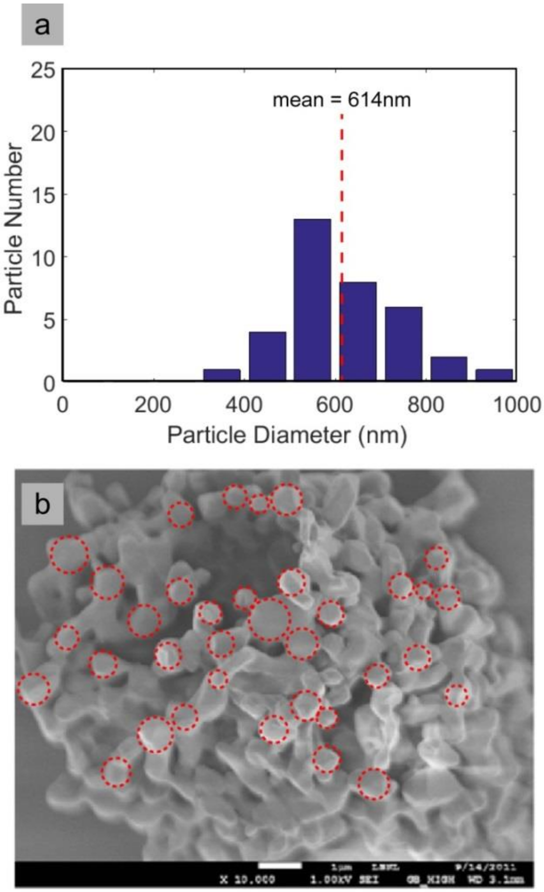

**Figure 4.10: a)** Particle size distribution with a mean size of 614 nm. **b)** The particle size distribution on top of the SEM image from Kim et al.[61] reproduced with permission from Wiley.

Kim et. al.[61] investigated the performance of carbon free LTO electrodes and compared these to electrodes with electrodes containing 10% carbon content, which showed identical behaviour up to 10C. The authors concluded that lithiation begins near the current collector side, and propagates towards the electrolyte side via percolation channels, therefore electronic limitations appear to have minimal effect on the performance of the carbon-free LTO battery. Using the provided electrode specifications[61] (electrode thickness: 40 μm, LTO volume loading: 87% for the carbon free and 69% for the electrode with 10% carbon, separator: Celgard 2500 [98] [99]) simulations were performed. Because the porosity was not specified, a typical porosity of 35% was assumed for the simulations. LTO showed a wide particle size distribution with particles reaching up to 1 μm.[61] For the simulations the particle size distribution was represented by a lognormal distribution of 35 particles with a mean radius of 307 nm (0.61 µm particle size) and aggregates reaching up to 500 nm radius (1 µm particle size), see Figure 4.10.

The simulation results for the capacities are in excellent agreement with the experimental observations of Kim et al.[61] as shown in Figure 4.11. Various effective electronic conductivities for the LTO electrode where tested for the highest C-rate (10C), showing no effect on the capacity down to 0.05 S/m (Figure 4.12). Simulating carbon free LTO differs from a simulation that includes carbon black in the active material volume fraction ($PL_c$) and probably[60, 61] also in the electronic conductivity (σ). Both parameters ($PL_c$, σ) are shown to have no effect on the capacity when simulating batteries with the specific characteristics reported by Kim et. al.[61], thus explaining the equivalent results seen experimentally for the 40 µm electrodes. Kim et. al.[61] also investigated much thicker (80 µm) carbon-free electrodes, showing no capacity at 10C and only 10% capacity at a 5C rate. It was argued that this is the consequence of Li-ion depletion in the pores close to the current collector, induced by an increased tortuosity usually observed in thicker electrodes.[61, 100] The present model was used to investigate this mechanism. The simulations for the 80 $\mu$m electrodes indicate that this scenario can be matched by increasing the Bruggeman exponent from the ideal -0.5 to -1.5 and reducing the porosity to ~30%. Alternatively, leaving the porosity at 35%, by increasing the Bruggeman exponent from the ideal -0.5 to -1.5 and reducing the electronic conductivity to 0.05 S/m, we can closely match the zero capacity at 10C and 9% capacity at 5C. For the thick electrode the low capacities could be the result of contributions coming both from transport and electronic limitations. For consistency we performed the simulations of the 40 µm electrode again with the increased tortuosity and the low electronic conductivity, and observed zero capacity loss compared to the results presented in Figure 4.11. It is clear that even if the electronic conductivity of the carbon free electrodes is lower than in the electrode containing carbon black, it wouldn't show in the electrochemical experiment of the 40 µm electrode at rates up to 10C, but it would show for thicker ones. In addition, assuming effective electronic conductivities below 0.1 S/m results in bulk lithiation (phase separating particles) which begins close to the current collector side, in agreement with the mechanism proposed by Kim et. al.

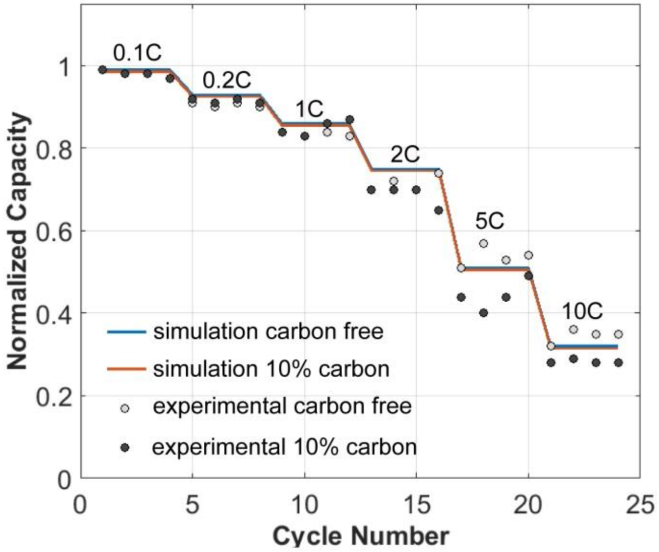

**Figure 4.11:** Comparison between experimental (dots)[61] and the simulated (line) capacities for the battery reported by Kim et al.[61]

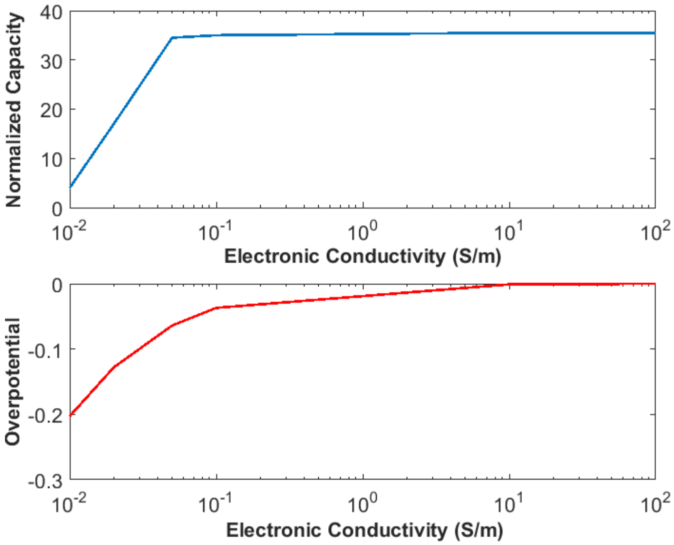

**Figure 4.12:** Effective electronic conductivities vs. normalized capacity and overpotential at 10C for the 40 μm battery presented by Kim et. al.[61] The overpotential on the y axis of the bottom figure refers to the isolated contribution of electronic conductivity to the total overpotential and is measured as the voltage drop from the voltage obtained for the highest electronic conductivity. The x-axis is logarithmic.

Evaluating the results presented in this section, we conclude that a reasonably accurate electrode description may be achieved with the well-established modeling assumptions (BV and shrinking core) and the practicality of a 1D model, despite the physical limitations discussed above. Because of the differences in the voltage curve, a different voltage cutoff would produce different results for the simulated vs. experimental results, in the case of a transport/transfer limited system (e.g. flatter simulated line would lose much more capacity than the curved experimental line for a cutoff at 1.2V). Cutoff at 1V, however, is the only relevant cutoff voltage encountered in literature and commercial applications. Despite the potential mismatch, capacity behavior is reproduced for extreme cases of currents and electrode morphologies. Even when extreme transport and transfer electrode characteristics are limiting the electrode (battery 2 and 3), capacities are well reproduced. An exact match of the voltage curve, however, would be the next step in the LTO phase field model, where including more realistic models of mixed ion-electron transfer, a better morphological description and/or multidimensional modeling might be the key elements for an improved material description.

### 4.3.3 Electrode Optimization

The good agreement with experiments shown in the previous section motivate the use of the developed porous phase field model to predict and explain the macroscopic electrochemical performance of LTO electrodes. In the next section we use the predictive power of the model to systematically evaluate the capacity as a function of particle size and particle size distribution, as well as the electrode thickness and porosity for different C-rates, providing guidelines for optimal LTO electrode design. Figure 4.13a shows the maximum capacity that can be obtained in single particles over a wide range of particle sizes and C-rates, hence for the conditions in which Li-ion transport through the electrolyte and electronic conductivity do not play a role. For example, when aiming at a maximum energy density battery operating at 2C, Figure 4.13a indicates that particles with a radius of 250 nm would give more than 90% of the theoretical capacity. Figure 4.13a shows that LTO nanoparticles (radius < 40 nm) can be lithiated completely, even at rates of 100C, consistent with experiments.[6, 52, 101-103]

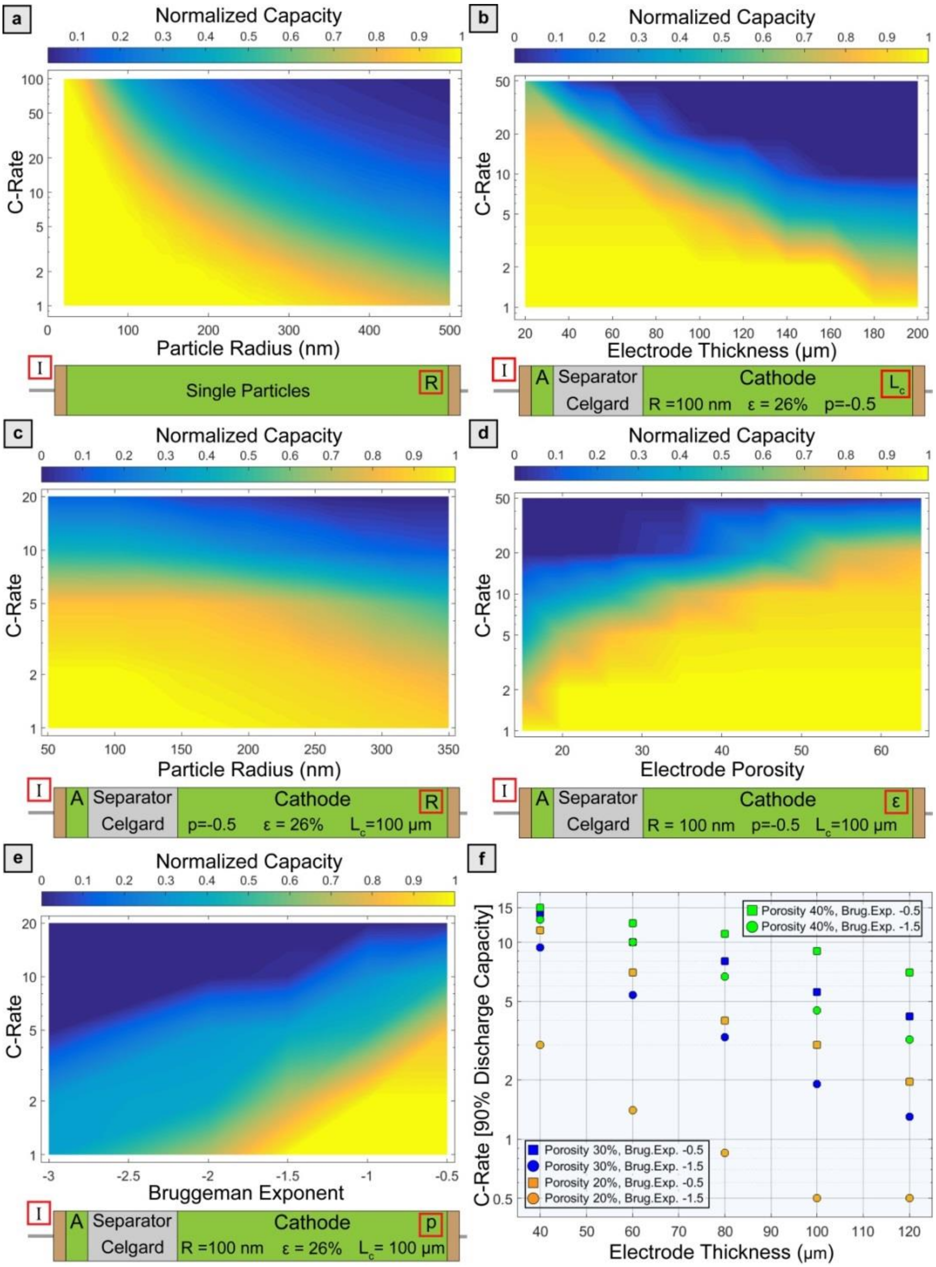

**Figure 4.13: a)** Capacities obtained from LTO single particle simulations over a wide range of particle sizes and C-rates. **b) c) d) e)** Capacities obtained from LTO porous electrode simulations. The electrode properties are shown in the schematic electrode representation below each figure. The parameters in the red squares are the ones being varied. **f)** Maximum C-rate delivering 90% of the nominal discharge capacity as a function of electrode thickness for different combinations of porosity and Bruggeman exponent. The particle radius is 100 nm.

When Li-ion diffusion through the LTO is at the nanoscale ($5 < R < 50$ nm),[6, 52, 101-103] and the contribution of the Li-ion transport through the electrolyte and electronic conductivity to the overpotential are minimized (typically by high porosities, high surface areas, thin electrodes and the use of conductive coatings), LTO can indeed reach a high fraction of the theoretical capacity at 200C[6].

In Figure 4.14a, a capacity map, similar to Figure 4.13a, is provided with the simulation results for small nano-crystallites and extremely high discharge rates. In addition, we report various half-cell scenarios in Figure 4.14b aiming at high capacity retention at ultra-high discharge rates.

The limitations presented in Figure 4.13a most likely hold true for diffusion within particles consisting of single grains. This is quite important as particles consisting of multiple grains would behave differently. Generally, it has been shown that the introduction of more grain boundaries and thus phase interfaces enhances the Li-ion and electronic conductivity, ultimately boosting the electrochemical performance.[35, 51, 104]. There are many studies that aim at creating larger secondary particles consisting of smaller primary particles, showing superior electrochemical behaviour.[6] For example, Wang et. al.[51] managed to synthesize monodisperse secondary particle spheres with a radius of 220 nm that consist of nano-sized primary particles which perform extremely well (68% capacity at 30C). This capacity is doubled compared to the limitations indicated in Figure 4.13a and is attributed to the large number of transforming grains that will effectively create additional interfaces between the end member phases, thus enhancing diffusion.[34, 35, 43, 51]

It has also been argued that the macroscopic two-phase separation falls apart in nano-domains under equilibrium conditions[34], or even the possibility for a percolation mechanism with multiple phase interfaces during the lithiation process[104, 105]. As thoroughly discussed in the previous section our 1D model does not indicate the formation of multiple phase-interface fronts although a better description could be achieved by adding more dimensions.

As the LTO particle size can be decisive for the rate dependent performance, also the size distribution is expected to have a significant impact on the rate dependent capacity[6, 52, 55]. An indication of the capacity decrease as a result of the presence of larger particles can be obtained from Figure 4.13a. In the case of lognormally distributed particles large particles make up a large part of the electrode solid volume, Figure 4.15 compares the capacity obtained from a log-normal particle distribution around a mean particle radius of 100 and 50 nm with different standard deviations.

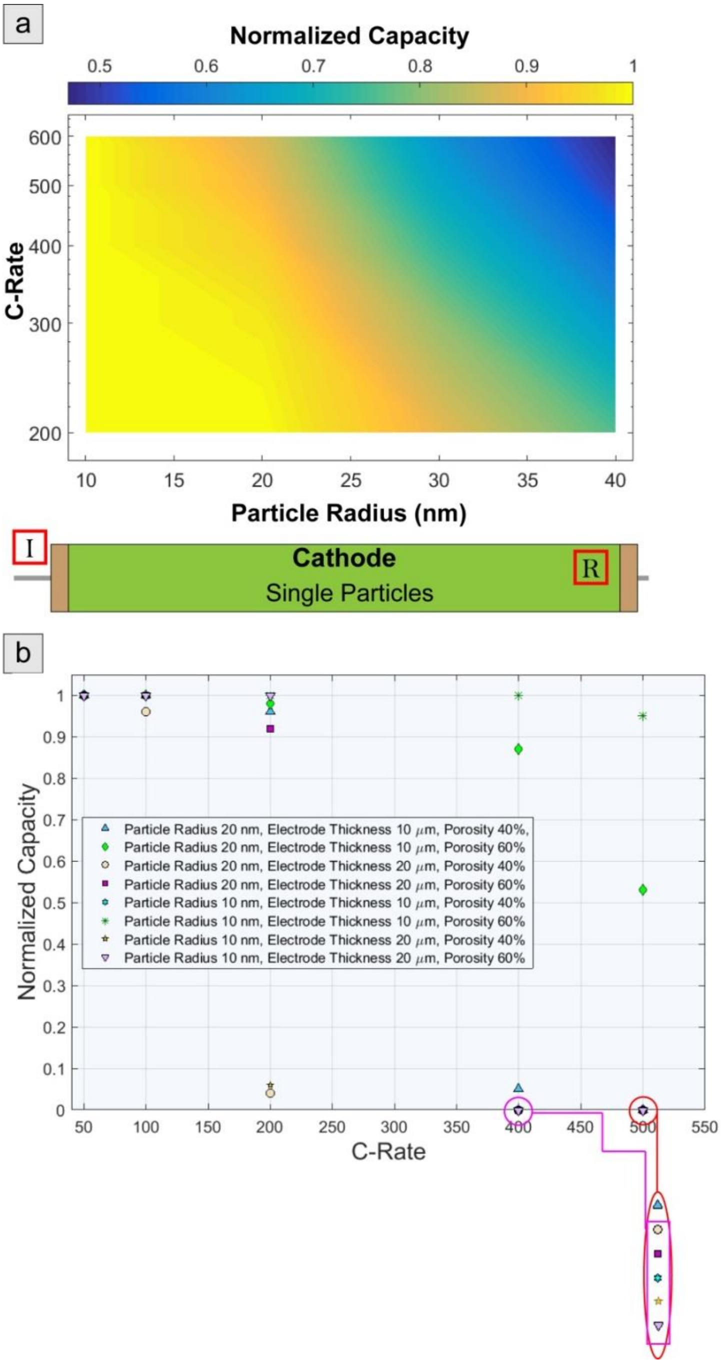

**Figure 4.14: a)** Capacity of LTO single nano-particles for a range of C-rates. Please note that the limits of the colorbar are different. **b)** Various scenarios of small nano-particles in full electrodes, showing that high capacities at extremely high rates are possible.

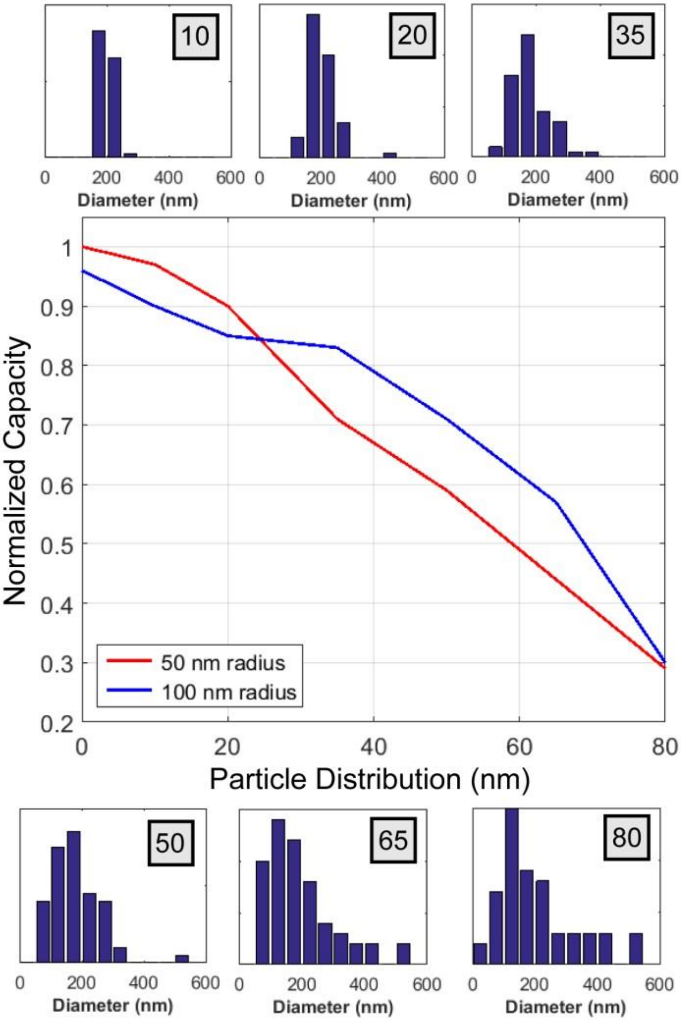

**Figure 4.15:** Capacity obtained from lognormal distributions of particles with a radius of 100 nm and 50nm and standard deviation between 0 and 80 nm at 10C. Example distributions for the particles with a mean radius of 100 nm are presented.

This demonstrates how a wider particle size distribution lowers the capacity, underlining the importance of monodisperse electrode particles to maximize the capacity of Li-ion battery electrodes. A sharper drop in capacity is predicted for particle size distributions with a smaller average size because of the relatively larger impact of the largest particles in such a distribution. In conclusion, the simulations show that avoiding large particle aggregation is of primary importance to achieve improved capacity retention at high discharge rates.

The porous electrode simulations, shown in Figures 4.13b, c, d, e and f illustrate how electrode thickness, particle size, porosity, tortuosity and the separator influence the capacity as a function of C-rate. For these simulations a realistic active particle fraction of 80% active material, 10% PVDF binder and 10% carbon black is used, resulting in an active material volume loading of 69%. The Celgard 2500[98, 106] separator was implemented because it is often employed in both experimental and modeling studies. In Figure 4.13b, simulations were performed for monodisperse particles with a radius of 100 nm and the porosity of the electrode was fixed at 26%, a typical commercial porosity for electrodes, and the electrode thickness as well as the C-rate was varied. The declining capacity with increasing electrode thickness is the result of Li-ion transport limitations through the electrolyte in the electrode pores. For example, a single particle with a radius of 100 nm is expected to give more than 80% capacity at 20C (Figure 4.13a). However, for a porous electrode this is only achieved for extremely thin electrodes because with increasing electrode thickness the Li-ion transport through the electrolyte will increasingly dominate the overpotential. This is also demonstrated in Figure 4.13c, where the electrode thickness is fixed at 100 $\mu$m and the particle size is systematically varied. When comparing with the single particle simulations in Figure 4.13a this shows that the particle size is almost irrelevant for thick electrodes. For example at 5C discharge rate the capacity dependence is dominated by transport, the capacity is almost constant and equal to the one determined by electrode thickness as depicted in Figure 4.13b, and nanosizing (reducing the radius to 50nm) has no effect on the capacity.

In Figures 4.13d and e the electrode thickness is kept constant at 100 $\mu$m and the porosity and tortuosity were varied. Tortuosity, as introduced in the methods section, appears to have a really strong influence on the capacity. The ideal Bruggeman exponent is -0.5, which refers to monodisperse spherical particles, emphasizing the importance of a synthesis process able to achieve spherical morphology and monodispersity. This is better demonstrated in Figure 4.13f, in which parameters that seem to have the biggest influence on capacity are combined into a 5D plot. It shows the maximum C-rate delivering 90% of the nominal discharge capacity as a function of electrode thickness for different combinations of porosity and Bruggeman exponent. The particle radius was 100nm. As an example, we observe that the less torturous 20% porous electrode outperforms the much more torturous 30% porous one, showing the potential gain in energy density.

In Figure 4.16a, a similar heat-map to Figure 4.13b, where all parameters are kept the same except from a higher porosity of 40% for those aiming at high rate performances, is presented.

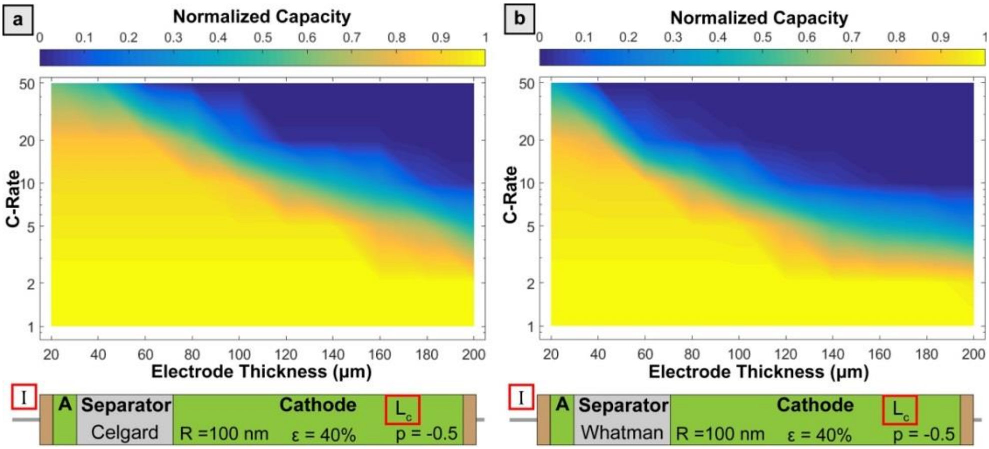

**Figure 4.16: a)** Capacity as a function of electrode thickness for different C-rates with a Celgard 2500[98, 99] separator. **b)** Capacity as a function of electrode thickness for different C-rates with a Whatman GF 260[67] separator.

Because of the additive character of the overpotentials, the choice of the separator will most likely affect battery performance in transport limited systems. We demonstrate this in Figure 4.16b, where for comparison a heat map is created implementing the Whatman glass fiber (GF) 260 separator[67], which is also a common choice in literature and was the separator used for batteries 1, 2 and 3. Results indicate that the extremely small thickness (25 μm) and medium porosity (55%) of the Celgard 2500 separator outperforms the large thickness (200 μm) and high porosity (87%) of the Whatman GF, especially at high C-rates. This explains why in literature we mostly encounter Celgard 2500 separators in papers aiming at high rate performance. Since the main characteristics of a separator are described in terms of porosity and thickness this result can be generalized and can be compared with other separators.

Based on the LTO phase field model simulations for batteries 1 to 3 a Ragone plot was calculated (Figure 4.17). It is based on the present phase field model for a LTO anode combined with a high voltage spinel $LiNi_{0.5}Mn_{1.5}O_4$ (LMNO) cathode, assuming that the LTO anode limits the performance. The weight of the full cell was determined by matching the LMNO and LTO capacities.

We also assumed equivalent potential losses for the two electrodes producing a constant voltage difference of 3.15 V (4.7 -1.55).[107]. For scaling the batteries towards realistic practical energy and power densities, scaling factors based on the characteristics of each electrode were used with the lowest value (17%)[108] for the highly porous and thin electrode (battery 1) and the highest (44%)[108] for the thick and less porous one (battery 3). The results in Figure 4.17 are comparable with those reported for a $Li_{4+3x}Ti_5O_{12}/Li_{y+0.16}Mn_{1.84}O_4$ cell. [38]

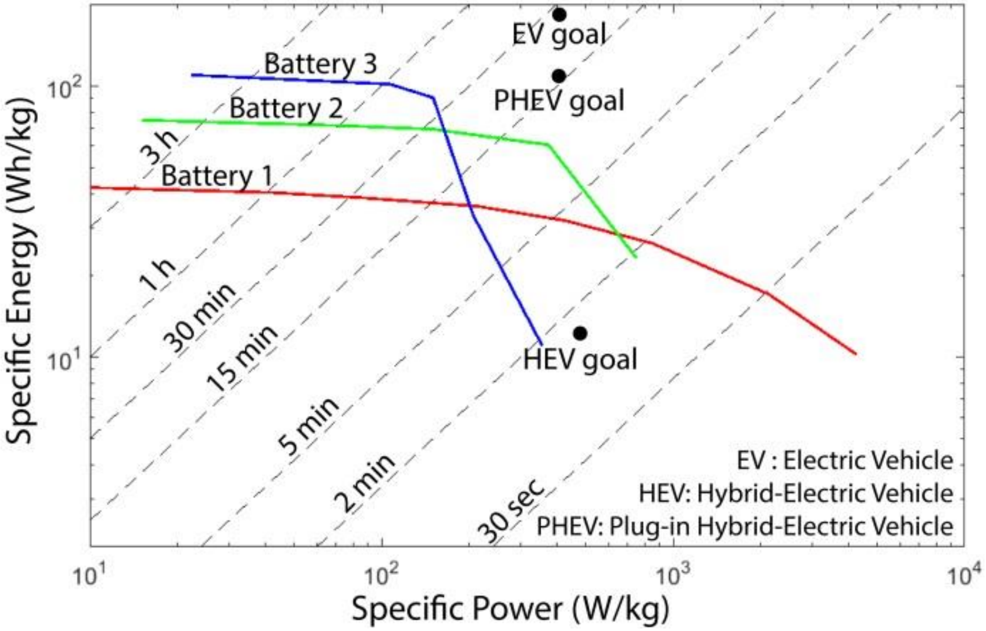

**Figure 4.17:** Ragone plot of LMNO – LTO batteries, the dashed lines indicates the particular discharge times. Batteries 1, 2 and 3 refer to full cells (LMNO – LTO) where the characteristics of the LTO electrode are the same with the ones presented for battery 1, 2 and 3 respectively. The practical energy and power density was determined by scaling battery 1 with 17%, battery 2 with 30% and battery 3 with 44%. The EV, PHEV and HEV goals are determined by the U.S. Department of Energy commercialization goals[38].

### 4.3.4 Active Particle Fraction in LTO Electrodes

An important aspect of the performance of complete electrodes is the active particle fraction. When the active particle fraction is larger, the total current is distributed over a large fraction of the particles. However, when the active particle fraction is small, the current is more localized, which could produce hotspots that may be detrimental for the cycle life of batteries. Li et. al. investigated both computationally and experimentally the active particle fraction in LFP electrodes, reporting a strong dependence on cycle rate and direction.[109] It was observed that in case the current exceeds a certain rate (~9C) the LFP electrode attains concurrent Li-ion insertion. In this way they bridged contradictory reports suggesting particle-by-particle[69, 110] and concurrent[111, 112] insertion behaviour in LFP electrodes.[109] For any phase-separating active material, such a range of rate-dependent phase transformation pathways is a general prediction of multiphase porous electrode theory[70, 75, 77].

With the LTO phase field model we investigated the active particle fraction of the battery 1 LTO electrode as a function of C-rate and state of charge. The criterion applied for defining a particle as actively transforming is the formation of a propagating phase interface. Our findings indicate that the active particle fraction shows a strong dependence with increasing rate, very similar to what was predicted for LFP electrodes.[109] In addition, Figures 4.18b to e demonstrate that the active particle fraction strongly depends on the state of charge. This effect was quantified by plotting the active particle fraction in terms of the number, surface and volume of particles that are active vs. the state of charge during discharge in Figure 4.18b to e. In Figure 4.18a the active particle fraction (average value for each C-rate) and current density as a function of rate is presented. Simulations demonstrate that at the initial stages of lithiation all particles lithiate in a solid solution manner (note that this does not qualify as active according to our definition and thus shows up as zero activity in Figure 4.18b to e.

The prediction that the LTO particles remain in a solid solution lithiation state, above the 3% expected based on the regular solution model, is the consequence of an absence of a thermodynamic driving force to exit the metastable region, as discussed in section 4.3.1. Even though all particles begin the lithiation process with a solid solution mechanism, the number of particles that will continue and begin the two-phase transformation towards the $Li_7Ti_5O_{12}$ phase strongly depends on the C-rate. This effect is also predicted for LFP electrodes and is explained by the presence of a transformation barrier in phase separation electrodes. This barrier is defined by the potential difference between the local maxima and the middle point of the diffusional chemical potential of Li in the phase separating material particles.[109] When the electrode ensemble potential is below the activation barrier, particles are lithiated up to the spinodal point (the end-point of the metastable region), but when the barrier is crossed the particles activate and lithiate further.[109] Transformation at low rates occurs in a strict sequential order, where small particles are lithiated first (particle-by-particle lithiation). This is evident in Figures 4.18b to d, where at the initial stages of discharges the number of active particles and active particle surface that are active is higher than the active volume fraction, while this situation is reversed in the latter stages of discharge. In Figure 4.18a a sharp rise in the active particle fraction is observed for currents around 9C, as the material gradually shifts form a particle-by-particle to a concurrent lithiation mechanism. Small particles still have a small edge in the lithiation order, but as the overpotential driving force[109] is increasing with increasing C-rate, more and more particles are lithiated concurrently and at 20C rate all of the particles are actively transforming. In retrospect, in terms of active particle fractions LTO behaves similar to LFP, which suggests that these results are general for phase separating electrodes, as predicted theoretically[75, 77, 109], although more analysis is required to support this conclusion. For LTO, a particle-by-particle reaction mechanisms was proposed by Kitta et. al. at low rates (0.3C) via electron energy loss spectroscopy[71] which is in agreement with our simulations of the active particle fraction at 0.2C rate in Figure 4.18b.

The prediction that at low currents only a very small fraction of the particles carry the current may lead to a maximum in the surface current density at a certain C-rate, which can lead to local hot spots that enhance electrolyte degradation locally. By taking the average active surface fraction of each C-rate we construct a plot quantifying this behaviour for battery 1 in Figure 4.18a. We observe that such a maximum is not present, implicating that the increasing C-rate is the dominating factor, even though the active particle fraction scales proportionately with the C-rate.

Finally, we examine if the prediction of a concurrent solid solution reaction anticipated for the initial stages of lithiation has a physical dimension. Song et. al.[60] and Kim et. al.[105] performed electrochemical tests in carbon-free electrodes. Both groups observed a color change from white to black in the LTO electrode, indicating a sharp change of the conductive properties, before the start of the characteristic voltage plateau. Thus it was suggested that the phase equilibrium does not take place from fully insulating $Li_4Ti_5O_{12}$ particles as believed, but from an already conducting $Li_{4+d}Ti_5O_{12}$ phase.[60] This means that LTO becomes conductive before the two-phase transition begins. In addition, Kim et. al.[105], visualized the phase propagation through optical microscopy and μ-XAS. An initial fast lithiation wave was observed that occurs throughout the electrode at the very beginning of the lithiation process, making it conductive, followed by a secondary wave of bulk lithiation.[105] The second wave of bulk lithiation follows a particle-by-particle lithiation mechanism, it begins at the regions in closest contact with the current collector as the reaction remains somewhat sluggish.[105]

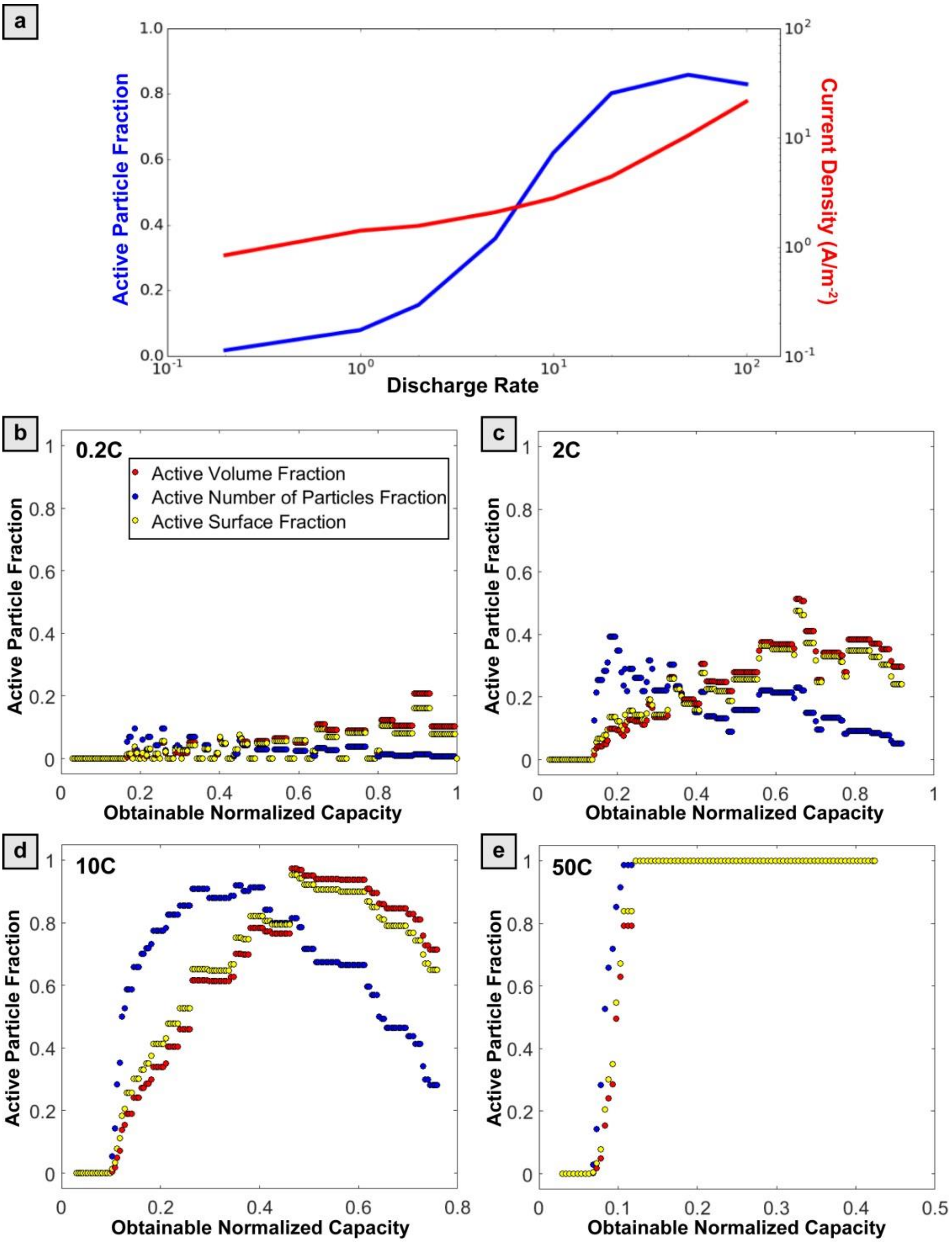

**Figure 4.18: a)** Active particle fraction (based on the active surface) and current density of battery 1 as a function of rate. Active particle fraction (based on active volume, surface and number of particles) vs. obtainable normalized capacity of battery 1 for various rates **b)** 0.2C **c)** 2C **d)** 10C **e)** 50C.

The present simulations are in agreement with the above descriptions. The concurrent character of the solid solution insertion observed in the phase field model at the initial stages of lithiation could explain the experimentally observed[105] initial lithiation wave that occurs throughout the electrode, making the material conductive. This initial wave is followed by a secondary lithiation wave in the bulk (phase separation in the particles), the sequence and concentration gradient of which depends on the particle size, wiring and C-rate. Electrode simulations with zero-carbon content are presented previously, where the proposed mechanism[61, 105] of the secondary bulk lithiation beginning close to the current collector which propagates towards the electrolyte side is discussed.

## 4.4 Conclusions

The developed LTO phase field model can accurately reproduce and predict electrochemical behavior. The model integrates DFT data in an effort to include a complete thermodynamic description that leads to phase separating particles. It captures the fundamental physics of LTO electrodes, while explaining and predicting battery performance and the various rate-limiting factors. The study covers a wide rate of C-rates, particle sizes, electrode morphologies and different separators. In addition, guidelines for optimized electrode performance are given. The importance of monodispersity is emphasized, along with the importance of the balance between transport and electronic effects. Finally, insight is provided regarding the LTO lithiation mechanism by a thorough examination of the active particle fraction. A particle-by-particle lithiation mechanism is confirmed for low C-rates, in agreement with experiments, and above approximately 9C a concurrent lithiation mechanism is predicted, a behavior which is similar to the one observed for LFP electrodes.

# References

**1**. Goodenough, J.B.; Park, K. S. The Li-Ion Rechargeable Battery: A Perspective. *J. Am. Chem. Soc.* 2013, 135, 1167-1176.

**2**. Dunn, B.; Kamath, H.; Tarascon, J. M. Electrical Energy Storage for the Grid: A Battery of Choices. *Science* 2011**,** 334, 928-935.

**3**. Tarascon, J. M.; Armand, M. Issues and challenges facing rechargeable lithium batteries. *Nature* 2001, 414, 359-367.

**4**. Sun, X. C.; Radovanovic, P. V.; Cui, B. Advances in spinet $Li_4Ti_5O_{12}$ anode materials for lithium-ion batteries. *New J. Chem.* 2015, 39, 38-63.

**5**. Goriparti, S.; Miele, E.; De Angelis, F.; Di Fabrizio, E.; Zaccaria, R. P.; Capiglia, C. Review on recent progress of nanostructured anode materials for Li-ion batteries. *J. Power Sources* 2014, 257, 421-443.

**6**. Zhao, B.; Ran, R.; Liu, M. L.; Shao, Z. P. A comprehensive review of $Li_4Ti_5O_{12}$-based electrodes for lithium-ion batteries: The latest advancements and future perspectives. *Mater. Sci. Eng. R.* 2015, 98, 1-71.

**7**. Colbow, K. M.; Dahn, J. R.; Haering, R. R. Structure and Electrochemistry of the Spinel Oxides $LiTi_2O_4$ and $Li_{4/3}Ti_{5/3}O_4$. *J. Power Sources* 1989, 26, 397-402.

**8**. Kavan, L.; Prochazka, J.; Spitler, T. M.; Kalbac, M.; Zukalova, M. T.; Drezen, T.; Gratzel, M. Li insertion into $Li_4Ti_5O_{12}$ Spinel - Charge capability vs. particle size in thin-film electrodes. *J. Electrochem. Soc.* 2003, 150, A1000-A1007.

**9**. Bach, S.; Pereira-Ramos, J. P.; Baffier, N. Electrochemical properties of sol-gel $Li_{4/3}Ti_{5/3}O_4$. *J. Power Sources* 1999, 81, 273-276.

**10**. Scharner, S.; Weppner, W.; Schmid-Beurmann, P. Evidence of two-phase formation upon lithium insertion into the $Li_{1.33}Ti_{1.67}O_4$ spinel. *J. Electrochem. Soc.* 1999, 146, 857-861.

**11**. Mahmoud, A.; Amarilla, J. M.; Lasri, K.; Saadoune, I. Influence of the synthesis method on the electrochemical properties of the $Li_4Ti_5O_{12}$ spinel in Li-half and Li-ion full-cells. A systematic comparison. *Electrochim. Acta* 2013, 93, 163-172.

**12**. Zaghib, K.; Dontigny, M.; Guerfi, A.; Charest, P.; Rodrigues, I.; Mauger, A.; Julien, C. M. Safe and fast-charging Li-ion battery with long shelf life for power applications. *J. Power Sources* 2011**,** 196, 3949-3954.

**13**. Amatucci, G. G.; Badway, F.; Du Pasquier, A.; Zheng, T. An asymmetric hybrid nonaqueous energy storage cell. *J. Electrochem. Soc.* 2001, 148, A930-A939.

**14**. Ohzuku, T.; Ueda, A.; Yamamoto, N. Zero-Strain Insertion Material of $Li[Li_{1/3}Ti_{5/3}]O_4$ for Rechargeable Lithium Cells. *J. Electrochem. Soc.* 1995, 142, 1431-1435.

**15**. Ronci, F.; Reale, P.; Scrosati, B.; Panero, S.; Albertini, V. R.; Perfetti, P.; di Michiel, M.; Merino, J. M. High-resolution in-situ structural measurements of the $Li_{4/3}Ti_{5/3}O_4$ "Zero-Strain" insertion material. *J. Phys. Chem. B* 2002, 106, 3082-3086.

**16**. Yi, T. F.; Jiang, L. J.; Shu, J.; Yue, C. B.; Zhu, R. S.; Qiao, H. B. Recent development and application of $Li_4Ti_5O_{12}$ as anode material of lithium ion battery. *J. Phys. Chem. Solids* 2010, 71, 1236-1242.

**17**. Sun, L. Q.; Cui, R. H.; Jalbout, A. F.; Li, M. J.; Pan, X. M.; Wang, R. S.; Xie, H. M. $LiFePO_4$ as an optimum power cell material. *J. Power Sources* 2009, 189, 522-526.

**18**. Reale, P.; Fernicola, A.; Scrosati, B. Compatibility of the $Py_{24}$TFSI-LiTFSI ionic liquid solution with $Li_4Ti_5O_{12}$ and $LiFePO_4$ lithium ion battery electrodes. *J. Power Sources* 2009, 194, 182-189.

**19**. Zaghib, K.; Simoneau, M.; Armand, M.; Gauthier, M., Electrochemical study of $Li_4Ti_5O_{12}$ as negative electrode for Li-ion polymer rechargeable batteries. *J. Power Sources* 1999, 81, 300-305.

**20**. Toshiba Toshiba's SCiB Rechargeable Battery. http://www.scib.jp/en/, accessed : 1-2-2017.

**21**. Co., P. E. Padre LTO battery. http://www.pdbattery.com/20000-cycles-lto-battery.html, accessed : 1-2-2017.

**22**. Long, A. T. Cycle life LTO battery, Rechargeable LTO Battery. http://www.made-in-china.com/showroom/lithium-batterys/product-detailCXYJIBPMHxpV/China-Long-Cycle-Life-Lto-Battery-Rechargeable-Lto-Battery.httml, accessed : 1-2-2017.

**23**. Power Lithium titanate (LTO) Cells - Techical Advantages. http://www.ev.-power.eu/LTO-Tech, accessed : 1-2-2017.

**24**. He, Y. B.; Li, B. H.; Liu, M.; Zhang, C.; Lv, W.; Yang, C.; Li, J.; Du, H. D.; Zhang, B. A.; Yang, Q. H.; Kim, J. K.; Kang, F. Y. Gassing in $Li_4Ti_5O_{12}$-based batteries and its remedy. *Sci. Rep. Uk* 2012, 2, 913.

**25**. Belharouak, I.; Koenig, G. M.; Tan, T.; Yumoto, H.; Ota, N.; Amine, K. Performance Degradation and Gassing of $Li_4Ti_5O_{12}/LiMn_2O_4$ Lithium-Ion Cells. *J. Electrochem. Soc.* 2012, 159, A1165-A1170.

**26**. Yuan, T.; Tan, Z. P.; Ma, C. R.; Yang, J. H.; Ma, Z. F.; Zheng, S. Y. Challenges of Spinel $Li_4Ti_5O_{12}$ for Lithium-Ion Battery Industrial Applications. *Adv. Energy Mater.* 2017, *7*, 1601625.

**27**. Yi, T. F.; Yang, S. Y.; Xie, Y. Recent advances of $Li_4Ti_5O_{12}$ as a promising next generation anode material for high power lithium-ion batteries. *J. Mater. Chem. A* 2015, 3, 5750-5777.

**28**. Lin, X.; Pan, F.; Wang, H. Progress of $Li_4Ti_5O_{12}$ anode material for lithium ion batteries. *Mater. Technol.* 2014, 29, A82-A87.

**29**. Deschanv.A; Raveau, B.; Sekkal, Z. Synthesis and Crystallographic Study of New Solid Solution of Spinelle $Li_{1+x}Ti_{2-x}O_4$. *Mater. Res. Bull.* 1971, 6, 699-704.

**30**. Kataoka, K.; Takahashia, Y.; Kijima, N.; Akimoto, J.; Ohshima, K. Single crystal growth and structure refinement of $Li_4Ti_5O_{12}$. *J. Phys. Chem. Solids* 2008, 69, 1454-1456.

**31**. Cava, R. J.; Murphy, D. W.; Zahurak, S.; Santoro, A.; Roth, R. S. The Crystal-Structures of the Lithium-Inserted Metal-Oxides $Li_{0.5}TiO_2$ Anatase, $LiTi_2O_4$ Spinel, and $Li_2Ti_2O_4$. *J. Solid State Chem.* 1984, 53, 64-75.

**32**. Murphy, D. W.; Cava, R. J.; Zahurak, S. M.; Santoro, A. Ternary $Li_xTiO_2$ Phases from Insertion Reactions. *Solid State Ionics* 1983, 9-10, 413-417.

**33**. Safronov, D. V.; Novikova, S. A.; Skundin, A. M.; Yaroslavtsev, A. B. Lithium intercalation and deintercalation processes in $Li_4Ti_5O_{12}$ and $LiFePO_4$. *Inorg. Mater.* 2012, 48, 57-61.

**34**. Wagemaker, M.; van Eck, E. R. H.; Kentgens, A. P. M.; Mulder, F. M. Li-Ion Diffusion in the Equilibrium Nanomorphology of Spinel $Li_{4+x}Ti_5O_{12}$. *J. Phys. Chem. B* 2009, 113, 224-230.

**35**. Ganapathy, S.; Vasileiadis, A.; Heringa, J. R.; Wagemaker, M. The fine line between a two-phase and solid solution phase transformation and highly mobile interfaces in spinel $Li_{4+x}Ti_5O_{12}$. *Adv. Energy Mater.* 2016, 7, 1601781.

**36**. Lu, X.; Zhao, L.; He, X. Q.; Xiao, R. J.; Gu, L.; Hu, Y. S.; Li, H.; Wang, Z. X.; Duan, X. F.; Chen, L. Q.; Maier, J.; Ikuhara, Y. Lithium Storage in $Li_4Ti_5O_{12}$ Spinel: The Full Static Picture from Electron Microscopy. *Adv. Mater.* 2012, 24, 3233-3238.

**37**. Kashkooli, A. G.; Lui, G.; Farhad, S.; Lee, D. U.; Feng, K.; Yu, A. P.; Chen, Z. W. Nano-particle size effect on the performance of $Li_4Ti_5O_{12}$ spinel. *Electrochim. Acta* 2016, 196, 33-40.

**38**. Christensen, J.; Srinivasan, V.; Newman, J. Optimization of lithium titanate electrodes for high-power cells. *J. Electrochem. Soc.* 2006, 153, A560-A565.

**39**. Stewart, S.; Albertus, P.; Srinivasan, V.; Plitz, I.; Pereira, N.; Amatucci, G.; Newman, J. Optimizing the performance of lithium titanate spinel paired with activated carbon or iron phosphate. *J. Electrochem. Soc.* 2008, 155, A253-A261.

**40**. Wagemaker, M.; Simon, D. R.; Kelder, E. M.; Schoonman, J.; Ringpfeil, C.; Haake, U.; Lutzenkirchen-Hecht, D.; Frahm, R.; Mulder, F. M. A kinetic two-phase and equilibrium solid solution in spinel $Li_{4+x}Ti_5O_{12}$. *Adv. Mater.* 2006, 18, 3169.

**41**. Kitta, M.; Akita, T.; Tanaka, S.; Kohyama, M. Two-phase separation in a lithiated spinel $Li_4Ti_5O_{12}$ crystal as confirmed by electron energy-loss spectroscopy. *J. Power Sources* 2014, 257, 120-125.

**42**. Tanaka, S.; Kitta, M.; Tamura, T.; Maeda, Y.; Akita, T.; Kohyama, M. Atomic and electronic structures of $Li_4Ti_5O_{12}/Li_7Ti_5O_{12}$ (001) interfaces by first-principles calculations. *J. Mater. Sci.* 2014, 49, 4032-4037.

**43**. Schmidt, W.; Bottke, P.; Sternad, M.; Gollob, P.; Hennige, V.; Wilkening, M., Small Change-Great Effect: Steep Increase of Li Ion Dynamics in $Li_4Ti_5O_{12}$ at the Early Stages of Chemical Li Insertion. *Chem. Mater.* 2015, 27, 1740-1750.

**44**. Wilkening, M.; Iwaniak, W.; Heine, J.; Epp, V.; Kleinert, A.; Behrens, M.; Nuspl, G.; Bensch, W.; Heitjans, P. Microscopic Li self-diffusion parameters in the lithiated anode material $Li_{4+x}Ti_5O_{12}$ (0 <= x <= 3) measured by Li-7 solid state NMR. *Phys. Chem. Chem. Phys.* 2007, 9, 6199-6202.

**45**. Hain, H.; Scheuermann, M.; Heinzmann, R.; Wunsche, L.; Hahn, H.; Indris, S., Study of local structure and Li dynamics in $Li_{4+x}Ti_5O_{12}$ (0 <= x <= 5) using Li-6 and Li-7 NMR spectroscopy. *Solid State Nucl. Mag.* 2012, 42, 9-16.

**46**. Chen, Y. C.; Ouyang, C. Y.; Song, L. J.; Sun, Z. L. Lithium ion diffusion in $Li_{4+x}Ti_5O_{12}$: From ab initio studies. *Electrochim. Acta* 2011**,** 56, 6084-6088.

**47**. Ziebarth, B.; Klinsmann, M.; Eckl, T.; Elsasser, C. Lithium diffusion in the spinel phase $Li_4Ti_5O_{12}$ and in the rocksalt phase $Li_7Ti_5O_{12}$ of lithium titanate from first principles. *Phys. Rev. B* 2014, 89, 174301.

**48**. Kavan, L.; Gratzel, M. Facile synthesis of nanocrystalline $Li_4Ti_5O_{12}$ (spinel) exhibiting fast Li insertion. *Electrochem. Solid St.* 2002, 5, A39-A42.

**49**. Rho, Y. H.; Kanamura, K., $Li^+$ ion diffusion in $Li_4Ti_5O_{12}$ thin film electrode prepared by PVP sol-gel method. *J. Solid State Chem.* 2004, 177, 2094-2100.

**50**. Takami, N.; Hoshina, K.; Inagaki, H. Lithium Diffusion in $Li_{4/3}Ti_{5/3}O_4$ Particles during Insertion and Extraction. *J. Electrochem. Soc.* 2011, 158, A725-A730.

**51**. Wang, C.; Wang, S. A.; He, Y. B.; Tang, L. K.; Han, C. P.; Yang, C.; Wagemaker, M.; Li, B. H.; Yang, Q. H.; Kim, J. K.; Kang, F. Y. Combining Fast Li-Ion Battery Cycling with Large Volumetric Energy Density: Grain Boundary Induced High Electronic and Ionic Conductivity in $Li_4Ti_5O_{12}$ Spheres of Densely Packed Nanocrystallites. *Chem. Mater.* 2015, 27, 5647-5656.

**52**. Wang, C.; Wang, S.; Tang, L. K.; He, Y. B.; Gan, L.; Li, J.; Du, H. D.; Li, B. H.; Lin, Z. Q.; Kang, F. Y. A robust strategy for crafting monodisperse $Li_4Ti_5O_{12}$

nanospheres as superior rate anode for lithium ion batteries. *Nano Energy* 2016, 21, 133-144.

**53**. Singh, G. K.; Ceder, G.; Bazant, M. Z. Intercalation dynamics in rechargeable battery materials: General theory and phase-transformation waves in $LiFePO_4$. *Electrochim. Acta* 2008, 53, 7599-7613.

**54**. Tang, M.; Belak, J. F.; Dorr, M. R. Anisotropic Phase Boundary Morphology in Nanoscale Olivine Electrode Particles. *J. Phys. Chem. C* 2011, 115, 4922-4926.

**55**. Guo, Q. J.; Wang, Q.; Chen, G.; Shen, Q. X.; Li, B. Enhancing the electrochemistry performance of $Li_4Ti_5O_{12}$ for Li-ion battery anodes by a sol-gel assisted molten salt method and graphene modification. *RSC Adv.* 2016, 6, 110032-110039.

**56**. Vaz, M. F.; Fortes, M. A. Grain-Size Distribution - the Lognormal and the Gamma-Distribution Functions. *Scripta Metall. Mater.* 1988, *22*, 35-40.

**57**. Chung, D. W.; Ebner, M.; Ely, D. R.; Wood, V.; Garcia, R. E. Validity of the Bruggeman relation for porous electrodes. *Modell. Simul. Mater. Sci. Eng.* 2013, 21, 074009.

**58**. Ouyang, C. Y.; Zhong, Z. Y.; Lei, M. S. Ab initio studies of structural and electronic properties of $Li_4Ti_5O_{12}$ spinel. *Electrochem. Commun.* 2007, 9, 1107-1112.

**59**. Zhang, Q. Y.; Li, X. Recent Developments in the Doped-$Li_4Ti_5O_{12}$ Anode Materials of Lithium-Ion Batteries for Improving the Rate Capability. *Int. J. Electrochem. Sc.* 2013, 8, 6449-6456.

**60**. Song, M. S.; Benayad, A.; Choi, Y. M.; Park, K. S. Does $Li_4Ti_5O_{12}$ need carbon in lithium ion batteries? Carbon-free electrode with exceptionally high electrode capacity. *Chem. Commun.* 2012, 48, 516-518.

**61**. Kim, C.; Norberg, N. S.; Alexander, C. T.; Kostecki, R.; Cabana, J. Mechanism of Phase Propagation During Lithiation in Carbon-Free $Li_4Ti_5O_{12}$ Battery Electrodes. *Adv. Funct. Mater.* 2013, 23, 1214-1222.

**62**. Young, D.; Ransil, A.; Amin, R.; Li, Z.; Chiang, Y. M. Electronic Conductivity in the $Li_{4/3}Ti_{5/3}O_4$-$Li_{7/3}Ti_{5/3}O_4$ System and Variation with State-of-Charge as a Li Battery Anode. *Adv. Energy Mater.* 2013, 3, 1125-1129.

**63**. Singh, D. P.; Mulder, F. M.; Wagemaker, M. Templated spinel $Li_4Ti_5O_{12}$ Li-ion battery electrodes combining high rates with high energy density. *Electrochem. Commun.* 2013, 35, 124-127.

**64**. Ebner, M.; Chung, D. W.; Garcia, R. E.; Wood, V. Tortuosity Anisotropy in Lithium-Ion Battery Electrodes. *Adv. Energy Mater.* 2014, 4, 1301278.

**65**. Bruggeman, D. A. G. Calculation of various physics constants in heterogenous substances I Dielectricity constants and conductivity of mixed bodies from isotropic substances. *Ann. Phys-Berlin* 1935, 24, 636-664.

**66**. Liu, Y.; Tang, D. P.; Zhong, H. X.; Zhang, Q. Y.; Yang, J. W.; Zhang, L. Z. Facile synthesis of nanostructured $Li_4Ti_5O_{12}$/PEDOT:PSS composite as anode material for lithium-ion batteries. *RSC Adv*. 2016, 6, 95512-95517.

**67**. Bergner, B. J.; Hofmann, C.; Schurmann, A.; Schroder, D.; Peppler, K.; Schreiner, P. R.; Janek, J. Understanding the fundamentals of redox mediators in Li-$O_2$batteries: a case study on nitroxides. *Phys. Chem. Chem. Phys*. 2015, 17, 31769-31779.

**68**. Cogswell, D. A.; Bazant, M. Z. Theory of Coherent Nucleation in Phase-Separating Nanoparticles. *Nano Lett.* 2013, *13*, 3036-3041.

**69**. Dreyer, W.; Jamnik, J.; Guhlke, C.; Huth, R.; Moskon, J.; Gaberscek, M. The thermodynamic origin of hysteresis in insertion batteries. *Nat. Mater*. 2010, 9, 448-453.

**70**. Ferguson, T. R.; Bazant, M. Z. Phase Transformation Dynamics in Porous Battery Electrodes. *Electrochim. Acta* 2014, 146, 89-97.

**71**. Kitta, M.; Akita, T.; Tanaka, S.; Kohyama, M. Characterization of two phase distribution in electrochemically-lithiated spinel $Li_4Ti_5O_{12}$ secondary particles by electron energy-loss spectroscopy. *J. Power Sources* 2013, *237*, 26-32.

**72**. Wilkening, M.; Amade, R.; Iwaniak, W.; Heitjans, P., Ultraslow Li diffusion in spinel-type structured $Li_4Ti_5O_{12}$ - A comparison of results from solid state NMR and impedance spectroscopy. *Phys. Chem. Chem. Phys.* 2007, 9, 1239-1246.

**73**. Srinivasan, V.; Newman, J. Discharge model for the lithium iron-phosphate electrode. *J. Electrochem. Soc.* 2004, 151, A1517-A1529.

**74**. Bazant, M. Z., Theory of Chemical Kinetics and Charge Transfer based on Nonequilibrium Thermodynamics. *Accounts Chem. Res.* 2013, 46, 1144-1160.

**75**. Ferguson, T. R.; Bazant, M. Z. Nonequilibrium Thermodynamics of Porous Electrodes. *J. Electrochem. Soc.* 2012, 159, A1967-A1985.

**76**. Open source MPET softwere, https://bitbucket.org/bazantgroup/mpet.

**77**. Smith, R. B.; Bazant, M. Z. Multiphase Porous Electrode Theory J. Electrochem. Soc. 2017, 164, E3291-E3310.

**78**. Cogswell, D. A.; Bazant, M. Z. Coherency Strain and the Kinetics of Phase Separation in $LiFePO_4$ Nanoparticles. *ACS Nano* 2012, 6, 2215-2225.

**79**. Bai, P.; Cogswell, D. A.; Bazant, M. Z. Suppression of Phase Separation in $LiFePO_4$ Nanoparticles During Battery Discharge. *Nano Lett.* 2011, 11, 4890-4896.

**80**. Bazant, M. Z. Thermodynamic Stability of Driven Open Systems and Control of Phase Separation by Electro-autocatalysis. *Faraday Discuss.* 2017, 199, 422-463.

**81**. Liu, H.; Strobridge, F. C.; Borkiewicz, O. J.; Wiaderek, K. M.; Chapman, K. W.; Chupas, P. J.; Grey, C. P. Capturing metastable structures during high-rate cycling of $LiFePO_4$ nanoparticle electrodes. *Science* 2014, 344, 6191.

**82**. Zhang, X. Y.; van Hulzen, M.; Singh, D. P.; Brownrigg, A.; Wright, J. P.; van Dijk, N. H.; Wagemaker, M. Rate-Induced Solubility and Suppression of the First-Order Phase Transition in Olivine $LiFePO_4$. *Nano Lett.* 2014, 14, 2279-2285.

**83**. Niu, J. J.; Kushima, A.; Qian, X. F.; Qi, L.; Xiang, K.; Chiang, Y. M.; Li, J. In Situ Observation of Random Solid Solution Zone in $LiFePO_4$ Electrode. *Nano Lett.* 2014, 14, 4005-4010.

**84**. Lim, J.; Li, Y. Y.; Alsem, D. H.; So, H.; Lee, S. C.; Bai, P.; Cogswell, D. A.; Liu, X. Z.; Jin, N.; Yu, Y. S.; Salmon, N. J.; Shapiro, D. A.; Bazant, M. Z.; Tyliszczak, T.; Chueh, W. C. Origin and hysteresis of lithium compositional spatiodynamics within battery primary particles. *Science* 2016, *353*, 566-571.

**85**. Zeng, Y.; Bazant, M. Z. Phase Separation Dynamics in Isotropic Ion-Intercalation Particles. *Siam J. Appl. Math.* 2014, 74, 980-1004.

**86**. Zhang, W.; Topsakal, M.; Cama, C.; Pelliccione, C. J.; Zhao, H.; Ehrlich, S.; Wu, L. J.; Zhu, Y. M.; Frenkel, A. I.; Takeuchi, K. J.; Takeuchi, E. S.; Marschilok, A. C.; Lu, D. Y.; Wang, F. Multi-Stage Structural Transformations in Zero-Strain Lithium Titanate Unveiled by in Situ X-ray Absorption Fingerprints. *J. Am. Chem. Soc.* 2017, 139, 16591-16603.

**87**. Smith, R. B.; Bazant, M. Z., Intercalation kinetics in multiphase layered materials. *J. Phys. Chem. C*, 2017, 121, 12505-12523

**88**. Bai, P.; Bazant, M. Z. Charge transfer kinetics at the solid-solid interface in porous electrodes. *Nat. Commun.* 2014, 5, 4585.

**89**. Kuznetsov, A. M.; Ulstrup, J. Electron Transfer in Chemistry and Biology: An Introduction to the Theory. 1999, ISBN: 978-0-471-96749-1.

**90**. Chidsey, C. E. D. Free-Energy and Temperature-Dependence of Electron-Transfer at the Metal-Electrolyte Interface. *Science* 1991, 251, 919-922.

**91**. Zeng, Y.; Smith, R. B.; Bai, P.; Bazant, M. Z. Simple formula for Marcus-Hush-Chidsey kinetics. *J. Electroanal. Chem.* 2014, 735, 77-83.

**92**. Smith, R. B.; Krishnan, Y.; McEldrew, M.; Fraggedakis, D.; Bai, P.; Bazant, M. Z. *unpublished*.

**93**. Thomas-Alyea, K. E.; Jung, C.; Smith, R. B.; Bazant, M. Z. In Situ Observation and Mathematical Modeling of Lithium Distribution within Graphite. *J. Electrochem. Soc.* 2017, 164, E3063-E3072

**94**. Shen, Y. B.; Eltzholtz, J. R.; Iversen, B. B., Controlling Size, Crystallinity, and Electrochemical Performance of $Li_4Ti_5O_{12}$ Nanocrystals. *Chem. Mater.* 2013, 25, 5023-5030.

**95**. Ganapathy, S.; Wagemaker, M. Nanosize Storage Properties in Spinel Li4Ti5O12 Explained by Anisotropic Surface Lithium Insertion. *ACS Nano* 2012, 6, 8702-8712.

**96**. Wagemaker, M.; Mulder, F. M.; Van der Ven, A. The Role of Surface and Interface Energy on Phase Stability of Nanosized Insertion Compounds. *Adv. Mater.* 2009, 21, 2703.

**97**. Ouyang, C. Y.; Shi, S. Q.; Lei, M. S. Jahn-Teller distortion and electronic structure of $LiMn_2O_4$. *J. Alloy Compd.* 2009, 474, 370-374.

**98**. Arora, P.; Zhang, Z. M. Battery separators. *Chem. Rev.* 2004, 104, 4419-4462.

**99**. Clegard http://www.ldcgm.com/Celgard/CELGARD-4550.pdf.

**100**. Thorat, I. V.; Stephenson, D. E.; Zacharias, N. A.; Zaghib, K.; Harb, J. N.; Wheeler, D. R. Quantifying tortuosity in porous Li-ion battery materials. *J. Power Sources* 2009, 188, 592-600.

**101**. Choi, J. H.; Ryu, W. H.; Park, K.; Jo, J. D.; Jo, S. M.; Lim, D. S.; Kim, I. D. Multi-layer electrode with nano-$Li_4Ti_5O_{12}$ aggregates sandwiched between carbon nanotube and graphene networks for high power Li-ion batteries. *Sci. Rep. - Uk* 2014, 4, 7334.

**102**. Chen, S.; Xin, Y. L.; Zhou, Y. Y.; Ma, Y. R.; Zhou, H. H.; Qi, L. M. Self-supported $Li_4Ti_5O_{12}$ nanosheet arrays for lithium ion batteries with excellent rate capability and ultralong cycle life. *Energy Environ. Sci.* 2014, 7, 1924-1930.

**103**. Li, N.; Chen, Z. P.; Ren, W. C.; Li, F.; Cheng, H. M. Flexible graphene-based lithium ion batteries with ultrafast charge and discharge rates. *P. Natl. Acad. Sci. USA* 2012, 109, 17360-17365.

**104**. Verde, M. G.; Baggetto, L.; Balke, N.; Veith, G. M.; Seo, J. K.; Wang, Z. Y.; Meng, Y. S. Elucidating the Phase Transformation of $Li_4Ti_5O_{12}$ Lithiation at the Nanoscale. *ACS Nano* 2016, 10, 4312-4321.

**105**. Kim, C.; Yu, Y. S.; Moyon, B.; Sirisopanaporn, C.; Richardson, T. J.; Cabana, J. Visualization of the Phase Propagation within Carbon -Free $Li_4Ti_5O_{12}$ Battery Electrodes. *J. Phys. Chem. C* 2016, 120, 29030-29038.

**106**. Clegard http://www.ldcgm.com/Celgard/CELGARD-4550.pdf.

**107**. Cho, H. M.; Chen, M. V.; MacRae, A. C.; Meng, Y. S. Effect of Surface Modification on Nano-Structured $LiNi_{0.5}Mn_{1.5}O_4$ Spinel Materials. *ACS Appl. Mater. Inter.* 2015, 7,16231-16239.

**108**. Malik, M.; Dincer, I.; Rosen, M. A. Review on use of phase change materials in battery thermal management for electric and hybrid electric vehicles. *Int. J. Energy Res.* 2016, 40, 1011-1031.

**109**. Li, Y. Y.; El Gabaly, F.; Ferguson, T. R.; Smith, R. B.; Bartelt, N. C.; Sugar, J. D.; Fenton, K. R.; Cogswell, D. A.; Kilcoyne, A. L. D.; Tyliszczak, T.; Bazant, M. Z.; Chueh, W. C. Current-induced transition from particle-by-particle to concurrent intercalation in phase-separating battery electrodes. *Nat. Mater.* 2014, 13, 1149-1156.

**110**. Delmas, C.; Maccario, M.; Croguennec, L.; Le Cras, F.; Weill, F., Lithium deintercalation in LiFePO(4) nanoparticles via a domino-cascade model. *Nat Mater* 2008, 7, 665-671.

**111**. Laffont, L.; Delacourt, C.; Gibot, P.; Wu, M. Y.; Kooyman, P.; Masquelier, C.; Tarascon, J. M. Study of the $LiFePO_4/FePO_4$ two-phase system by high-resolution electron energy loss spectroscopy. *Chem. Mater.* 2006, 18, 5520-5529.

**112**. Badi, S. P.; Wagemaker, M.; Ellis, B. L.; Singh, D. P.; Borghols, W. J. H.; Kan, W. H.; Ryan, D. H.; Mulder, F. M.; Nazar, L. F. Direct synthesis of nanocrystalline $Li_{0.90}FePO_4$: observation of phase segregation of anti-site defects on delithiation. *J. Mater. Chem.* 2011, 21, 10085-10093.

# 5

# Thermodynamics and Kinetics of Na-Ion Insertion into Hollandite-$TiO_2$ and O3-Layered $NaTiO_2$: an Unexpected Link between Two Promising Anode Materials for Na-Ion Batteries

«ἐὰν μὴ ἔλπηται ἀνέλπιστον, οὐκ ἐξευρήσει, ἀνεξερεύνητον ἐὸν καὶ ἄπορον»

“If (he) doesn’t expect the unexpected, (he) will not discover it; for it is difficult to discover and intractable”

Heraclitus

Heraclitus, *FRAGMENTS*, [F18], text and translation by T. M. Robinson, University of Toronto Press, 2003.

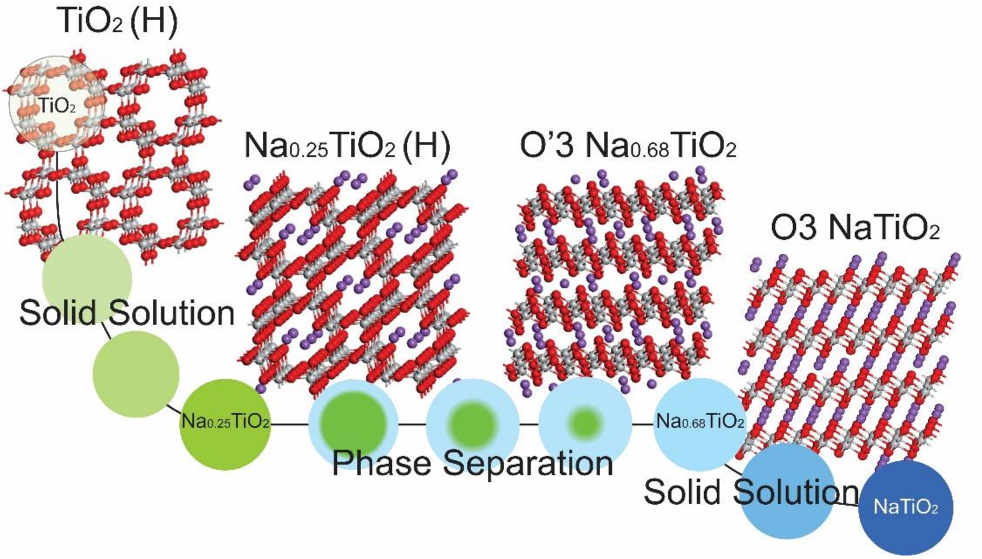
TiO2 (H)
TiO2
Na0.25TiO2 (H)
O'3 Na0.68TiO2
O3 NaTiO2
Solid Solution
Na0.25TiO2
Phase Separation
Na0.68TiO2
Solid Solution
NaTiO2

## Abstract

First principle DFT calculations are used to study the thermodynamic and kinetic properties of Na-ion insertion in $TiO_2$ hollandite, a potential anode for Na-ion batteries. The experimentally observed phase transformation from tetragonal $TiO_2$ (I4/m) to monoclinic $Na_{0.25}TiO_2$ (I2/m) is confirmed. At high Na-ion concentrations the calculated formation energies predict a first order phase transition towards the layered O'3-$Na_{0.68}TiO_2$ structure. Further sodiation initiates a solid solution reaction towards the layered O3-$NaTiO_2$ phase, which was recently brought forward as a promising anode for Na-ion batteries. This transformation irreversibly transforms the one dimensional Hollandite tunnel structure into the layered structure, and potentially brings forward an alternative route towards the preparation of the hard to prepare O3-$NaTiO_2$ material. Energy barrier calculations reveal fast Na-ion diffusion at low concentrations and sluggish diffusion upon reaching the $Na_{0.25}TiO_2$ phase, rationalizing why experimentally the $Na_{0.5}TiO_2$ phase is not achieved. Detailed analysis of the kinetic behaviour in the hollandite structure via Molecular Dynamics simulations reveal the importance of correlated atomic motions and dynamic lattice deformations for the Na-ion diffusion. In addition, exceptional Na-ion kinetics were predicted for the layered O'3-$Na_{0.75}TiO_2$ phase through a dominating divacancy hopping mechanism.

Based on the homonymous paper:
Vasileiadis, A.; Wagemaker, M. Thermodynamics and Kinetics of Na-Ion Insertion into Hollandite-$TiO_2$ and O3-Layered $NaTiO_2$: An Unexpected Link between Two Promising Anode Materials for Na-Ion Batteries. Chem. Mater. 2017, 29, 1076-1088.

## 5.1 Introduction

The high gravimetric and volumetric energy density of Li-ion batteries revolutionized modern society by enabling mobile applications such as laptops, tablets and mobile phones. However, the increasing demand for Li-ion batteries by the development of electrical cars and static storage for instance in houses, challenges the practical abundance of lithium world-wide[1, 2].

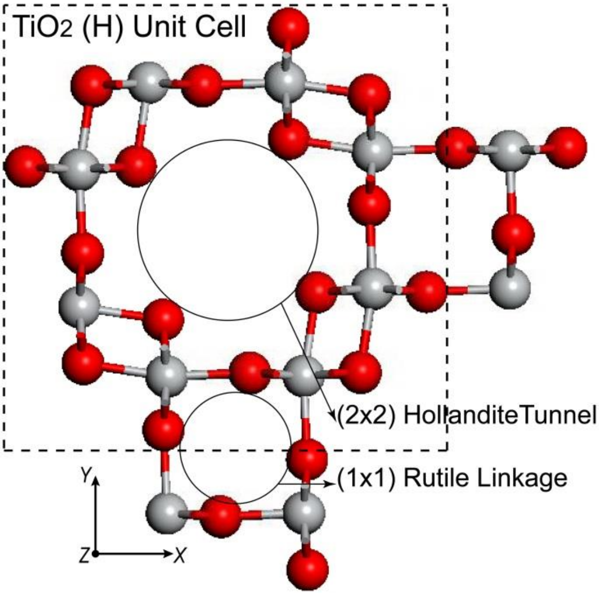

**Figure 5.1:** Crystal structure of $TiO_2$ (H), Ti atoms are located in the centre of the $TiO_6$ octaedra that share both edges forming the large 2x2 tunnel, rutile linkage channels connect the hollandite channels, the dashed line encloses one unit cell, red spheres represent O atoms while grey ones represent Ti atoms.

A highly promising alternative charge carrier, already considered by the scientific community decades ago, is Sodium being much more abundant and displaying comparable redox potentials and insertion behaviour[3, 4] compared to Lithium. Sodium, however, has a larger ionic radius compared to Lithium imposing larger volume changes on the host structure lattice which is detrimental for the cycle life[5]. Although several materials have been reported as candidates for Na-ion positive electrodes, Na-ion anode materials are scarcely reported on. Because Na-ion intercalation into graphite layers appears not possible[6], research focuses mainly on other carbonaceous materials such as hard carbons[7, 8] and petroleum cokes[9] while non-carbonaceous alloys[10] and vanadium oxides[11, 12] are investigated as well. $TiO_2$ polymorphs are well studied as negative electrode materials for Li-ion batteries, primarily because of the success of spinel $Li_4Ti_5O_{12}$[13-16] and anatase[17-20] and secondarily because of rutile[21], layered $TiO_2$[22], brookite and ramsdellite[23]. Recently those polymorphs were also investigated as potential negative electrode materials for Na-ion insertion[24-28].

Amongst them, the layered O3-$NaTiO_2$ was identified as one of the most promising Na-ion anode candidates due to its exceptional electrochemical performance and the ability to intercalate Na-ions without large volume changes (<1%)[25]. Early studies of the layered O3-$NaTiO_2$ resulted in limited intercalation behavior[29] and a substantial diffusion barrier[30]. Recently Wu et al.[25] showed that reducing the water content and expanding the voltage window results in excellent capacity (150 mAh/g) and reversibility between the $Na_{0.5}TiO_2$ and $NaTiO_2$ phases. The same group[25] performed DFT calculations to determine the energy barriers indicating exceptionally good kinetic behaviour. In-situ X-ray diffraction revealed an O3 to O'3 phase transition[25] where the O'3 notation refers to the structures resulting from the monoclinic distortion of the O3 layered $NaTiO_2$[31]. This is a very common reduction amongst O3 type compounds and it is accounted to Na vacancy ordering[31]. The O3 notation refers to the type of oxygen coordination of the inserted ion (O for octahedral) and the repetition number of transition metal stacks (3) in the layered structure[25].

A much less investigated polymorph is $TiO_2$ Hollandite, noted as $TiO_2$ (H), that was first reported in 1989[32] where potassium was extracted from the original $K_xTiO_2$ ($0.13<x<0.25$) structure. The tetragonal hollandite structure is indexed by the I4/m space group symmetry (Figure 5.1) for which the large hollandite 2x2 channel aligned with the c-axis was immediately recognised as a potential pathway for ion diffusion and insertion. The large 2x2 channels are linked via rutile channels that are referred to as rutile linkage. The Li-ion insertion properties were investigated by Noailles et al. [33] reporting a voltage profile around 1.5 V, low reversibility, high polarisation and capacities far below the theoretical capacity of 335 mAh/g offered by the $Ti^{3+/4+}$ redox couple. The initial capacity of 160mAh/g was never recovered and a reversible capacity of only 36 mAh/g resulted. Gutierrez-Florez et al.[34] managed to obtain a higher reversible capacity. Much later Sakao et al.[35, 36] re-examined hollandite $TiO_2$ (H) managing a reversible capacity of 147 mAh/g for 50 cycles. Sakao et al.[36] demonstrated that a larger K content (residual from the synthesis) plunges the electrochemical performance explaining the early results of Noailles et al.[33] About four Li-ions per unit cell ($Li_{0.5}TiO_2$)

reside in the hollandite 2x2 channel while the 1x1 rutile linkage remains empty. Upon lithiation the symmetry reduces to monoclinic (I2/m) due to the structural distortion induced by Li-ion ordering in the 2x2 channel, the consequence of cation repulsions[33].

Na-ion insertion in $TiO_2$ (H) has been investigated by Perez-Florez et all[37] reporting a reversible capacity of 85 mAh/g after an initial first discharge of 280 mAh/g. The proposed reversible Na-ion insertion mechanism starts with a solid solution reaction followed by a phase transition from the original hollandite tetragonal symmetry (I4/m) to the monoclinic (I2/m) reaching the composition $Na_{0.25}TiO_2$ with a relatively small volume change upon Na-ion insertion of 1.1%. Up to date it is unclear why the practical capacity appears to be limited to the $Na_{0.25}TiO_2$ composition and what happens beyond this composition and how that affects the structure and Na-ion kinetics. To establish the theoretical possibilities and limitations as a Na-ion insertion electrode material computational approaches may be of large interest. In the present work, DFT is used to predict and reveal the structure, thermodynamics and Na-ion kinetics of $TiO_2$ (H) upon Na-ion insertion which to the best of our knowledge has not been attempted previously. The resulting formation enthalpies and derived voltages vs Na/$Na^+$ give insight into the insertion mechanism and structural evolution of the material. Energy barrier calculations shed light on what limits the performance of the $TiO_2$ (H) as an anode material for Na-ion batteries. Thorough investigation of the kinetic mechanisms reveals the importance of correlated atomic motions and lattice dynamics for ionic diffusion which is suggested to be of general importance for computational research. At high Na-ion concentrations the DFT results predict a first order phase transition towards the O3 layered $NaTiO_2$. Although, this thermodynamic path cannot be induced during battery cycling it may provide a novel and more facile route towards the synthesis of the layered $NaTiO_2$ material which has recently been shown to have excellent Na-ion electrode properties. Thereby, the present ab-initio study provides insight in two potential Na-ion electrode materials $TiO_2$ (H) and layered O3 $Na_xTiO_2$.

## 5.2 Computational Methods

DFT calculations were performed in the plane wave code VASP[38]. Valence-core interactions were probed with the projector augmented wave approach (PAW)[39] with cores of [Ar] for Ti, [He] for O, and [Ne] for Na. All calculations were integrated with the gradient-corrected (GGA) exchange correlation functional of Perdew et al.[40] and treated with the tetrahedron method with Bloch corrections. The titanium oxide host structures were optimized by relaxation of their respective experimental values obtained from literature. Structure relaxations required a high energy cutoff of 520 eV and a Monkhorst-Pack k-point set to achieve convergence better than 2 meV/atom. Total energies resulted from a second self-consistent calculation such that the k-point grid can recover from the lattice changes upon Na insertion. For comparison selected calculations were performed using a Hubbard correction parameter (DFT+U method[41-43]) $U_{eff}$ = 4.2 eV to account for the tendency of regular DFT calculations to overestimate the electron delocalization of d and f orbitals, which is well known for systems with strongly localized and correlated electronic ground states [41, 44-46]. In addition, a few Li-ion configurations were studied to probe differences between the Li-ion and Na-ion charge carriers. To predict the activation energy for Na-ion hopping in the $TiO_2$ (H) the nudge elastic band method[47] was applied using the climbing image modification[48, 49]. In this way a string of Na-ion positions that describe the possible diffusion pathway is relaxed to the minimum energy path. The total energy difference between the saddle point and the initial local minima represents the activation barrier ($E_a$) of the Na-ion hopping. In order to capture phase transformations and/or the importance of atomic motions upon migration, we also implemented the solid state nudge elastic band method (ss-NEB)[50] that allows the lattice parameters to relax. All nudge elastic band (NEB) barrier calculations were executed in large supercells (1x1x3) with lattice parameters exceeding 10 Å in order to avoid interactions between images of Na being moved[51]. Additionally, to obtain a concrete and complete picture of the kinetics we performed molecular dynamic (MD) calculations for 190 up to 400 ps with a 2 fs time step at 600 K. By determining the amount of hops the mean jump rate $\nu$ according to $\nu = J/(Nt)$ was calculated where J represents the number of transitions in the MD simulation, N the total number of Na-ions in the supercell and t the total simulation time. The respective activation barriers for the various jumps are calculated using transitional state theory formulated as $E_a = -kT \ln(\nu/\nu_0)$[52] where $\nu_0$ represents the attempt frequency, typically assumed to be $10^{13}$ $sec^{-1}$ [53], k is Boltzmann constant and T the temperature. Diffusion coefficient calculations were performed based on the random-walk atomistic model[51, 52, 54, 55]. The diffusion coefficient can be expressed as:

$$D = \gamma \lambda^2 \Gamma$$

where $\gamma = 1/N_d$ with $N_d$ matching the number of directions (dimensions) in the crystal towards the ion can hop to, λ represents the distance between the jumps and Γ is the jump frequency where the temperature dependence is introduced as:

$$\Gamma = \nu_0 e^{-\frac{Ea}{kT}}$$

Finally, we can write

$$D_{Na} = D_0 e^{-\frac{E_a}{kT}}$$

with

$$D_0 = \gamma \lambda^2 \nu_0$$

a temperature independent pre-exponential. Finally, when applicable, an estimate of the self-diffusion coefficient was obtained based on the mean square displacement (MSD) resulting from the molecular dynamic calculations according to the formula $D = MSD/(2N_d t)$[56] where t represents the total simulation time.

## 5.3 Dilute-Limit Na-Ion and Li-Ion Insertion in $TiO_2$ (H)

The $TiO_2$ (H) structure was optimized starting at the experimental values[32] using a 6x6x8 k-point grid. Total energy calculations upon Na and Li ion insertion were performed in a 1x1x2 supercell that contains in total 48 host atoms ($Ti_{16}O_{32}$). The resulting lattice parameters, see Table 5.1, were slightly larger than those experimentally observed, an overestimation that is typically encountered when using the GGA method[57].

**Table 5.1:** Experimental vs. DFT predicted lattice parameters of the hollandite $TiO_2$ unit cell.

| $TiO_2$ (H) | a(Å) | b(Å) | c(Å) | α,β,γ (deg) |
|---|---|---|---|---|
| GGA | 10.302 | 10.302 | 2.980 | 90 |
| Experimental | 10.161(3) | 10.161(3) | 2.910(1) | 90 |

The structure reveals the presence of 1x1 rutile channels and the larger 2x2 hollandite channels, together providing six interstitial positions to accommodate cations as illustrated by Figure 5.2. The first three interstitial sites, Wyckoff notations 4c, 2a, 8h', are coplanar in the xy plane intersecting the z-axis at z=0.5, as shown in Figure 5.2a. The next two interstitial sites, Wyckoff notations 8h and 2b, are coplanar in the xy plane intersecting the z-axis at z=0 and finally the 4e site is positioned at (0,0,z) as shown in Figure 5.2b. According to Tompsett[58] the 8h' and 8h sites can be distinguished despite the fact that they hold the same Wyckoff position because the 8h' site is positioned very close to the co-planar 2a position creating a different coordination compared to that of the 8h site[58]. Na-ion and Li-ion insertion was simulated by accommodating the cations in all available lattice sites and allowing relaxation of the ionic positions and lattice parameters, as well as allowing symmetry changes towards the lowest energy configuration.

Introducing a single Na-ion in the $Ti_{16}O_{32}$ supercell results in the $Na_{0.06}TiO_2$ composition, representing the dilute limit of Na-ion insertion, the relaxation results of which are presented in Table 5.2. At dilute compositions Na-ions prefer the center of hollandite tunnel (2a site), where in all cases sodium inserted in the coplanar 8h' position relaxed towards the 2a site. For the 4e (0,0,z) position the relaxation depends on the z-coordinate of the Na-ions. For (0,0,z<0.3) the Na-ions relaxes towards the lowest energy 2a site and for z>0.3 the Na-ions remain near the starting (4e) position, a configuration with a slightly higher energy, indicating the presence of a barrier for the relaxation towards the 2a site. In contrast, for Li-ion insertion at the dilute limit ($Li_{0.06}TiO_2$) the lowest energy Li-ion position is the 8h site followed by the h' site, both closer to the channel wall leading to short Li-O distances (Figure 5.3a).

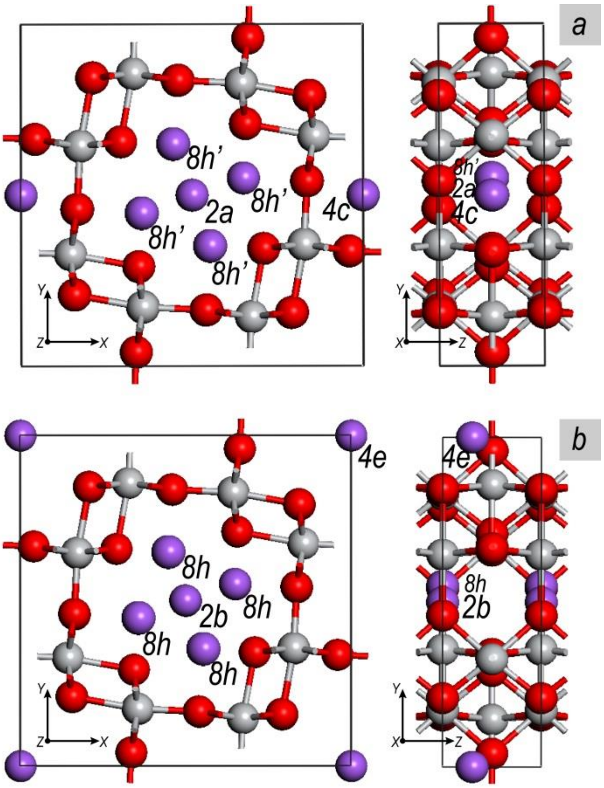

**Figure 5.2: a)** 2a, 4c and 8h’ coplanar positions, red spheres represent O atoms, grey Ti and purple Na-ions. **b**) 2b, 8h, 4e positions, red spheres represent O, grey Ti and purple Na-ions.

The different positions in the channel can be attributed to the difference in Na-ion and Li-ion radius. In these structures where the bonds are largely ionic, the coordination number of a cation within a polyhedron of anions depends on the relative size of the cation and the anion. As a general rule, the most preferable coordination occurs when the cation size exactly fits or is slightly larger than the interstice geometrical space offered by the polyhedron. Cations with smaller ionic radius will be able to “rattle” in the relatively large interstitial space making the structure energetically unfavourable and are most stable at the next lower coordination[59]. Even though Pauling’s first rule[59] is an oversimplification, treating atoms as hard spheres in a closed packed arrangement, it appears to apply consistently in all Ti oxide structures[60-65]. The Li-ion radius allows a maximum 6-fold coordination (octahedral position) or a 4-fold coordination (tetrahedral) with a small energy penalty. Depending on the local environment, however, the tetrahedral coordination could be more stable compared to the octahedral coordination as illustrated by the rutile[61] and LTO[66, 67] structures. When residing in the 2a position of the 2x2 hollandite channel the Li-ion is coordinated by 4 primary and 4 secondary (8 oxygen atoms in total) which introduces a large energy penalty forcing the Li-ion towards the tunnel wall. The resulting Li-O interatomic distances for the 3 closest oxygen atoms are between 1.997 and 2.124 Å, similar to what is found in other oxide hosts like $TiO_2$ anatase (1.940 to 2.245 Å)[60] $LiCoO_2$ (2.11 Å)[68] or LFP (2.095 to 2.167Å)[69]. In contrast, Na-ions are large enough to be accommodated in the 2a position (previously occupied by an equally large potassium ion during the synthesis process to stabilize the 2x2 tunnel).

**Table 5.2:** Relative formation energies of Na-ion and Li-ion occupancy of the different interstitial sites in the $(Na,Li)_{0.063}Ti_{16}O_{32}$ hollandite supercell. Energies are given with respect to the lowest energy site. In addition for the Na-ion case both DFT and DFT + U (4.2) calculations were performed.

| ion site | ΔE (Na-ion) (meV) DFT | ΔE (Na-ion) (meV) DFT+U (4.2) | ΔE (Li-ion) (meV) DFT |
|---|---|---|---|
| 2a | 0 | 0 | 310 |
| 8h' | 1* | 4* | 4 |
| 4e | 38* | 15* | 310* |
| 8h | 84 | 84 | 0 |
| 2b | 143 | 169 | 618 |
| 4c | 3348 | 3431 | 1040 |

* In those cases the Na/Li-ion relaxed towards the nearby 2a position, resulting either in exactly the 2a position (and formation energy) or a position very near to the 2a position (with a slightly larger formation energy).

The large formation energy for the Na-ion and Li-ion located at the 4c position, within the rutile linkage channel, indicates that this position is unlikely to occur at low concentrations. The octahedral position offered by the rutile channel is too small compared to the Na-ion radius leading to significant lattice distortions (1.9% volume change) which raises the energy compared to the Li-ion. Na-ion insertion in the octahedral rutile position was further investigated by performing DFT calculations of Na-ion insertion in the rutile $TiO_2$ structure. The rutile $TiO_2$ structure is strongly distorted by the Na-ion occupancy of the octahedral position causing volume changes of 2.2% even at the small Na-ion concentration in the

$Na_{0.06}TiO_2$ composition. The resulting Na-O distances after relaxation amount 2.04 and 2.21 Å, values practically equivalent with that of the distorted 4c site in the hollandite structure when occupied by a Na-ion (2.05 and 2.23 Å). The DFT calculations predict a negative insertion voltage (-0.5V vs $Na^+/Na$ - $Na_{0.06}TiO_2$) for Na-ion insertion in rutile $TiO_2$ indicating Na-ion insertion is energetically unfavourable.

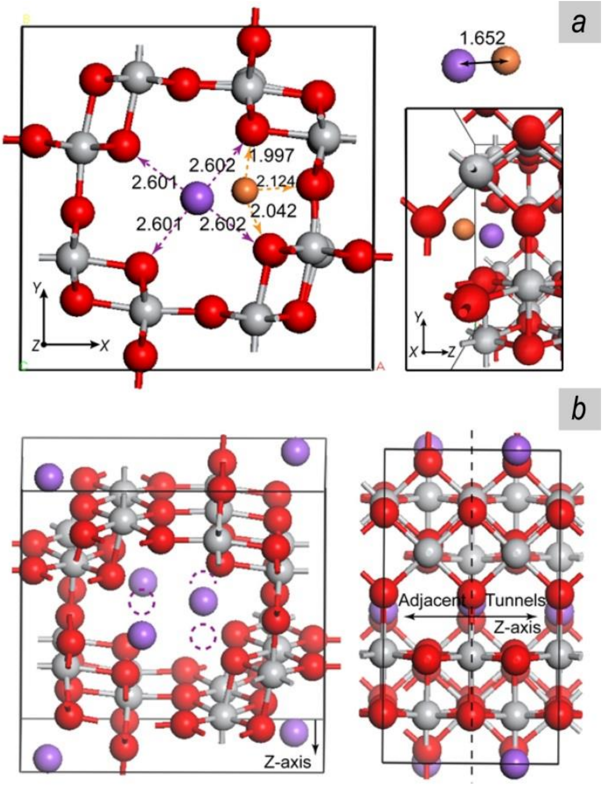

**Figure 5.3: a)** Na-ion versus Li-ion positions in the dilute limit $(Na,Li)_1Ti_{16}O_{32}$. The atomic distances are reported in Angstroms, purple spheres represent Na-ions, orange Li-ions, red O atoms and grey Ti atoms. **b)** Lowest energy configuration at intermediate Na concentration $Na_{0.25}TiO_2$ where Na-ions occupy alternating 8h positions forming a zig-zag chain of Na-ions in the 2x2 hollandite channels, maximizing the Na-Na distances driven by Coulombic repulsion, purple spheres represent Na-ions, red O atoms and grey Ti atoms.

Further Na-ion insertion affects the formation energies of the ionic positions drastically. Compositions above $Na_{0.125}TiO_2$ cause Na-ion occupation in adjacent 2x2 hollandite channels, forcing Na-ions previously occupying the 2a site to shift towards the 8h position. In the $Ti_{16}O_{32}$ hollandite supercell, which contains four 2x2 channels, this effect occurs when a third Na-ion is inserted ($Na_{0.19}TiO_2$). Adding one additional Na-ion in the hollandite superstructure, resulting in $Na_{0.25}TiO_2$, where the lowest energy configuration is characterized by a zigzag-8h occupation along the c-axis (shown in Figure 5.3b) thereby occupying half of the 8h positions.

Columbic forces appear responsible for this configuration as the 2a-2a distance between adjacent tunnels is around 3 Å whereas for diagonal Na-ion occupation of 8h positions in $Na_{0.25}TiO_2$, the distance is 3.75 Å. Electrostatic repulsion might not be the only criterion as the 8h’-8h’ zigzag configuration can provide even greater distance between the Na ions (4.3Å). Apparently, the oxygen coordination provided by the 8h position is more favourable compared to the 8h’ position.

## 5.4 The Monoclinic $Na_{0.25}TiO_2$ (H) Phase

The DFT predicted $Na_{0.25}TiO_2$ phase is in good agreement with the experimental result first reported by Perez-Florez et al.[37]. The starting $TiO_2$ (H) tetragonal I4/m symmetry is reduced to the monoclinic I2/m symmetry resulting in a significant reduction of the b-lattice parameter, 3% as determined by the present DFT calculations compared to 2.6% reported experimentally[37], along with an increase in the $\beta^o$ angle. For X-ray diffraction this results in splitting of the hollandite $TiO_2$ {020} reflection into the {200} and {002} reflections of the $Na_{0.25}TiO_2$ monoclinic lattice. In Table 5.3 the experimentally determined lattice parameters are compared to the values predicted by the present DFT calculations. Based on the DFT predicted structures the powder diffraction patterns were calculated, shown in Figure 5.4b, illustrating good agreement with the experimentally obtained patterns[37]. Figure 5.4b demonstrates the phase transition between the tetragonal and monoclinic structures by the splitting of the second and third reflections.

**Table 5.3:** Comparison of the monoclinic $Na_{0.25}TiO_2$ unit cell parameters between the experimental and presently predicted values, The volume change is calculated with respect to the empty host. Note that the b-lattice parameter of the tetragonal phase changes into the c-lattice parameter in the monoclinic symmetry.

| Method | Experiment Values[37] | DFT |
|---|---|---|
| s.g. | I2/m | I2/m |
| a(Å) | 10.4509(14) | 10.585 |
| b(Å) | 2.9674(3) | 2.9705 |
| c(Å) | 9.88497(11) | 9.988 |
| β(°) | 90.683(2) | 90.55 |
| ΔV | 1.1% | 0.72% |

Interatomic distances between Ti and O atoms are between 1.963 and 2.046 Å while distances between Na-ions and the closest O atoms are between 2.392 and 2.471 Å for both the relaxed experimental and predicted phases. The diagonal distance connecting the two Na-ions is 3.748 Å in the DFT predicted phase and 3.762 in the experimental (DFT-relaxed) phase. The presence of nearby Na-ions in adjacent 2x2 channels reduces the Na-O distance when compared to the dilute limit ($Na_{0.6}TiO_2$), effectively pushing Na-ions towards the wall of the channel. The 2a towards 8h position shift appears responsible for the tetragonal to monoclinic phase transition as the b-lattice parameter is reduced and the $\beta^{o}$ angle is increased at the $Na_{0.19}TiO_2$ composition. This result is consistent with XRD data[37] reporting broadening of the peaks for increasing Na content above x=0.17. In Figure 5.4a the lowest energy $Na_{0.25}TiO_2$ monoclinic phase is presented.

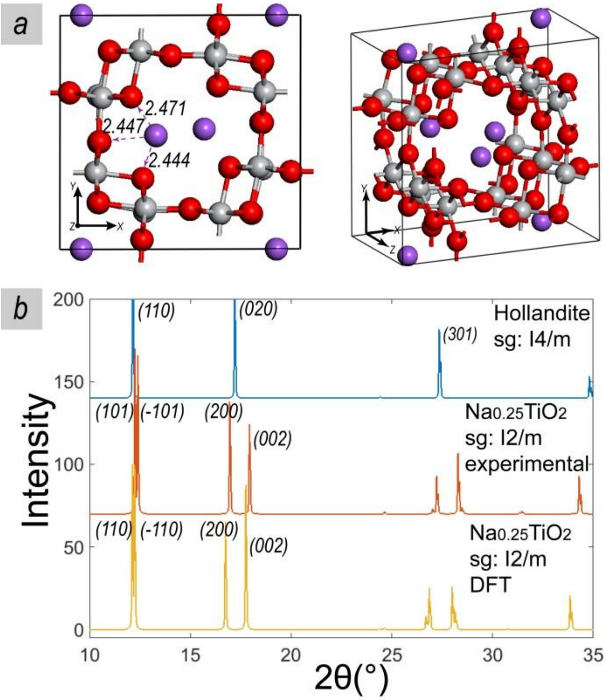

**Figure 5.4: a)** $Na_{0.25}TiO_2$ as predicted by DFT, corresponding to a specific capacity of 85 mAh/g of specific capacity, where red balls represent O atoms, grey balls Ti and purple balls represent Na ions. The arrows indicate the distance in Angstroms between Na ions and nearest oxygens atoms at the wall of the tunnel. **b)** From top to bottom, the calculated XRD pattern of the empty hollandite structure predicted by DFT, the calculated pattern based on the experimental XRD lattice parameters of $Na_{0.25}TiO_2$[37] and the calculated XRD pattern of the DFT predicted $Na_{0.25}TiO_2$ phase.

## 5.5 Formation Enthalpies and the Voltage Profile

To study the thermodynamic stability of the $Na_xTiO_2$ intercalation system the formation enthalpies of 72 symmetrically inequivalent configurations are plotted in Figure 5.5a according to[70-72]:

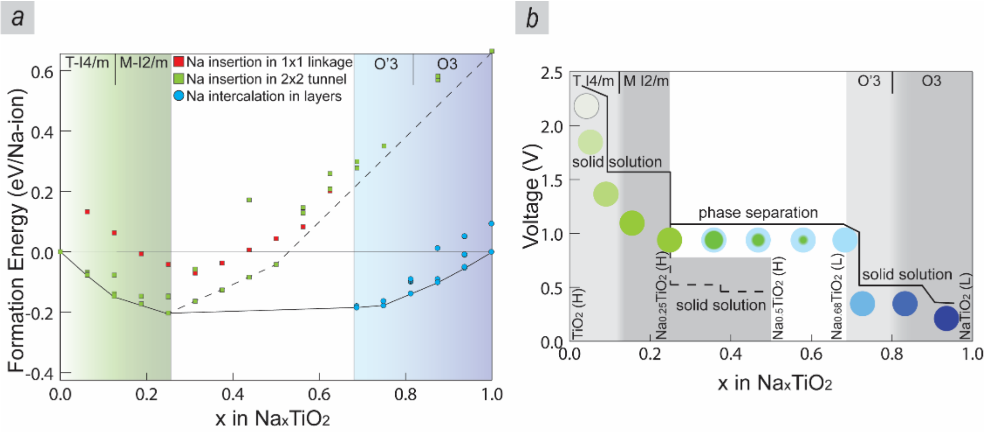

**Figure 5.5: a)** Formation energies and convex hull upon Na insertion in the $TiO_2$ (H) structure. Squares refer to configurations were the hollandite skeleton is preserved and they are coloured green for Na insertion in the 2x2 channels or red for at least one Na inserted in the 1x1 rutile linkage. Blue circles correspond to the layered structure, the solid line represents the convex hull and the dashed line represents the convex hull without considering the monoclinic to layered phase transition. **b)** Voltage profile for Na-ion insertion into TiO2 (H) resulting from the DFT energy calculations. At approximately 1 volt the constant voltage indicates a first order phase transition leading to the layered $Na_{0.68}TiO_2$ phase. The dashed line indicates the voltage when the hollandite structure is maintained, as it appears in practice. (H) indicates the hollandite structure (either tetragonal or monoclinic) and (L) indicates the layered structure, T-I4/m stands for tetragonal and M-I2/m for the monoclinic lattice.

$$E_{form} = E - xE_{NaTiO_2} - (1 - x)E_{TiO_2}$$

The formation enthalpy, $E_{form}$, reflects the relative stability of each configuration with respect to phase separation into a fraction x of $NaTiO_2$ and a fraction $(1 - x)$ of $TiO_2$. E is the energy of a specific arrangement at concentration x, $E_{NaTiO_2}$ is the energy of the titanium structure while accommodating the maximum amount of Na ions (in this case the maximum reference phase responds to a 1 to 1 Na/Ti ratio) and $E_{TiO_2}$ is the total energy of the empty titanium dioxide host. Thereby, negative formation energies, energies below 0 eV, are thermodynamically favourable compared to the reference phases and thus are likely to occur. The convex hull is constructed by the line connecting the most stable structures at each composition giving insight in the relative stability of intermediate phases and the structural evolution upon Na-ion insertion.

All intermediate compositions up to $Na_{0.25}TiO_2$ (Figure 5.5a) are at or very near the convex hull predicting at room temperature a solid solution transformation from the tetragonal to monoclinic phase. The reduction in symmetry is a consequence of the gradual change in the interaxial lattice angle $\beta$ initially at $90^o$ for the tetragonal starting phase. On atomic scale this is initiated by the shift in Na-ion occupancy from the 2a to the 8h position upon sodiation. Several electrode materials lithiate/sodiate either partially or completely via a solid solution mechanism leading to a gradual change in the unit cell edge length. To the best of our knowledge, Na-ion insertion in $TiO_2$ hollandite is the first where a solid solution reaction results in a change in symmetry through the gradual change in interaxial lattice angle, although this is conceptually not different from a gradual change in the unit cell edge length. This result is in agreement with experimental observations by XRD[37] where the monoclinic phase is starting to be distinguished from $Na_{0.17}TiO_2$ until the completely monoclinic $Na_{0.25}TiO_2$ composition resulting in a biphasic region of unreacted and reacting phases. Note that the absence of a voltage plateau in the voltage profile also suggests a solid solution mechanism. The difference in formation energy between configurations with Na in the 2x2 channel and configurations with at least one Na in the 1x1 rutile channel appears constant (210meV) with respect to the Na insertion into the 2x2 channels in the tetragonal range ($0<x<0.125$) and lower but still constant (165meV) in the monoclinic regime ($0.125<x<0.25$).

Interestingly, further sodiation reveals a two phase reaction mechanism between the monoclinic $Na_{0.25}TiO_2$ and $Na_{0.68}TiO_2$ structures. During this phase transition the Hollandite skeleton changes completely towards a layered structure that is recognised to be the O’3 layered $Na_{0.68}TiO_2$ phase, indexed by the C2/m symmetry[73]. Formation of the layered structure requires the Na-ions to enter the rutile linkage tunnels along the z-direction. Due to the large distortions caused by this the Ti-O bonds will break, opening the lattice to form Ti slabs as shown in Figures 5.6a and b. This transformation appears irreversible because removal of the Na-ions from the layered structure does not result in the original hollandite lattice. Further Na-ion insertion of the layered $Na_{0.68}TiO_2$ structure proceeds through a solid solution reaction up to the fully sodiated structure (O3-$NaTiO_2$) which was recently reported as a promising anode for Na-ion batteries[25]. Thereby $TiO_2$ (H) can be fully sodiated to the theoretical maximum capacity of 335 mAh/g offered by the $Ti^{+4}/Ti^{+3}$ redox couple. Clearly, the irreversibility of this process prevents accessing this capacity reversibly, but Na-ion insertion of $TiO_2$ (H) may offer a novel route towards the layered $NaTiO_2$ material. The characteristics of the O3 layered $NaTiO_2$ predicted by DFT will be discussed in the next section

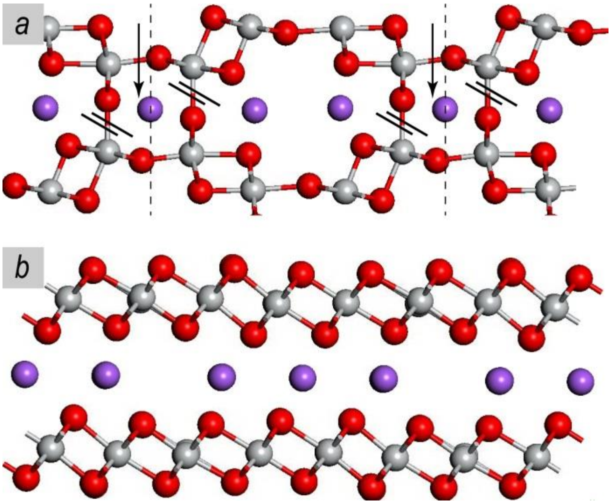

**Figure 5.6: a)** Na-ion configuration before relaxations ($Na_{0.68}TiO_2$) with Na-ions inserted in the rutile-linkage tunnel, as indicated by the black arrows. The black lines indicate the bonds that are broken by this configurations resulting in the layered structure. **b)** The layered $Na_{0.68}TiO_2$ structure. In both figures the red spheres represent O atoms, grey Ti atoms and purple the Na-ions

The predicted phase transition towards the O3 layered $Na_xTiO_2$ structure appears not to occur during electrochemical Na-ion insertion[37] down to 0.2 V, although the formation energies in Figure 5.5a suggest it is energetically favourable to form at high Na-concentrations. This may be explained by the large energy required to insert Na-ions in the rutile linkage channels, as indicated by Figure 5.5a, which is necessary to break the Ti-O bonds, and additionally by a large kinetic energy barrier. The alternative is that the metastable hollandite structure is retained, as indicated by the dashed line in Figure 5.5. Perez-Florez et al.[37] reports a continuous evolution of the lattice parameters in the 0.75 to 0.5V voltage range suggesting a solid solution reaction upon Na-ion insertion in the monoclinic phase, although no conclusive evidence for this was shown down to 0.2V. It was assumed that Na-ion insertion above x=0.25 is restricted due to the introduction of short Na-Na distances[37]. The present formation enthalpies predict that Na-ion insertion should be possible at least up to x=0.5 in $Na_xTiO_2$ (Figure 5.5a) suggesting that the

Na-ion kinetics, which will be addressed below, restricts the capacity of the hollandite $TiO_2$ structure. In the monoclinic solid solution regime the calculations predict a total volume change of 2.4% from the $TiO_2$ towards the $Na_{0.5}TiO_2$ composition. This is larger compared to the 1% volume change from the $TiO_2$ towards the $Na_{0.25}TiO_2$ composition, but still relatively small suggesting that mechanical failure will not restrict the cycle life. The present calculations predict that Na-ion insertion proceeds through a solid solution reaction in the concentration range $0.25<x<0.5$ during which the monoclinic b-lattice parameter continuously decreases and the $\beta^o$ angle increases in agreement with the observation by Perez-Florez et al.[37]. The final monoclinic $Na_{0.5}TiO_2$ phase, is characterized by the I2/m symmetry with lattice parameters $a = 11.14Å$, $b = 2.97Å$, $c = 9.79Å$ and an angle $\beta = 90.6^o$. In this configuration, Na-ions reside in the 8h positions that are empty in the dilute zig-zag configuration shown in Figure 5.3b. The presence of the extra Na-ions leads to shorter bonding to the oxygen atoms in the tunnel wall (2.281, 2.284, 2.349 Å) compared to the distances in the $Na_{0.25}TiO2$ phase.

Based on the formation energies in Figure 5.5 the voltage profile at 0 K can be calculated. The potential difference between the positive and negative electrodes is determined by the difference in $Na/Na^+$ potential according to the Nernst equation[71, 74]:

$$V(x) = -\frac{\mu_{Na}(x) - \mu_{Na}^{ref}(x)}{e}$$

The chemical potential is per definition the derivative of the free energy with respect to the ion concentration which, disregarding the entropy, leads to the following expression[74]:

$$\overline{V}(x) = -\frac{E_{Na_xTiO_2} - xE_{Na} - E_{TiO_2}}{xe}$$

where $\overline{V}$ is the average intercalation voltage and the energies represent total energies of the indicated compositions. The voltage profile is depicted in Figure 5.5b. As discussed for the formation energies in Figure 5.5a a solid solution reaction is expected between $TiO_2$ (H) and $Na_{0.25}TiO_2$ (H). However, the voltage plateaus in Figure 5a appear at 0 K because the formation energies of $Na_{0.063}TiO_2$ (H) and $Na_{0.19}TiO_2$ (H) are located only a few meV above the convex hull. Following the most stable convex hull in Figure 5.5a this is followed by a first order phase transition to the layered $Na_{0.68}TiO_2$ (L) structure. However, as discussed above, in practice the hollandite structure appears to be maintained following the dashed voltage curve shown in Figure 5.5b.

## 5.6 Towards the O3 Layered $NaTiO_2$ Structure

The DFT calculations predict that sodiation of the hollandite structure up to the $NaTiO_2$ composition results in the layered O3 type $NaTiO_2$ phase, characterized by the hexagonal R-3m group (note that an equivalent definition in the monoclinic phase C2/m is also possible). Na-ions in the O3 lattice are octahedral coordinated with oxygen atoms while the transition metal (Ti) stacking has a repetition of three in the perpendicular direction to Na layers (c-axis).[25, 75] Table 5.4 compares the structure of the predicted layered $NaTiO_2$ composition with that reported experimentally[25]. DFT significantly overestimated the c-lattice parameter (by 0.3 Å). In the equivalent C2/m definition this translates into a significantly smaller $\beta^o$ angle, $97^o$ compared to $107.9^o$ reported experimentally[25].

**Table 5.4:** Comparison between experimental and calculation results for the O3 layered $NaTiO_2$ structure (unit cell)

| Method | Experiment Value[25] | Experimental Values Relaxed with DFT | Predicted Values upon Sodiating with DFT |
|---|---|---|---|
| s.g. | R-3M | R-3M | R-3M |
| a(Å) | 3.037(1) | 2.991 | 2.993 |
| b(Å) | 3.037(1) | 2.991 | 2.993 |
| c(Å) | 16.260(2) | 16.569 | 16.5713 |
| γ(°) | 120 | 120 | 120 |
| ΔE(meV) | - | 0 | +15 |

To investigate the properties of the layered structure, the configurations in the $0.5<x<1$ compositional range were calculated by DFT (note that the energies of the layered $0.68<x<1$ compositions were already shown in Figure 5.5). The resulting convex hull is presented in Figure 5.7a and the voltage profile in Figure 5.7b. The convex hull depicts a solid solution intercalation mechanism throughout the sodiation range ($0.5<x<1$) as the lowest energy configurations are on, or slightly above (<<25meV) the convex hull. The DFT calculations predict that the

O3 to O’3 transition occurs at $Na_{0.81}TiO_2$ in good agreement with the experimental observation by Wu et al. [25]. XRD patterns were calculated based on the most stable configurations (located on the convex hull in Figure 5.7a). The results are shown in Figure 5.7c focussing on small diffraction angles in order to distinguish the O3 and O’3 phases. Volume changes calculated in the layered regime are almost negligible (0.8%) prolonging excellent cycle-life, in agreement with the 0.4% volume change determined experimentally[25]. The calculated voltage profile is in agreement with the experimental one[25] (Figure 5.7d), predicting slightly lower voltages, an underestimation which is common when utilizing the GGA method[76].

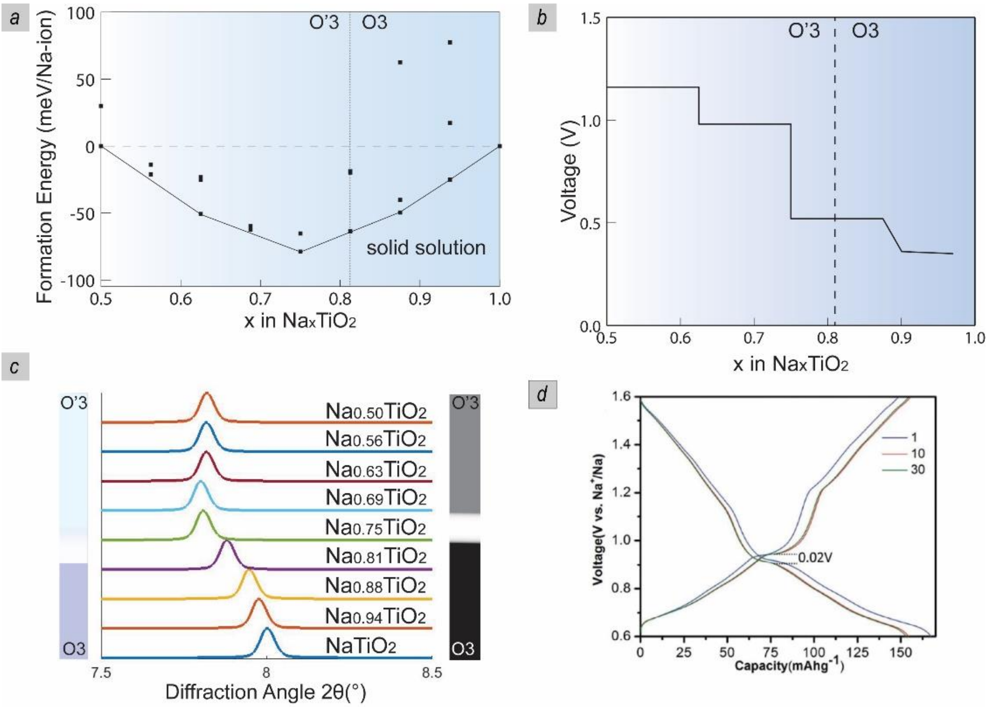

**Figure 5.7: a)** Convex hull based on DFT calculations of the layered $Na_xTiO_2$ structure for $0.5<x<1.0$. **b)** Voltage profile of Na intercalation in the O3/O’3 layered $Na_xTiO_2$. **c)** Calculated powder diffraction data from the lowest energy configurations at each concentration step. The left bar indicates the predicted O3 and O’3 regimes and the bar on the right side the experimentally found O3 and O’3 regimes based on in-situ XRD[25]. **d)** Experimental voltage profile reproduced from ref 25 with permission from The Royal Society of Chemistry.

## 5.7 Na-Ion Diffusion

To predict the Na-ion diffusion mechanism in the hollandite and layered titanate structures, molecular dynamic (MD) calculations were performed at 600 K for total simulation times ranging from 190 to 400 ps. In addition, solid state nudge elastic band methods (NEB, ss-NEB[50]) were used to predict the energy barriers for diffusion. In the hollandite structure the diffusion pathway is one dimensional through the 2x2 tunnels parallel to the z-axis. An overview of possible jumps is presented in Figure 5.8.

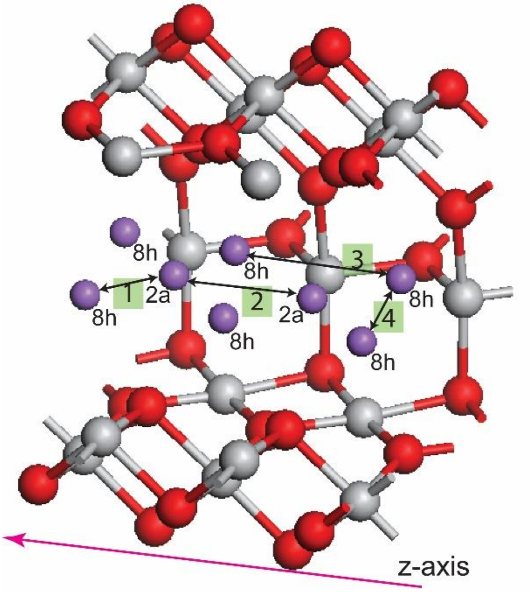

**Figure 5.8:** Possible jumps inside the 2x2 hollandite tunnels where the 1,2 and 3 jumps can contribute to macroscopic diffusion and jump number 4 represents a co-planar local jump not contributing to the macroscopic diffusion.

Within the dilute concentration range (0<x<0.125), where the structure is tetragonal, there is a single Na-ion per pair of adjacent 2x2 hollandite tunnels along the z direction. This creates a large variety of possible hops due to the large available space offered by the 2x2 tunnel. Our results depict extremely high jump rates along the z-direction either by a direct 2a-2a jump passing through the intermediate 2b position (2a-2b-2a) or by a curved hop passing through an intermediate 8h position (2a-8h-2a). The Na-ion density obtained from the MD simulation performed in the dilute limit, shown in Figure 5.9a - b, demonstrates that the Na-ion is highly mobile as it appears broadly delocalized around the lowest energy 2a position. It partially occupies the less favourable 4e position (see Table 5.2) during the majority of the simulation time (>70%). The maximum Na-ion density is predicted to be located at the lowest energy 2a site where it is located approximately 20% of the total simulation time. Fluctuations around the 2a positions indicate that the Na-ion jumps back and forth towards the coplanar 8h' position. Consistent with the thermodynamic analysis, the 8h' site is energetically unfavourable (see Table 5.2) forcing the Na-ion back to the 2a position during the calculation on average within 6 femto seconds. Even larger oscillations occur near the 4e positions, during the transition between two adjacent 2a sites, building up momentum to initiate a subsequent transitions. Figure 5.9a depicts a large number of these curved Na-ion pathways near the 4e position and Figure 5.9c illustrates a schematic representation of the oscillations. By counting the number of hops between the respective interstitial sites during the 200 ps MD-simulation the energy barriers can be predicted, see Methods sections, which appear in excellent agreement with the ss-NEB results shown in Table 5.5. However, a significantly different 2a-8h energy barrier is found compared to NEB without lattice parameter relaxations. MD simulations take into account the lattice dynamics, which are also better captured by the ss-NEB methods[50], indicating the importance of the lattice dynamics for the Na-ion diffusion in the hollandite structure. In addition, the 2a-8h transitions appear to activate the tetragonal to monoclinic phase transition, which is accompanied by a change in the lattice parameter, a process that is also better captured by ss-NEB calculations[50].

The Molecular Dynamic simulations also reveal that a 2a-8h jump may result in occupation of the 8h site for a few pico seconds, indicating this site to be metastable Remaining in the x-y plane the Na-ion is shown to easily jump towards the coplanar 8h position (8h-2b-8h) before it relaxes towards the lower energy 2a site. In addition, many transitions go through multiple sites where the most frequently occurring are the 2a-8h-2b-2a, 2a-2b-8h-2a and 2a-8h'-8h-8h'-2a site sequences. This can be attributed to the low energy barrier and small jump distance for coplanar hops (8h'-2a , 2b-8h) as illustrated by Table 5.5.

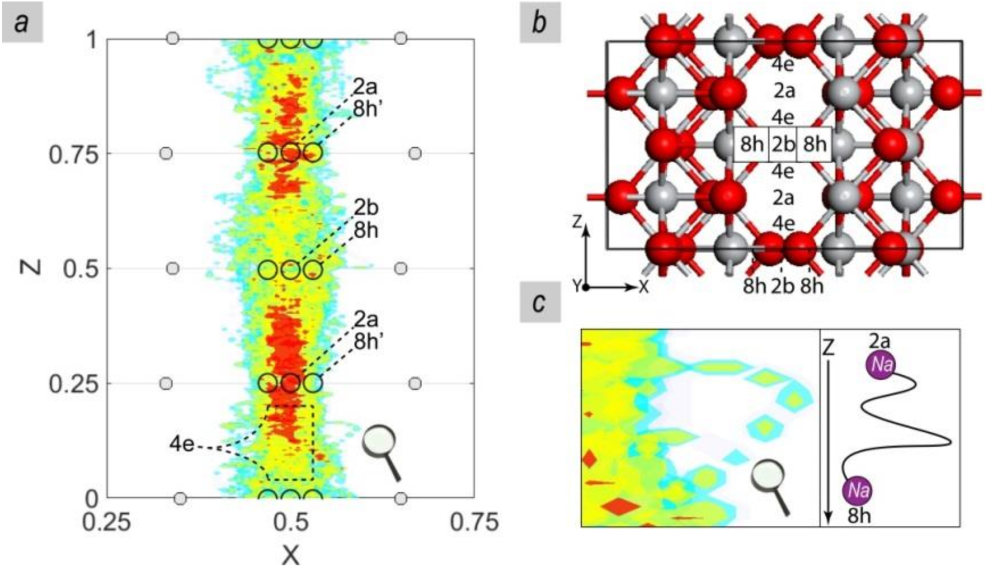

**Figure 5.9: a)** Na-ion density plot in the xz-plane integrated over the 200 ps molecular dynamic calculation for the dilute limit $Na_{0.06}TiO_2$ (only one Na-ion in the supercell). From red to blue represents the decreasing Na-ion density. The grey dots represent the nearest Ti atoms (left and right) of the tunnel. The various interstitial sites are indicated. In order to make the 2a and 2b positions in the xz plane visible the 8h' and 8h positions that are perpendicular to the z-axis (and consequently hiding the 2a and 2b positions) are not indicated. **b)** The xz-plane in the supercell for comparison with Figure 9a. **c)** Zoom in to one of the Na-ion paths caused by oscillations near the 4e position and schematic representation of the oscillating mechanism that dominates the 2a-8h hop.

The Na-ion kinetics in the monoclinic concentration range (0.125<x<0.25) are very similar to that in the dilute limit. Adjacent tunnels with only one Na-ion behave identical with respect the dilute limit analysis presented above. Upon the introduction of a second Na-ion per adjacent tunnels, Na migration from the 2a site to the 8h site is initiated enabling the observed phase transition (from tetragonal to monoclinic), a transition easily activated according to our calculations.

However, in the $Na_{0.25}TiO_2$ (H) phase, where the zig-zag occupancy of the 8h sites appears most stable, the Na-ion diffusion changes drastically. Figure 5.10a, b illustrates the Na-ion density plot resulting from the MD simulation of the respective phase for 400 ps at 600 K. In contrast to the connected Na-ion density between adjacent 2x2 tunnels at the dilute limit, the Na-ion densities around the 8h positions appears at this composition almost isolated, indicating poor mobility along the diffusion coordinate. Within the 400 ps simulation time only a couple of forward transitions in the z-direction occurred during the simulation, depicted by the thin light-green paths in Figure 5.10a, b. Apparently, the energy barrier for diffusion is too large to be probed quantitatively by the MD simulations due to the limited simulation time. A larger number of transitions are predicted to occur between the co-planar 8h sites, however, these reflect local jumps that do not contribute to the macroscopic diffusion. The MD simulations reveal that the local co-planar 8h-8h jumps are highly correlated with the local co-planar 8h-8h jumps in the adjacent 2x2 tunnel. The Na-ion hops occur simultaneously for both adjacent Na-ions thereby maintaining the lowest energy zig-zag configuration, most likely driven by columbic repulsions to maximize the distance between the Na-ions. This mechanism is depicted in Figure 5.10d, e. Another correlated reaction mechanism, qualitatively captured by the MD simulations, governs the forward jump depicted in Figure 5.10c. This correlated jump is initiated in the middle of a 8h-8h coplanar hop where additional Na-ion fluctuations lead to Coulombic interactions that result in Na-ion migration along the z direction and thus macroscopic diffusion. In addition, a 200 ps molecular dynamic simulation for the $Na_{0.31}TiO_2$ (H) phase was performed where a third Na-ion is introduced per pair of adjacent 2x2 tunnels. The MD simulations results in no macroscopic and co-planar diffusion as the interactions between Na-ions dominate, resulting in even more localized Na-ion densities (not shown) compared to that in Figure 5.10. In this configuration the 8h-8h forward jump presented in Figure 5.8 appears to contribute to macroscopic diffusion. At this concentration the NEB calculations did not converge, most likely due to the close coexistence of Na-ions in the tunnel. Analysis beyond the dilute limit has been shown before to be less trivial as the significant Na concentration causes interactions between the charged carriers[77]. Nevertheless, the 8h-8h forward jump was calculated after removing all but one hopping Na-ion in the lattice parameters of the $Na_{0.31}TiO_2$ phase revealing an extremely high barrier of 0.68 eV, in qualitative agreement with the present MD results that indicate poor Na-ion dynamics.

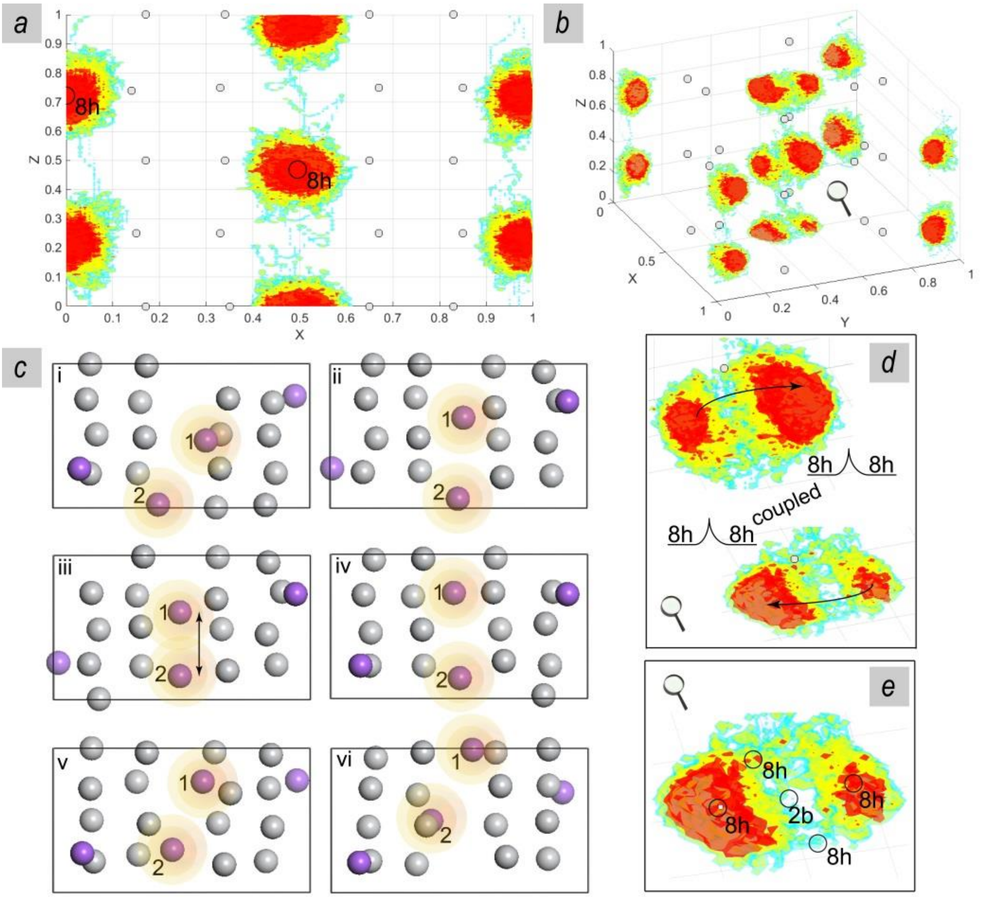

**Figure 5.10: a), b)** 3D Na-ion density plot integrated over the 400 ps of molecular dynamic calculation of $Na_{0.25}TiO_2$ (4 Na-ions in the supercell). **c)** Time lapse in the xz plane illustrating a simultaneous forward jump. **d)** Transition mechanism showing the correlated Na-ion 8h-8h coplanar hops thereby maintaining the preferable Na-ion zig-zag configuration, presented in the same plane as Figure 10b. **e)** Zoom of the Na-ion density to indicate the relevant interstitial positions, the 2b and 8h positions exist in the xy-plane that is perpendicular to the z-axis where macroscopic diffusion occurs.

The Na-ion kinetics in the layered O3/O’3 $Na_xTiO_2$ has already been studied in detail by Wu et al.[25] who applied the nudge elastic band method, utilizing the di-vacancy hopping mechanism[78]. The resulted barriers were reported to be smaller than 0.22 eV, for both the O3 and O’3 layered configurations indicating exceptionally good kinetics[25]. This result is in contrast to previous reports indicating a large barrier of 0.75 eV[30]. For comparison, we performed an 190 ps MD simulation of the O’3 $Na_{0.75}TiO_2$ phase at 600 K. The calculated activation energy (see methods) for Na-ion migration was found to be 0.28 eV in good agreement with the results reported by Wu et al.[25]. The di-vacancy hopping mechanism, that is considered dominant regarding Na and Li-ion hopping in O3 layers[25, 78, 79], dictates that the Na-ion diffusion occurs through an adjacent tetrahedral site that acts as a local minimum. This mechanism was clearly observed during the MD simulation as shown in Figure 5.11.

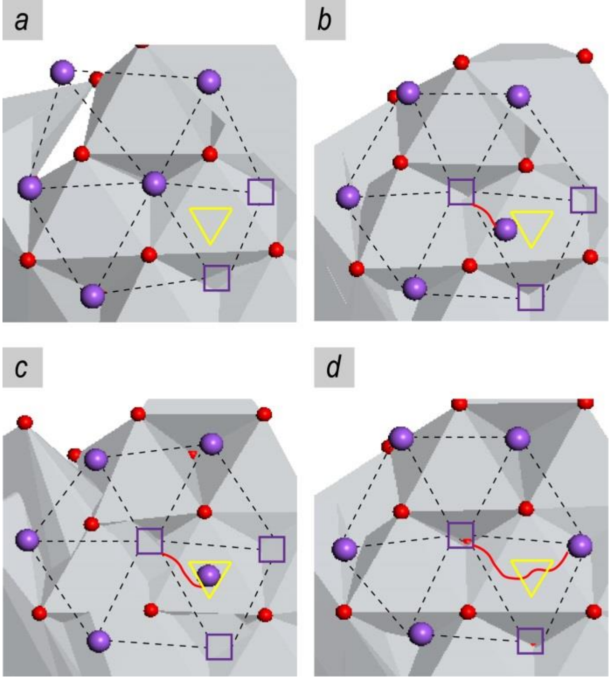

**Figure 5.11:** Divacancy hopping mechanism as seen perpendicularly to the plane formed by Na-ions, the Na-ion passes through a tetrahedral site. The sequence is completed within 1.2 ps.

Based on the activation energy calculations, an estimate of the diffusion coefficient was calculated using the random-walk atomistic model and, when applicable, the mean square displacement (MSD) obtained from the molecular dynamic calculations (see methods section). The diffusion coefficient at room temperature ranges from $D_{TST} = 9.65 \cdot 10^{-6}$ to $4.2 \cdot 10^{-9} cm^2/sec$ at the dilute limit decreasing to $D_{TST} = 3.8 \cdot 10^{-15} cm^2/sec$ at higher Na concentrations (x=0.31), indicating that Na-ion insertion beyond $Na_{0.25}TiO_2$ (H) is difficult. In addition, the presence of defects in the 1D diffusion tunnels can be expected to lower these diffusion coefficients, motivating nano-structuring to enable usage of the thermodynamically feasible $Na_{0.5}TiO_2$ phase.

**Table 5.5:** Energy barriers for Na diffusion calculated by NEB, ss-NEB and the MD-simulations. Numbers in path illustration indicate the paths presented in Figure 5.8.

| x in $Na_xTiO2$ | Path | Path | Method | $E_a$ (eV) | Distance(Å) |
|---|---|---|---|---|---|
| x=0.03 (H) | 2 | 2a-(2b)-2a | NEB | 0.32 | 2.98 |
| x=0.03 (H) | 2 | 2a-(2b)-2a | SS-NEB | 0.16 | 2.98 |
| x=0.06 (H) | 2 | 2a-(2b)-2a | MD | 0.15 | 2.98 |
| x=0.03 (H) | 1 | 2a-8h | NEB | 0.72 | 1.68 |
| x=0.03 (H) | 1 | 2a-8h | SS-NEB | 0.12 | 1.68 |
| x=0.06 (H) | 1 | 2a-8h | MD | 0.19 | 1.68 |
| x=0.06 (H) | 4 | 8h-8h (in plane) | MD | 0.26 | 1.325/1.874 |
| x=0.06 (H) | - | 2b-8h (in plane) | MD | 0.19 | 0.937 |
| x=0.06 (H) | - | 8h-2b (in plane) | MD | 0.19 | 0.937 |
| x=0.25 (H) | coupled | 8h-8h (in plane) | MD | 0.15 | 1.325/1.874 |
| x=0.25 (H) | - | 8h-2b (in plane) | MD | 0.23 | 0.937 |
| x=0.25 (H) | coupled | 8h-8h forward | MD | ∞ | 2.97 |
| x=0.31 (H) | 3 | 8h-8h forward | NEB | 0.68 | 2.97 |
| x=0.31 (H) | coupled | 8h-8h forward | MD | ∞ | 2.97 |
| x=0.75 (L) | - | divacancy | MD | 0.28 | 3.10 |

For the layered structure we obtained $D_{MSD} = 5.7 \cdot 10^{-9} cm^2/sec$, based on the MSD at room temperature and $D_{TST} = 6.3 \cdot 10^{-8} cm^2/sec$ based on transitional state theory. The second value is significantly larger because it takes into account back and forth jumps that do not contribute in macroscopic diffusion. This large diffusion coefficient is in good agreement with rate capability experiments[25] underlining that the layered structure is a promising anode for Na-ion batteries.

## 5.8 Conclusive Remarks

The present DFT study of the thermodynamic and kinetic properties of Na-ion insertion in Hollandite $TiO_2$ brings forward a detailed understanding of the phase transition behaviour and Na-ion kinetics showing good agreement with most of the experimental observations. Initially, Na-ion insertion leads to a solid solution reaction causing a monoclinic symmetry reduction (I4/m to I2/m) towards the $Na_{0.25}TiO_2$ composition. During this transformation the structural changes are very small suggesting a promising cycle life. In the dilute limit, low energy barriers are predicted suggesting fast Na-ion diffusion at the early stages of insertion. At the $Na_{0.25}TiO_2$ composition and beyond, the Na-ion diffusion drops dramatically, giving a rational for the experimental observation that Na-ion insertion does not proceed beyond $Na_{0.25}TiO_2$ phase, although the DFT predicts that the $Na_{0.5}TiO_2$ composition can be achieved at 0.4 V vs $Na/Na^+$.

Detailed consideration of the Na-ion kinetics from the molecular dynamic (MD) simulations shows that large space of the 2x2 tunnel in the Hollandite structure results in complex atomic transitions that appear responsible for the high Na-ion mobility at the early stages of Na-ion insertion. MD simulations beyond the dilute limit, reveal a highly correlated diffusion mechanisms within the 2x2 tunnel, most likely driven by the strong columbic interactions between the Na-ions that lowers the number of successful transitions. These results are anticipated to be of general importance to similar structured materials such as $MnO_2$ hollandite.

At larger Na-ion concentrations, a first-order phase transformation is predicted towards the O’3-$Na_{0.63}$TiO2 endmember structure. Further Na-ion insertion initiates a solid solution reaction that results in the layered O3-$NaTiO_2$ material, a promising anode candidate with excellent crystallinity and large capacity reported previously. The full thermodynamic path ($TiO_2$ (H) to O3-$NaTiO_2$), however, is not reversible but may be considered an alternative preparation route towards the layered structure. So far the layered O3-$NaTiO_2$ material is being prepared via a solid state reaction to reduce anatase - $TiO_2$[25, 73, 80] requiring high temperatures up to $1000^0$C in the presence of Na-metal under an Argon flow for several hours . Although the preparation of hollandite is also not facile, as it requires mixing of $K_2CO_3$ and anatase $TiO_2$ for 8 hours followed by acid treatment to remove K at low temperatures for 10 hours[37], using $TiO_2$ (H) as a starting material might present an opportunity for a preparation route towards the layered material requiring lower annealing temperatures.

Within the layered $Na_xTiO_2$ regime a solid solution insertion mechanism transforms the O3 layered $Na_xTiO_2$ structure for compositions $1<x<0.81$ to the O’3 layered $Na_xTiO_2$ structure for compositions $0.81<x<0.5$, in good agreement with experiments. For the O’3 $Na_{0.75}TiO_2$ phase the MD simulation capture the predicted divacancy hopping mechanism, calculating a small energy barrier (0.27 eV) that suggests excellent Na-ion kinetics.

# References

**1**. Kundu, D.; Talaie, E.; Duffort, V.; Nazar, L. F. The Emerging Chemistry of Sodium Ion Batteries for Electrochemical Energy Storage. *Angew. Chem. Int. Ed. Engl*. 2015, 54, 3431-3448.

**2**. Kim, S. W.; Seo, D. H.; Ma, X. H.; Ceder, G.; Kang, K. Electrode Materials for Rechargeable Sodium-Ion Batteries: Potential Alternatives to Current Lithium-Ion Batteries. *Adv. Energy Mater*. 2012, 2, 710-721.

**3**. Palomares, V.; Casas-Cabanas, M.; Castillo-Martinez, E.; Han, M. H.; Rojo, T. Update on Na-based battery materials. A growing research path. *Energy Environ. Sci*. 2013, 6, 2312-2337.

**4**. Kubota, K.; Komaba, S. Review-Practical Issues and Future Perspective for Na-Ion Batteries. *J. Electrochem. Soc*. 2015, 162, A2538-A2550.

**5**. Sawicki, M.; Shaw, L. L. Advances and challenges of sodium ion batteries as post lithium ion batteries. *RSC Adv*. 2015, 5, 53129-53154.

**6**. Asher, R. C. A Lamellar Compound of Sodium and Graphite. *J. Inorg. Nucl. Chem*. 1959, 10, 238.

**7**. Stevens, D. A.; Dahn, J. R. The mechanisms of lithium and sodium insertion in carbon materials. *J. Electrochem. Soc*. 2001, 148, A803-A811.

**8**. Luo, W.; Bommier, C.; Jian, Z. L.; Li, X.; Carter, R.; Vail, S.; Lu, Y. H.; Lee, J. J.; Ji, X. L. Low-Surface-Area Hard Carbon Anode for Na-Ion Batteries via Graphene Oxide as a Dehydration Agent. *ACS Appl. Mater. Inter*. 2015, 7, 2626-2631.

**9**. Alcantara, R.; Mateos, J. M. J.; Tirado, J. L. Negative electrodes for lithium and sodium-ion batteries obtained by heat-treatment of petroleum cokes below 1000 degrees C. *J. Electrochem. Soc*. 2002, 149, A201-A205.

**10**. Jow, T. R.; Shacklette, L. W.; Maxfield, M.; Vernick, D. The Role of Conductive Polymers in Alkali-Metal Secondary Electrodes. *J. Electrochem. Soc*. 1987, 134, 1730-1733.

**11**. Didier, C.; Guignard, M.; Denage, C.; Szajwaj, O.; Ito, S.; Saadoune, I.; Darriet, J.; Delmas, C. Electrochemical Na-Deintercalation from $NaVO_2$. *Electrochem. Solid St*. 2011, 14, A75-A78.

**12**. Kim, H.; Kim, D. Y.; Kim, Y.; Lee, S. S.; Park, K. Na Insertion Mechanisms in Vanadium Oxide Nanotubes for Na-Ion Batteries. *ACS Appl. Mater. Inter.* 2015, 7, 1477-1485.

**13**. Deng, J. Q.; Lu, Z. G.; Belharouak, I.; Amine, K.; Chung, C. Y. Preparation and electrochemical properties of $Li_4Ti_5O_{12}$ thin film electrodes by pulsed laser deposition. *J. Power Sources* 2009, 193, 816-821.

**14**. Kavan, L.; Prochazka, J.; Spitler, T. M.; Kalbac, M.; Zukalova, M. T.; Drezen, T.; Gratzel, M. Li insertion into $Li_4Ti_5O_{12}$ (Spinel) - Charge capability vs. particle size in thin-film electrodes. *J. Electrochem. Soc.* 2003, 150, A1000-A1007.

**15**. Ohzuku, T.; Ueda, A.; Yamamoto, N. Zero-Strain Insertion Material of $Li[Li_{1/3}Ti_{5/3}]O_4$ for Rechargeable Lithium Cells. *J. Electrochem. Soc.* 1995, 142, 1431-1435.

**16**. Colbow, K. M.; Dahn, J. R.; Haering, R. R. Structure and Electrochemistry of the Spinel Oxides $LiTi_2O_4$ and $Li_{4/3}Ti_{5/3}O_4$. *J. Power Sources* 1989, 26, 397-402.

**17**. Wagemaker, M.; Borghols, W. J. H.; van Eck, E. R. H.; Kentgens, A. P. M.; Kearley, G. L.; Mulder, F. M. The influence of size on phase morphology and Li-ion mobility in nanosized lithiated anatase $TiO_2$. *Chem. Eur. J.* 2007, 13, 2023-2028.

**18**. Koudriachova, M. V.; Harrison, N. M.; de Leeuw, S. W. Open circuit voltage profile for Li-intercalation in rutile and anatase from first principles. Solid State Ionics 2002, 152, 189-194.

**19**. Cava, R. J.; Murphy, D. W.; Zahurak, S.; Santoro, A.; Roth, R. S. The Crystal-Structures of the Lithium-Inserted Metal-Oxides $Li_{0.5}TiO_2$ Anatase, $LiTi_2O_4$ Spinel, and $Li_2Ti_2O_4$. *J. Solid State Chem.* 1984, 53, 64-75.

**20**. Rai, A. K.; Anh, L. T.; Gim, J.; Mathew, V.; Kang, J.; Paul, B. J.; Song, J.; Kim, J. Simple synthesis and particle size effects of $TiO_2$ nanoparticle anodes for rechargeable lithium ion batteries. *Electrochim. Acta* 2013, 90, 112-118.

**21**. Pfanzelt, M.; Kubiak, P.; Fleischhammer, M.; Wohlfahrt-Mehrens, M. TiO2 rutile-An alternative anode material for safe lithium-ion batteries. *J. Power Sources* 2011, 196, 6815-6821.

**22**. Chiba, K.; Kijima, N.; Takahashi, Y.; Idemoto, Y.; Akimoto, J. Synthesis, structure, and electrochemical Li-ion intercalation properties of $Li_2Ti_3O_7$ with $Na_2Ti_3O_7$-type layered structure. *Solid State Ion.* 2008, 178, 1725-1730.

**23**. Aravindan, V.; Lee, Y. S.; Yazami, R.; Madhavi, S. $TiO_2$ polymorphs in 'rocking-chair' Li-ion batteries. *Mater. Today* 2015, 18, 345-351.

**24**. Wu, L. M.; Bresser, D.; Buchholz, D.; Giffin, G. A.; Castro, C. R.; Ochel, A.; Passerini, S. Unfolding the Mechanism of Sodium Insertion in Anatase $TiO_2$ Nanoparticles. *Adv. Energy Mater.* 2015, 5, 1401142.

**25**. Wu, D.; Li, X.; Xu, B.; Twu, N.; Liu, L.; Ceder, G. NaTiO2: a layered anode material for sodium-ion batteries. *Energy. Environ. Sci.* 2015, *8*, 195-202.

**26**. Wu, L. M.; Buchholz, D.; Bresser, D.; Chagas, L. G.; Passerini, S. Anatase $TiO_2$ nanoparticles for high power sodium-ion anodes. *J. Power Sources* 2014, 251, 379-385.

**27**. Zhao, L.; Pan, H. L.; Hu, Y. S.; Li, H.; Chen, L. Q. Spinel lithium titanate ($Li_4Ti_5O_{12}$) as novel anode material for room-temperature sodium-ion battery. *Chinese Phys. B* 2012, *21*, 079901.

**28**. Sun, Y.; Zhao, L.; Pan, H. L.; Lu, X.; Gu, L.; Hu, Y. S.; Li, H.; Armand, M.; Ikuhara, Y.; Chen, L. Q.; Huang, X. J. Direct atomic-scale confirmation of three-phase storage mechanism in $Li_4Ti_5O_{12}$ anodes for room-temperature sodium-ion batteries. *Nat. Commun.* 2013, 4, 1870.

**29**. Delmas, C.; Maazaz, A.; Hagenmuller, P. Crystal-Chemistry and Fast Ionic-Conductivity of Sodium and Potassium Phases Having Cristobalite-Related Structures. *Solid State Ion.* 1983, 9-10, 83-88.

**30**. Wang, Y. S.; Yu, X. Q.; Xu, S. Y.; Bai, J. M.; Xiao, R. J.; Hu, Y. S.; Li, H.; Yang, X. Q.; Chen, L. Q.; Huang, X. J. A zero-strain layered metal oxide as the negative electrode for long-life sodium-ion batteries. *Nat. Commun.* 2013, 4, 2365.

**31**. Lei, Y. C.; Li, X.; Liu, L.; Ceder, G. Synthesis and Stoichiometry of Different Layered Sodium Cobalt Oxides. *Chem. Mater.* 2014, 26, 5288-5296.

**32**. Latroche, M.; Brohan, L.; Marchand, R.; Tournoux, M. New Hollandite Oxides - $TiO_2$ (H) and $K_{0.06}TiO_2$. *J. Solid State Chem.* 1989, 81, 78-82.

**33**. Noailles, L. D.; Johnson, C. S.; Vaughey, J. T.; Thackeray, M. M. Lithium insertion into hollandite-type $TiO_2$. *J. Power Sources* 1999, 81, 259-263.

**34**. Gutierrez-Florez, M. T.; Kuhn, A.; Garcia-Alvarado, F. Lithium intercalation in $K_xTi_8O_{16}$ compounds. *Int. J. Inorg. Mater.* 1999, 1, 117-121.

**35**. Sakao, M.; Kijima, N.; Akimoto, J.; Okutani, T. Synthesis, crystal structure, and electrochemical properties of hollandite-type $K_{0.008}TiO_2$. *Solid State Ion.* 2012, 225, 502-505.

**36**. Sakao, M.; Kijima, N.; Akimoto, J.; Okutani, T., Lithium insertion and extraction properties of hollandite-type $K_xTiO_2$ with different K content in the tunnel space. *Solid State Ion.* 2013, 243, 22-29.

**37**. Perez-Flores, J. C.; Baehtz, C.; Kuhn, A.; Garcia-Alvarado, F. Hollandite-type $TiO_2$: a new negative electrode material for sodium-ion batteries. *J. Mater. Chem. A* 2014, 2, 1825-1833.

**38**. Kresse, G.; Furthmuller, J. Efficiency of ab-initio total energy calculations for metals and semiconductors using a plane-wave basis set. *Comp. Mater. Sci.* 1996, 6, 15-50.

**39**. Blochl, P. E. Projector Augmented-Wave Method. *Phys. Rev. B* 1994, *50*, 17953-17979.

**40**. Perdew, J. P.; Burke, K.; Ernzerhof, M. Generalized gradient approximation made simple. *Phys. Rev. Lett.* 1996, 77, 3865-3868.

**41**. Anisimov, V. I.; Zaanen, J.; Andersen, O. K. Band Theory and Mott Insulators - Hubbard-U Instead of Stoner-I. *Phys. Rev. B* 1991, 44, 943-954.

**42**. Anisimov, V. I.; Solovyev, I. V.; Korotin, M. A.; Czyzyk, M. T.; Sawatzky, G. A. Density-Functional Theory and Nio Photoemission Spectra. *Phys. Rev. B* 1993, 48, 16929-16934.

**43**. Morgan, B. J.; Watson, G. W. Role of Lithium Ordering in the $Li_xTiO_2$ Anatase - Titanate Phase Transition. *J. Phys. Chem. Lett.* 2011, 2, 1657-1661.

**44**. Zhou, F.; Cococcioni, M.; Marianetti, C. A.; Morgan, D.; Ceder, G. First-principles prediction of redox potentials in transition-metal compounds with LDA + U. *Phys. Rev. B* 2004, 70, 235121.

**45**. Fabris, S.; de Gironcoli, S.; Baroni, S.; Vicario, G.; Balducci, G. Taming multiple valency with density functionals: A case study of defective ceria. *Phys. Rev. B* 2005, 71,.

**46**. Hu, Z. P.; Metiu, H. Choice of U for DFT plus U Calculations for Titanium Oxides. *J. Phys. Chem. C* 2011, 115, 5841-5845.

**47**. Henkelman, G.; Jonsson, H. Improved tangent estimate in the nudged elastic band method for finding minimum energy paths and saddle points. *J. Chem. Phys.* 2000, 113, 9978-9985.

**48**. Henkelman, G.; Uberuaga, B. P.; Jonsson, H. A climbing image nudged elastic band method for finding saddle points and minimum energy paths. *J. Chem. Phys.* 2000, 113, 9901-9904.

**49**. Sheppard, D.; Terrell, R.; Henkelman, G. Optimization methods for finding minimum energy paths. *J. Chem. Phys.* 2008, 128, 134106.

**50**. Sheppard, D.; Xiao, P. H.; Chemelewski, W.; Johnson, D. D.; Henkelman, G. A generalized solid-state nudged elastic band method. *J. Chem. Phys.* 2012, 136, 074103.

**51**. Morgan, D.; Van der Ven, A.; Ceder, G. Li conductivity in $Li_xMPO_4$ (M = Mn, Fe, Co, Ni) olivine materials. *Electrochem. Solid St.* 2004, 7, A30-A32.

**52**. Vineyard, G. H. Frequency Factors and Isotope Effects in Solid State Rate Processes. *J. Phys. Chem. Solids* 1957, *3*, 121-127.

**53**. Van der Ven, A.; Ceder, G.; Asta, M.; Tepesch, P. D. First-principles theory of ionic diffusion with nondilute carriers. *Phys. Rev. B* 2001, 64, 18430.

**54**. Yamada, A.; Chung, S. C.; Hinokuma, K. Optimized $LiFePO_4$ for lithium battery cathodes. *J. Electrochem. Soc.* 2001, 148, A224-A229.

**55**. Kutner, R. Chemical Diffusion in the Lattice Gas of Non-Interacting Particles. *Phys. Lett. A* 1981, 81, 239-240.

**56**. de Klerk, N. J. J.; Wagemaker, M. Diffusion Mechanism of the Sodium-Ion Solid Electrolyte $Na_3PS_4$ and Potential Improvements of Halogen Doping. *Chem. Mater.* 2016, 28, 3122-3130.

**57**. Lee, S. H.; Kang, J. H.; Kang, M. H. Structural properties of semiconductors in the generalized gradient approximation. *J. Korean Phys. Soc.* 1997, 31, 811-814.

**58**. Tompsett, D. A.; Islam, M. S. Electrochemistry of Hollandite alpha-$MnO_2$: Li-Ion and Na-Ion Insertion and $Li_2O$ Incorporation. *Chem. Mater.* 2013, 25, 2515-2526.

**59**. Kingery, W. D.; Chiang, Y-M.; Birnie, D. *Physical Ceramics: Principles for Ceramic Science and Engineering*. WILEY: USA, 1997.

**60**. Wagemaker, M.; Kearley, G. J.; van Well, A. A.; Mutka, H.; Mulder, F. M. Multiple li positions inside oxygen octahedra in lithiated $TiO_2$ anatase. *J. Am. Chem. Soc.* 2003, 125, 840-848.

**61**. Koudriachova, M. V.; Harrison, N. M.; de Leeuw, S. W. Density-functional simulations of lithium intercalation in rutile. *Phys. Rev. B* 2002, 65, 235423.

**62**. Reddy, M. A.; Kishore, M. S.; Pralong, V.; Varadaraju, U. V.; Raveau, B. Lithium intercalation into nanocrystalline brookite $TiO_2$. *Electrochem. Solid. St.* 2007, 10, A29-A31.

**63**. Hu, Y. S.; Kienle, L.; Guo, Y. G.; Maier, J. High lithium electroactivity of nanometer-sized rutile $TiO_2$. *Adv. Mater.* 2006, 18, 1421–1426.

**64**. Koudriachova, M. V.; Harrison, N. M. Li sites and phase stability in $TiO_2$-anatase and Zr-doped $TiO_2$-anatase. *J. Mater. Chem.* 2006, *16*, 1973-1977.

**65**. Koudriachova, M. V.; Harrison, N. M.; de Leeuw, S. W. Effect of diffusion on lithium intercalation in titanium dioxide. *Phys. Rev. Lett.* 2001, 86, 1275-1278.

**66**. Schmidt, W.; Bottke, P.; Sternad, M.; Gollob, P.; Hennige, V.; Wilkening, M. Small Change-Great Effect: Steep Increase of Li Ion Dynamics in $Li_4Ti_5O_{12}$ at the Early Stages of Chemical Li Insertion. *Chem. Mater.* 2015, 27, 1740-1750.

**67**. Wagemaker, M.; Simon, D. R.; Kelder, E. M.; Schoonman, J.; Ringpfeil, C.; Haake, U.; Lutzenkirchen-Hecht, D.; Frahm, R.; Mulder, F. M. A kinetic two-phase and equilibrium solid solution in spinel $Li_{4+x}Ti_5O_{12}$. *Adv. Mater.* 2006, 18, 3169–3173.

**68**. Santana, J. A.; Kim, J.; Kent, P. R. C.; Reboredo, F. A. Successes and failures of Hubbard-corrected density functional theory: The case of Mg doped $LiCoO_2$. *J. Chem. Phys.* 2014, 141, 164706.

**69**. Yuan, L. X.; Wang, Z. H.; Zhang, W. X.; Hu, X. L.; Chen, J. T.; Huang, Y. H.; Goodenough, J. B. Development and challenges of $LiFePO_4$ cathode material for lithium-ion batteries. *Energy Environ. Sci.* 2011, 4, 269-284.

**70**. Wagemaker, M.; Van Der Ven, A.; Morgan, D.; Ceder, G.; Mulder, F. M.; Kearley, G. J. Thermodynamics of spinel $Li_xTiO_2$ from first principles. *Chem. Phys.* 2005, 317, 130-136.

**71**. Dalton, A. S.; Belak, A. A.; Van der Ven, A. Thermodynamics of Lithium in $TiO_2$ (B) from First Principles. *Chem. Mater.* 2012, 24, 1568-1574.

**72**. Van der Ven, A.; Aydinol, M. K.; Ceder, G.; Kresse, G.; Hafner, J. First-principles investigation of phase stability in $Li_xCoO_2$. *Phys. Rev. B* 1998, 58, 2975-2987.

**73**. A. Maazaz, C. D. a. P. H., A study of the $Na_xTiO_2$ System by electrochemical deintercalation *J. Incl. Phenom.* 1982, *1*, 45-51.

**74**. Aydinol, M. K.; Kohan, A. F.; Ceder, G.; Cho, K.; Joannopoulos, J. Ab initio study of lithium intercalation in metal oxides and metal dichalcogenides. *Phys. Rev. B* 1997, 56, 1354-1365.

**75**. Delmas, C.; Fouassier, C.; Hagenmuller, P. Structural Classification and Properties of the Layered Oxides. *Physica B & C* 1980, 99, 81-85.

**76**. Seo, D. H.; Urban, A.; Ceder, G. Calibrating transition-metal energy levels and oxygen bands in first-principles calculations: Accurate prediction of redox potentials and charge transfer in lithium transition-metal oxides. *Phys. Rev. B* 2015, 92, 115118

**77**. Meng, Y. S.; Arroyo-de Dompablo, M. E. First principles computational materials design for energy storage materials in lithium ion batteries. *Energy Environ. Sci.* 2009, 2, 589-609.

**78**. Van der Ven, A.; Bhattacharya, J.; Belak, A. A. Understanding Li Diffusion in Li-Intercalation Compounds. *Accounts Chem. Res.* 2013, 46, 1216-1225.

**79**. Van der Ven, A.; Ceder, G. Lithium diffusion in layered $Li_xCoO_2$. *Electrochem. Solid St.* 2000, 3, 301-304.

**80**. Clarke, S. J.; Fowkes, A. J.; Harrison, A.; Ibberson, R. M.; Rosseinsky, M. J. Synthesis, structure, and magnetic properties of $NaTiO_2$. *Chem. Mater.* 1998, 10, 372-384.

# 6

# Ab-initio Study of Sodium Insertion in the λ-$Mn_2O_4$ and Dis/Ordered λ-$Mn_{1.5}Ni_{0.5}O_4$ Spinels

«Ἀρχὴν δὲ τῶν πάντων ὕδωρ ὑπεστήσατο»

“Water is the universal primary substance”

Thales

Diogenes Laertius, *Lives of Eminent Philosophers*, *THALES*, Book I , 27, with an English translation by R.D. Hicks, Harvard University Press, Cambridge, 1972.

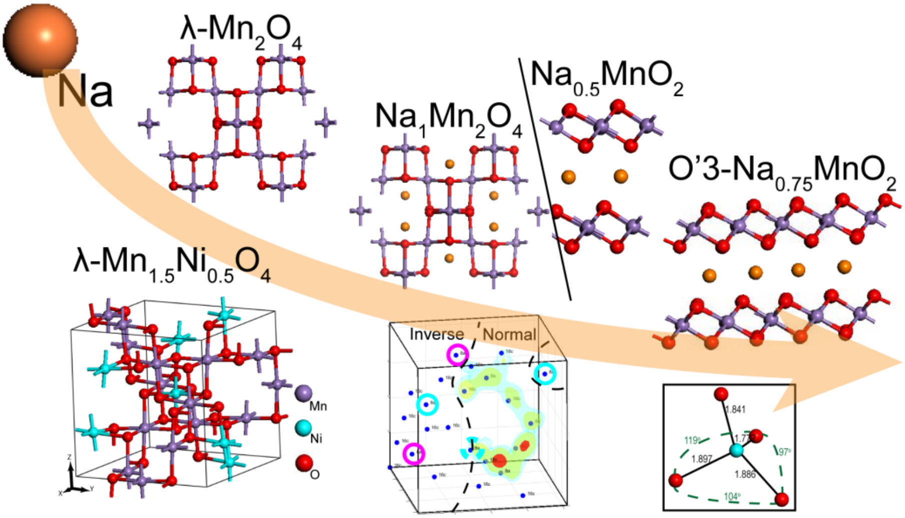
Na
λ-Mn₂O₄
Na₁Mn₂O₄
Na₀.₅MnO₂
O'3-Na₀.₇₅MnO₂
λ-Mn₁.₅Ni₀.₅O₄
Mn
Ni
O
Inverse
Normal
1.841
1.897
1.886
119°
97°
104°

## Abstract

The main challenge of sodium ion batteries is cycling stability, which is usually compromised due to strain induced by sodium insertion. Reliable high-voltage cathode materials are needed to compensate the generally lower operating voltages of Na-ion batteries compared to Li-ion ones. Herein, density functional theory (DFT) computations are used to evaluate the thermodynamic, structural, and kinetic properties of the high voltage λ-$Mn_2O_4$ and λ-$Mn_{1.5}Ni_{0.5}O_4$ spinel structures as cathode materials for sodium ion batteries. Determination of the enthalpies of formation reveal the reaction mechanisms (phase separation vs. solid solution) during sodiation, while structural analysis underlines the importance of minimising strain, in order to retain the metastable sodiated phases. For the λ-$Mn_{1.5}Ni_{0.5}O_4$ spinel, a thorough examination of the Mn/Ni cation distribution (dis/ordered variants) is performed. The exact sodiation mechanism is found to be dependent on the transition metal ordering in a similar fashion to the insertion behaviour observed in the Li-ion system. The preferred reaction mechanism for the perfectly ordered spinel is phase separation throughout the sodiation range, while, in the disordered spinel, the phase separation terminates in the $0.625<x<0.875$ concentration range, and is followed by a solid solution insertion reaction. Na-ion diffusion in the spinel lattice is studied using DFT as well. Energy barriers of 0.3 – 0.4 eV are predicted for the pure spinel comparing extremely well with the ones for the Li-ion and being significantly better than the barriers reported for multivalent ions. Additionally, Na-ion macroscopic diffusion through the 8a-16c-8a 3D network is demonstrated via molecular dynamics (MD) simulations. For the λ-$Mn_{1.5}Ni_{0.5}O_4$, MD simulations at 600 K bring forward a normal to inverse spinel half-transformation, common for spinels at high temperatures, showing the contrast in Na-ion diffusion between the normal and inverse lattice. The observed Ni migration to the tetrahedral sites at room temperature MD simulations explains the kinetic limitations experienced experimentally. Therefore, this work provides a detailed understanding of the (de)sodiation mechanisms of high voltage λ-$Mn_2O_4$ and λ-$Mn_{1.5}Ni_{0.5}O_4$ spinel structures, which are of potential interest as cathode materials for sodium ion batteries.

Based on the homonymous paper:
Vasileiadis, A.; Carlsen, B.; de Klerk, N. J. J.; Wagemaker, M. Ab-initio Study of Sodium Insertion in the λ-$Mn_2O_4$ and Dis/Ordered λ-$Mn_{1.5}Ni_{0.5}O_4$ Spinels. *in press* Chem. Mater. 2018

## 6.1 Introduction

Conventional power sources are being rapidly replaced by renewable power sources as demanded for a sustainable energy future. Successful implementation of these renewable power sources would benefit from large scale electrochemical storage, both to lift the intermittency in power generation and to provide grid stabilisation.[1] For this application, state-of-the-art Li-ion batteries are anticipated to be costly, and, therefore, the scientific interest has been directed towards alternative, cost-effective and environmentally benign battery chemistries.[2, 3]

Sodium ion and sodium aqueous batteries (SIBs, SABs) have been extensively studied in the last decade.[4, 5] Utilising Na-ion as a charge carrier ensures abundance and availability compared to its Li-ion counterpart.[6] Furthermore, the replacement of organic electrolytes with water in SABs provides a reduction in production cost and increases safety, by practically eliminating the flammability of the system.[7] These batteries, however, do have their own challenges. The larger Na ionic radius, as compared to the Li ionic radius, often causes greater lattice distortions, which may compromise cycle life.[8] In addition, for an aqueous system, the dissociation potential of water restricts the battery voltage, and thereby the amount of candidate electrode materials and it limits the maximum power and energy density.[7, 9] However, for stationary storage, gravimetric and volumetric energy, as well as power density demands are less stringent. For the commercialisation of large-scale battery applications, the primary criteria are cost-effectiveness, stability and environmental friendliness, for which sodium aqueous systems appear to be promising candidates.[4, 7]

Extensive research over the last five years has produced a large variety of electrode materials for sodium ion battery systems, with phosphate and oxide based structures dominating the scene.[4] Amongst them, the manganese oxide family stands out, offering many different structures suitable for Na-ion insertion, such as the layered P2, P3, and O3 type structures, and the spinel structures.[10-13] In this study, we will focus on the delithiated $\lambda\text{-}Mn_2O_4$ and $\lambda\text{-}Mn_{1.5}Ni_{0.5}O_4$ ($\lambda$-MNO) spinels, the lattice of which offers tetrahedral (8a) and octahedral (16c) interstitial positions, capable of Na insertion, along with a 3D Na-ion diffusion network.

Initial electrochemical sodiation of the pure spinel ($\lambda\text{-}Mn_2O_4$) has been shown to cause a partial phase transition from the spinel to the O’3 layered structure, caused by lattice deformations induced by Na insertion,[14, 15] thus questioning the stability of the $\lambda\text{-}Na_1Mn_2O_4$ structure. On the other hand, more recent experiments suggest that reversible Na-ion (de)insertion into the spinel framework is possible, by initially filling the 8a tetrahedral sites and then the remaining 16c octahedral sites.[16, 17] Taking advantage of the stability in aqueous electrolytes, $\lambda\text{-}Mn_2O_4$ has been successfully implemented in SABs systems, showing high capacities and rate capabilities, and stable cycling behaviour at neutral pH.[16, 17] Furthermore, the cost-effectiveness of SABs of $\lambda\text{-}Mn_2O_4$ spinel structure has been demonstrated.[16] In addition to Na, the pure spinel is also interesting in the context of its ability to store multivalent charge carriers such as Ca, Al, Zn and Mg, as shown both experimentally[18] and computationally[19]. Based on the smaller ionic radii of Zn and Mg compared to that of Na, these charge carriers are expected to be more easily inserted.[18]

The $\lambda\text{-}MNO$ spinel can be indexed by the $P4_332$ space group if Ni is ordered on the metal sublattice, or by the $Fd\overline{3}m$ space group if Mn and Ni are randomly distributed on the metal sublattice. [20-25] The Ni distribution, and thus the resulting symmetry, strongly depends on the synthesis route of the lithiated counterpart ($\lambda\text{-}LMNO$), from which the delithiated host is obtained via electrochemical or chemical Li deinsertion.[10, 11, 21, 24, 25] Sodiation of the ordered and the disordered $\lambda - MNO$ spinels was recently studied by Kim and colleagues, who reported reversible Na (de)insertion in the tetrahedral (8a) interstitial sites of the spinel lattice.[10, 11] A flat voltage plateau in the region of 3.65 V vs. $Na/Na^+$ is reported, which is 0.56 V higher than in the pure spinel[10], followed by a sharp voltage decline toward the $\lambda\text{-}Na_1Mn_{1.5}Ni_{0.5}O_4$ phase.[10, 11] Both the ordered and the disordered phase display mixed phase separation and solid solution reaction pathways, the concentration ranges of which appear to depend on the cycling conditions.[10, 11] Similar to Li-ion batteries[20, 25],the disordered phase exhibits better electrochemical performance, even though both the ordered and disordered structures have similar Li-ion diffusion coefficients.[11] Considerable kinetic barriers which hinder complete desodiation are reported, and nanosizing is suggested to achieve good performance.[10, 11]

Herein, a thorough ab-initio study of the thermodynamic and kinetic properties of the Na-ion insertion of $\lambda\text{-}Mn_2O_4$ and the various phases of the $\lambda\text{-}Mn_{1.5}Ni_{0.5}O_4$ ($\lambda\text{-}MNO$) spinels is presented. Detailed structural and thermodynamic analysis throughout the sodiation process aims to clarify key experimental observations regarding phase stability and reaction mechanisms. The Mn/Ni distribution in the $\lambda\text{-}MNO$ lattice is shown to determine the sodiation reaction mechanism, in a fashion that closely resembles the behaviour observed in Li-ion batteries[26, 27]. In combination with a detailed investigation of Na-ion diffusion mechanics, a comprehensive picture of the fundamental processes is brought forward, in the context of which, experimental optimisation criteria[11] are addressed.

## 6.2 Computational Methods

Spin-polarised density functional theory (DFT) calculations were performed using the Vienna Ab-initio Simulation Package (VASP).[28] The PBE exchange correlation, functional of Perdew and colleagues.[29, 30], was implemented, and valence-core interactions were probed with the projector-augmented wave approach (PAW)[31]. The calculations were carried out with Hubbart U-corrections to correctly capture the behaviour of heavily localised electronic ground states.[32, 33] Effective U-J parameters of $U_{eff}$ = 3.9 and $U_{eff}$ = 6.4 were used for Mn and Ni respectively, based on previous DFT studies[19, 34-36]. An energy cut-off energy of 520 eV and a 4x4x4 k-point mesh were selected in order to ensure accurate calculations, and total energies were obtained from successive self-consistent calculations

Total energies of the ferromagnetic (FM) and various antiferromagnetic (AFM) configurations were calculated, with the FM solutions giving the lowest energy in both the $\lambda$-$Mn_2O_4$ and the $\lambda$-$Mn_{1.5}Ni_{0.5}O_4$. Therefore, all simulations were initialised with FM ordering. Although an AFM ordering has been experimentally reported[37], according to the Goodenough-Kanamoru rule, a FM description might be appropriate considering the ridge sharing between oxygen octahedra.[38] For the lithiated $\lambda$-$Li_1Mn_{1.5}Ni_{0.5}O_4$ phase, both experiments and calculations reveal that AF ordering is more stable than FM ordering.[39, 40] However, subtle differences in the calculated voltage profiles (0.03V) are reported, when comparing AFM and FM descriptions[39]. For simplicity, in this study we retain the FM description throughout the computations.

The thermodynamic stability of the Na-insertion systems was determined by calculating the enthalpies of formation ($H_f$), according to equation 6.1:[41, 42]

$$H_f = E_{Na_xHost} - xE_{Na_{x_{max}}Host} - (1-x)E_{Host} \qquad 6.1$$

where $H_f$ represents the relative stability of a particular configuration, $E_{Na_xHost}$ is the total crystal energy of the particular configuration, with x fractional sodium concentration, $E_{Na_{x_{max}}Host}$ is the energy of the fully sodiated structure, and $E_{Host}$ is the energy of the empty host. The average sodium-insertion equilibrium voltage can be derived, based on the difference in the Gibbs free energy between the sodiated and de-sodiated phases:

$$\overline{V} = \frac{-[E_{Na_xHost} - (x-y)E_{Na_s} - E_{Na_yHost}]}{(x-y)e} \qquad 6.2$$

This difference can be linked to the total energy change of the system throughout the sodiation process, according to equation 6.2[43, 44], where $E_{Na_xHost}$ and $E_{Na_yHost}$ are the total energies of the $Na_xHost$ and $Na_yHost$ configurations, respectively. $E_{Na_s}$ is the sodium energy and e is the electron charge.

Na diffusion was studied with the nudge elastic band (NEB) method, utilising the climbing image approach, and, additionally, with molecular dynamics (MD) simulations. For the dilute vacancy limit of the pure spinel, the 8a - 16c energy path was converged and symmetrically replicated to create an 8a - 16c - 8a path. To ensure viable computational times for the MD simulations, the energy cut-off energy and the k-point sampling were reduced to 400 eV and 1x1x1, respectively. The total simulation time was between 0.25 and 0.5 ns at a constant temperature of 600 K and 300 K. Each time-step was set to 2 fs, and the first 2.5 ps were discarded as equilibration time. Analysis of MD simulations, activation barriers, and diffusion coefficients was done according to the approach reported recently[45]. In one of the MD simulations (600 K) of the $\lambda - Mn_2O_4$ spinel, the lattice broke down to a collection of particles after 0.45 ns. As will be discussed herein, this may be due to the metastability of the spinel phase. Analysis was performed only for the timeframe where the spinel framework remained intact. Proper determination of activation energies and diffusion coefficients via MD calculations, would require more and longer MD simulations, at higher temperatures, in larger supercells. For this reason, we refrain from presenting a quantitative behaviour and we will use the MD picture as an insightful qualitative tool.

The optimised unit cells of the λ-$Mn_2O_4$ and $Mn_{1.5}Ni_{0.5}O_4$ crystal structures contain 48 atoms ($Mn_{16}O_{32}$, $Mn_{12}Ni_4O_{32}$). The 8 formula units provide 16 sodium insertion steps to reach a 1 to 1 ratio between the transition metals and sodium. For the disordered λ-(Li)$Mn_{1.5}Ni_{0.5}O_4$ phase, a slight stoichiometric excess of Mn[10, 20], oxygen deficiencies[23, 25, 46] or partial fluorine replacement[10] have been reported. For the purposes of this study, the stoichiometry will be kept constant to the standard ratio of 1 Ni for every 3 Mn atoms. The selection of the representative λ-$Mn_{1.5}Ni_{0.5}O_4$ hosts was based on the relaxation and energy minimisation of inequivalent configurations, differing in the Ni/Mn distribution in both the lithiated and empty spinel, and it will be thoroughly discussed in the next section.

## 6.3 $\lambda$-$Mn_2O_4$ and $\lambda$-$Mn_{1.5}Ni_{0.5}O_4$ Host Structures

The structure of $\lambda$-$Mn_2O_4$ spinel was relaxed, starting from the experimentally determined structure[47]. The relaxed $\lambda$-$Mn_2O_4$ configuration represents the cubic $Fd\bar{3}m$ unit cell shown in Figure 6.1. The spinel structure offers two types of interstitial sites: the tetrahedral (8a) and the octahedral (16c).

Experimentally, the most common way of obtaining the empty spinel structures ($\lambda$-$Mn_2O_4$, $\lambda$-$Mn_{1.5}Ni_{0.5}O_4$) is by synthesising the lithiated phases ($LiMn_2O_4$, $LiMn_{1.5}Ni_{0.5}O_4$), where lithium occupies the tetrahedral interstitial position. Either with chemical[14, 17] or electrochemical[10, 14] delithiation, lithium is removed from the lattice, thus leaving vacant tetrahedral sites for subsequent sodium insertion. This implies that the empty host configurations will be determined by the lithiated host structures, and thus, are relevant to investigate. Where the pure spinel is indexed by the $Fd\bar{3}m$ space group, the symmetry of the Ni doped $LiMn_{1.5}Ni_{0.5}O_4$ spinel depends on the cation distribution. Depending on the synthesis route.[21, 24, 25], the result is either a faced-centred cubic spinel lattice (space group $Fd\bar{3}m$), when Ni and Mn randomly occupy the transition metal sublattice, or a lower-symmetry cubic primitive spinel lattice (space group $P4_332$), when Ni and Mn are ordered on the transition metal sublattice[20-25].

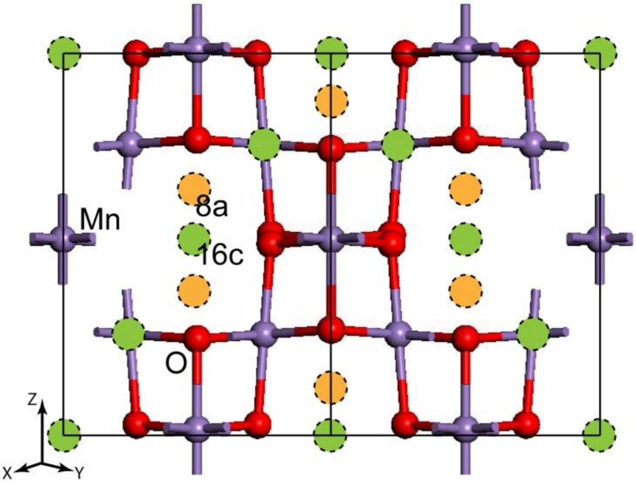

**Figure 6.1:** Unit cell of the pure spinel $\lambda$-$Mn_2O_4$, green and orange circles indicate the interstitial tetrahedral (8a) and octahedral (16c) sites, respectively. Red and purple spheres represent O and Mn atoms, respectively.

Prior to the selection of the $\mathrm{Mn_{1.5}Ni_{0.5}O_4}$ host structures, total crystal energies of all the inequivalent, Mn/Ni configurations of both the fully lithiated ($\mathrm{Li_1Mn_{1.5}Ni_{0.5}O_4}$) and delithiated ($\mathrm{Mn_{1.5}Ni_{0.5}O_4}$) phases of the $\mathrm{Fd\bar{3}m}$ lattice, in one unit cell, were determined. The total energies provide a thermodynamic argument on the selection of the $\mathrm{Mn_{1.5}Ni_{0.5}O_4}$ host structures. We chose to examine the lithiated phases ($\mathrm{Li_1Mn_{1.5}Ni_{0.5}O_4}$) as well, because of the preparation method. As it was discussed in the previous paragraph, host structures cannot be prepared directly in the sodiated form ($\mathrm{Na_1Mn_{1.5}Ni_{0.5}O_4}$), but come from the delithiated spinels. However, this link holds true assuming that the host framework remains unchanged upon cycling, keeping the same Ni distribution. As we will unravel in a later stage of this paper, Ni is mobile in the host framework, and thus, there is a possibility of Ni rearrangement, leading to interconversion between the various configurations.

The lowest energy configuration of the fully lithiated phase exhibits Ni ordering in the transition metal sites, resulting in the $\mathrm{P4_332}$ symmetry. This is in agreement with previous DFT results[26] and experimental studies, which suggest that the disordered phase appears at higher annealing temperatures[25], thus, indicating that the ordered structure is the most stable configuration of $\mathrm{Li_1Mn_{1.5}Ni_{0.5}O_4}$. The ordered structure (Figure 6.2a) was selected for the present computational study, and it will be referred to as $\mathrm{P-Mn_{1.5}Ni_{0.5}O_4}$, named after the initial letter of its symmetry. Additionally, the lowest energy disordered configuration (second lowest overall) having a random distribution of Ni in the spinel lattice ($\mathrm{Fd\bar{3}m}$) was selected, and is shown in Figure 6.2b. We will refer to the disordered variant as $\mathrm{F1-Mn_{1.5}Ni_{0.5}O_4}$, as it will represent the disordered variant described by the $\mathrm{Fd\bar{3}m}$ lattice.

When investigating all the inequivalent $\mathrm{Mn_{1.5}Ni_{0.5}O_4}$ configurations, however, the lowest energy configuration exhibits Ni clustering in side-sharing octahedra (Figure 6.2d). The relative Ni position in the lattice forms a tetrahedron with a Ni-Ni distance of 2.887 Å. This is the smallest Ni-Ni distance possible, resulting in segregation of the Ni and Mn atoms. Ni clustering within the unit cell can be regarded as a different ordered state, where the symmetry results in the P-43m space group, with Ni occupying the 4e position. This Ni configuration is often regarded as unrealistic[26, 27], and it is in fact the highest energy structure according to our calculations when minimising all the $\mathrm{Li_1Mn_{1.5}Ni_{0.5}O_4}$ inequivalent configurations. Nonetheless, it may be a relevant configuration under delithiated or desodiated (charged) conditions and will be studied as an extreme opposite case to the ordered structure. We will refer to this configuration as $\mathrm{C-Mn_{1.5}Ni_{0.5}O_4}$

structure, with the letter C referring to the word “clustered”. Another $\mathrm{Mn_{1.5}Ni_{0.5}O_4}$ configuration with high Ni clustering is presented in Figure 6.2c**.** This structure will be studied as another disordered representative ($\mathrm{Fd\bar{3}m}$), referenced as $\mathrm{F2-Mn_{1.5}Ni_{0.5}O_4}$. In this case, the four nickel atoms form a tetrahedron with vertices in adjacent sites. The tetrahedron has an isosceles triangle as a base with one side 2.84 Å and the other two 4.93 Å long, creating angles of 35.3 and 73.4 degrees respectively. Since Ni can occupy discrete transition metal sites in the spinel lattice, Ni placement in $\mathrm{F2-MNO}$ is the second most clustered distribution.

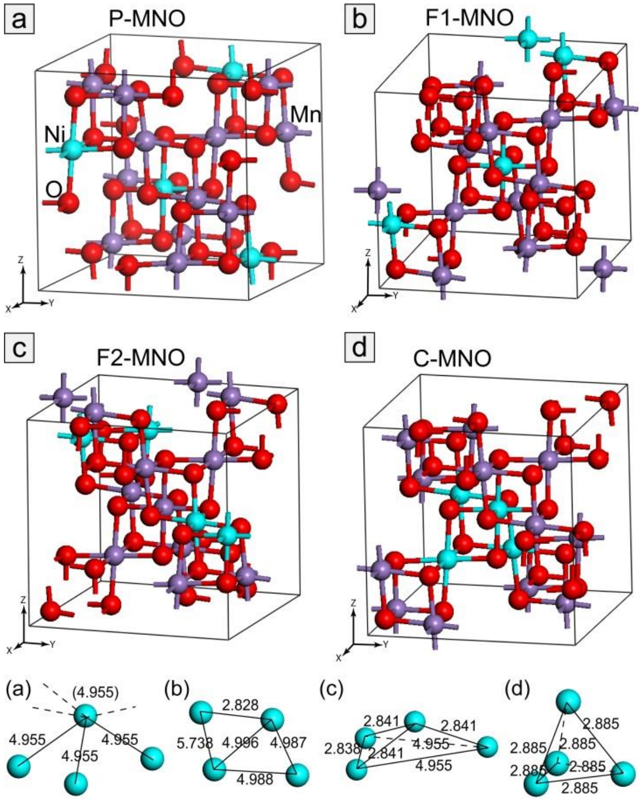
a
P-MNO
Ni
Mn
O
b
F1-MNO
c
F2-MNO
d
C-MNO
(a)
(4.955)
4.955
4.955
4.955
(b)
2.828
5.738
4.996
4.987
4.988
(c)
2.841
2.841
2.838
2.841
4.955
4.955
(d)
2.885
2.885
2.885
2.885
2.885
2.885

**Figure 6.2:** Unit cells of the **a)** ordered $\mathrm{P-Mn_{1.5}Ni_{0.5}O_4}$ configuration **b)** disordered $\mathrm{F1-Mn_{1.5}Ni_{0.5}O_4}$ configuration. **c)** disordered $\mathrm{F2-Mn_{1.5}Ni_{0.5}O_4}$ configuration. **d)** $\mathrm{C-Mn_{1.5}Ni_{0.5}O_4}$ configuration exhibiting Ni clustering. Below, the relative Ni position within one unit cell is presented.

A qualitative trend observed by the minimisation of the inequivalent spinel variants ($Mn_{1.5}Ni_{0.5}O_4$, $Li_1Mn_{1.5}Ni_{0.5}O_4$) is that the fully lithiated spinels are stabilised by having the Ni atoms separated as far as possible, whereas the empty spinels are stabilised by the formation of Ni clusters. However, the relative stability of the two configurations is quite different. In the $Li_1Mn_{1.5}Ni_{0.5}O_4$ case, there is a clear energy preference for the ordered phase (Figure 6.3). On the other hand, in the empty host case, the energies of all configurations lie within a range of only 25 meV per unit cell.

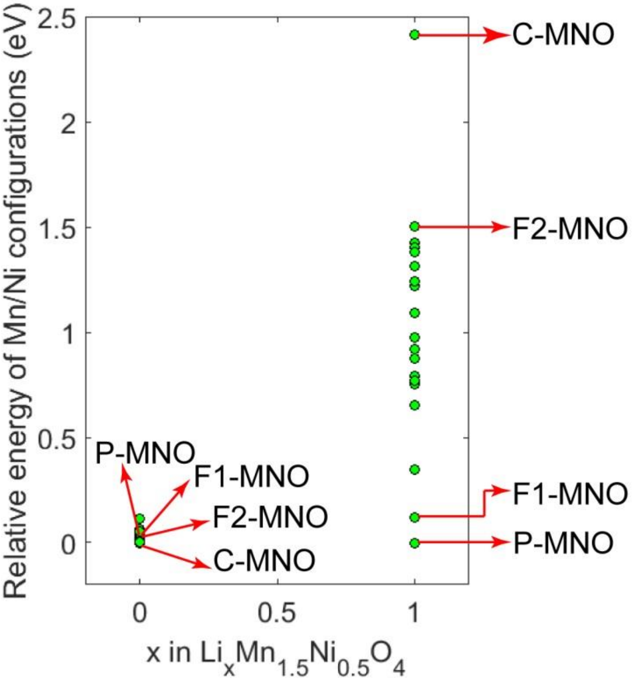

**Figure 6.3:** Mn/Ni inequivalent energy configurations in the empty and filled structure.

This indicates that a direct synthesis of the empty spinel, if possible, will not lead to the $C-Mn_{1.5}Ni_{0.5}O_4$ or $F2-Mn_{1.5}Ni_{0.5}O_4$ structures. The mixing entropy in room temperature would favour a truly disordered phase, where Mn and Ni randomly occupy the octahedral sites. In addition, a direct synthesis process seems difficult as shown by Kitchaev and colleagues[48].

The lattice parameters of all relevant structures mentioned above are compared with experimental values in Table 6.1. For all structures, the lattice parameters are in good agreement with the experimental ones, showing differences of 2.5%, which is a typical overestimation when utilising the Hubbart correction method.[26, 49-51] Small differences are observed between the λ-MNO variants, with the ordered structure having the smallest lattice parameters, which is in agreement with a previous experiment.[25]

**Table 6.1:** Comparison between experimental and simulated lattice parameters

| $\lambda$-$Mn_2O_4$ | a (Å) |
|---|---|
| DFT | 8.242 |
| Experimental[47] | 8.064 |
| $\lambda - Mn_{1.5}Ni_{0.5}O_4$ | a (Å) |
| (P) DFT | 8.142 |
| (P) Experimental[25] | 8.005 |
| (F1) DFT | 8.159 |
| (F2) DFT | 8.163 |
| (C) DFT | 8.162 |

## 6.4 Na-Ion Insertion in $\lambda$-$Mn_2O_4$

The convex hull (Figure 6.4a), obtained for Na insertion into $\lambda$-$Mn_2O_4$, indicates that sodiation initially occurs via a two-phase separation from the empty spinel phase towards the $Na_1Mn_2O_4$ phase. During this first-order phase transition, inserted Na-ions are accommodated on the tetrahedral 8a positions, which provides a considerably lower energy environment (> 165 meV), compared to the octahedral 16c positions. This is followed by a subsequent phase separation transition from $Na_1Mn_2O_4$ towards $Na_2Mn_2O_4$, during which the additional Na-ions are accommodated by the octahedral 16c sites. At the same time, the Na-ions in the 8a sites migrate to the remaining 16c sites. The predicted phase separation mechanisms suggest that, at 0 K, the sodiation process can be described by equations 6.3 and 6.4:

$$(\,)_{8a}[\,]_{16c}[Mn_2]_{16d}[O_4]_{32e} \rightarrow (Na_1)_{8a}[\,]_{16c}[Mn_2]_{16d}[O_4]_{32e} \qquad 6.3$$

$$(Na_1)_{8a}[\,]_{16c}[Mn_2]_{16d}[O_4]_{32e} \rightarrow (\,)_{8a}[Na_2]_{16c}[Mn_2]_{16d}[O_4]_{32e} \qquad 6.4$$

This is in agreement with the more general proposed insertion equations[17] 6.5 and 6.6.

$$(\,)_{8a}[\,]_{16c}[\mathrm{Mn_2}]_{16d}[\mathrm{O_4}]_{32e} \rightarrow (\mathrm{Na_x})_{8a}[\,]_{16c}[\mathrm{Mn_2}]_{16d}[\mathrm{O_4}]_{32e} \qquad 6.5$$

$$(\mathrm{Na_x})_{8a}[\,]_{16c}[\mathrm{Mn_2}]_{16d}[\mathrm{O_4}]_{32e} \rightarrow (\mathrm{Na_x})_{8a}[\mathrm{Na_y}]_{16c}[\mathrm{Mn_2}]_{16d}[\mathrm{O_4}]_{32e} \qquad 6.6$$

The large volume change of 16% upon formation of $\mathrm{Na_1Mn_2O_4}$, which increases to 26% upon reaching the fully sodiated $\mathrm{Na_2Mn_2O_4}$ phase, as shown in Figure 6.4b, suggests that mechanical stresses will cause mechanical degradation upon cycling. In addition, considering that the material is predicted to phase separate, the significant lattice mismatch between the end-member phases $(\mathrm{Mn_2O_4}, \mathrm{Na_1Mn_2O_4}, \mathrm{Na_2Mn_2O_4})$ may lead to crack formation and mechanical failure upon cycling. Indeed, mechanical degradation has been reported experimentally[10, 15, 17] where XRD peak broadening was ascribed to lattice strain and partial amorphisation of the structure upon Na-ion insertion.[15, 17] Additionally, it has been observed[15] that Na insertion induces a partial phase transformation toward the layered $\mathrm{O'3-Na_xMnO_2}$ lattice. In a previous study, it was shown that such transformations can be predicted by DFT calculations.[52] In that case, it was demonstrated that Na-ion insertion into the rutile tunnel of hollandite $\mathrm{TiO_2}$ leads to a phase transformation towards the $\mathrm{O'3}$ layered lattice. For Na-ion insertion in the spinel λ-$\mathrm{Mn_2O_4}$ structure, however, such a transformation was not observed. This is in agreement with recent electrochemical tests in an aqueous environment, showing highly reversible (de)insertion behaviour of Na-ions in λ-$\mathrm{Mn_2O_4}$, and high rate capabilities.[16, 17] Despite the strain, no new phases were observed and the constant voltage (CV) peaks were ascribed to Na-ion insertion into 8a and 16c spinel sites.[16, 17] The metastability, however, of the sodiated spinel phases is evident in literature.[48, 53] Kitchaev and colleagues performed a thorough thermodynamic DFT study to investigate the phase selection upon synthesising a variety of $\mathrm{A_xMnO_2}$ polymorphs $(\alpha, \beta, \gamma, \delta, \lambda, \mathrm{R})$ with A = $\mathrm{Li^+}$, $\mathrm{Na^+}$, $\mathrm{Ca^{2+}}$, $\mathrm{K^+}$, $\mathrm{Mg^{2+}}$.[48] The spinel phase (λ) was found to be metastable compared to the layered O3 phase (δ), throughout the sodiation range, due to the incompatibility of the spinel interstitial sites with the large Na-ions.[48] This indicates the presence of a driving force towards the layered structure. In this study, in order to evaluate a possible spinel to layered transition, the O3 layered $\mathrm{NaMnO_2}$ phase was also optimised, starting from the experimental lattice.[54] By Na de-intercalation, the lowest energy configurations of the monoclinic phases were determined. The O3-layered enthalpies of formation with respect the spinel end-member phases are presented in Figure 6.4a, revealing the relative stability of the $MnO_2$ structures. To evaluate the presence of a thermodynamic driving force behind the spinel-layered structure transformation, the average voltages between the spinel phases ($\lambda$-$Mn_2O_4$, $Na_1Mn_2O_4$) and the monoclinic layered phases ($O'3 - Na_{0.75}MnO_2$, $O'3 - Na_{0.5}MnO_2$) were determined, and are presented in comparison with the calculated voltage profile while remaining in the spinel structure ($\lambda$-$Mn_2O_4$, $Na_1Mn_2O_4$, $Na_2Mn_2O_4$) in Figure 6.4c.

The two plateaus (blue lines) in Figure 6.4c reflect the two spinel-spinel phase separation mechanisms predicted, according to the convex hull ($\lambda$-$Mn_2O_4$ → $Na_1Mn_2O_4$ and $Na_1Mn_2O_4$ → $Na_2Mn_2O_4$). Our calculations indicate that the first reaction occurs at 3.2 V, and the second at 2.3 V, in good agreement with experiments[10, 15]. The slight slope in the experimental voltage profile might be the result of the large lattice mismatch during the phase transition, which usually leads to poor Na-ion kinetics over the phase interfaces and grain boundaries, inducing large overpotentials. An example of a similar voltage evolution behaviour is the lithiation of anatase $TiO_2$. The phase transition between $Li_{0.5}TiO_2$ and $LiTiO_2$ shows a clear plateau during extremely slow cycling and/or for very small particle sizes, while during standard cycling conditions, a slope is seen, due to kinetically induced overpotentials.[55] A thick phase interface layer is also linked with a large gradient penalty ($\kappa$), penalising the coexistence of two phases.[56] Therefore, the inserted spinel system will be more susceptible to suppression of phase separation. Suppression of the phase separation mechanism can be achieved either by high currents[57-60], or by reducing the particle size to the thickness of the phase interface layer[55], as simulated and shown experimentally for LFP and anatase $TiO_2$ electrodes. Thus, given the correct conditions, partial mixing of the end-member phases (solid solution) might be possible, leading to a sloping voltage curve.

The average voltages between the empty spinel and the $O'3 - Na_{0.5}MnO_2$ layered phase (3.28 eV), and the spinel $Na_1Mn_2O_4$ and the layered $O'3 - Na_{0.75}MnO_2$ phase (2.65V) (green lines in Figure 6.4c) appear higher compared to the voltages of the $Mn_2O_4$ to $Na_1Mn_2O_4$ (3.19V) and $Na_1Mn_2O_4$ to $Na_2Mn_2O_4$ (2.3 V) spinel-spinel phase transition respectively. This result rationalises the experimental observation[15] of a partial phase transformation toward the layered structure as an alternative sodiation route. Such a phase transition would require a significant amount of time because of the substantial kinetic barriers that must be overcome, although, at high Na concentrations, it could be catalysed by a gradual deformation of the spinel lattice, due to strain. This is consistent with experiments showing that the partial formation of the layered phase appears after 10 cycles.[15]

For completion, the calculated sodiation voltage profile of the layered structure is presented in Figure 6.4d showing good agreement with experiments[54].

The $\mathrm{Na_1Mn_2O_4}$ spinel structure was found to be metastable in another DFT study[53] as well, this time compared to the post spinel $\mathrm{CF-NMO}$ phase. Herein, the $\mathrm{CF-NMO}$ structure was computationally optimised starting from the experimental lattice[61]. The $\mathrm{Na_1Mn_2O_4}$ spinel phase is found to be metastable compared to both the layered and the CF phase, in agreement with previous results[48, 53]. However, the CF phase appears only at higher pressures and temperatures[61] and thus only the comparison with the O3 phases is relevant to battery cycling.

Retaining the spinel framework intact would require steps for minimising strain, which may be catalysing unwanted transformations during Na insertion. Suppression of the phase separation, as discussed above, is a good example. High rate cycling might be beneficial, not only by suppressing the first order phase transition, but also simply by not providing sufficient time for the sluggish undesired phase transformations to occur. Nanosizing may be beneficial within this context, potentially suppressing phase separation and lowering strain, although surfaces may also be the starting point towards undesired phase transitions.

Another important consideration, when implementing spinel structures, is cation disorder leading to the conversion from a normal to an inverse spinel lattice. In the normal spinel, of $\mathrm{AB_2O_4}$ stoichiometry, A cations (in our case Na and/or vacancies) occupy the tetrahedral interstitial sites and B (in our case Mn and/or Ni when studying MNO) occupy the octahedral spinel sites. In the inverse spinel, B occupy all the tetrahedral and half the octahedral sites, while A occupies the remaining octahedral sites.[62] Conversion to the inverse spinel structure under extreme conditions is a well-known problem creating kinetic limitations in the electrode.[19, 63] Bhattacharya and colleagues methodically studied the normal vs. inverse spinel stability for Li-ion batteries of various spinel oxides at 0 K, including (de)lithiated $\mathrm{Mn_2O_4}$.[62] With regard to the lithiated phase, the normal spinel is reported to be thermodynamically much more favourable (~1 eV/ $\mathrm{Li_1Mn_2O_4}$[62]) .[62] Here, similar to its Li counterpart, the normal spinel is found to be much more stable (0.97 eV/ $\mathrm{Na_1Mn_2O_4}$) compared to the inverse spinel of $Na_1Mn_2O_4$ stoichiometry, as shown in Figure 6.4e. Additionally, it should be noted that with regard to the delithiated $\mathrm{Mn_2O_4}$ phase, the normal spinel is reported as only 23 meV lower in energy than the inverse spinel, raising concerns on the stability of the delithiated/desodiated state.[62]

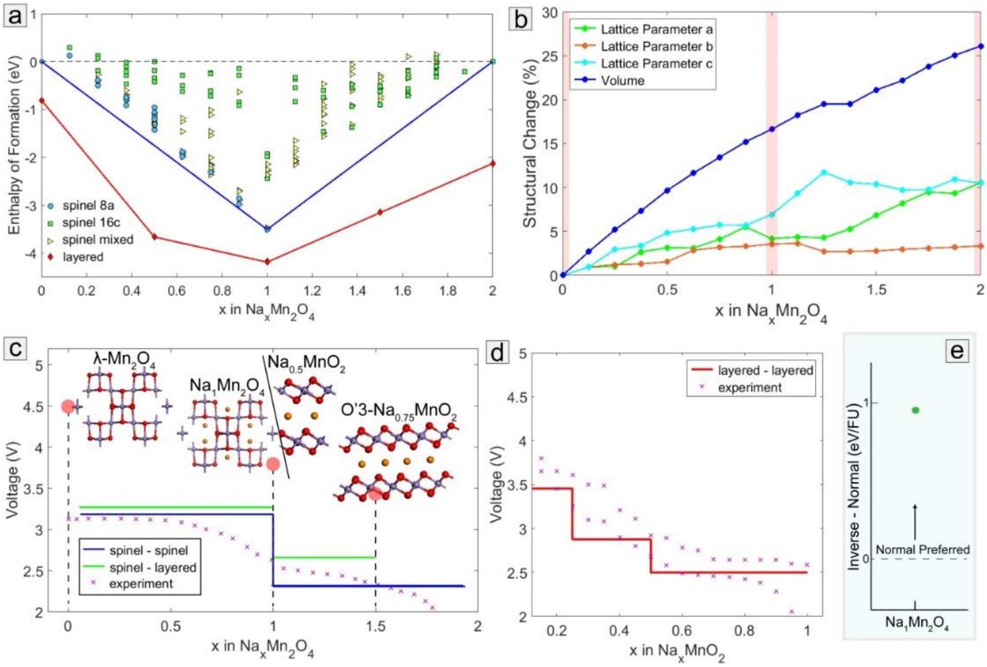

**Figure 6.4: a)** Enthalpies of formation and convex hull of Na insertion in λ-$Mn_2O_4$ and layered O3 $MnO_2$. Cyan circles, green squares and yellow triangles represent Na inserting into only 8a, only 16c and mixed spinel interstitial sites respectively. Red diamonds represent Na intercalation in the O3 layered structure. Blue and red lines follow the lowest enthalpy path of the spinel and layered structure respectively. **b**) Structural changes during Na insertion in λ-$Mn_2O_4$; the light red vertical lines indicate the stable phases during the sodiation process. **c**) Calculated (blue line) vs. experimental[10, 15] (scatter) voltage profile of Na insertion in λ-$Mn_2O_4$. The experimental data were normalised according to what is considered as full capacity reaching the $Na_1Mn_2O_4$ and $Na_1Mn_{1.5}Ni_{0.25}O_4$ phase[10, 15]. The green lines indicate the average voltages between the spinel and the layered $O'3 - Na_{0.5}MnO_2$ and $O'3 - Na_{0.75}MnO_2$ monoclinic phases. (please note the different stoichiometric notation). **d)** Calculated (red line) vs. experimental[54] (scatter) voltage profile of Na intercalation in the layered O3 structure. **e**) The relative stability of the normal vs. inverse spinel for the $Na_1Mn_2O_4$ concentration, where FU is the $Na_1Mn_2O_4$ formula unit.

All Mn-O bonds in the empty host (λ-$Mn_2O_4$) are close to an average value of 1.944 Å, which is slightly higher compared to a previous DFT study, which cited 1.914 Å, and the experimentally determined value of 1.910 Å.[64] The $Na_1Mn_2O_4$ phase retains the spinel framework, although the symmetry is reduced due to Jahn-Teller-distortions (JT distortion), a commonly observed phenomenon in octahedral transition metal complexes.[50, 51, 64, 65]. In the $Na_1Mn_2O_4$ phase, the insertion of Na, which donates its electron to the spinel lattice, reduces half of the $Mn^{4+}$ to $Mn^{3+}$.

The $Mn^{3+}$ octahedra exhibit an elongation of two of the Mn-O bonds, as depicted in Figure 6.5, which illustrates the local atomic structures and oxidation states of the Mn octahedra for the stable end-member phases. The two longer Mn-O bonds of the $Mn^{3+}$ octahedra have an average value of 2.285 Å, while the other bonds have an average value of 1.950 Å. With regard to the $Mn^{4+}$ octahedra, all Mn-O bonds show an average value of 1.980 Å. This result causes changes in the unit cell parameters, increasing the $c$-axis by 0.28 Å compared to the $b$-axis, while the latter becomes 0.13 Å longer than the $a$ lattice parameter; see Figure 6.4b and Table 6.2. Compared to the lithiated spinel[64], the sodiated system shows a 65% larger distortion, due to the larger ionic radius of the Na-ions. It is important to acknowledge that the presented Jahn-Teller-distortions are not unique. There is an infinate number of orderings that satisfy the bond length criteria explored within.[66] To obtain the lowest energy orderings (zigzag or collinear depending on the system) a full investigation according to the work of Radin et. al. is required.[66].

**Table 6.2:** Lattice parameters of the end member phases

| | a (Å) | b (Å) | c (Å) | Mn oxidation state |
|---|---|---|---|---|
| $Mn_2O_4$ | 8.242 | 8.242 | 8.242 | 4+ |
| $Na_1Mn_2O_4$ | 8.686 | 8.535 | 8.813 | 3+/4+ |
| $Na_2Mn_2O_4$ | 9.110 | 8.517 | 9.106 | 3+ |

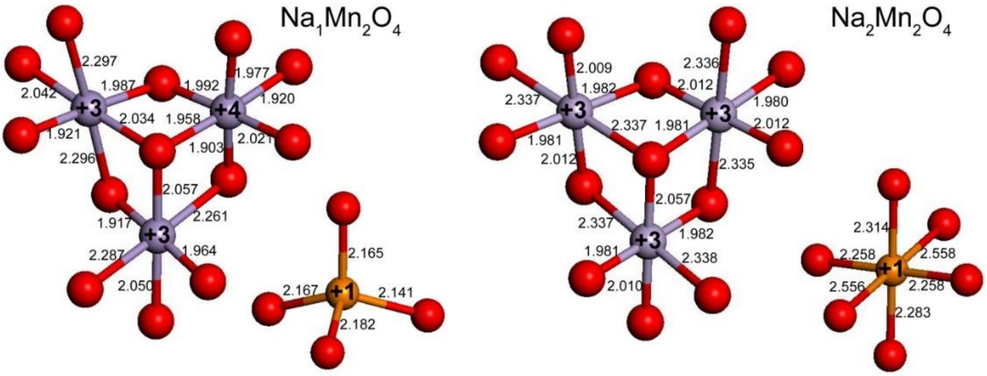
$Na_1Mn_2O_4$
+3
+4
+3
+1
2.297
2.042
1.987
1.921
2.034
2.296
1.992
1.977
1.920
1.958
1.903
2.021
2.057
2.261
1.917
2.287
1.964
2.050
2.165
2.167
2.141
2.182
$Na_2Mn_2O_4$
+3
+3
+3
+1
2.009
2.337
1.982
1.981
2.337
2.012
2.336
2.012
1.980
1.981
2.012
2.335
2.057
2.337
1.982
1.981
2.338
2.010
2.314
2.258
2.558
2.556
2.258
2.283

**Figure 6.5**: Local atomic environment and oxidation states of Mn octahedra and Na tetrahedra

The computations reproduce the cubic to tetragonal (I41/amd) lattice[10, 15] transformation when Na is inserted to the 16c sites to form the $\mathrm{Na_2Mn_2O_4}$ composition, similar to the Li analog[67].Only $\mathrm{Mn^{3+}}$ is present in this composition, and as a result, the $a$ and $c$ lattice constants become equal again, due to alternating elongations in the respective octahedra (Figure 6.5).

## 6.5 Na-Ion Insertion in λ-$\mathrm{Mn_{1.5}Ni_{0.5}O_4}$ and Mn/Ni Ordering – Reaction Mechanisms Dependence

Experimentally, Na-ion insertion in MNO spinel structures occurs up to a maximum composition of λ-$\mathrm{Na_1Mn_{1.5}Ni_{0.5}O_4}$, where the Na ions occupy the tetrahedral 8a sites.[10, 11] For this reason, DFT simulations were performed within this concentration range. In agreement with experimental observations, the present simulations resulted in a Na-ion occupancy of the tetrahedral 8a sites in the case of λ-$\mathrm{Na_1Mn_{1.5}Ni_{0.5}O_4}$ composition.

Enthalpies of formation of the $\mathrm{P, F1, F2}$ and $\mathrm{C-MNO}$ structures were determined as a function of Na content. The convex hull, the tie line that connects the lowest energy configurations is shown for each of the MNO phases in Figure 6.6a. Interestingly, significantly different sodiation mechanisms are predicted for the 4 MNO phases.

The ordered structure ($\mathrm{P-MNO}$) exhibits unstable intermediate phases during sodiation, except for two of the $\mathrm{Na_{0.5}Mn_{1.5}Ni_{0.5}O_4}$ configurations, which are more stable by 52 meV, compared to the reference phases. Thus, the perfectly ordered material is expected to exhibit two first order phase transitions: between $0 < x < 0.5$ and between $0.5 < x < 1$. Considering that the enthalpy of formation of the $\mathrm{Na_{0.5}Mn_{1.5}Ni_{0.5}O_4}$ configuration is comparable to the thermal energy associated with room temperature (25 meV), in practice, one first order phase transition between the end-member phases may be observed.

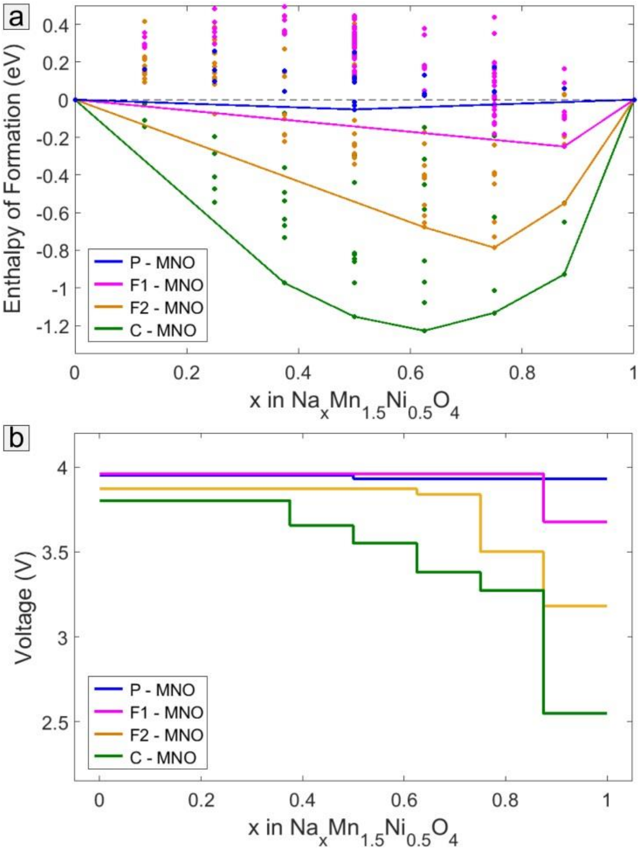

**Figure 6.6:** For the $\mathrm{P}, \mathrm{F1}, \mathrm{F2}$ and $\mathrm{C-MNO}$ structures **a)** Enthalpies of formation and convex hulls of Na-ion insertion and **b)** Voltage profiles.

For the disordered phases ($\mathrm{F1}$ and $\mathrm{F2-MNO}$), a notable shift in the stability of the intermediate configurations is predicted. At large sodium compositions, several configurations are predicted to be thermodynamically stable. Consequently the disordered structure is expected to follow a two-phase reaction between $0 < x < 0.875$ and $0 < x < 0.625$ in the case of $\mathrm{F1}$ and $\mathrm{F2-MNO}$, respectively, followed by a solid solution reaction towards the $\mathrm{Na_1Mn_{1.5}Ni_{0.5}O_4}$ composition. A phase separation region that terminates at $x = 0.75$ might also occur for both the disordered spinels, since the convex line of the $\mathrm{F1}$ and $\mathrm{F2}$ variants is within 30 meV of $\mathrm{Na_{0.75}Mn_{1.5}Ni_{0.5}O_4}$ and $\mathrm{Na_{0.625}Mn_{1.5}Ni_{0.5}O_4}$, respectively. Regarding the $\mathrm{C-MNO}$ lattice, configurations at lower sodium concentrations fall on the convex hull, resulting in a much smaller two phase region between $0 < x < 0.375$, where further sodiation is predicted to follow a solid solution reaction.

The enthalpies of formation allows us to predict the voltages, at 0 K, as shown in Figure 6.6b. The ordered phase ($P-MNO$) exhibits two voltage plateaus, reflecting the two phase transitions. For the $F1, F2$ and $C-MNO$ spinels, however, the voltage plateau, and thus the two phase region, terminates before reaching the $Na_1Mn_{1.5}Ni_{0.5}O_4$ endmember composition, and it is followed by a potential drop via several compositions, indicating a solid solution mechanism. The two voltage plateaus of the $P-MNO$ structure are very similar in voltage, a direct consequence of the marginal stability difference of the lowest energy $Na_{0.5}Mn_{1.5}Ni_{0.5}O_4$ compared to the endmember phases. The same holds for the two first voltage plateaus of the disordered $F2-MNO$ structure, as observed in Figure 6.6b.

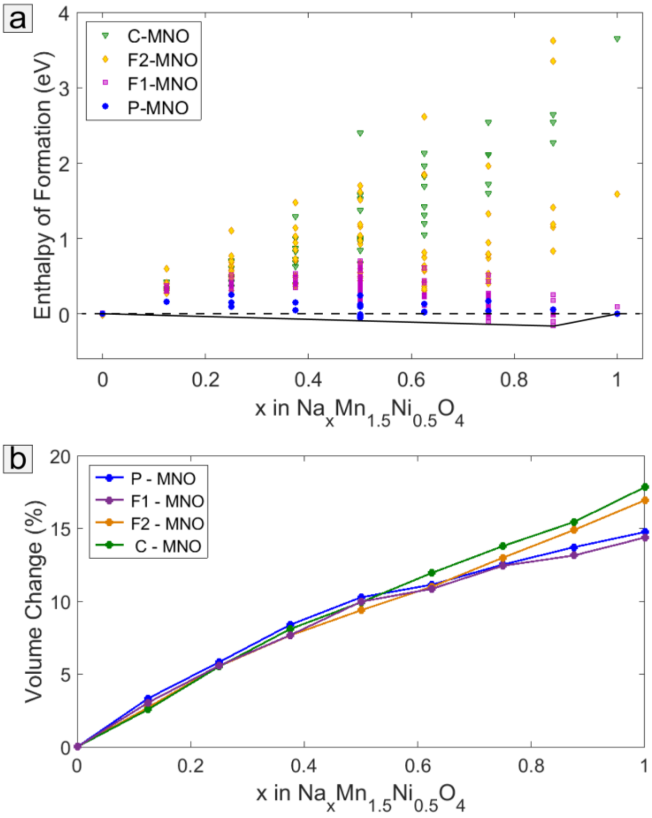

**Figure 6.7: a)** Enthalpies of formation referenced to the P-MNO structure. **b)** Volume changes for the MNO variants throughout the sodiation process

To better demonstrate the relative stability of the $\mathrm{P, F1, F2}$ and $\mathrm{C-MNO}$ structures throughout the sodiation range, the enthalpy of formation figure was redrawn (Figure 6.7a) with respect to the $\mathrm{P-MNO}$ structure. Referring all $\mathrm{MNO}$ to the $\mathrm{P-MNO}$ configuration will not only enable a direct comparison of the relative stability at a given composition but will additionally explain the effect of ordering on the energy environment of the structure during sodiation. Furthermore, in the latter section of this paper, we show Ni migrating from its original position in the host lattice. Considering that Ni is mobile in the host structure, the relative stability plot can reveal the driving forces that might lead to interconversions between the various configurations during sodiation. For example, the disordered $\mathrm{F1-MNO}$ variant is more stable than the $\mathrm{P-MNO}$ in the 0.75<x<0.875 concentration region. Assuming interconversions are fully accessible within (de)sodiation timescales, both ordered and disordered structures are expected to phase separate up to the disordered $\mathrm{F1-Na_{0.875}Mn_{1.5}Ni_{0.5}O_4}$ phase (Figure 6.7a).

Volume changes throughout the concentration range are presented in Figure 6.7b. Comparing the $\mathrm{Na_1Mn_{1.5}Ni_{0.5}O_4}$ configurations, we observe that the $\mathrm{F1}$ and $\mathrm{P-MNO}$ have the lowest volume change, followed by the Ni clustered variants $\mathrm{F2}$ and $\mathrm{C-MNO}$. The $\mathrm{P-MNO}$ displays the largest volume change, however, at the initial stages of sodiation, the structures with a more clustered Ni distribution appear to change less, as Na insertion occurs in the vicinity of the Ni cluster.

Kim and colleagues monitored the sodiation of both ordered (P) and disordered (F) $\mathrm{MNO}$ spinels ex-situ, in-situ, and in operando by X-ray diffraction, as well as with PITT and GITT measurements.[10, 11] For the ordered phase the phase separation region was reported for a concentration range of $0 < x < 0.93$.[11] The disordered phase was shown to display a first order phase transition up to x = 0.88, followed by a solid solution towards the endmember $\mathrm{Na_1Mn_{1.5}Ni_{0.5}O_4}$ phase.[11] Interestingly, the experimentally observed phase separation region varies depending on the experimental method, ending at $\mathrm{x} = 0.70$, $x = 0.78$, $x = 0.87$, and $x = 0.88$ in $\mathrm{Na_xMn_{1.5}Ni_{0.5}O_4}$, when measured at C/60 with X-ray[10], C/40 with X-ray[10], with GITT[10], and GITT[11], respectively. This was rationalised by the dynamic character of operando by X-ray diffraction, which affects the phase separation region, in contrast to the GITT measurements, which keep the system closer to thermodynamic equilibrium.[10] Subsequent Na (de)insertion in the ordered and disordered spinel structures was experimentally investigated as well.[11] A vast variety of two-phase regions and solid solution reaction mechanisms were reported, which appear to be different for the two structures, but also appear to depend on the cycling conditions.[11]

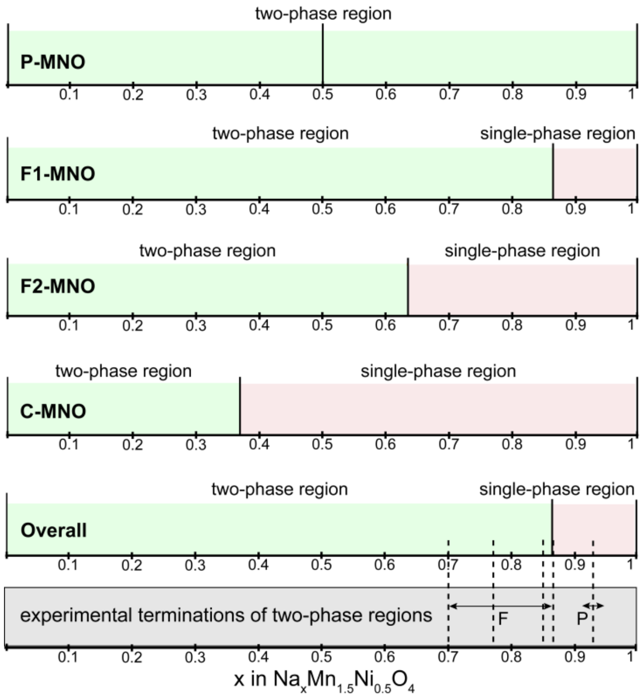

**Figure 6.8:** Reaction mechanisms of the $\mathrm{P, F1, F2}$ and $\mathrm{C-MNO}$ structures during sodiation at 0K. Solid vertical lines indicate the range of the two phase separation (light green colour) and single phase regions (light red colour). The "overall" thermodynamic profile refers to the lowest enthalpy path predicted when considering the relative stability of all configurations (Figure 6.7a). Below, the dashed lines indicate the experimentally determined[10, 11] terminations of the two-phase region in both disordered (F) and ordered (P) structures.

The thermodynamic behaviour, at 0 K, of the different spinel structures considered within, in comparison with experimental results[10, 11], is summarized in Figure 6.8. The simulations suggest that the Ni distribution through the spinel lattice alters the sodiation reaction mechanism, effectively modifying the extent of the phase separation region in good agreement with the experimental picture. The small differences in stability between the various configurations predicted at present may be easily bridged by the kinetically induced overpotentials or interconversion due to Ni rearrangement, rationalising the diversity of reaction pathways observed experimentally. In addition, different preparation methods may result in different Ni distributions, which strongly influence the relative stability. However, we should be very critical when using Figure 6.8 to draw comparisons with experiments. Since the reaction mechanisms predicted herein refer to 0 K, the comparison presented has a speculative character. A complete phase stability study[27] will be needed to estimate the temperature dependence at which the ordered states disorder, forming a solid solution. Gaining a more detailed insight would require Monte Carlo (MC) simulations of numerous configurations, similar to the approach followed by Lee et al.[27].

Also with regard to Li-ion insertion into $\lambda - \mathrm{MNO}$, the impact of Mn/Ni ordering has been observed.[26, 27] A favourable alternating pattern of lithium and vacancies in the spinel lattice was reported.[26] The "uniform"[27] disordered configuration was found to have a Mn/Ni arrangement that was compatible with this preferable Li/Va arrangement. Thus, the ground state of the disordered spinel was predicted to be the intermediate $\mathrm{Li_{0.5}Mn_{1.5}Ni_{0.5}O_4}$ phase, explaining the origin of the small voltage step experimentally observed at this concentration.[26] Various two phase regions were observed, up to a maximum composition of 0.5<x<1, depending on the Mn/Ni ordering in LMNO variants, indicating the importance of the local Mn/Ni environment.[26] By utilising grand canonical Monte Carlo (MC) simulations, the phase diagrams of perfectly ordered and partially ordered spinels were obtained, which showed a clear correlation between the cation distribution and the reaction mechanisms.[27] One of the key findings suggests that the more ordered the material is, the less likely it is to access a solid solution region. On the other hand, increasing the Ni/Mn disorder, in the Li-ion system, stabilises configurations at high Li contents, effectively enhancing the stability of solid solutions.[27] The enthalpy of formation results of this study suggest the same behaviour in the case of the Na-ion system, in line with previous experimental demonstrations[10, 11], as well as with the present prediction regarding phase transformation behaviour. In addition, for the Li-ion system, a "uniform"[27] disordered distribution of Ni induces the largest solid solution reaction region, which is suggested to be achievable by controlled synthesis.[27]

Examining the $\mathrm{Na_{0.5}Mn_{1.5}Ni_{0.5}O_4}$ lowest energy configurations of the P and $\mathrm{F1 - MNO}$ structures, reveals that Na-ions order in a Na-Va-Na-Va arrangement, same to the Li-ion case. The higher stability of the $\mathrm{Na_{0.5}Mn_{1.5}Ni_{0.5}O_4}$ P configuration results in the small voltage step which is observed in Figure 6.6b. In Li-ion systems, this attribute is predicted and experimentally experienced in disordered spinels.[26] The difference between the two ions may be attributed to the larger structural penalties experienced by Na-ion insertion affecting the local preferable Na/Va – Mn/Ni arrangement. There is a probability that other disordered configurations (such as the "uniform"[27] disordered distribution) might lead to a more stable $\mathrm{Na_{0.5}Mn_{1.5}Ni_{0.5}O_4}$ phase. Considering the experiments, this seems unlikely in the Na-ion case, given that no such voltage step is observed for either of the phases, as this effect is probably smoothened out in room temperature due to local disorder[26].

Tuning of the termination of the phase separation region will lead to a better electrochemical performance, enabling the advantages (better cycling stability and kinetics) of solid solution insertion mechanisms.[10, 11] Herein, the maximum solid solution region was determined with regard to the Ni clustered spinel. Considering the energy analysis in section 6.3, and the relative stability results, presented in Figure 6.7a, the clustered host is highly unlikely to occur. Since the Na system is found to behave extremely similar with the Li-ion system, it is expected that similar aproaches[26, 27] for improving the solid solution region are applicable. Similar to the Li system, here we find that avoiding the ordered structure is of primary importance, since it resists the most solid solution insertion.

## 6.6 Na-Ion Kinetics, Ni Migration and Inverse Spinel Insights via MD Simulations

To evaluate the kinetic properties of Na-ions in the spinel lattices, nudge elastic band (NEB) and molecular dynamics (MD) calculations were employed, based on DFT. The spinel framework provides a diagonal 3D diffusion network for Na-ions connecting the tetrahedral (8a) positions via the metastable octahedral (16c) sites (Figure 6.9a).

For the $\mathrm{Mn_2O_4}$ structure, the Na-ion migration path for the tetrahedral network was determined both at the high vacancy limit and at the dilute vacancy limit, using the NEB method (Figure 6.9b). We converged DFT+U NEB calculations, even though they are usually regarded difficult to converge due to the high metastability of the intermediate electronic states[19]. In line with earlier findings[19, 65, 68], the similarity of the DFT+U and DFT results indicates that DFT + U does not necessarily lead to better results with regard to ion migration.

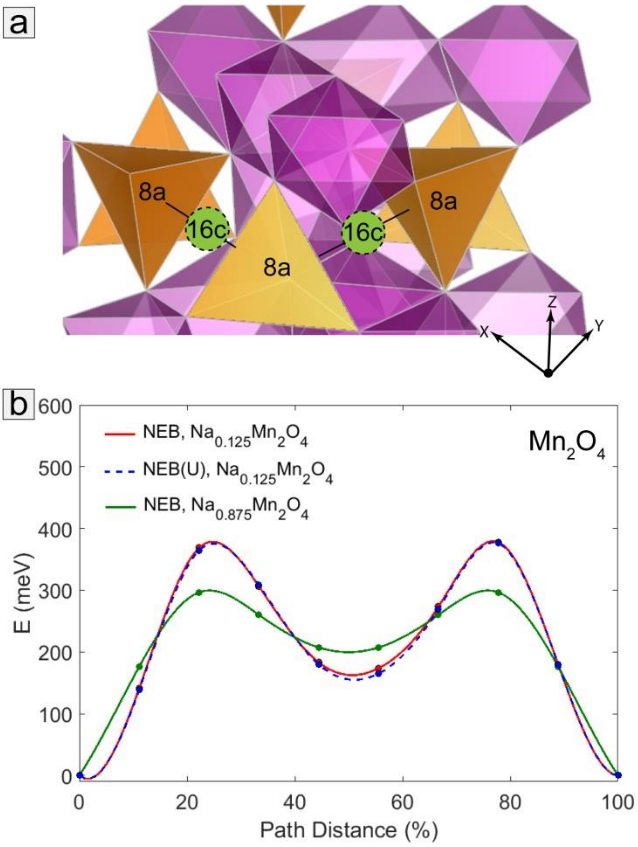

**Figure 6.9: a)** Schematic representation of the 3D diffusion network in the spinel lattice. **b)** Na-ion migration paths between the tetrahedral sites at the high vacancy limit (red solid and blue dashed lines) and at the dilute vacancy limit (green solid line) determined with NEB. The dashed blue line represents the DFT + U calculation.

In Figure 6.10, the predicted Na-ion migration path (purple colour) is integrated on top of multivalent ion and Li-ion migration paths obtained from literature[19]. The divalent ions $Zn^{2+}$ and $Mg^{2+}$ display high barriers between 0.85 and 1.00 eV and 0.60 and 0.80 eV respectively. $Ca^{2+}$ (0.20 – 0.50 eV), on the other hand, demonstrates barriers close to $Li^{+1}$ (0.40 – 0.60 eV). Finally $Na^{+1}$, exhibiting energy barriers between 0.30 and 0.40 meV, outperforms the $Zn^{2+}$, $Mg^{2+}$ multivalent carriers, having comparable values to $Ca^{2+}$ and $Li^{+1}$, despite its larger ionic radius. Low Na-ion energy barriers have also been reported for layered cathode and anode materials, as for instance, the O3 (0.20 – 0.28 eV) and P3 (0.20 – 0.48 eV) $Na_xCrO_2$ cathode material[69], the P2 (0.12 – 0.19 meV) and P3 (0.22 –

0.25 eV) $NaTiO_2$ anode material[70], and the O3 (0.125 – 0.28 eV) $NaTiO_2$ anode material[52, 71]. Kinetic concerns rise in case of strong electrostatic repulsions between the Na ions that can occur either in structures that allow Na – Na close neighbouring occupation (~1.6 Å)[69], or by close interstitial Na - Na coexistence along the diffusion coordinate, blocking diffusion[52]. Generally, however, Na-ion kinetics look consistently facile in most materials, indicating that mobility is not a major concern, leaving cycling stability as the primary obstacle for NABs implementation.

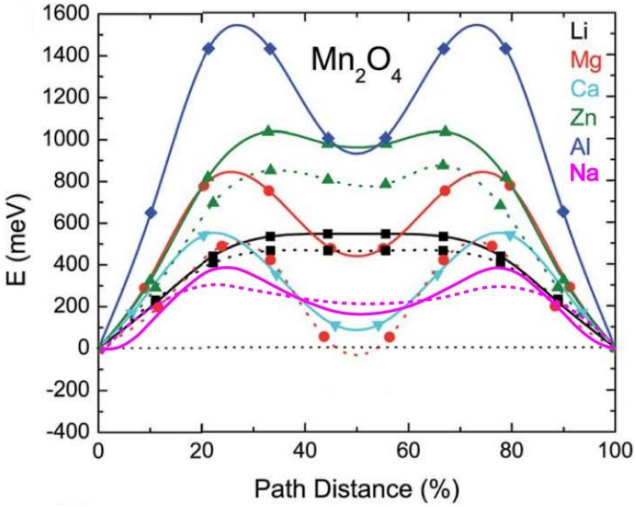

**Figure 6.10:** Migration barriers of multivalent ions and Li, reproduced from literature[19] published by The Royal Society of Chemistry. The lines for the Li, Mg, Ca, Zn, and Al represent the computed minimum energy paths for migration between the tetrahedral sites in the $Mn_2O_4$ spinel at the high vacancy limit (solid line) and dilute vacancy limit (dotted line), i.e. one mobile species per supercell.[19] The present Na-ion migration path (purple color) has been added to the original figure.

To further investigate the kinetic picture revealed by the NEB method, MD simulations were performed based on DFT. The Na-ion density plot for a 440 ps simulation of 1 Na-ion diffusing in the $Mn_2O_4$ unit cell lattice ($Na_{0.125}Mn_2O_4$) at 600K is presented in Figure 6.11a. The Na-ion density indicates high Na mobility through the 8a-16c-8a sublattice, responsible for macroscopic diffusion, predicted within the MD timescales. The displacement of the atoms is presented in Appendix D.

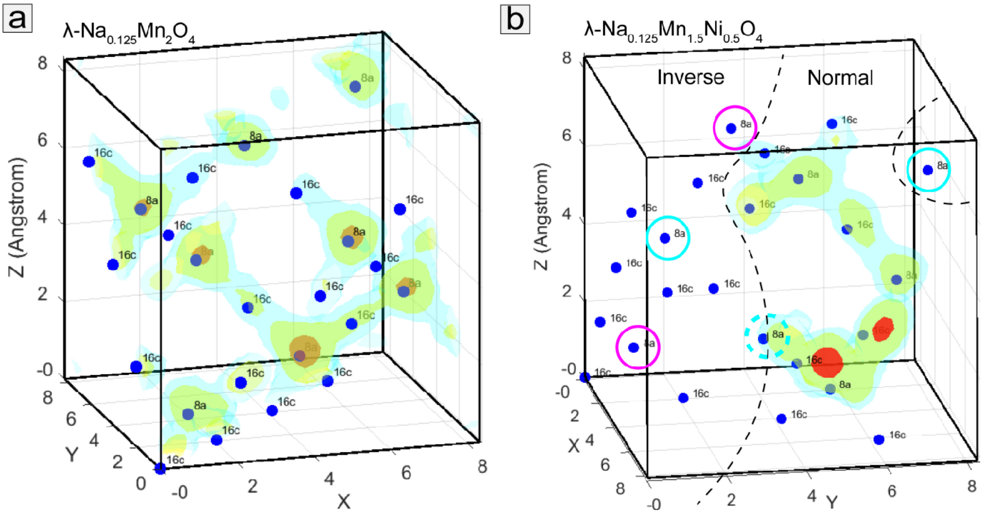

**Figure 6.11: a)** Na-ion density during 440 ps MD simulation at 600 K for the $Na_{0.125}Mn_2O_4$ phase **b)** Na-ion density during 440 ps MD simulation at 600 K for the $F2 - Na_{0.125}Mn_{1.5}Ni_{0.5}O_4$ phase.

NEB convergence was not achieved for the MNO spinel structures due to large forces along the migration path. However, MD calculations provide insight regarding both stability and kinetics. An MD simulation for the $F2 - Na_{0.125}Mn_{1.5}Ni_{0.5}O_4$ variant was performed at 600 K for 440 ps. The Na-ion density map of 1 diffusing Na-ion in the $F2 - MNO$ structure is presented in Figure 6.11b, and the atom displacements are presented in Appendix D. MD simulations predict that Ni atoms diffuse from the transition metal site into the 8a sites of the spinel structure. This occurs relatively fast (within ~45 ps out of the total 440 ps). Mn atoms are migrating as well, albeit later, during the MD simulation (at approximately ~89 ps out of the total 440). The structure appears to equilibrate after 100 ps (Figure 6.12), retaining the spinel framework. The Ni and Mn migration is a clear indication that the $F2 - Na_{0.125}Mn_{1.5}Ni_{0.5}O_4$ configuration is transforming towards the inverse spinel structure at high temperatures. In total, 4 out of the 8 tetrahedral (and only partially the 5th) sites where occupied by Ni or Mn atoms, while the transition metal octahedral sites where occupied by vacancies, indicating that half of the material transformed to the inverse spinel configuration, whereas the other half remained in the normal spinel form (Figure 6.11b). Thereby, the MD simulations confirm that at elevated temperatures, many compounds with spinel lattices display both the normal and inverse cation arrangements, as experimentally observed.[62] The Na ion density (Figure 6.11b) is in the normal spinel configuration, where the Na-ion appears mobile. Ni and Mn are blocking the tetrahedral sites in the inverse spinel region, effectively prohibiting access to half of the unit cell, at least within the short time scale that can be simulated via MD. This demonstrates the superior kinetics of the normal spinels, confirming that a network of tetrahedral sites offers faster ion transport than a network of octahedral sites.[62, 72] The dashed cyan circle in Figure 6.11b represents a tetrahedral 8a site that was partially occupied by Ni during the MD simulation, with Ni being able to hop back to its original transition metal octahedral site. It is also observed (Figure 6.11b), that when Na resides close to the normal/inverse boundary (dashed cyan circle) of the unit cell, it spends most of the time near a 16c octahedral environment.

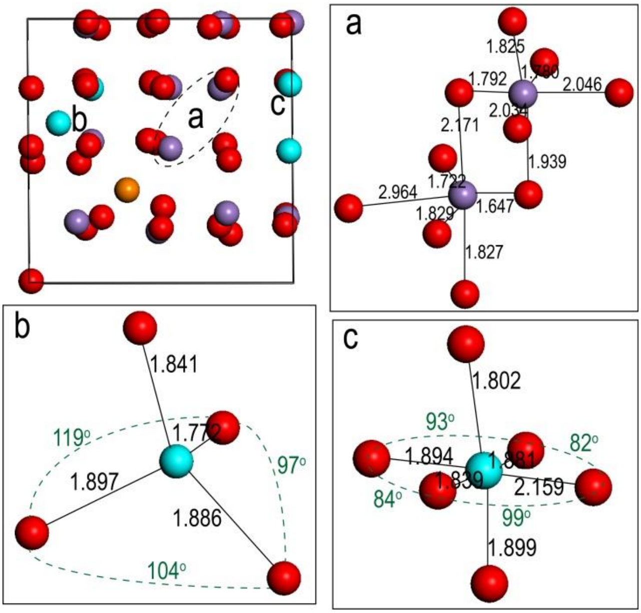

**Figure 6.12:** Snapshot of the equilibrated $\mathrm{F2-Na_{0.125}Mn_2O_4}$ structure after 150 ps of the MD simulation at 300 K and local environments of **a)** two Mn octahedral positions, one of the octahedral sites is very distorted **b)** the tetrahedral Ni coordination **c)** the transition metal octahedral Ni coordination.

With regard to $\mathrm{F1}$ and $\mathrm{P-Na_{0.125}Mn_2O_4}$ spinel structures, the MD simulations at 600 K reveal Ni migration into the tetrahedral sites, demonstrating that this phenomenon is independent of the Ni/Mn configuration. Contrary to the F2 spinel, no Mn migration was observed. The equilibration of the ordered

$P-Na_{0.125}Mn_2O_4$ variant revealed that, within 500 ps, all 4 Ni atoms migrated and occupied tetrahedral positions, effectively blocking Na diffusion. Na mainly remained in its original position throughout the MD simulation. In addition, once two or more Ni occupy the tetrahedral positions, Na stabilises in an octahedral environment for the rest of the simulation. Snapshots of the $P-Na_{0.125}Mn_2O_4$ structure throughout the MD simulation are presented in Figure 6.13. Atom displacements are presented in Appendix D.

Even though quantitative characterisation of the MD results was not achieved, an interesting qualitative trend was discovered, where Ni (and even Mn) was shown to migrate into the tetrahedral sites, lowering the Na-ion diffusion. This migration leads to the inverse spinel structure and creates the conditions for interconversion between the various Ni/Mn configurations. Stability tests with the Bhattacharya and Wolverton method[62] for all Ni/Mn inverse spinel replacements is suggested to strengthen this argument. Although this is a subject for future work, beyond the length and focus of this study.

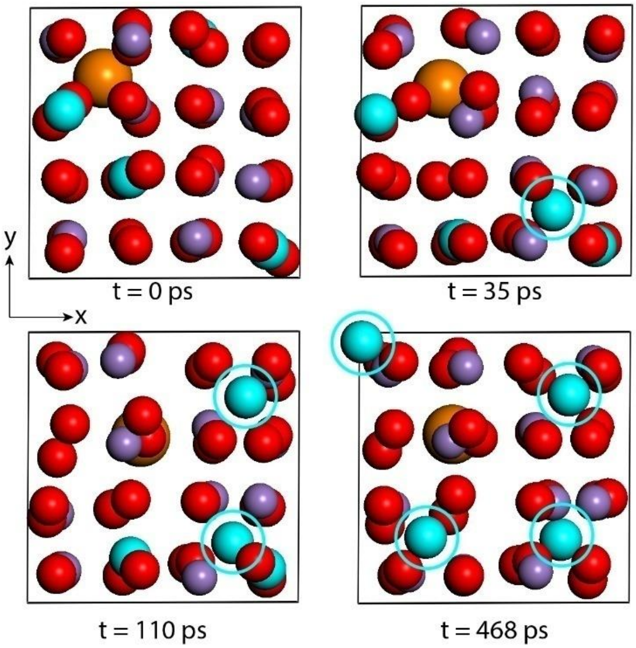

**Figure 6.13:** Snapshots of the $P-Na_{0.125}Mn_2O_4$ structure throughout the 500 ps MD simulation at 600 K: (top-left) only Na occupies a tetrahedral position; (bottom-right) all 4 Ni occupy tetrahedral positions

There is experimental evidence that $Ni^{+4}$ migrates into the tetrahedral sites during Li extraction[24, 25], rationalising the present predictions for its Na-ion counterpart. Experimentally, with regard to Ni doped variants, it has been observed that after the initial sodiation, there is a significant difficulty in extracting all the Na-ions out of the sodiated structure.[10, 11] Ni migration, as revealed by MD simulations and/or partial conversion into the inverse structure may rationalise this. The tetrahedral diffusion network at low Na concentrations is blocked, hindering Na movement and possibly trapping some part of the Na. In other words, when regions close to the surface are de-sodiated, the low Na concentration may lead to Ni migration towards tetrahedral sites, and/or partial formation of the inverse spinel, thus hindering full de-sodiation. Since we observed at least once Ni hopping back to its transition metal site within MD timescales, we speculate that re-sodiating the material may promote Ni to migrate back to its original octahedral position, potentially explaining why such kinetic difficulty is experienced only during de-sodiation.

## 6.7 Conclusions

Key thermodynamic and kinetic properties of Na-ion insertion in the λ-$Mn_2O_4$ and λ-$Mn_{1.5}Ni_{0.5}O_4$ spinels are revealed, adding to the understanding and facilitating improvement of the high voltage cathode materials for Na-ion batteries.

Full sodiation of the pure spinel was found to be thermodynamically possible. Two two-phase separation mechanisms are predicted, occuring at 3.2V and 2.4V, vs. $Na/Na^+$, where Na is accommodated in the 8a and 16c interstitial positions respectively. This is in agreement with experiments conducted in aqueous environment, showing reversible Na-ion insertion. All the spinel sodiated phases, however, are found to be metastable compared to O’3/O3 layered and post spinel structures. Lattice distortions upon Na (de)insertion may catalyse these phase transitions upon sodium cycling, rationalising experimental findings of structural destabilization and partial phase tranformation towards the O’3 layered lattice. The large lattice mismatch predicted for the endmember phases is expected to have an important effect in the cycling performance. Strain minimisation should be prioritised to avoid material breakdown and/or phase transformations. Strain minimisation could be achieved by nanosizing and fast cycling, suppressing the phase separation mechanism into solid solution Na-ion insertion (which is likely, considering the expected phase-coexistence energy penalty). This will improve the cycle life, and moreover the kinetics, as well as aid in avoiding the often sluggish diffusion over phase interfaces. Rapid Na-ion hopping is predicted by energy barrier calculations that are comparable to and lower than the ones predicted for Li-ion and multivalent ions respectively. This was confirmed with MD simulations showing Na-ion diffusivity at short MD timescales. This means that once the structure destabilisation and kinetic phase-interface limitations are overcome, good kinetic performance is expected, in agreement with experiments reporting an excellent rate capability.

With regard to the λ-$Mn_{1.5}Ni_{0.5}O_4$ spinel, we investigated several ordered/disordered phases, differing in the Ni distribution within the spinel lattice. The exact sodiation mechanism depends on the transition metal ordering, similar to the equivalent Li-ion structures. The Ni distribution greatly affects the relative stability of the intermediate phases, and thus, the reaction mechanisms. The ordered spinel is expected to sodiate via phase separation, exhibiting no solid solution. The disordered spinels, however, show stable intermediate phases in the $0.625 < x < 0.875$ ($Na_xMn_{1.5}Ni_{0.5}O_4$) concentration range, either by lowering the energy landscape due to a preferable Ni/Mn - Na/Va arrangement at this concentration range, or by raising the energy of the fully sodiated endmember. Therefore, mixed reaction pathways of phase separation, and solid solution reaction mechanisms are predicted in excellent agreement with experiments. This behaviour is similar to that of the equivalent Li-ion structures. MD simulations revealed that Ni can diffuse from the TM site into the tetrahedral position (even at room temperature), which explains the kinetic limitations experienced experimentally during Na extraction. In addition, MD simulations point out that the λ-$Mn_{1.5}Ni_{0.5}O_4$ spinel converts into the inverse spinel under high temperatures, hindering Na-ion kinetics. MD results open up new possibilities in the study of inverse spinels and the effect on kinetic performance. Finally, Ni migration and partial transformation towards the inverted spinel may be considered phenomena of general interest, as they are also encountered in Li-ion batteries that show similar electrochemical behaviour.

# References

**1.** Mulder, F. M. Implications of diurnal and seasonal variations in renewable energy generation for large scale energy storage. *J. Renewable Sustainable Energy* 2014**,** 6, 033105

**2.** Palomares, V.; Casas-Cabanas, M.; Castillo-Martinez, E.; Han, M. H.; Rojo, T. Update on Na-based battery materials. A growing research path. *Energy Environ. Sci.* 2013, 6, 2312-2337.

**3.** Kim, S. W.; Seo, D. H.; Ma, X. H.; Ceder, G.; Kang, K. Electrode Materials for Rechargeable Sodium-Ion Batteries: Potential Alternatives to Current Lithium-Ion Batteries. *Adv. Energy Mater.* 2012, 2, 710-721.

**4.** Dai, Z. F.; Mani, U.; Tan, H. T.; Yan, Q. Y. Advanced Cathode Materials for Sodium-Ion Batteries: What Determines Our Choices? *Small Methods* 2017, 1, 1700098.

**5.** Xiang, X. D.; Zhang, K.; Chen, J. Recent Advances and Prospects of Cathode Materials for Sodium-Ion Batteries. *Adv. Mater.* 2015, 27, 5343-5364.

**6.** Kubota, K.; Komaba, S., Review-Practical Issues and Future Perspective for Na-Ion Batteries. *J. Electrochem. Soc.* 2015, 162, A2538-A2550.

**7.** Kim, H.; Hong, J.; Park, K. Y.; Kim, H.; Kim, S. W.; Kang, K. Aqueous Rechargeable Li and Na Ion Batteries. *Chem. Rev.* 2014, 114, 11788-11827.

**8.** Sawicki, M.; Shaw, L. L. Advances and challenges of sodium ion batteries as post lithium ion batteries. *RSC Adv.* 2015, 5, 53129-53154.

**9.** Luo, J. Y.; Cui, W. J.; He, P.; Xia, Y. Y. Raising the cycling stability of aqueous lithium-ion batteries by eliminating oxygen in the electrolyte. *Nat. Chem.* 2010, 2, 760-765.

**10.** Kim, J. R.; Amatucci, G. G., Structural and Electrochemical Investigation of $Na^+$ Insertion into High-Voltage Spinel Electrodes. *Chem. Mater.* 2015, 27, 2546-2556.

**11.** Kim, J. R.; Amatucci, G. G., $NaMn_{2-x}Ni_xO_4$ Derived from Mesoporous $LiMn_{2-x}Ni_xO_4$ High-Voltage Spinel Cathode Materials for Na-Ion Batteries. *J. Electrochem. Soc.* 2016, 163, A696-A705.

**12.** Li, X.; Wu, D.; Zhou, Y. N.; Liu, L.; Yang, X. Q.; Ceder, G. O3-type $Na(Mn_{0.25}Fe_{0.25}Co_{0.25}Ni_{0.25})O_2$: A quaternary layered cathode compound for rechargeable Na ion batteries. *Electrochem. Commun.* 2014, 49, 51-54.

**13**. Yuan, D. D.; Hu, X. H.; Qian, J. F.; Pei, F.; Wu, F. Y.; Mao, R. J.; Ai, X. P.; Yang, H. X.; Cao, Y. L. P2-type $Na_{0.67}Mn_{0.65}Fe_{0.2}Ni_{0.15}O_2$ Cathode Material with High-capacity for Sodium-ion Battery. *Electrochim. Acta* 2014, 116, 300-305.

**14.** Tarascon, J. M.; Guyomard, D. G.; Wilkens, B.; Mckinnon, W. R.; Barboux, P. Chemical and Electrochemical Insertion of Na into the Spinel Lambda-$MnO_2$ Phase. *Solid State Ionics* 1992, 57, 113-120.

**15.** Yabuuchi, N.; Yano, M.; Kuze, S.; Komaba, S. Electrochemical behavior and structural change of spinel-type $Li[Li_xMn_{2-x}]O_4$ (x=0 and 0.2) in sodium cells. *Electrochim. Acta* 2012, 82, 296-301.

**16**. Whitacre, J. F.; Wiley, T.; Shanbhag, S.; Wenzhuo, Y.; Mohamed, A.; Chun, S. E.; Weber, E.; Blackwood, D.; Lynch-Bell, E.; Gulakowski, J.; Smith, C.; Humphreys, D. An aqueous electrolyte, sodium ion functional, large format energy storage device for stationary applications. *J. Power Sources* 2012, 213, 255-264.

**17.** Zhang, Y.; Yuan, C. L.; Ye, K.; Jiang, X.; Yin, J. L.; Wang, G. L.; Cao, D. X., An aqueous capacitor battery hybrid device based on Na-ion insertion-deinsertion in lambda-$MnO_2$ positive electrode. *Electrochim. Acta* 2014, 148, 237-243.

**18.** Yuan, C. L.; Zhang, Y.; Pan, Y.; Liu, X. W.; Wang, G. L.; Cao, D. X., Investigation of the intercalation of polyvalent cations ($Mg^{2+}$, $Zn^{2+}$) into lambda-$MnO_2$ for rechargeable aqueous battery. *Electrochim. Acta* 2014, 116, 404-412.

**19.** Liu, M.; Rong, Z. Q.; Malik, R.; Canepa, P.; Jain, A.; Ceder, G.; Persson, K. A. Spinel compounds as multivalent battery cathodes: a systematic evaluation based on ab initio calculations. *Energy Environ. Sci.* 2015, 8, 964-974.

**20.** Cabana, J.; Casas-Cabanas, M.; Omenya, F. O.; Chernova, N. A.; Zeng, D. L.; Whittingham, M. S.; Grey, C. P. Composition-Structure Relationships in the Li-Ion Battery Electrode Material $LiNi_{0.5}Mn_{1.5}O_4$. *Chem. Mater.* 2012, 24, 2952-2964.

**21.** Amdouni, N.; Zaghib, K.; Gendron, F.; Mauger, A.; Julien, C. M. Structure and insertion properties of disordered and ordered $LiNi_{0.5}Mn_{1.5}O_4$ spinels prepared by wet chemistry. *Ionics* 2006, 12, 117-126.

**22.** Idemoto, Y.; Narai, H.; Koura, N. Crystal structure and cathode performance dependence on oxygen content of $LiMn_{1.5}Ni_{0.5}O_4$ as a cathode material for secondary lithium batteries. *J. Power Sources* 2003, 119, 125-129.

**23.** Pasero, D.; Reeves, N.; Pralong, V.; West, A. R. Oxygen nonstoichiometry and phase transitions in $LiMn_{1.5}Ni_{0.5}O_4$-delta. *J. Electrochem. Soc.* 2008, 155, A282-A291.

**24.** Rana, J.; Glatthaar, S.; Gesswein, H.; Sharma, N.; Binder, J. R.; Chernikov, R.; Schumacher, G.; Banhart, J. Local structural changes in $LiMn_{1.5}Ni_{0.5}O_4$ spinel cathode material for lithium-ion batteries. *J. Power Sources* 2014, 255, 439-449.

**25**. Kim, J. H.; Myung, S. T.; Yoon, C. S.; Kang, S. G.; Sun, Y. K. Comparative study of $LiNi_{0.5}Mn_{1.5}O_4$-delta and $LiNi_{0.5}Mn_{1.5}O_4$ cathodes having two crystallographic structures: $Fd\bar{3}m$ and $P4_332$. *Chem. Mater.* 2004, 16, 906-914.

**26.** Lee, E.; Persson, K. A. Revealing the coupled cation interactions behind the electrochemical profile of $Li_xNi_{0.5}Mn_{1.5}O_4$. *Energy Environ. Sci.* 2012, 5, 6047-6051.

**27.** Lee, E.; Persson, K. A. Solid-Solution Li Intercalation as a Function of Cation Order/Disorder in the High-Voltage $Li_xNi_{0.5}Mn_{1.5}O_4$ Spinel. *Chem. Mater.* 2013, 25, 2885-2889.

**28.** Kresse, G.; Furthmuller, J. Efficiency of ab-initio total energy calculations for metals and semiconductors using a plane-wave basis set. *Comput. Mater. Sci.* 1996, 6, 15-50.

**29.** Perdew, J. P.; Burke, K.; Ernzerhof, M. Generalized gradient approximation made simple. *Phys. Rev. Lett.* 1996, 77, 3865-3868.

**30.** Lee, S. H.; Kang, J. H.; Kang, M. H. Structural properties of semiconductors in the generalized gradient approximation. *J. Korean Phys. Soc.* 1997, 31, 811-814.

**31.** Blochl, P. E., Projector Augmented-Wave Method. *Phys. Rev. B* 1994, 50, 17953-17979.

**32.** Anisimov, V. I.; Zaanen, J.; Andersen, O. K. Band Theory and Mott Insulators - Hubbard-U Instead of Stoner-I. *Phys. Rev. B* 1991, 44, 943-954.

**33.** Anisimov, V. I.; Solovyev, I. V.; Korotin, M. A.; Czyzyk, M. T.; Sawatzky, G. A. Density-Functional Theory and Nio Photoemission Spectra. *Phys. Rev. B* 1993, 48, 16929-16934.

**34.** Jain, A.; Hautier, G.; Ong, S. P.; Moore, C. J.; Fischer, C. C.; Persson, K. A.; Ceder, G. Formation enthalpies by mixing GGA and GGA plus U calculations. *Phys. Rev. B* 2011, 84, 045115.

**35.** Wang, L.; Maxisch, T.; Ceder, G. Oxidation energies of transition metal oxides within the GGA+U framework. *Phys. Rev. B* 2006, 73, 195107

**36.** Kim, H.; Kim, D. J.; Seo, D. H.; Yeom, M. S.; Kang, K.; Kim, D. K.; Jung, Y. Ab Initio Study of the Sodium Intercalation and Intermediate Phases in $Na_{0.44}MnO_2$ for Sodium-Ion Battery. *Chem. Mater.* 2012, 24, 1205-1211.

**37.** Greedan, J. E.; Raju, N. P.; Wills, A. S.; Morin, C.; Shaw, S. M.; Reimers, J. N., Structure and magnetism in lambda-$MnO_2$. Geometric frustration in a defect spinel. *Chem. Mater.* 1998, 10, 3058-3067.

**38.** Noda, Y.; Ohno, K.; Nakamura, S. Momentum-dependent band spin splitting in semiconducting $MnO_2$: a density functional calculation. *Phys. Chem. Chem. Phys.* 2016, 18, 13294-13303.

**39.** Biskup, N.; Martinez, J. L.; de Dompablo, M. E. A. Y.; Diaz-Carrasco, P.; Morales, J. Relation between the magnetic properties and the crystal and electronic structures of manganese spinels $LiNi_{0.5}Mn_{1.5}O_4$ and $LiCu_{0.5}Mn_{1.5}O_{4-\delta}$ ($0 < \delta < 0.125$). *J. Appl. Phys.* 2006, 100, 093908.

**40.** Kitchaev, D. A.; Peng, H. W.; Liu, Y.; Sun, J. W.; Perdew, J. P.; Ceder, G. Energetics of MnO2 polymorphs in density functional theory. *Phys. Rev. B* 2016, 93, 045132.

**41.** Van der Ven, A.; Aydinol, M. K.; Ceder, G.; Kresse, G.; Hafner, J. First-principles investigation of phase stability in LixCoO2. *Phys. Rev. B* 1998, 58, 2975-2987.

**42.** Wagemaker, M.; Van Der Ven, A.; Morgan, D.; Ceder, G.; Mulder, F. M.; Kearley, G. J. Thermodynamics of spinel $Li_xTiO_2$ from first principles. *Chem. Phys.* 2005, 317, 130-136.

**43.** Aydinol, M. K.; Kohan, A. F.; Ceder, G.; Cho, K.; Joannopoulos, J. Ab initio study of lithium intercalation in metal oxides and metal dichalcogenides. *Phys. Rev. B* 1997, 56, 1354-1365.

**44.** Islam, M. S.; Fisher, C. A. J. Lithium and sodium battery cathode materials: computational insights into voltage, diffusion and nanostructural properties. *Chem. Soc. Rev.* 2014, 43, 185-204.

**45.** de Klerk, N. J. J. ; Wagemaker, M. Analysis of Diffusion in Solid-State Electrolytes through MD Simulations, Improvement of the Li-Ion Conductivity in β-$Li_3PS_4$ as an Example. *ACS Appl. Energy Mater.* 2018, 1, 3230-3242

**46.** Xia, H.; Meng, Y. S.; Lu, L.; Ceder, G. Electrochemical properties of nonstoichiometric $LiNi_{0.5}Mn_{1.5}O_{4-\delta}$ thin-film electrodes prepared by pulsed laser deposition. *J. Electrochem. Soc.* 2007, 154, A737-A743.

**47.** Vadlamani, B.; An, K.; Jagannathan, M.; Chandran, K. S. R. An In-Situ Electrochemical Cell for Neutron Diffraction Studies of Phase Transitions in Small Volume Electrodes of Li-Ion Batteries. *J. Electrochem. Soc.* 2014, 161, A1731-A1741.

**48.** Kitchaev, D. A.; Dacek, S. T.; Sun, W. H.; Ceder, G., Thermodynamics of Phase Selection in $MnO_2$ Framework Structures through Alkali Intercalation and Hydration. *J. Am. Chem. Soc.* 2017, 139, 2672-2681.

**49.** Tompsett, D. A.; Islam, M. S. Electrochemistry of Hollandite alpha-MnO2: Li-Ion and Na-Ion Insertion and $Li_2O$ Incorporation. *Chem. Mater.* 2013, 25, 2515-2526.

**50.** Karim, A.; Fosse, S.; Persson, K. A., Surface structure and equilibrium particle shape of the $LiMn_2O_4$ spinel from first-principles calculations. *Phys. Rev. B* 2013, 87, 075322.

**51.** Ning, F. H.; Xu, B.; Shi, J.; Su, H. B.; Wu, M. S.; Liu, G.; Ouyang, C. Y. Ab initio investigation of Jahn-Teller-distortion-tuned Li-ion migration in lambda-$MnO_2$. *J. Mater. Chem. A* 2017, 5, 9618-9626.

**52.** Vasileiadis, A.; Wagemaker, M. Thermodynamics and Kinetics of Na-Ion Insertion into Hollandite-$TiO_2$ and O3-Layered $NaTiO_2$: An Unexpected Link between Two Promising Anode Materials for Na-Ion Batteries. *Chem. Mater.* 2017, 29, 1076-1088.

**53.** Ling, C.; Mizuno, F. Phase Stability of Post-spinel Compound $AMn_2O_4$ (A = Li, Na, or Mg) and Its Application as a Rechargeable Battery Cathode. *Chem. Mater.* 2013, 25, 3062-3071.

**54.** Ma, X. H.; Chen, H. L.; Ceder, G., Electrochemical Properties of Monoclinic $NaMnO_2$. *J. Electrochem. Soc.* 2011, 158, A1307-A1312.

**55.** de Klerk, N. J. J.; Vasileiadis, A.; Smith, R. B.; Bazant, M. Z.; Wagemaker, M. Explaining key properties of lithiation in $TiO_2$-anatase Li-ion battery electrodes using phase field modeling *Phys. Rev. Mater.* 2017, 1, 025404.

**56.** Bazant, M. Z. Theory of Chemical Kinetics and Charge Transfer based on Nonequilibrium Thermodynamics. *Accounts Chem. Res.* 2013, 46, 1144-1160.

**57.** Bai, P.; Cogswell, D. A.; Bazant, M. Z. Suppression of Phase Separation in $LiFePO_4$ Nanoparticles During Battery Discharge. *Nano Lett.* 2011, 11, 4890-4896.

**58.** Zhang, X. Y.; van Hulzen, M.; Singh, D. P.; Brownrigg, A.; Wright, J. P.; van Dijk, N. H.; Wagemaker, M. Direct view on the phase evolution in individual $LiFePO_4$ nanoparticles during Li-ion battery cycling. *Nat. Commun.* 2015, 6, 8333.

**59.** Zhang, X. Y.; van Hulzen, M.; Singh, D. P.; Brownrigg, A.; Wright, J. P.; van Dijk, N. H.; Wagemaker, M. Rate-Induced Solubility and Suppression of the First-Order Phase Transition in Olivine $LiFePO_4$. *Nano Lett.* 2014, 14, 2279-2285.

**60.** Niu, J. J.; Kushima, A.; Qian, X. F.; Qi, L.; Xiang, K.; Chiang, Y. M.; Li, J. In Situ Observation of Random Solid Solution Zone in $LiFePO_4$ Electrode. *Nano Lett.* 2014, 14, 4005-4010.

**61.** Akimoto, J.; Awaka, J.; Kijima, N.; Takahashi, Y.; Maruta, Y.; Tokiwa, K.; Watanabe, T., High-pressure synthesis and crystal structure analysis of $NaMn_2O_4$ with the calcium ferrite-type structure. *J. Solid State Chem.* 2006, 179, 169-174.

**62.** Bhattacharya, J.; Wolverton, C. Relative stability of normal vs. inverse spinel for 3d transition metal oxides as lithium intercalation cathodes. *Phys. Chem. Chem. Phys.* 2013, 15, 6486-6498.

**63.** Bhattacharya, J.; Van der Ven, A. Phase stability and nondilute Li diffusion in spinel $Li_{1+x}Ti_2O_4$. *Phys. Rev. B* 2010, 81, 104304.

**64.** Ouyang, C. Y.; Shi, S. Q.; Lei, M. S. Jahn-Teller distortion and electronic structure of $LiMn_2O_4$. *J. Alloys Compd.* 2009, 474, 370-374.

**65.** Xu, B.; Meng, S., Factors affecting Li mobility in spinel $LiMn_2O_{4-\alpha}$ first-principles study by GGA and GGA plus U methods. *J. Power Sources* 2010, 195, 4971-4976.

**66.** Radin, M. D.; Van der Ven, A., Simulating Charge, Spin, and Orbital Ordering: Application to Jahn-Teller Distortions in Layered Transition-Metal Oxides. *Chem. Mater.* 2018, 30, 607-618.

**67.** Ohzuku, T.; Kitagawa, M.; Hirai, T. Electrochemistry of Manganese-Dioxide in Lithium Nonaqueous Cell .3. X-Ray Diffractional Study on the Reduction of Spinel-Related Manganese-Dioxide. *J. Electrochem. Soc.* 1990, 137, 769-775.

**68.** Dathar, G. K. P.; Sheppard, D.; Stevenson, K. J.; Henkelman, G., Calculations of Li-Ion Diffusion in Olivine Phosphates. *Chem. Mater.* 2011, 23, 4032-4037.

**69.** Mo, Y. F.; Ong, S. P.; Ceder, G. Insights into Diffusion Mechanisms in $P_2$ Layered Oxide Materials by First-Principles Calculations. *Chem. Mater.* 2014, 26, 5208-5214.

**70.** Guo, S. H.; Sun, Y.; Yi, J.; Zhu, K.; Liu, P.; Zhu, Y. B.; Zhu, G. Z.; Chen, M. W.; Ishida, M.; Zhou, H. S. Understanding sodium-ion diffusion in layered P2 and P3 oxides via experiments and first-principles calculations: a bridge between crystal structure and electrochemical performance. *NPG Asia Mater.* 2016, 8, e266.

**71.** Wu, D.; Li, X.; Xu, B.; Twu, N.; Liu, L.; Ceder, G., $NaTiO_2$: a layered anode material for sodium-ion batteries. *Energy Environ. Sci.* 2015, 8, 195-202.

**72.** Bhattacharya, J.; Van der Ven, A. First-principles study of competing mechanisms of nondilute Li diffusion in spinel $Li_xTiS_2$. *Phys. Rev. B* 2011, 83, 144302.

# Summary

Computational modeling is shaping the fundamental understanding of key thermodynamic and kinetic properties in batteries, the importance of which is undeniable for the implementation of next-generation batteries, mobile and large-scale applications (chapter 1). In the present thesis, we employ density functional theory (DFT) at the nanoscale and phase field modeling at the mesoscale (chapter 2) to study both state-of-the-art and novel battery chemistries.

In chapter 3, we computationally explore the atomic scale mechanism that governs the (dis)charging (lithiation and delithiation) of the defective spinel $Li_{4+x}Ti_5O_{12}$ (LTO) structure. Modern battery applications require high power density as well as a stable cycle life. One of the most stable anode materials that can be cycled for thousands of times with excellent capacity retention is LTO. Although well studied and widely used commercially, the nature of the phase transition and the role of interfaces raises many questions, fed by the difficulty to distinguish the two end-member phases ($Li^{8a}$ and $Li^{16c}$ domains) with various experimental techniques. Using DFT and molecular dynamics (MD) calculations, we show that the interface between the two end-member phases is stabilized by the Li atoms present in the host structure ($Li^{16d}$), creating the conditions for intimate mixing of the $Li^{8a}$ and $Li^{16c}$ domains. The domains, however, remain separated at the nanoscale, revealing a true thermodynamic first-order phase transition. This prediction explains both the previous solid solution interpretations and the observation of domain structures. The $Li^{16d}$ atoms also play a pivotal role in the kinetics of the system, allowing facile transitions between the $Li^{8a}/Li^{16c}$ domain interface configurations. These transitions induce rapidly moving interfaces between the $Li^{8a}$ and $Li^{16c}$ domains, explaining the excellent kinetic performance.

Having obtained an in–depth understanding at the nanoscale with DFT, we employ phase field modeling to study the mesoscale behavior of LTO in realistic electrode morphologies (chapter 4). Capturing the nature of the phase transition (phase separation) in porous electrode theory is proven to be of key importance to efficiently describe electrode behavior. We can successfully reproduce experimental results for a variety of electrode morphologies and a wide current range. Our model offers insight in important battery aspects such as the Li-ion depth profile in the solid electrode, the overpotential contributions of several processes to the total overpotential and the active particle fraction as a function of the state of charge and the C-rate. Being able to determine the rate limiting factors enabled optimization of the LTO electrodes through a number of capacity maps that can guide experimentalists. The performance of the solid LTO nanoparticles

particles is excellent, allowing full lithiation in a matter of a few seconds. This is, however, away from all practical applications. For battery morphologies aimed for commercial use, electrode thickness, porosity and tortuosity play a pivotal role in performance.

Starting in chapter 5, we study the Na-ion battery chemistry via the DFT method, which offers a cheap and sustainable alternative to Li-ion, aimed for large-scale applications suitable for implementing renewable energy sources. Following the sodiation of the hollandite $TiO_2$ anode material, we confirm the phase transition from tetragonal $TiO_2$ (I4/m) to monoclinic $Na_{0.25}TiO_2$ (I2/m). A two-phase separation mechanism was predicted upon further sodiation, transforming the hollandite structure to the O'3 layered $Na_{0.68}TiO_2$ phase. Further sodiation initiates a solid solution reaction towards the layered O3-$NaTiO_2$ phase, which was recently brought forward as a promising anode for Na-ion batteries. The thermodynamic analysis provides insight in the preferred reaction mechanism throughout the sodiation process. Investigation of the kinetic performance reveals excellent Na-ion kinetics reaching the $Na_{0.25}TiO_2$ phase, where diffusion slows down due to the Coulomb interactions along the 1D diffusion channels, explaining the experimentally observed limitations. Excellent kinetics were predicted for the layered regime where the dominant divacancy hopping mechanism was directly observed via MD simulations.

Chapter 6 continues the investigation regarding Na-ion battery chemistries, this time for the high-voltage spinel $\lambda\text{-}Mn_2O_4$ and $\lambda\text{-}Mn_{1.5}Ni_{0.5}O_4$ materials. The pure spinel is predicted to be metastable compared to the O3 layered phase, rationalizing experimental results showing a partial phase transformation. The importance of strain minimization is also stretched. For the $\lambda\text{-}Mn_{1.5}Ni_{0.5}O_4$, we explore the role of Ni in tuning the reaction mechanisms and reveal Ni migration in the host structure. This explains the kinetic limitations explored experimentally and brings forward a normal to inverse spinel half-transformation.

Overall, this work, bridges computationally several length-scales (from nanoscale to mesoscale) by implementing thermodynamic parameters determined with DFT into mesoscale modeling. Our results underline that in order to achieve an accurate description of an electrode material, the nature of the phase transition needs to be computationally captured. This approach paves the way for a more concrete and complete electrode description, enhancing the descriptive and predictive character of battery modeling. In addition, the present thesis sheds light on the strengths and limitations of Na-ion batteries, contributing to the understanding and implementation of battery systems suitable for sustainable energy applications.

# Samenvatting

Computermodelleren vormt het fundamentele begrip van de belangrijkste thermodynamische en kinetische eigenschappen van batterijen, waarvan het belang niet ontkend kan worden voor de implementatie van de volgende generatie batterijen, voor zowel mobiele en grootschalige toepassingen (hoofdstuk 1). Om moderne en nieuwe chemie voor batterijen te bestuderen gebruiken wij in dit proefschrift dichtheidsfunctionaaltheorie (DFT) voor de nanoschaal en fasenveldmodellering voor de mesoschaal (hoofdstuk 2).

In hoofdstuk 3 onderzoeken wij computationeel het mechanisme dat op atomaire schaal het (ont)laden (lithiatie en delithiatie) van de $Li_{4+x}Ti_5O_{12}$ (LTO) defecte spinel structuur bepaald. Moderne batterij toepassingen moeten zowel een hoge vermogensdichtheid als een stabiel levenscyclus hebben. Een van de meest stabiele anodematerialen, die duizenden cycli gebruikt kan worden met uitstekend capaciteitsbehoud, is LTO. Alhoewel het goed bestudeerd is en alom gebruikt wordt voor commerciële toepassingen roept de aard van de faseverandering en de rol van grensvlakken vele vragen op. Deze vragen worden gevoed doordat de twee eindfases ($Li^{8a}$ en $Li^{16c}$ domeinen) moeilijk van elkaar te onderscheiden zijn met experimentele technieken. Met DFT en moleculaire dynamica (MD) berekeningen laten wij zien dat de grensvlakken tussen de twee eindfases gestabiliseerd worden door de lithium atomen die aanwezig zijn in de accomoderende structuur ($Li^{16d}$), wat de condities creëert voor intieme vermenging tussen de $Li^{8a}$ en $Li^{16c}$ domeinen. De domeinen blijven echter gescheiden op de nanoschaal, wat een thermodynamische eerste-orde fasescheiding onthuld. Deze voorspelling verklaard de voorgaande vaste-oplossing interpretaties van experimenten, alsmede de observaties van domeinstructuren. De $Li^{16c}$ atomen spelen ook een doorslaggevende rol in de kinetiek van het systeem door gemakkelijke overgangen tussen $Li^{8a}/Li^{16c}$ domeingrenzen mogelijk te maken. Deze overgangen veroorzaken snel bewegende grensvlakken tussen de $Li^{8a}/Li^{16c}$ domeinen, wat de uitstekende kinetische prestaties verklaard.

Na met DFT een diep begrip verkregen te hebben over de nanoschaal gebruiken wij fasenveldmodellering om het mesoschaal gedrag van LTO in realistische elektrodemorfologieën te bestuderen (hoofdstuk 4). Het correct beschrijven van de aard van de faseovergang (fasescheiding) is van cruciaal belang om in poreuze electrode theorie het elektrodegedrag efficiënt te beschrijven. Experimentele resultaten van een variëteit aan elektrodemorfologieën en een breed bereik aan stroomsterktes kunnen wij hiermee succesvol reproduceren. Ons model geeft ook inzicht in belangrijke aspecten van batterijen, zoals het diepteprofiel van

Li-ionen in de elektrode, de bijdrage van verschillende processen aan de totale overpotentiaal en de actieve deeltjesfractie als functie van ontladingstoestand en ontlaadsnelheid. De mogelijkheid om de snelheidsbeperkende factoren te bepalen maakt de optimalisatie van LTO elektrodes mogelijk doormiddel van een aantal capaciteitskaarten die experimentalisten richting kan geven. De prestaties van de LTO nanodeeltjes is uitstekend, wat volledige lithiatie in enkele seconden mogelijk maakt. Dit is echter ver verwijderd van alle praktische toepassingen. Voor batterijmorfologieën gericht op commerciële toepassingen spelen de elektrodedikte, porositeit en de bochtigheidscoëfficiënt een essentiële rol.

In hoofdstuk 5 wordt gestart met het bestuderen van de chemie van Na-ion batterijen, die een goedkoop en duurzaam alternatief bieden voor Li-ion batterijen en vooral gericht zijn op grootschalige toepassingen voor de implementatie van hernieuwbare energiebronnen. Door de natriatie van het anode materiaal hollandiet $TiO_2$ te volgen bevestigen wij de faseovergang van tetragonaal $TiO_2$ (I4/m) naar monoklien $Na_{0.25}TiO_2$ (I2/m). Een fasescheidingsmechanisme wordt voorspeld als de natriatie doorgezet wordt, wat de hollandietstructuur transformeert naar de gelaagde O’3 $Na_{0.68}TiO_2$-fase. Verdere natriatie leidt tot een vaste-oplossingreactie naar de gelaagde O3-$NaTiO_2$ fase, wat onlangs als een veelbelovende anode voor Na-ion batterijen is gepresenteerd. Deze thermodynamische analyse geeft inzicht in het geprefereerde reactiemechanisme gedurende het natriatieproces. Onderzoek naar de kinetische prestaties onthuld uitstekende Na-ion kinetiek tot aan het bereiken van de $Na_{0.25}TiO_2$-fase, waar diffusie langzamer wordt door de Coulombinteracties tussen de eendimensionale diffusiekanalen, wat experimenteel geobserveerde beperkingen verklaard. Uitstekende kinetiek is ook voorspeld voor het gelaagde regime, waarin het dominante mechanisme van dubbele vacaturesprongen rechtstreeks is geobserveerd door middel van MD simulaties.

In hoofdstuk 6 wordt verder gegaan met het onderzoek naar materialen voor Na-ion batterijen, meer specifiek naar de hoogvoltage spinelmaterialen λ-$Mn_2O_4$ en λ-$Mn_{1.5}Ni_{0.5}O_4$. Er wordt voorspeld dat het zuivere spinel metastabiel is in vergelijking met de O3-gelaagde fase, wat experimentele resultaten die een gedeeltelijke faseovergang laten zien verklaard. Het belang van vervorming van de kristalstructuur wordt ook benadrukt. Voor λ-$Mn_{1.5}Ni_{0.5}O_4$ verkennen wij hoe Ni gebruikt kan worden om het reactiemechanisme aan te passen en onthullen wij dat er Ni-migratie optreedt in de accomoderende structuur. Deze resultaten verklaren de kinetische beperkingen die experimenteel ontdekt zijn en laat de transformatie van de normale structuur naar de inverse spinel structuur zien.

In zijn geheel overbrugd het werk in dit proefschrift verscheidene lengteschalen (van nanoschaal naar mesoschaal) door het implementeren van thermodynamische parameters bepaald met DFT in modellen op de mesoschaal. Onze resultaten benadrukken dat voor een nauwkeurige beschrijving van een elektrodemateriaal de aard van de faseovergang computationeel correct beschreven moet worden. Deze aanpak effent de weg voor een concretere en completere beschrijving van elektrodes, wat batterijmodellen een beter beschrijvend en voorspellend karakter geeft. Daarnaast verhelderd dit proefschrift de mogelijkheden en beperkingen van Na-ion batterijen, wat bijdraagt aan het begrijpen en het implementeren van batterijsystemen die geschikt zijn voor duurzame energietoepassingen.

# Appendix

## A.

The following tables present the calculated energy barriers E for a variety of options for the studied supercells, t is the total simulation time. The temperature of the first three tables is 520 K and the threshold time of the last table is 0.1 ps.

| Composition | t (ps) | Equilibration Time (ps) | Threshold Time (ps) | E (eV) 8a → 16c | E (eV) 16c → 8a |
|---|---|---|---|---|---|
| A:$Li_{5.2}Ti_5O_{12}$ | 185 | 3 | 0.1 | 0.28 | 0.28 |
| A:$Li_{5.2}Ti_5O_{12}$ | 185 | 30 | 0.1 | 0.28 | 0.28 |
| A:$Li_{5.2}Ti_5O_{12}$ | 185 | 60 | 0.1 | 0.29 | 0.29 |
| A:$Li_{5.2}Ti_5O_{12}$ | 185 | 80 | 0.1 | 0.30 | 0.30 |
| A:$Li_{5.2}Ti_5O_{12}$ | 185 | 100 | 0.1 | 0.31 | 0.31 |

| Composition | t (ps) | Equilibration Time (ps) | Threshold Time (ps) | E (eV) 8a → 16c | E (eV) 16c → 8a |
|---|---|---|---|---|---|
| A:$Li_{5.2}Ti_5O_{12}$ | 185 | 100 | 0 | 0.30 | 0.30 |
| A:$Li_{5.2}Ti_5O_{12}$ | 185 | 100 | 0.1 | 0.31 | 0.31 |
| A:$Li_{5.2}Ti_5O_{12}$ | 185 | 100 | 0.2 | 0.33 | 0.33 |
| A:$Li_{5.2}Ti_5O_{12}$ | 185 | 100 | 0.3 | 0.35 | 0.35 |
| A:$Li_{5.2}Ti_5O_{12}$ | 185 | 100 | 0.4 | 0.36 | 0.36 |

| Composition | t (ps) | Equilibration Time (ps) | Threshold Time (ps) | E (eV) 8a → 16c | E (eV) 16c → 8a |
|---|---|---|---|---|---|
| A:$Li_{5.2}Ti_5O_{12}$ | 185 | 3 | 0 | 0.27 | 0.27 |
| A:$Li_{5.2}Ti_5O_{12}$ | 185 | 3 | 0.1 | 0.28 | 0.28 |
| A:$Li_{5.2}Ti_5O_{12}$ | 185 | 3 | 0.2 | 0.30 | 0.30 |
| A:$Li_{5.2}Ti_5O_{12}$ | 185 | 3 | 0.3 | 0.31 | 0.31 |
| A:$Li_{5.2}Ti_5O_{12}$ | 185 | 3 | 0.4 | 0.31 | 0.31 |

| Composition | T (K) | t (ps) | Equilibration Time (ps) | E (eV) 8a → 16c | E (eV) 16c → 8a |
|---|---|---|---|---|---|
| A:$Li_{5.2}Ti_5O_{12}$ | 300 | 96 | 3 | 0.19 | 0.19 |
| A:$Li_{5.2}Ti_5O_{12}$ | 420 | 85 | 3 | 0.24 | 0.24 |
| A:$Li_{5.2}TO_{12}$ | 520 | 185 | 3 | 0.28 | 0.28 |
| A:$Li_{5.2}Ti_5O_{12}$ | 600 | 70 | 3 | 0.30 | 0.31 |
| B:$Li_{5.7}Ti_5O_{12}$ | 600 | 54 | 3 | 0.29 | 0.29 |

## B.

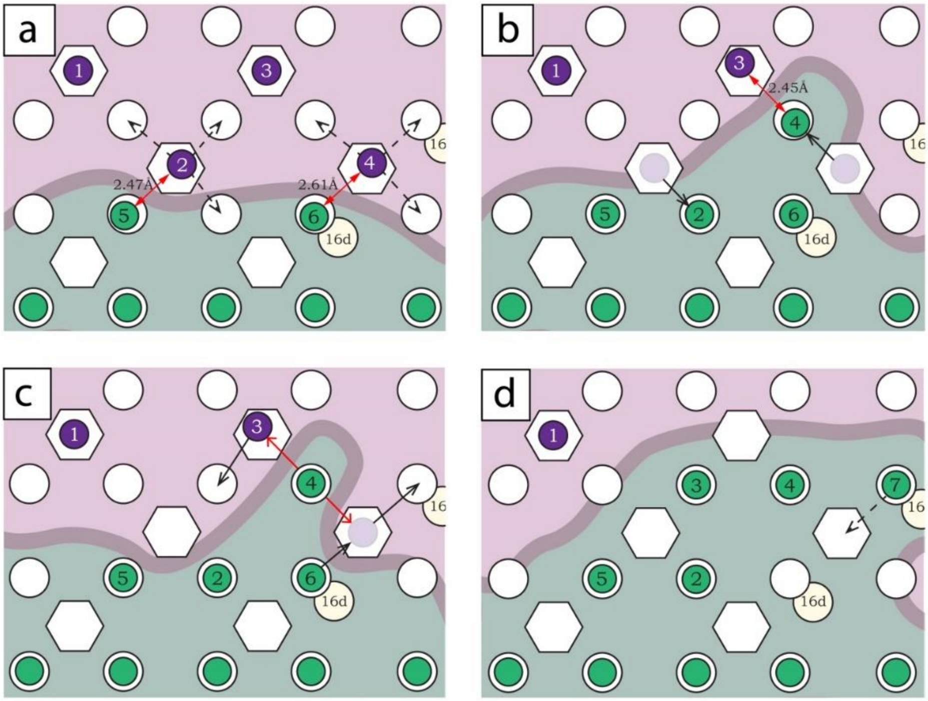

**Figure A1:** Time lapse that depicts the Li-ion reaction mechanisms as viewed from the xz plane of a small part of the 2x1x2 supercell at the first ps of the MD simulation, dashed lines indicate the possibility of hop while the solid line the hop that actually occurs. The red line reflects the type 1 interface configurations presented in the report

Figure A1 begins with a mixed 16c/8a site occupation described in the main text. Here we depict another simultaneous hop (Figure A1b). In the next instance, from the variety of jumps along the interface Li6 is hopping towards an 8a (Figure 10c). If this happens the system will be in an energetically unfavorable mixed occupation state where Li in a 16c site is in between two 8a sites. For this reason, the system is forced to another simultaneous jump (Figure A1c) that spontaneously forces $Li_6$ and $Li_3$ in adjacent 16c positions. This is another rare example of 16c-8a-16c hop where the Li-ion resides in the intermediate site for less than 0.01ps. This jump sequence trapped $Li_2$ within the bulk of the 16c phase. Until the end of the simulation the interface does not pass by Li2 that does not hop once in the remaining 185ps of the simulation (Figure A1d).

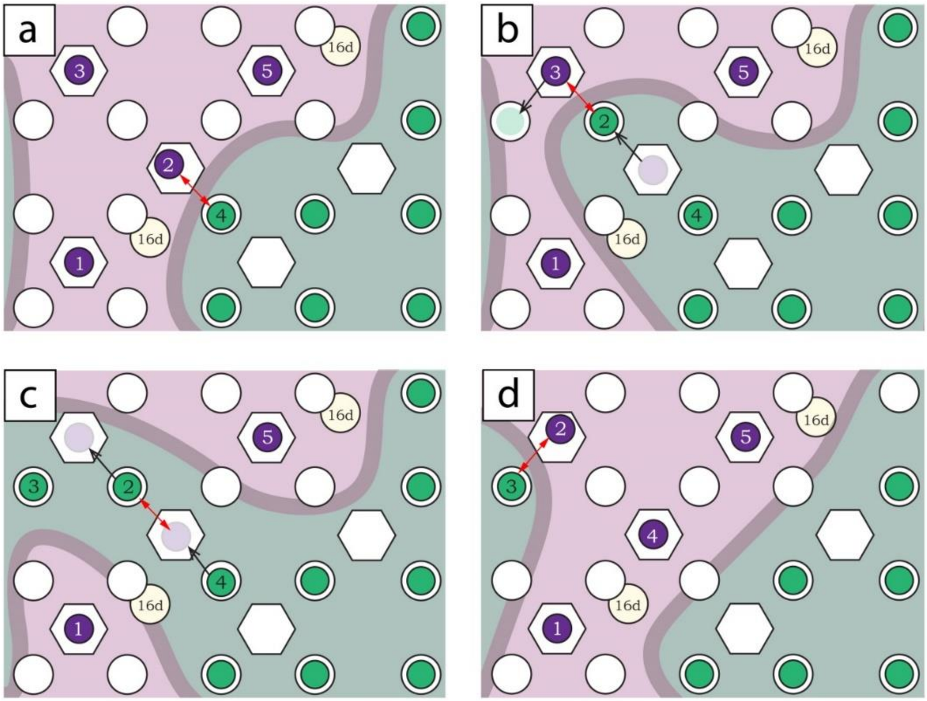

**Figure A2:** Time lapse that depicts the Li-ion reaction mechanisms as viewed from the xz plane of a small part of the 2x1x2 supercell around 110ps in the simulation. This figure shows an example of a jump occurring at 110 ps were a correlated hops are still possible even in equilibrium while at the same time it depicts a way of cutting through a thin Li-poor domain.

**C**

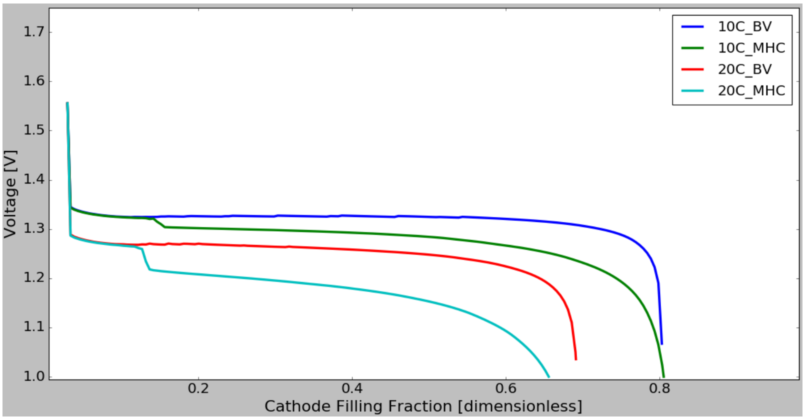

**Figure A3:** Voltage profiles of preliminary implementation of MHC kinetics vs. the state-of-the-art BV kinetics for identical LTO electrodes at 10 and 20C.

**D**

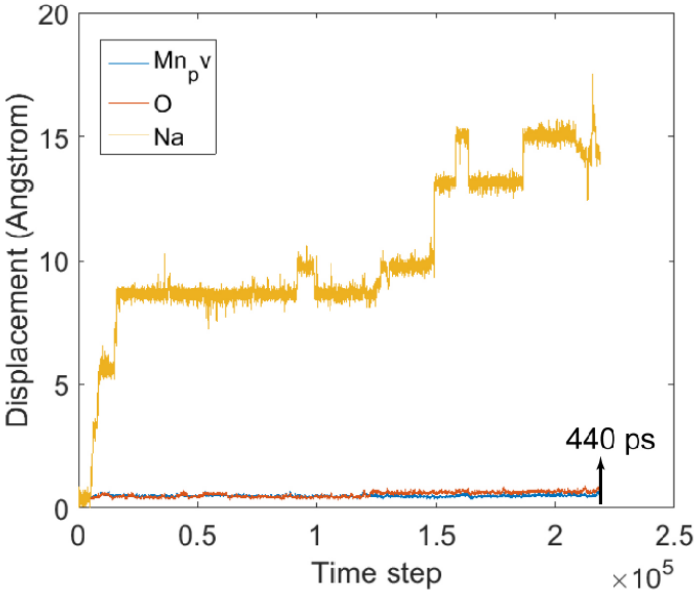

**Figure A4:** Atom displacements for a 440 ps MD simulation of the pure MO phase at 600 K

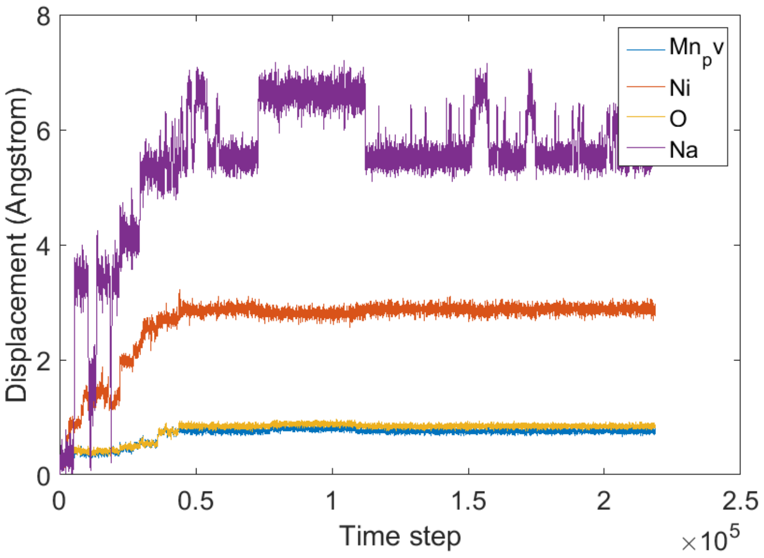

**Figure A5:** Atom displacements for a 440 ps MD simulation of the F2 - MNO phase at 600 K

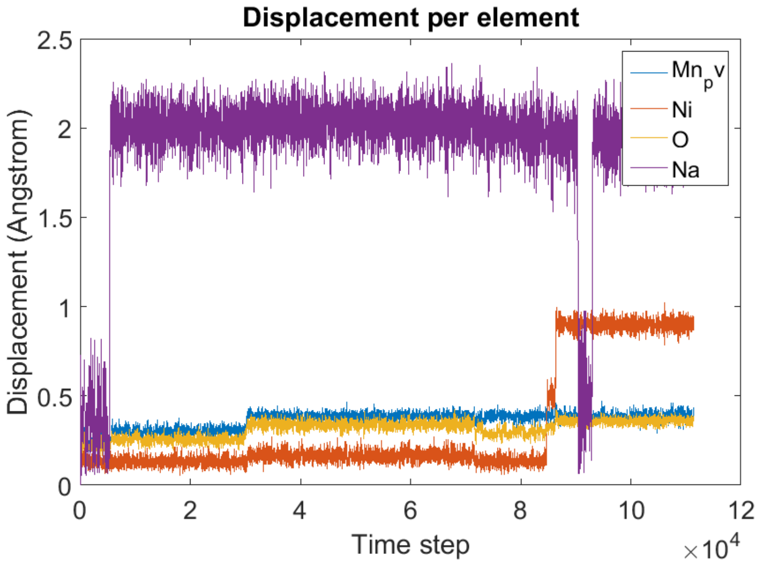

**Figure A6:** Atom displacements for a 440 ps MD simulation of the F2 - MNO phase at 300 K

# List of Publications

## Publications related to this thesis

**1.** Swapna Ganapathy[†], Alexandros Vasileiadis[†], Jouke R. Heringa, Marnix Wagemaker - The Fine Line between a Two-Phase and Solid-Solution Phase Transformation and Highly Mobile Phase Interfaces in Spinel $Li_{4+x}Ti_5O_{12}$.

(† co-first author)

*Advanced Energy Materials*, **2017** DOI: 10.1002/aenm.201601781

**2.** Alexandros Vasileiadis, Niek J. J. de Klerk, Raymond B. Smith, Swapna Ganapathy, Peter Paul R. M. L. Harks, Martin Z. Bazant and Marnix Wagemaker - Toward Optimal Performance and In-Depth Understanding of Spinel $Li_4Ti_5O_{12}$ Electrodes through Phase Field Modeling.

*Advanced Functional Materials*, **2018** DOI: 10.1002/adfm.201705992

**3.** Alexandros Vasileiadis, Marnix Wagemaker - Thermodynamics and Kinetics of Na-Ion Insertion into Hollandite- TiO2 and O3-Layered NaTiO2: An Unexpected Link between Two Promising Anode Materials for Na-Ion Batteries

*Chemistry of Materials*, **2017** DOI: 10.1021/acs.chemmater.6b03928

**4.** Alexandros Vasileiadis, Brian Carlsen, Niek J. J. de Klerk, Marnix Wagemaker - Ab-initio Study of Sodium Insertion in the λ-$Mn_2O_4$ and Dis/Ordered λ-$Mn_{1.5}Ni_{0.5}O_4$ Spinels.

*Chemistry of Materials*, **2018** (in press)

**Other publications**

**5.** Niek J. J. de Klerk[†], Alexandros Vasileiadis[†], Raymond B. Smith, Martin Z. Bazant and Marnix Wagemaker - Explaining key properties of lithiation in TiO2-anatase Li-ion battery electrodes using phase-field modeling.

(† co-first author)

*Physical Review Materials,* **2017** DOI: 10.1103/PhysRevMaterials.1.025404

**6.** Shasha Lv, Tomas Verhallen, Alexandros Vasileiadis, Frans Ooms, Yaolin Xu, Zhaolong Li, Zhengcao Li, Marnix Wagemaker - Operando monitoring the lithium spatial distribution of lithium metal anodes.

*Nature Communications,* **2018** DOI: 10.1038/s41467-018-04394-3

**7.** Aleksandra Ioannidou, Alexandros Vasileiadis, Dimitris Melas - Time lag between the tropopause height and Be-7 activity concentrations on surface air.

*Journal of Environmental Radioactivity*, **2014** DOI:10.1016/j.jenvrad.2013.12.013

**8.** Nicolas C. Habisreutinger, Remco Van der Jagt, Alexandros Vasileiadis, Pengpeng Shao, Xiao Feng, Marnix Wagemaker, Sybrand Van der Zwaag, Atsushi Nagai – Innovative ambivalent lithium/sodium ion energy storage with aromatic di-imide build up Covalent Organic Framework.

(in preparation)

# Conferences

**1.** The Fine Line Between a Two-Phase and Solid-Solution Transformation in $Li_{4+X}Ti_5O_{12}$, The 18th International Meeting on Lithium Batteries (IMLB), June 19 – 24, 2016 Chicago – Illinois, U.S.A. (poster presentation)

**2**. Explaining Key Properties of Lithiating $TiO_2$-Anatase: A Phase Field Model for Materials with Multiple Phases, The 18th International Meeting on Lithium Batteries (IMLB), June 19 – 24, 2016 Chicago – Illinois, U.S.A. (poster contribution)

**3.** Toward Optimal Performance and In-Depth Understanding of Spinel $Li_4Ti_5O_{12}$ Electrodes through Phase Field Modeling, The 19th International Meeting on Lithium Batteries (IMLB), June 17 – 22, 2018 Kyoto – Japan. (poster presentation)

**4**. Tunable Organic Polymers for Sodium Aqueous Batteries. The 19th International Meeting on Lithium Batteries (IMLB), June 17 – 22, 2018 Kyoto – Japan. (poster contribution)

**5.** The Fine Line Between a Two-Phase and Solid-Solution Transformation in $Li_{4+X}Ti_5O_{12}$, 67th Annual Meeting of the International Society of Electrochemistry (ISE), 21 – 26 August, 2016, The Hague, The Netherlands (poster presentation)

**6.** Time lag between the tropopause height and the levels of $^7$Be concentration in near surface air Nuclear physics conference 19th Hellenic Nuclear Physics Society Symposium, 28-29 May, 2010, Thessaloniki, Greece (oral presentation)

**7.** Time lag between the tropopause height and the levels of $^7$Be concentration, International Conference on Environmental Radioactivity - New Frontiers and Developments, 25 to 27 October 2010, Rome, Italy (poster presentation)

# Acknowledgments

I would like to express my sincere thanks to the people who contributed to the completion of this PhD Thesis.

I am deeply grateful to my promotor, Dr. ir. Marnix Wagemaker, who offered a warm and productive working environment, creating the conditions for academic and personal development. He supported my efforts and guided me through all stages of this paper, with his valuable advice and suggestions, his keen encouragement and on-going monitoring of my research. His rigorous treatment and scientific guidance enabled me to achieve a deeper understanding of battery science and made this work meaningful and fruitful.

Furthermore, I would like to express my gratitude to my promotor Prof. dr. Ekkes Brück for his insightful comments and his very efficient and thorough remarks on my thesis.

I would also heartily like to thank the other excellent members of my examination committee for their careful consideration of my thesis.

Next, I would like to express my sincere gratitude to Prof. of MIT Martin Z. Bazant and Dr. Raymond B. Smith, who gave me a heartfelt welcome, integrating me to their group, giving me the opportunity to work in a highly stimulating research environment and generously offered their help whenever I asked for it. Their in-depth battery of knowledge shaped my understanding of modeling electrode materials.

I am also incredibly thankful to the academic and technical team of FAME and SEE for their effective cooperation, constructive feedback and willingness to help me to finish this doctoral dissertation, each one from their own position: Prof. dr. F.M. Mulder, dr. Swapna Ganapathy, dr. Jouke R. Heringa, dr. ir. Niels H. van Dijk, dr. Kees Goubitz, dr. Erik M. Kelder, Michel P. Steenvoorden and Frans G.B. Ooms.

I would especially like to thank all my SEE and FAME colleagues and students for their scientific discussions, collaboration and their friendliness and kindness over the years we have worked together: Bass, Bauke, Brian, Carla, Casper, Chandra, Chadi, Chao, Chuang, Deepak, Eveline, Kajan, Kun Shen, Martjin, Michael, Ming, Niek, Peter-Paul, Remco, Shiv, Thang, Tomas, Violetta, Yaolin and Zhaolong. Special thanks also to the secretaries Nicole and Ilse for their help in administration issues and organizing trips.

Last but not least, I would like to express my deepest love to my biggest supporters, my family. Thank you for constantly putting my happiness before your own and for all the opportunities you have given me in order to reach the utmost success.

*Alexandros Vasileiadis*

*April - 2018*

# Curriculum Vitae

Alexandros Vasileiadis was born on April 12th, 1988 in Larisa, central Greece. His family moved to Thessaloniki where he received primary and secondary education. In September 2006, he enrolled in the Physics Department of the Aristotle University of Thessaloniki. In 2011, he was awarded a bachelor degree with a specialization in atmospheric physics. During his studies, he participated in the renewable energy oriented workshop held by the German Academic Exchange Service (DAAD Alumni Workshop 2010, Thessaloniki, Greece, May 2010). He also participated in several conferences. Additionally he worked as a computer lab assistant at the Aristotle University and taught physics at a vocational senior high school to students wishing admission to technological university faculties

In September 2012, he moved to the Netherlands, beginning his Master's studies in Sustainable Energy Technology at the Tecnische Universiteit Delft (TU Delft). There, he mastered the fundamental principles and novel technologies of renewable energy sources. In the context of his master's studies, he completed various group projects including a niche-management analysis on the implementation of photovoltaics in Greece and a system integration project aimed at designing an energy autonomous system suited for a ten-building, diving center on the island of Kelyfos, Greece. He, also, worked as an international student coach (August, 2013) organizing and participating in activities with new students at TU Delft. Realizing that the number one challenge of energy supply in the future is energy storage, he focused on the specialization of "hydrogen and electrochemical energy systems" where he was first introduced to the Li and Na-ion battery technologies. He completed his master's thesis entitled: "Titanium oxide structures as potential electrode materials for Na-ion batteries" for which he performed experimental and computational work. In June 2014, he obtained his Master's of Science and Engineering degree, earning the title of Ir.

His increasing interest in energy storage led him to pursue a Ph.D. degree at the section of Fundamental Aspects of Material and Energy (FAME), Department of Radiation Science Technology of TU Delft, under the supervision of Dr. Ir. Marnix Wagemaker, producing the results presented in this doctoral thesis and developing his knowledge through a number of fruitful collaborations and conferences. In the course of his studies (2015), he conducted research as an Ph.D. student visitor at the Massachusetts Institute of Technology (MIT) joining the group of Professor and Executive Officer of Chemical Engineering and Professor of Mathematics, Martin Z. Bazant. During his visit, he trained in computational science with modeling. He also participated in micro-beam diffraction experiments at the European Synchrotron Radiation Facility (ESRF) in Grenoble, France (2015-2017). Furthermore, he taught student groups and individuals, as teaching assistant to the battery course and daily supervisor of several master’s and bachelor students.